

NON-REDUNDANT APERTURE MASKING  
INTERFEROMETRY WITH ADAPTIVE OPTICS:  
DEVELOPING HIGHER CONTRAST IMAGING TO  
TEST BROWN DWARF AND EXOPLANET  
EVOLUTION MODELS

A Dissertation

Presented to the Faculty of the Graduate School  
of Cornell University

in Partial Fulfillment of the Requirements for the Degree of  
Doctor of Philosophy

by

David Bernat

January 2012

© 2012 David Bernat  
ALL RIGHTS RESERVED

NON-REDUNDANT APERTURE MASKING INTERFEROMETRY WITH  
ADAPTIVE OPTICS: DEVELOPING HIGHER CONTRAST IMAGING TO  
TEST BROWN DWARF AND EXOPLANET EVOLUTION MODELS

David Bernat, Ph.D.

Cornell University 2012

This dissertation presents my study of Non-Redundant Aperture Masking Interferometry (or *NRM*) with Adaptive Optics, a technique for obtaining high-contrast infrared images at diffraction-limited resolution. I developed numerical, statistical, and on-telescope techniques for obtaining higher contrast, in order to build an imaging system capable of resolving massive Jupiter analogs in tight orbits around nearby stars. I used this technique, combined with Laser Guide Star Adaptive Optics (LGSAO), to survey known brown dwarfs for brown dwarf and planetary companions. The diffraction-limited capabilities of this technique enable the detection of companions on short period orbits that make Keplerian mass measurement practical. This, in turn, provides mass and photometric measurements to test brown dwarf evolution (and atmosphere) models, which require empirical constraints to answer key questions and will form the basis for models of giant exoplanets for the next decade.

I present the results of a close companion search around 16 known brown dwarf candidates (early L dwarfs) using the first application of NRM with LGSAO on the Palomar 200" Hale Telescope. The use of NRM allowed the detection of companions between 45-360 mas in  $K_s$  band, corresponding to projected physical separations of 0.6-10.0 AU for the targets of the survey. Due to unstable LGSAO correction, this survey was capable of detecting primary-secondary contrast ratios

down to  $\Delta K_s \sim 1.5\text{-}2.5$  (10:1), an order of magnitude brighter than if the system performed at specification. I present four candidate brown dwarf companions detected with moderate-to-high confidence (90%-98%), including two with projected physical separations less than 1.5 AU. A prevalence of brown dwarf binaries, if confirmed, may indicate that tight-separation binaries contribute to the total binary fraction more significantly than currently assumed, and make excellent candidates for dynamical mass measurement. For this project, I developed several new, robust tools to reject false positive detections, generate accurate contrast limits, and analyze NRM data in the low signal-to-noise regime.

In order to increase the sensitivity of NRM, a critical and quantitative study of quasi-static wavefront errors needs to be undertaken. I investigated the impact of small-scale wavefront errors (those smaller than a sub-aperture) on NRM using a technique known as spatial filtering. Here, I explored the effects of spatial filtering through calculation, simulation, and observational tests conducted with an optimized pinhole and aperture mask in the PHARO instrument at the 200" Hale Telescope. I find that spatially filtered NRM can increase observation contrasts by 10-25% on current AO systems and by a factor of 2-4 on higher-order AO systems. More importantly, this reveals that small scale wavefront errors contribute only modestly to the overall limitations of the NRM technique without very high-order AO systems, and that future efforts need focus on temporal stability and wavefront errors on the scale of the sub-aperture. I also develop a formalism for optimizing NRM observations with these AO systems and dedicated exoplanet imaging instruments, such as Project 1640 and the Gemini Planet Imager. This work provides a foundation for future NRM exoplanet experiments.

## BIOGRAPHICAL SKETCH

David Bernat started along a trajectory towards this point early, but cemented his direction shortly after watching the Mars Pathfinder and Sojourner rover land on the surface of Mars on July 4, 1997. Later that fall, he attended the California Institute of Technology to earn a Physics B.S. while immersed in a spirited and creative scientific and academic environment. After considering multiple post-graduation options in science and engineering, but wanting to explore an application of physics outside the academic environment, he moved to New York City in 2002 to work as a strategist at Goldman Sachs in the Foreign Exchange, Currency, and Commodities sector. This opportunity became one of the most striking and stimulating experiences of his life so far. Watching the operation of the global financial machine from the inside-out during one of the most contentious and complex times during the aftermath of 9/11 and the run-up to the Iraq War has shaped his view of the world, civic citizenry, and the growth potential of well-administered organizations. He worked on projects ranging from price evaluations of derivatives on the Federal Reserve Interest Rate to projections of risk and loss by corporate and catastrophic default. In 2004, he left Goldman Sachs to move to Munich, Germany, to provide technical support at the Max Planck Institute for Physics and the DESY particle accelerator while applying to graduate schools. The following year, he began his study at Cornell University. Following his early passion for quantum mechanics and general relativity, he quickly began researching with Prof. Rachel Bean to investigate modification to General Relativity that could give rise to the perceived cosmological acceleration of the Universe observed today. One research paper later, and upon hearing that space-based spectrographs had just detected the presence of water gas in the atmosphere of *a planet in another solar system*, he moved four floors downward to start his graduate research with Prof. James Lloyd.

As a scientist, David's primary ambition is to conduct research. Yet he feels strongly that a key component to being an effective scientist is a desire to communicate research and to generate the development of teaching programs and the scientific community. During his six years at Cornell University, he maintained active roles in the Physics Graduate Society, Astronomy Graduate Network, and the Graduate and Professional Student Assembly. He wrote for the Ask an Astronomer @ Cornell service, and has written and produced for the Ask an Astronomer Podcast series. For his successful completion of science journalism courses and a publishing prospectus for a book on exoplanets, David earned a Science Communication minor at Cornell. David completed this dissertation in September 2011.

To my parents, who put a good head on my shoulders.

To my friends, who helped keep it there.

## ACKNOWLEDGEMENTS

Like any pursuit into the challenging and unknown, I am thankful for the friends and colleagues who shared in the venture. This page describes all the people I have to thank for helping me complete the trip and for adding to the pleasure of the journey.

### **Professional Acknowledgements**

Many colleagues in the scientific community contributed to various aspects of this dissertation and helped to make this work larger than the sum of my ideas. For their scientific advice, I extend my gratitude to the members of my dissertation committee: James Lloyd, Ira Wasserman, Ivan Bazarov, and Bruce Lewenstein. I benefited from multiple discussions and pieces of guidance from each one of them, and in particular James Lloyd, my dissertation advisor, for his supervision and for demanding the best research from me.

I would like to thank Peter Tuthill, Michael Ireland, and Frantz Martinache, my collaborators in the small world of NRM, for teaching me the basics in my fledgling graduate days and then numerous suggestions and recalibrations of direction throughout this work.

I have enjoyed countless spirited and informative conversations with excellent scientists at and beyond my university which have been integral to my development as a scientist. In particular, I would like to point out Jason Wright, who provided several key elements to my first NRM publication and whose acute understanding of our field enabled him to point out the constellations among my pinpoints of ideas. I am especially grateful to Peter Tuthill and Anand Sivaramakrishnan for providing needed perspective throughout the last two years and for allowing me to learn countless intangibles from their seemingly unending supply of wisdom.

In addition, I am indebted to the staff at Palomar Observatory, including Jean Mueller, for her long and dedicated night-time hours and quick operation at the controls. I am grateful to Jeff Hickey, Rich DeKany, Antonin Bouchez, and the Palomar AO Team for keeping the control room spirited and developing the excellent instruments which serve as the backbone for this research. And, finally, Laurie McCall, who confirms that no successful operation runs without steady support behind the scenes.

I would also like to thank my first graduate advisor, Rachel Bean, for indulging my eagerness to explore general relativity and for leading me through my first whirlwind year as a graduate student and my first publication. She showed me that with patience, genuisosity, and depth of skill, that I can grow in leaps and bounds; her hands-on-style helped affirm my own teaching and mentorship style that has rewarded me so today.

### **UnProfessional Acknowledgements**

In both undergraduate and graduate school, I have been fortunate to have been immersed in an amazing, vibrant scientific and social environment that continually provided opportunities to befriend wonderful people and scientists. These friends and colleagues shared in my joys and troubles; provided ballast, beers, and distractions; and generally made my day to day experiences more joyful. I couldn't have done this without you, nor would I have chosen to. You know who you are. Thank you.

Many thanks to my cohort at Caltech, and I hope we maintain an enduring enthusiasm for all things science and civic.

In six years at Cornell, I taught ten semesters of students in physics and astronomy. My students perpetually reminded me that science will always be a subject of public curiosity. They gave me a place to direct my creative and productive

energies when those energies could not be productively directed toward research. (As research – unlike my students – has shown at times to be fitful, cranky, uncooperative, and rather impartial to my enthusiasms). Without their time to develop a skill set for teaching and mentoring, graduate school would have been a much more selfish and isolated endeavor.

I am thankful to Ann Martin, Laura Spitler, and David Kornreich for maintaining the Ask An Astronomer @ Cornell service, which has shown me that some of the hardest questions of all come from middle school children and retired engineers.

And finally, most importantly, I am thankful to my mom and dad for repeatedly indulging my wild-eyed naive desire and decision to enter the astronomy profession, despite the long incongruous hours and too-lengthy stays away from home in their times of need. Nothing in this work would have been possible without them and their constant support that reaches far beyond any description on this page.

## TABLE OF CONTENTS

Biographical Sketch . . . . .	iii
Dedication . . . . .	v
Acknowledgements . . . . .	vi
Table of Contents . . . . .	ix
List of Tables . . . . .	xii
List of Figures . . . . .	xiii
<b>1 Perspective</b>	<b>1</b>
1.1 Directly Imaging Faint Companions to Stars . . . . .	1
1.2 Brown Dwarfs as Massive Exoplanet Analogs . . . . .	8
1.3 The Organization of This Manuscript . . . . .	12
<b>2 Brown Dwarfs</b>	<b>14</b>
2.1 How does one identify a brown dwarf? . . . . .	14
2.2 The Current State of Brown Dwarf Atmosphere and Evolution Models	16
2.3 Using Mass Measurements to Test Evolution Models . . . . .	26
2.4 The Challenge of Resolving Brown Dwarf Binaries . . . . .	34
2.4.1 Angular Resolution for Brown Dwarf Dynamical Masses . . . . .	35
2.4.2 Primary-Secondary Contrasts for Brown Dwarf Companions	36
2.4.3 Adaptive Optics: Resolution . . . . .	39
2.4.4 Adaptive Optics: Contrast . . . . .	48
<b>3 Non-Redundant Aperture Masking Interferometry with Adaptive Optics</b>	<b>55</b>
3.1 Non-Redundant Aperture Masking Interferometry . . . . .	57
3.2 Observing Binaries with an Aperture Mask . . . . .	70
3.2.1 Closure Phase Signal . . . . .	70
3.2.2 Robust Measurement of Binary Parameters and Confidence Intervals . . . . .	74
3.2.3 Calculation of Contrast Limits . . . . .	79
<b>4 A Close Companion Search around L Dwarfs using Aperture Masking Interferometry and Palomar Laser Guide Star Adaptive Optics<sup>1</sup></b>	<b>82</b>
4.1 Abstract . . . . .	82
4.2 Introduction . . . . .	83
4.3 Observations and Data Analysis . . . . .	86
4.3.1 Observations . . . . .	86
4.3.2 Aperture Masking Analysis and Detection Limits . . . . .	89
4.4 Sixteen Brown Dwarf Targets - Four Candidate Binaries . . . . .	103
4.5 Discussion: Aperture Masking of Faint Targets . . . . .	105
4.6 Conclusion . . . . .	107

<b>5</b>	<b>The Use of Spatial Filtering with Aperture Masking Interferometry and Adaptive Optics<sup>1</sup></b>	<b>112</b>
5.1	Abstract . . . . .	112
5.2	Introduction . . . . .	113
5.3	Aperture Masking with Spatial Filtering . . . . .	116
5.3.1	Aperture Masking: Current Technique . . . . .	116
5.3.2	Aperture Masking: Why Spatial Filter? Calibration Errors. . . . .	117
5.3.3	Pinhole Filtering . . . . .	120
5.3.4	Post-Processing with a Window Function . . . . .	125
5.4	Simulated Observations . . . . .	126
5.4.1	Characterization and Simulation of Palomar’s Atmosphere . . . . .	127
5.4.2	Numerical Simulation . . . . .	128
5.5	The Palomar Pinhole Experiment . . . . .	130
5.5.1	Pinhole Implementation on PHARO . . . . .	130
5.5.2	Pinhole Size Optimization . . . . .	130
5.5.3	How Important Is Target Placement? . . . . .	132
5.5.4	Window Function: Optimal Size and the Palomar 9-Hole Mask . . . . .	133
5.6	Observations . . . . .	135
5.6.1	Pinhole Stability and Target Alignment . . . . .	137
5.6.2	Calibrators: Pinhole Filtering Produces Lower Closure Phase Variance and Higher Amplitudes . . . . .	138
5.6.3	Binaries: Lower Closure Phase Variance . . . . .	139
5.7	Summary of Results and Conclusions . . . . .	148
5.8	Discussion . . . . .	152
5.8.1	A Strategy for Future Pinhole Observations . . . . .	152
5.8.2	Extreme-AO Aperture Masking Experiments . . . . .	153
	Acknowledgements . . . . .	154
5.9	Pinhole Filtering: Inteferometry . . . . .	160
5.10	Spatial Structure of Closure Phase Redundancy Noise . . . . .	162
5.10.1	Baseline Visibility Measurement . . . . .	164
5.10.2	Instantaneous Closure Phase . . . . .	166
<b>6</b>	<b>Synthesis and Conclusions</b>	<b>170</b>
6.1	Refinement of the NRM with AO Technique: Results . . . . .	171
6.2	Refinement of the NRM with AO Technique: Future Work . . . . .	172
6.3	Study of Brown Dwarf Binaries using LGSAO: Results . . . . .	175
6.4	Study of Brown Dwarf Binaries using LGSAO: Future Work . . . . .	177
6.5	Future Explorations: Probing Evolution and Formation of Brown Dwarfs and Massive Jupiter Exoplanets . . . . .	179
6.5.1	New Paradigms of Planet Formation Driven by Direct Imaging . . . . .	179
6.5.2	A Growing Population of Nearby, Young Stars . . . . .	180
6.5.3	Feasibility of the Survey with Exoplanet Instruments and NRM . . . . .	181
6.6	Conclusions . . . . .	182

<b>A</b>	<b>Primer: Imaging Through a Turbulent Atmosphere with Adaptive Optics</b>	<b>186</b>
A.1	The Point Spread Function . . . . .	186
A.2	Atmospheric Turbulence and Adaptive Optics . . . . .	189
A.2.1	Kolmogorov Turbulence . . . . .	189
A.3	Adaptive Optics . . . . .	195

## LIST OF TABLES

2.1	Techniques For Resolving Closely Separated Brown Dwarf Companions . . . . .	41
2.2	Pros and Cons of Primary Type . . . . .	41
2.3	Survey Types For Brown Dwarf Companion Searches . . . . .	41
4.1	The Sixteen Very Low Mass Survey Targets . . . . .	100
4.2	Coordinates and characteristics of the sixteen very low mass targets observed in this sample. Photometry is taken from the 2MASS catalog. Spectral types (spectroscopic) and distances are taken from DwarfArchives.org, unless otherwise noted. <sup>a</sup> Distance measurements derived from J-band photometry and $M_J$ /SpT calibration data of Cruz et al. (2003) assuming a spectral type uncertainty of $\pm 1$ subclass. <sup>b</sup> Survey detection limits of Table 4.3 given in terms of secondary-primary mass ratio, assuming a co-eval system (same age and metallicity). Masses ratios are derived from the 5-Gyr (first row) and 1-Gyr (second row), solar-metallicity substellar DUSTY models of Chabrier et al. (2000), using J and K band photometry. <sup>s1</sup> Target previously observed by Reid et al. (2006). <sup>s2</sup> Target previously observed by Bouy et al. (2003) . . . . .	100
4.3	Survey Contrast Limits ( $\Delta K$ ) at 99.5% Confidence . . . . .	101
4.4	Detection contrast limits around primaries: <sup>a</sup> Primary-Secondary separations are given in units of mas, and the corresponding detection limits are in $\Delta K$ magnitudes. . . . .	101
4.5	Model Fits to Candidate Binaries . . . . .	102
5.1	Observation of Known Binaries With and Without Spatial Filter . . . . .	142
5.2	Astrometry and Alignment of Targets within Pinhole . . . . .	143
5.3	Alignment of Targets Within Pinhole and Estimated Closure Phase Misalignment Error. Position determined by center of interferograms, errors estimated from spread over twenty images. Values in parentheses include 40 mas uncertainty of the absolute pinhole position. Misalignment errors are calculated using the simulation of Section 5.5.3, assuming a Strehl of 15% in H and $CH4_s$ , 45% in $K_s$ and $Br\gamma$ , and 10% in J band. . . . .	143

## LIST OF FIGURES

- 1.1 Close-up of the diffraction core and first and second Airy rings of 6 second exposures of HIP 52942, taken with the Palomar AO system and PHARO instrument. The field of view is 600 mas. Contours are peak intensity divided by 1.05, 1.18, 1.33, 2., 2.5, 3.33, 5., 10., 20., and 50. Each row contains three images taken roughly ten seconds apart. The middle and bottom rows have sets of images taken 1 and 10 minutes after the first row, respectively. The tendency of speckles to 'pin' to the Airy rings is readily apparent, as well as a three-fold and four-fold symmetry of the speckle locations on the first Airy ring which evolves on minute timescales. (For instance, between the first and second image of the first row.) These produce flux variations as much as 10% of the peak (seventh contour). Variations on the second Airy ring of as much as 2-5% are also observed. These *quasi-static* speckles limit the image contrast. . . . 4
- 1.2 Comparison of imaging techniques in infrared H Band (Strehl  $\sim$  20%) at Palomar Hale 200" Telescope. Aperture Masking (red) routinely achieves  $\Delta H \sim 5.5$  magnitudes (150:1) at the diffraction limit, much better than direct imaging alone (black). Coronagraphy (blue), although capable of providing very high contrast is obscured at close separations by its Lyot stop. High contrast at close separations is crucial for the detection of brown dwarfs for dynamical mass measurements. An M-Brown dwarf binary (Contrast  $\sim$  4.0-5.0 magnitudes, 80-100:1) cannot be detected by direct imaging at a separation closer than about  $3 \lambda/D$ ; the system would have a period of at least 9 years. Aperture Masking can detect these binaries over a more expansive range, and with much shorter periods. Companions detected by coronagraphy are rarely able to provide dynamical masses. . . . . 6
- 1.3 Comparison of a resolved binary with direct imaging (left) and aperture masking (right). Good wavefront correction by the adaptive optics system reveals a sharp, Airy function point spread function, though the first Airy ring partially obscures the presence of a 6:1 companion (at an angle of 25 degrees counterclockwise of horizontal). Even with good correction, speckles are visible, including one pinned to the Airy ring at due south. The large aperture masking point spread function contains many features; these are not speckles, but rather well-defined structure which allows for the calibrated removal of wavefront noise. Although no companion is identifiable by eye, processing of the aperture masking image clearly reveals the presence of the companion, with much higher precision. . . . . 7

2.1	Color-magnitude diagrams of substellar objects plotted against modeled atmospheres and blackbody curves. (Left) Absolute J v. J-K color magnitude diagram. Curves indicate theoretical isochrones for substellar objects at ages of 0.5, 1.0, and 5.0 Gyr through a range of masses using the brown dwarf models of Burrows et al. (1997) and their blackbody counterpart. The difference between blackbody colors and model colors is immediately apparent. The prototype T dwarf, Gl 229B, and prototype L dwarf, GD 165B, are plotted for comparison. Notice that the L dwarf does not show an indication of particularly bluer-than-blackbody colors. (Right) Absolute J v. J-H color magnitude diagram. Figure from Burrows et al. (1997) . . . . .	17
2.2	Bolometric correction for K band photometry and Effective temperature as functions of spectral type from Golimowski et al. (2004) (Top) Bolometric corrections can be used to obtain total luminosity, $L_{bol}$ , from K band photometry. (Bottom) By making certain assumptions about the brown dwarf radius, effective temperature can be estimated from total luminosity. (See text.) Notice the plateau of temperature marking the transition from L and T dwarf classes . . . . .	21
2.3	Infrared photometry of low mass stars as a function of effective temperature. Photometric colors are primarily a function of effective temperature and predominantly dependent on the physical chemistry of the brown dwarf atmospheres. In the absence of spectra, broadband photometric colors are a proxy for spectral type and temperature. Low mass curves (M0 and later) use photometry of Baraffe et al. (2003) and the spectral type- $M_J$ relation of Cruz et al. (2003). High mass curves use the mass-luminosity relations of Henry & McCarthy (1993). The infrared photometry of a blackbody is drawn for comparison; the infrared flux brightening of dusty stars (M6 and later) and brown dwarfs is readily apparent.	23
2.4	Evolution of luminosity tracks for low mass stars (blue), brown dwarfs (green), and planets (red) from Burrows et al. (1997). Object masses (in $M_{sun}$ ) are marked at the right-side end of the tracks. The top set of lines (0.08-0.20 $M_{sun}$ ) trace out the evolution of low mass stars; note the onset of fusion at 0.5-1.0 Gyr and further stabilization of luminosity, while brown dwarfs continue to dim. The shoulder of brief, but constant luminosity early in the evolution of stars and brown dwarfs signals the brief fusion of primordial deuterium. . . . .	27

2.5	<p>Evolution of effective temperature for low mass stars (blue), brown dwarfs (green), and planets (red) from Burrows et al. (2001). These sets of lines are the same as in Figure 2.4. Horizontal lines mark the evolution from spectra classes M to L and L to T. Note that the lowest mass hydrogen burning stars evolve into L dwarfs, and that all brown dwarfs start as M dwarfs. Because brown dwarfs evolve through to later spectral types for the entirety of their lifetime, unlike stars which stabilize after <math>\sim 1</math> Gyr, spectral type without age is a poor indicator of brown dwarf mass. The orange filled circles mark the 50% depletion of deuterium; the magenta circles mark the 50% depletion of lithium. Since brown dwarfs less massive than <math>\sim 0.060 M_{sun}</math> never deplete their primordial lithium, the presence of lithium in L dwarf spectra is an indicator that the object is a brown dwarf. . . . .</p>	28
2.6	<p>Effective Temperature as a function of mass for low mass stars and brown dwarfs using the evolutionary models of Baraffe et al. (2003). Unlike stellar objects, the temperatures of brown dwarfs cool significantly with age; for any temperature derived from photometry, nearly every brown dwarf mass may be possible if age is not constrained. Conversely, while temperature changes rapidly early, brown dwarfs cool more slowly after several billion years, and precisely measured masses (<math>\sim 10\%</math>) give little constraint to age. Low mass curves (M0 and later) use photometry of Baraffe et al. (2003) and the spectral type-<math>M_J</math> relation of Cruz et al. (2003). High mass curves use the mass-luminosity relations of Henry &amp; McCarthy (1993). . . . .</p>	29
2.7	<p>Infrared photometry of low mass stars and brown dwarfs (J band, blue; K band, red) using the models of Baraffe et al. (2003). Eight magnitudes (1500:1 Flux Ratio) separate solar mass stars and the most massive brown dwarfs at an age of 1 Gyr. Brown dwarfs dim with age, spanning roughly eight magnitudes between 100 Myr and 5 Gyr. Low mass stars and L dwarfs are red in infrared color, this changes rapidly at the onset of the T dwarf spectral class. . . . .</p>	30
2.8	<p>Orbital period for a <math>0.070 M_{\odot}</math> brown dwarf companion as a function of semi-major axis and primary spectral type. Wide-separated binaries orbit too slowly to track their orbits (and obtain dynamical masses) in a practical length of time. In order to obtain the system mass measurements in less than five years of observing, binaries with physical separations less than 3 AU need to be targeted. . . . .</p>	37

2.9	Primary-Secondary Contrast Ratio of Binary Systems. Clearly, late-type stars offer more favorable contrast ratios than solar type stars. Particularly noteworthy is the rapid drop in brightness (a factor of 100) moving from L0 dwarfs (massive brown dwarfs) to T5 dwarfs (lighter brown dwarfs). Probing the entire mass range of brown dwarfs requires very high contrasts in the most favorable of cases. . . . .	40
2.10	Contrast and Resolution of Direct AO Imaging is inhibited by <i>speckle</i> noise, a diffraction effect of wavefront errors, and not photon noise. (Left) Total of 150 one second exposures of HIP 52942 in H band on April 12, 2009 (Strehl $\sim$ 20%). The first and second Airy ring can be clearly seen, as well as a diffuse halo peppered with speckles. A black circle is drawn at $1.22\lambda/2r_a$ using the AO actuator spacing for $r_a$ . This approximates the extent of the halo. (Right) The variance of each pixel is calculated as a function of distance from the primary and averaged azimuthally. The measured variance is compared to the calculated photon noise for the point spread function. As seen, speckle noise is a factor of $\sim$ 30x higher than photon noise. NRM/Aperture masking leads to an increase in contrast precisely because closure phases are able to calibrate out the effect of these speckle-producing wavefront errors. This figure is an empirical analog to Racine et al. (1999), Fig. 2. . . . .	43
2.11	Absolute visual magnitude as a function of spectral type. Late type stars and brown dwarfs grow quickly faint in the visible and are too faint to drive adaptive optics systems. For this reason, companion searches which aim image with high angular-resolution (e.g. for dynamical mass measurements) must use primaries earlier (and brighter) than about M3 if natural guide stars are to be used.	47
2.12	Close-up of the diffraction core and first and second Airy rings of 6 second exposures of HIP 52942, taken with the Palomar AO system and PHARO instrument. The field of view is 300 mas in radius, roughly that necessary to resolve binaries with periods short enough to measure brown dwarf masses. Contours are peak intensity divided by 1.05, 1.18, 1.33, 2., 2.5, 3.33, 5., 10., 20., and 50. Each row contains three images taken roughly ten seconds apart. The middle and bottom rows have sets of images taken 1 and 10 minutes after the first row, respectively. The tendency of speckles to pin to the Airy rings is readily apparent, as well as a three-fold and four-fold symmetry of the speckle locations on the first Airy ring which evolves on minute timescales. (Between, for instance, the first and second image of the first row.) These produce flux variations as much as 10% of the peak (seventh contour). Variations on the second Airy ring of as much as 2-5% are also observed. These <i>quasi-static</i> speckles limit the image contrast. . . . .	50

2.13	Primary-Secondary Contrast Ratio Detectable with Direct AO Imaging. The fundamental challenge of high contrast direct imaging at high angular resolution is to distinguish quasi-static speckles from true companions. Because quasi-static speckles vary too slowly to average out, it is their mean brightness that sets the companion detection limit. These speckles can be up to 10% peak brightness at the location of the first Airy ring. Above is the detection contrast limit imposed by quasi-static speckles for 10 minutes of direct imaging of HIP 52942 in H band. NRM achieves higher contrasts not by distinguishing companions from speckles, but by generating an observable that is not affected by the wavefront errors which produce the speckles (i.e, closure phases) . . . . .	51
2.14	Comparison of imaging techniques in infrared H Band (Strehl $\sim$ 20%) at Palomar Hale 200" Telescope. Aperture Masking (red) routinely achieves $\Delta H \sim 5.5$ magnitudes (150:1) at the diffraction limit, much better than direct imaging alone (black). Coronagraphy (blue), although capable of providing very high contrast is obscured at close separations by its Lyot stop. High contrast at close separations is crucial for the detection of brown dwarfs for dynamical mass measurements. An M-Brown dwarf binary (Contrast $\sim$ 4.0-5.0 magnitudes, 80-100:1) cannot be detected by direct imaging at a separation closer than about $3 \lambda/D$ ; the system would have a period of at least 9 years. Aperture Masking can detect these binaries over a more expansive range, and with much shorter periods. Companions detected by coronagraphy are rarely able to provide dynamical masses. . . . .	52
3.1	The sparse, non-redundant aperture mask used for observations at the Hale 200" Telescope at Palomar Observatory. Each pair of sub-apertures acts as an interferometer of a unique baseline length and orientation. Overdrawn is one such baseline. The 9-hole mask produces thirty-six baselines total; the point spread function of the mask is a set of thirty-six overlapping fringes underneath a large Airy envelope. . . . .	58

- 3.2 An example of a two and three hole aperture mask. For each, the mask, point spread function, and power spectrum are shown. (Left Middle) The pair of sub-apertures interfere to produce a fringe with spacing  $(\lambda/\vec{b}_1)$  underneath an Airy envelope of characteristic size  $\lambda/d_{sub}$ . Notice the fringes are oriented in the direction of the baseline. (Left Bottom) The power spectrum shows that such a mask allows the transmission of only two spatial frequencies  $(\pm\vec{b}_1/\lambda)$  which contain the same information; such a mask allows one to measure this Fourier component of the source brightness distribution. (Right Top) A three hole aperture mask. (Right Middle) Each pair of sub-apertures interfere to produce a fringe, three in total. This is reflected in the power spectrum, which shows the transmission of six frequencies (three unique). Additionally, closure phases can be used for a mask with three or more baselines to significantly reduce the effect of wavefront errors (see text). . . . . 60
- 3.3 Factors which alter the baseline phase. (Left) Wavefront errors atop a sub-aperture will shift the baseline phase. The shift in the baseline phase will equal the wavefront phase error. This is the primary way in which turbulence and optical errors impact baseline (and closure) phase measurements. (Middle) The location of the target is encoded in the baseline phase. Determination of the position of a target on the sky has been transformed into a challenge to accurately measuring the baseline phase. (Right) Each object in a binary system produces a sinusoidal intensity pattern on the detector which add (in intensities) to produce a composite sinusoidal pattern with a different amplitude and phase; the resulting amplitude and phase will depend on the binary characteristics. The resolution of a companion has been transformed into a challenge to accurately measuring phase. . . . . 63
- 3.4 Monte Carlo simulation showing that all signal is virtually unrecoverable if phase noise is larger than about 150 degrees. Successive averaging of a Gaussian variable usually reduces its measurement error by  $N^{-1/2}$ ; this is not the case for successive averaging of phasors when phase variance is large. Each data point shows the measurement uncertainty of the phase of  $\sum_N \exp(ix)$ , if  $x$  is a mean-zero Gaussian variable with standard deviations ranging from 3 to 180 degrees. If the phase error of  $x$  is small, successive averaging leads to an  $N^{-1/2}$  improvement of error after N measurements. As the phase error approaches about 150 degrees, averaging is unable to recover that the mean phase is zero after any number of measurements by this approach. . . . . 64

3.5	Closure phases increases the precision with which long-baseline Fourier content can be measured. The x-axis is the set of eighty-four closure phases that can be extracted from a single image of the Palomar 9-hole mask. Each closure phase is constructed from sets of three baselines. Here we compare the variation of these baseline phases to the variation of the closure phase. Plotted in black are the closure phases obtained from twenty aperture masking images; for each closure phase, the individual baseline phases are overplotted (red, blue, green). As can be seen, the the closure phases (black) vary by about $\sim 3.3$ degrees across the twenty separated exposures. Compare this to the individual baseline phases (red, blue, green), which vary by 30-35 degrees. This is a tenfold increase in fidelity by using closure phases. . . . .	68
3.6	Illustration of the phases as a function of baseline induced by a 2:1 contrast binary separated by 150 mas using the Palomar 9-hole aperture mask. The phase signal of an unresolved single star is shown for comparison. (Middle) Showing the target phase as a function of baseline, overplotted by the thirty-six spatial frequencies sampled by the Palomar mask. The uniform spatial frequency (or uv-coverage) coverage of the Palomar mask ensures sensitivity to companions at all separations and orientations. (Bottom) Showing the baseline-phase relation collapsed to one dimension. The companion induces a phase offset of up to 30 degrees for many baselines; with typical measurement precisions of a few degrees <i>per closure phase</i> , this companion is readily detected at very high confidence. . . . .	73
3.7	Determination of fit confidence with Monte Carlo is more conservative. Data is drawn from NRM observations of L-dwarf binary 2M 0036+1806 (Bernat et al., 2010). The goodness-of-fit statistic here is $\Delta\chi^2=6.55$ and is compared to a distribution generated from fits to simulated single stars, resulting in a fit confidence of 96% (Monte Carlo). Notice that comparing this value to a $\chi^2$ distribution with three degrees of freedom (Analytic) results in a much higher confidence of fit. . . . .	80
4.1	The aperture mask inserted at the Lyot Stop in the PHARO detector. Insertion of the mask at this location is equivalent to masking the primary mirror. . . . .	91

4.2	Interferogram and power spectrum generated by the aperture mask. (Left) The interferogram image is comprised of thirty-six overlapping fringes, one from each pair of holes in the aperture mask. (Right) The Fourier transform of the image shows the thirty-six (positive and negative) transmitted frequencies. (Right, inset and overlay) Closure phases are built by adding the phases of 'closure triangles': sets of three baseline vectors that form a closed triangle.	91
4.3	Estimating per-measurement weights for three closure phase data sets for target 2M 2238+4353. The data sets have comparatively high- (left), moderate- (center) and very low- (right) signal to noises. (Top) Plot of bispectrum (closure) phase vs. bispectrum amplitude. Note that larger amplitude data have smaller phase spreads, and a clear asymptotic mean can be identified in the high and moderate signal to noise cases. (Closure phase 43 contains no discernible signal, and would be removed from further analysis.) Low amplitude bispectra are swamped by read noise, introducing phase errors which are nearly uniformly distributed. The solid line estimates the relationship between per-measurement standard deviation and bispectrum amplitude. (Middle) Closure phase vs. approximate weighting. Note that the higher weighted points have lower per-measurement standard deviation. (Bottom) Resulting p.d.f. of the closure phase.	109
4.4	Proposed log-normal distribution of companion separation around L dwarf primaries from Allen (2007). The peak and width of the distribution have been constrained by previous surveys. The most likely distribution (solid line) and one sigma distributions (dashed lines) are shown. Despite the constraints, the distribution is noticeably uncertain in the region of separations searched by our survey. We opt to use a uniform prior for our Bayesian analysis, noting that such a prior may over signify companions closer than roughly 2 AU as compared to the Allen prior. Similarly, a confirmed detection of a close companion could indicated this distribution has been incorrectly described as log-normal (see text).	110
4.5	Contrast limits at 99.5% detection as a function of primary-companion separation: (left) The primary-secondary magnitude difference in $K_s$ detectable at 99.5% confidence. (right) The same detection limits in terms of the absolute magnitude of the companion.	110

4.6	Companion mass and mass ratio limits at 99.5% detection as a function of primary-companion separation: (top left) The primary-companion mass ratio detectable at 99.5% confidence. <i>Dashed</i> lines are for systems aged 5 Gyr; <i>Dot-dashed</i> lines are systems ages 1 Gyr. (top right) The same data in terms of companion mass. (middle/bottom left) As a function of separation and companion mass, this plot reveals the percentage of 5 Gyr (middle) and 1 Gyr (bottom) companions detectable at 99.5% given the data quality of the survey. Binaries in the white area would have been detected for 100% of the survey targets, followed by contour bands of 95%, 90%, 75%, 50%, 25%, and 10%. At the diffraction limit (110 mas), companions of mass $0.65 M_{\odot}$ would be resolved for 50% of our targets. (middle/bottom right) The same plot in terms of mass ratio. Diffraction limit sensitivity: 5 Gyr companions of mass $0.65 M_{\odot}$ ( $.038 M_{\odot}$ for 1 Gyr) would be resolved for 50% of our targets. Equivalently, our survey reached mass ratios of .83 (5 Gyr) and .55 (1 Gyr) for 50% of our targets at the diffraction limit. . . . .	111
5.1	Aperture masks are designed to be non-redundant, but some redundancy persists because of the finite sub-aperture size. (Left) The Palomar 9-hole Mask. Each pair of sub-apertures acts as an interferometer. (Center) A redundant mask. Two pairs of sub-apertures transmit the same baseline. As a result, the baseline carries redundancy noise into its closure phase. (Right) Because of the finite hole size, every baseline is redundant on sub-aperture scales. Spatially filtering the wavefront smoothes the wavefront phase, reducing noise from the sub-aperture redundancy. . . . .	143
5.2	Effect of the pinhole filter on sub-aperture scale phase variation. a) AO corrected wavefront phase. Small scale spatial inhomogeneities are apparent. b) The AO corrected wavefront with an overlay of the aperture mask. Notice that the wavefront phase is inhomogeneous within the sub-aperture. c) AO corrected wavefront after spatial filtering. The small scale features are smoothed out; the wavefront exhibits structure with a characteristic scale close to that of the sub-apertures. d) Within each sub-aperture, the spatially filtered phase is much more uniform. . . . .	144
5.3	Optical setup for pinhole filtered aperture masking interferometry at Palomar. One takes advantage of the coronagraphic capabilities of PHARO by inserting the aperture mask in the Lyot wheel and the spatial filter in the Slit wheel. . . . .	145

5.4	Imaging An Unresolved Targets Through a Pinhole. The point spread function of three targets is shown with a pinhole of size $6\lambda/D$ overlaid. Square root contrast scaling is used to highlight the truncated flux. (Left) The pinhole, located in an image plane, truncated the portion of electric field which forms the outer rings of the point spread function. In perfect seeing, the total flux blocked is very low. (Center) Wavefront errors dispel flux outward creating a diffuse halo around the target. The blocked flux increases, and more power aliases back into sub-aperture scales, resulting in closure phase errors. (Right) When asymmetrically truncated, the center of light shifts towards the pinhole center (black x). Each component of a binary is truncated differently, leading to errors in astrometry or contrast. . . . .	145
5.5	Effect of a Window Function. (Top Left) The aperture mask produces a set of interference fringes beneath an envelope of size $\lambda/d_{sub}$ , as seen in this Palomar 9-hole masking image. The central peak has been zeroed to highlight the envelope and outer rings. The radius of the white ring is $\lambda/d_{sub}$ .(Bottom Left) The power spectrum of the same interferogram, presented in units of baseline/D rather than spatial frequency. Each island of transmitted power (or <i>splodge</i> ) is of size $2d_{sub}$ . This is expected, as the transmission function is related to the autocorrelation of the mask. (Top Right) Using a window function of characteristic HWHM $\lambda/d_{sub}$ (here, a super-Gaussian) removes the interferogram wings and its associated read and wavefront noise. (Bottom Right) The window function produces a convolution kernel of size $\lambda/2\text{HWHM}$ . Notice that a window function larger than $0.5 \lambda/d_{sub}$ creates a kernel larger than $2d_{sub}$ and mixes neighboring splodges, adding redundancy noise. (see text) . . . . .	146
5.6	The RMS fit residuals of simulated data (H-band, no read noise) with pinholes of various size, analyzed with (solid line) and without (dashed line) a window function. The horizontal line is the measurement level without any pinhole in place. The pinhole filter is most effective within the range 11-14 $\lambda/D$ . . . . .	147
5.7	Misalignment of a single star within the pinhole introduces closure phase errors. (a) The Palomar 9-hole mask, overlaid with three closure triangles for which the misalignment errors are calculated. (b) Error due to misalignment at $1.6 \mu\text{m}$ (H band) as a function of target distance from the pinhole center. (Several azimuthal orientations are plotted for each separation.) (c) Closure phase errors at $2.2 \mu\text{m}$ ( $K_s$ band), in which the pinhole is smaller. In both cases, errors in visibility amplitude errors below .005 for the same ranges.	155

5.8	Window functions reduce closure phase error from read noise. These curves, from top to bottom, display the reduction in RMS closure phase error when read noise is 0% (top, solid), 0.2%, 0.4%, 0.6%, 1.0%, and 5.0% (bottom, dotted) of the peak image intensity. The optimal window function is typically of size $\sim \lambda/d_{sub}$ , or $\sim 12\lambda/D$ for the Palomar aperture mask, with higher read noise favoring tighter window functions. Smaller window functions quickly add large amounts of redundancy noise. (See text.) Note: Even with no read noise (solid curve), a window function reduces closure phase errors, indicating that the window function provides an effect similar to spatially filtering the wavefront. . . . .	156
5.9	Curves showing the effectiveness of the window function as in Figure 5.8, except the wavefront is static over an exposure. Most notably, a window function provides better spatial filtering when the wavefront is static (solid line). . . . .	157
5.10	Drops in flux transmission through the pinhole are driven by changes in AO performance. The binary GJ 623 was resolved in $K_s$ using twenty five masking images through the pinhole. The images which produced the best fitting closure phases (as measured by R.M.S. deviation from the model) also had the least flux blocked by the mask. Poor correction displaces more flux into the outer halo of the PSF, which is then blocked by the pinhole. Poor correction also leads to larger closure phase errors. This trend is not caused by misalignment or movement of the target within the pinhole (see text), but rather changes in AO correction. . . . .	158
5.11	Closure phase standard deviation (scatter) is reduced and baseline visibility amplitude is increased when observed through the pinhole filter. Data points are drawn from observations of 26 single stars. Horizontal lines are the median of the data (solid) and the simulated experiment (dashed). (Top Row) Closure phase scatter is reduced by 10 and 19 percent in H and $K_s$ band measurements, respectively. (Bottom Row) Visibility amplitude is increased by 14 and 18 percent in H and $K_s$ bands, respectively. In all cases, the simulation (model) predicts a larger reduction in noise (see Discussion). . . . .	159

6.1	Star-Planet Contrast of brown dwarfs and massive Jupiters (green tracks) orbiting a late-G star, plotted against anticipated P1640 NRM contrast limits (black lines). Youthful brown dwarfs and exoplanets are bright enough to be detected by NRM on P1640 and Gemini Planet Imager. Vertical lines (blue) plot the age of known, nearby moving groups. Note that planets of mass 6-9 $M_J$ are consistently detectable with the estimated performance using extreme-AO and precision wavefront control (see text). A brown dwarf of <i>any</i> mass can be detected most targets. . . . .	183
6.2	(Top) Histogram of visual magnitudes for all currently known moving group objects observable from Gemini Observatory. Fifty-three targets are $V < 8.5$ and ninety-one targets are $V < 9.5$ . I band magnitudes are 0.5 lower (i.e., $V-I=0.5$ ) for these targets. These sets represent $I < 8$ and $I < 9$ , respectively, in the AO sensing wavelength of the Palomar AO system. (Bottom) Histogram of distances for the 91 targets with $I < 9$ . The median distance is 45 pc, corresponding to physical separations of 1.8 - 7.2 AU for the Palomar NRM working angles. . . . .	184
A.1	The sparse, non-redundant aperture mask used for observations at the Hale 200" Telescope at Palomar Observatory. Each pair of sub-apertures acts as an interferometer of a unique baseline length and orientation. Overdrawn is one such baseline. The 9-hole mask produces thirty-six baselines total; the point spread function of the mask is a set of thirty-six overlapping fringes underneath a large Airy envelope. . . . .	201

# CHAPTER 1

## PERSPECTIVE

### 1.1 Directly Imaging Faint Companions to Stars

At the present in 2011, this decade opens at the era of directly imaged exoplanets. The successful detections of new planetary systems by transit and radial velocity methods during the last decade have fueled remarkable new advances and interest in high-contrast imaging. Whereas transit and radial velocity detections of exoplanets tell us volumes about the bulk and statistical properties of planetary systems, full characterization of individual planetary atmospheres awaits their successful (spectroscopic) imaging, and the use of complex chemical and thermodynamical models to interpret their atmospheres. As often stated in the literature, this is a challenge of very high contrast imaging, and one in which the fundamental limitations of which are also only recently being discovered.

The atmosphere introduces rapid phase variation into the incoming wavefront which, even after suppression by adaptive optics (AO) systems, produces diffraction effects which litter the image with bright speckles. The image noise is overwhelmingly dominated by the movement and random fluctuation of speckles (Racine et al., 1999); distinguishing true companions from bright speckles requires longer observations than initially anticipated (e.g., Racine's 'speckle tax') dampening the hopes of early, optimistic planet searches (e.g., Nakajima (1994)).

Speckles at close separations – those which inhibit high-angular resolution searches – are much more nefarious. Speckles are not placed randomly, but are preferentially *pinned* to the first and second Airy rings (Bloemhof et al., 2000,

2001; Sivaramakrishnan et al., 2003). Furthermore, the precise shape of the Airy rings and pinned location of the speckles shift on timescales of tens of seconds to tens of minutes (e.g., Hinkley et al. (2007)), driven by slowly varying instrumental wavefront errors. In recent years, the impact of these *quasi-static* wavefront errors have been extensively explored, mostly in the pursuit of high-contrast coronagraph observations Lafrenière et al. (2007). These wavefront errors evolve due to temperature or pressure changes, mechanical flexures, guiding errors, changing illumination of the primary mirror, or other phenomena (Marois et al., 2005, 2006). Those originating from optical components located after the wavefront sensor cannot be corrected by adaptive optics (named *non-common path wavefront errors*), and give rise to quasi-static speckle behavior.

Quasi-static speckles present a particularly difficult challenge for high contrast imaging: purely static speckles could be removed by calibration with a reference star (i.e., treated as a non-ideal point spread function), but quasi-static speckles evolve too quickly to calibrate and too slowly to effectively average out over even hour long exposures (Hinkley et al., 2007). Quasi-static speckles dominate long exposures within separations of 5-10 *arcseconds* at the Keck and Palomar Hale Telescopes, and longer exposures do not yield any higher contrasts (Macintosh et al., 2005; Metchev et al., 2003). My own investigation using the Palomar AO system and PHARO instrument show intensity variations of as much as 10% the peak flux over ten minute spans (2-5% on the second Airy ring), and pinned speckles that change locations irregularly (Figure 1.1). (Similar results were obtained with PHARO by Bloemhof et al. (2000).)

Unequivocally, *quasi-static speckles set the ultimate noise floor of high contrast imaging, generating a slowly varying distribution of flux that can be mistaken for*

*faint companions.*

Several techniques have been developed to differentiate and remove the quasi-static speckles simultaneously with observation of the science target. Angular Differential Imaging (ADI) employs multiple observation of the same target while changing the rotation of the primary mirror on the sky (Marois et al., 2006); the speckles move with the optical system rotation but target does not. Several newly commissioned instruments aim to exploit the inherent dependence of speckle behavior on wavelength (or polarization) by obtaining simultaneous images across multiple wavelengths (or polarizations) (Marois et al., 2005; Lenzen et al., 2004; Hinkley et al., 2009; Hinkley, 2009; Crepp et al., 2010). These include Project 1640 at Palomar (Hinkley et al., 2009), the Gemini Planet Imager (Macintosh et al., 2008), and SPHERE on VLT (Beuzit et al., 2006) which use integral field spectrographs for simultaneous chromatic imaging.

The work of this manuscript confronts the quasi-static imaging challenge using the technique of Non-Redundant Aperture Masking Interferometry (*NRM*, or *aperture masking*). NRM provides a powerful, established method for obtaining higher contrasts at diffraction-limit separations despite the atmospheric that produce speckles. Aperture masking employs a small metallic mask which transforms the pupil into an ad-hoc interferometric array; utilizing the unique structure of the transformed point spread function allows the construction of a dataset (i.e., *closure phases*, Jennison (1958); Lohmann et al. (1983); Baldwin et al. (1986); Haniff et al. (1987); Readhead et al. (1988); Cornwell (1989)) which retains the fidelity of high-resolution spatial information while discarding the effect of many wavefront error sources.

The heritage of aperture masking extends back to short-exposure speckle inter-

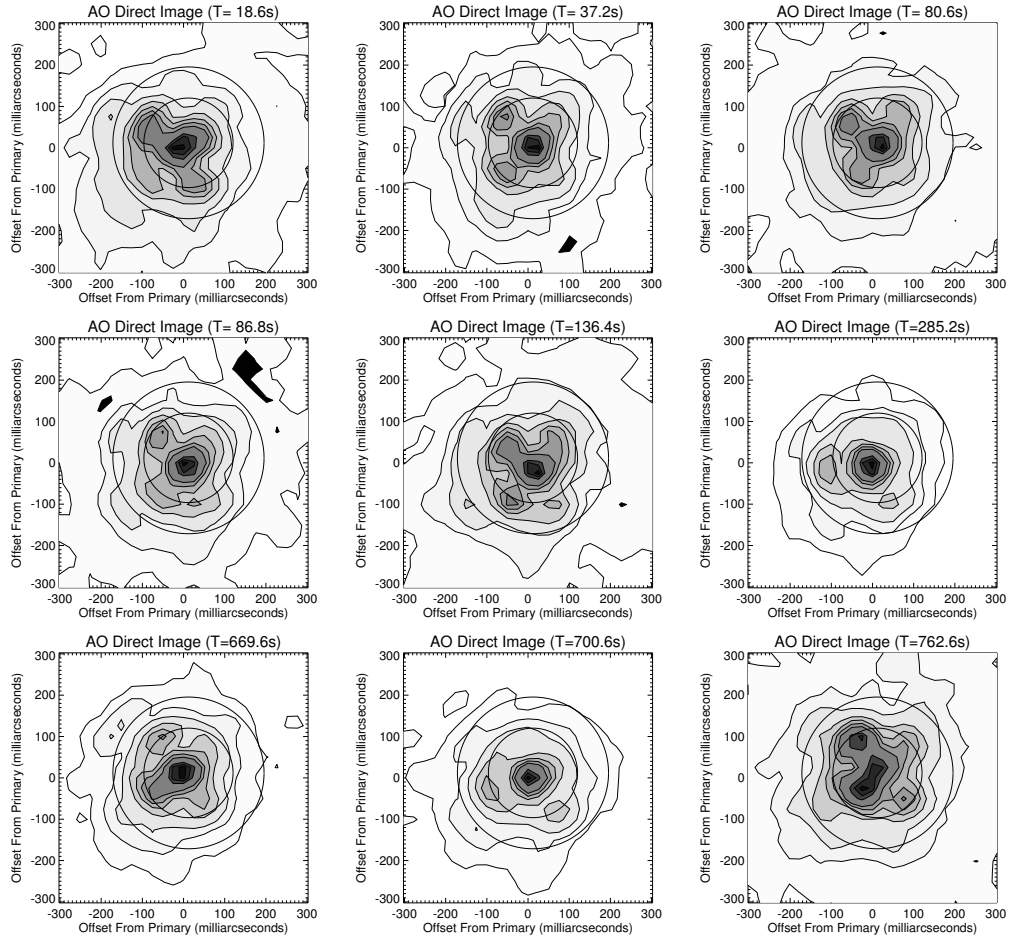


Figure 1.1: Close-up of the diffraction core and first and second Airy rings of 6 second exposures of HIP 52942, taken with the Palomar AO system and PHARO instrument. The field of view is 600 mas. Contours are peak intensity divided by 1.05, 1.18, 1.33, 2., 2.5, 3.33, 5., 10., 20., and 50. Each row contains three images taken roughly ten seconds apart. The middle and bottom rows have sets of images taken 1 and 10 minutes after the first row, respectively. The tendency of speckles to 'pin' to the Airy rings is readily apparent, as well as a three-fold and four-fold symmetry of the speckle locations on the first Airy ring which evolves on minute timescales. (For instance, between the first and second image of the first row.) These produce flux variations as much as 10% of the peak (seventh contour). Variations on the second Airy ring of as much as 2-5% are also observed. These *quasi-static* speckles limit the image contrast.

ferometry and non-redundant experiments (Weigelt, 1977; Roddier, 1986; Nakajima, 1988; Tuthill et al., 2000). The development of adaptive optics has altered the requirements of non-redundancy and short exposure times, but the technique remains highly effective for mitigating quasi-static instrumental wavefront errors. Importantly, the technique provides a method for mitigating or calibrating out the effect of quasi-static wavefront errors from a single image, i.e., before quasi-static wavefront errors evolve. These features allow aperture masking to reach much higher contrast in routine observing and a much lower noise floor, particularly at separations close to the primary and at the diffraction limit (Figure 1.2).

Aperture masking with adaptive optics is well-established for resolving stellar companions within the formal diffraction limit (down to  $0.5\lambda/D$ ) and at high contrasts (200:1 at  $\lambda/D$ ) (Tuthill et al., 2000; Lloyd et al., 2006; Ireland et al., 2008; Martinache et al., 2007). This range of high-resolution and high-contrast make aperture masking ideal for close companion searches. Binaries resolved with aperture masking also have higher precision photometry and relative astrometry.

The ultimate limitation of the NRM technique, although certainly due to quasi-static wavefront errors which cannot be mitigated by closure phases, has not been well-explored before the start of this body of work. The relationship between wavefront errors, AO performance, and closure phase errors will be critical for designing NRM experiments optimized for new systems, and ultimately, reaching planetary contrasts. In particular, their interplay at high-strehl ratio correction or with integral field spectrographs is completely unexplored. These various techniques aiming to solve the quasi-static imaging problem are *complementary*. Given that the exoplanet dedicated instruments (Project 1640, Gemini Planet Imager, and SPHERE) are equipped with aperture masks, now is the time to lay the groundwork for fu-

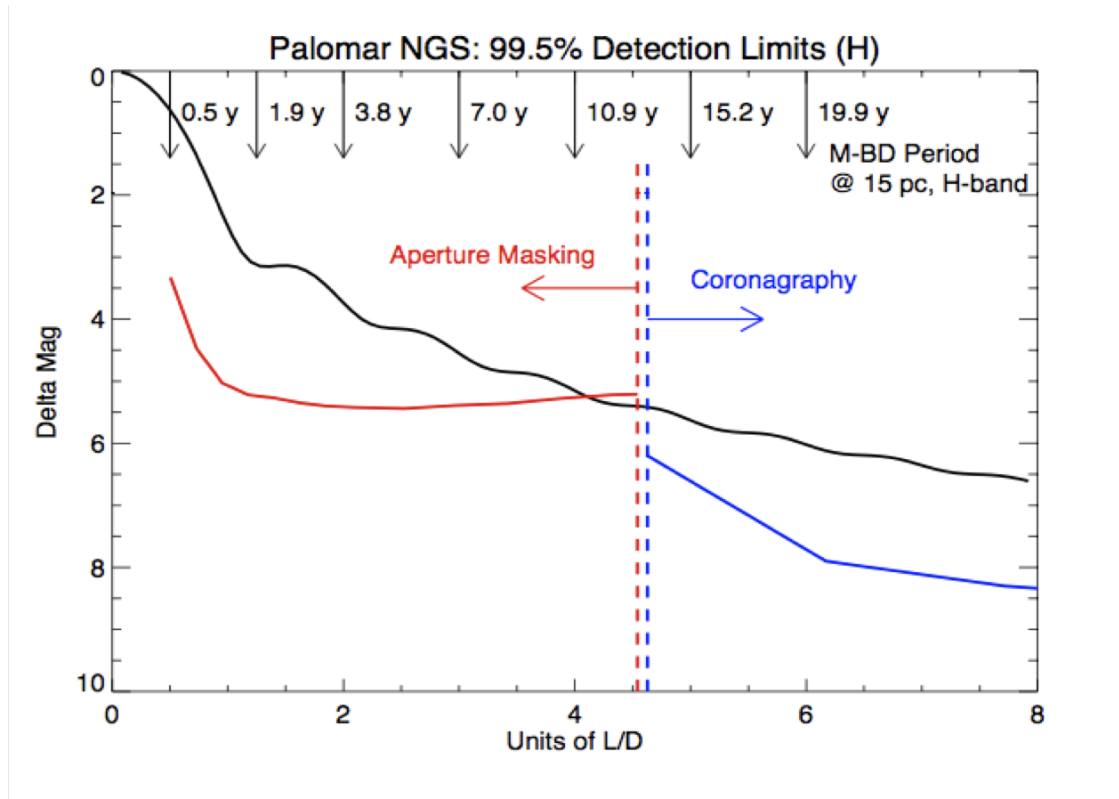


Figure 1.2: Comparison of imaging techniques in infrared H Band (Strehl  $\sim 20\%$ ) at Palomar Hale 200" Telescope. Aperture Masking (red) routinely achieves  $\Delta H \sim 5.5$  magnitudes (150:1) at the diffraction limit, much better than direct imaging alone (black). Coronagraphy (blue), although capable of providing very high contrast is obscured at close separations by its Lyot stop. High contrast at close separations is crucial for the detection of brown dwarfs for dynamical mass measurements. An M-Brown dwarf binary (Contrast  $\sim 4.0$ -5.0 magnitudes, 80-100:1) cannot be detected by direct imaging at a separation closer than about  $3 \lambda/D$ ; the system would have a period of at least 9 years. Aperture Masking can detect these binaries over a more expansive range, and with much shorter periods. Companions detected by coronagraphy are rarely able to provide dynamical masses.

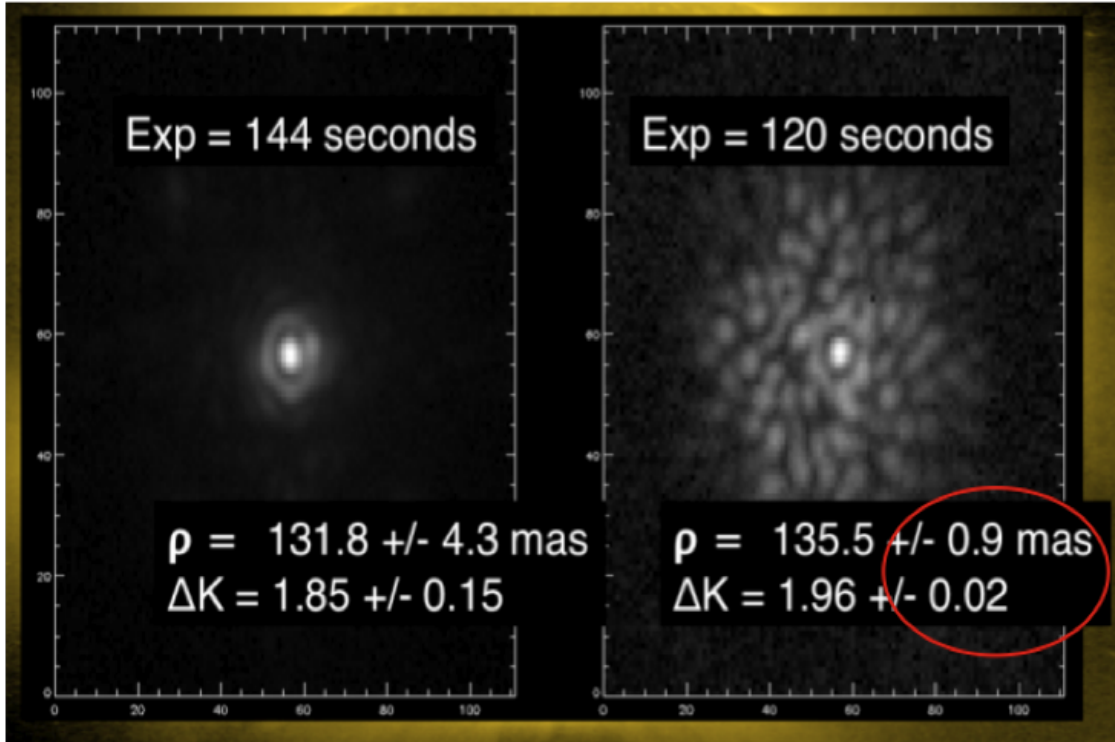


Figure 1.3: Comparison of a resolved binary with direct imaging (left) and aperture masking (right). Good wavefront correction by the adaptive optics system reveals a sharp, Airy function point spread function, though the first Airy ring partially obscures the presence of a 6:1 companion (at an angle of 25 degrees counterclockwise of horizontal). Even with good correction, speckles are visible, including one pinned to the Airy ring at due south. The large aperture masking point spread function contains many features; these are not speckles, but rather well-defined structure which allows for the calibrated removal of wavefront noise. Although no companion is identifiable by eye, processing of the aperture masking image clearly reveals the presence of the companion, with much higher precision.

ture NRM experiments aimed at planet detection. Among the scientific potential of NRM exoplanet imaging is the mass measurement of exoplanets, the full characterization of imaged planetary systems (including upcoming coronagraphic surveys, and e.g., Hinkley et al. (2011)), and exoplanets formed in situ by core accretion (Kraus et al., 2009).

## 1.2 Brown Dwarfs as Massive Exoplanet Analogs

The exoplanet’s more massive cousins in the substellar regime – brown dwarfs – still present many outstanding questions regarding their atmospheres, underlying physical characteristics, and formation processes. It is, perhaps, ironic that the first observational discoveries of these new objects were announced nearly simultaneously at the Cool Stars IX meeting in 1995: the first direct image of a confirmed brown dwarf (Nakajima et al., 1995; Oppenheimer et al., 1995), GJ 229B; and the first radial velocity discovery of an extrasolar Jupiter-mass planet (Mayor, 1995).

While brown dwarfs and exoplanets form in separate environments, they span similar ranges of mass and composition; much of the fundamental core of our understanding of the evolution, structure, and atmospheres of giant Jupiter-mass planets derives directly from extensions of brown dwarf models (Burrows et al., 2001). The natural physical and observational similarities between dim, cool brown dwarfs and much dimmer Jupiter-mass exoplanets provide brown dwarfs as an excellent laboratory to understand the underlying physical development and observational characteristics of Jupiter-class planets. This will remain true for the foreseeable future even after direct imaging searches begin to reveal exoplanets in droves; most of the physical insights drawn out of exoplanet images and low resolution spectra

will be extracted from evolution and atmospheric models. One can perhaps view the previous two decades of observational challenges to brown dwarf imaging as a template for the era of directly imaged planets, while recognizing that successful, concurrent observations of brown dwarfs directly add to our understanding of both classes of objects.

The formation of a brown dwarf begins in the same protostellar dust regions that produce stars, yet an unknown process curbs mass accretion before the brown dwarf has enough mass to raise its core temperatures to the levels necessary to ignite hydrogen fusion (Kumar, 1963; Hayashi & Nakano, 1963). Instead, brown dwarfs support themselves against gravitational collapse by a combination of electron degeneracy and Coulomb pressure. With no fusion energy production, brown dwarfs shine by converting their gravitational potential energy into luminosity, a process which alters the temperature and structure of brown dwarfs as they age. In this regard, brown dwarfs and Jupiter-mass planets share common mechanisms for structural morphology and evolution. Theoretical models estimate the bifurcation between stars and brown dwarfs to occur at about 0.072-0.075 solar masses ( $M_{\odot}$ ) for solar composition, or 75-80 times the mass of Jupiter ( $M_J$ )<sup>1</sup>. At formation, the most massive brown dwarfs reach temperatures as high as about 3200 K, but cool below 2000 K by one billion years. The temperature of a brown dwarf depends on its mass and age, but spans about 500-2000 K at one billion years and cooling as far as 300-1300 K by ten billion years.

Yet astronomy is a visual science: nearly everything we know about the universe has been deduced from the light which shines down upon our telescopes.

---

<sup>1</sup>No clear physical distinction can be made between brown dwarfs and planets, though the monicker *planet* is generally reserved for objects which are presumed to have formed in the debris disks of stars. Other authors chose a mass cutoff at  $13M_J$ , for brown dwarfs above this mass briefly ignite the fusion of primordial deuterium. The latter definition assures that planets never engage in fusion. This work will chose for the former, formation-based definition.

And connecting the photometric and spectral properties of those distant pinpoints of light to physical parameters such as mass, radius, age, composition, and temperature is the fundamental challenge of stellar and substellar astrophysics. The development of astrophysical models of stars stands as one of the successes of the twentieth century: knowing the mass and metallicity of a star reveals the entire nature of that star including its spectral features, internal structural dynamics, and ultimate evolutionary future. No complete, robust, and empirically tested model exists for brown dwarfs or planets at this time.

It is more than the intrinsic faintness of brown dwarfs that makes them harder to observe and model. It is that brown dwarfs cool and evolve with age (a notoriously difficult parameter to measure precisely), adding an extra dimension to the development of models which connect observable features to fundamental physical parameters (i.e., mass, age, and composition).

In the two decades since the detection of the first brown dwarf, hundreds of isolated brown dwarfs have been imaged and spectra have been obtained by large scale surveys (such as 2MASS, Dahn et al. (2002)). These spectra have permitted the advancement of *atmospheric models* which relate the observed spectral features to properties of the atmosphere: surface temperature, molecular chemistry, and dust grain mechanics. These models convey a rich photochemistry of molecules and metallic dust forming in the atmospheres of brown dwarfs. Thousands of molecular species can be formed, and these molecules undergo interactions with radiation across a wide spectrum of infrared and mid-infrared wavelengths. Metallic dust forms clouds in the atmospheres of warm brown dwarfs that deplete metals from the atmosphere and drive chemical equilibria; at cooler temperatures, these dust grains rain out of the atmosphere. Both factors complicate the detailed modeling

of brown dwarf atmospheres in a way different than stars. Despite the numerous successes, state-of-the-art models lack opacity characterization of numerous chemical compounds at the pressures and temperatures of brown dwarfs and require finely tuned parameters to seed rainout of dust grains as brown dwarfs cool. More diverse empirical constraints are required to move these models forward.

But fundamental to the nature of brown dwarfs is their cooling through their lifetime, and understanding the *evolution* of a brown dwarf with age is a formidable task in its own right. *Evolution models* describe the internal structure, total luminosity output, radius, and temperature of a brown dwarf of a given mass and age (and, to a lesser degree, composition). In concert with atmospheric models, one has the basis for a complete model of brown dwarfs. The optical properties of the atmosphere necessarily affect the evolution of the brown dwarfs by regulating the bulk luminosity output, but evolution models are nonetheless relatively insensitive to the specific details of atmosphere models. Independently testing brown dwarf evolution models requires the measurement of masses, ages, and/or temperatures, in addition to photometry.

Brown dwarf binary systems serve as an excellent laboratory for testing evolution models. Tracking the system orbit provides measurement of (the system) mass; combined with accurate photometry (and hence total luminosity, c.f. Golimowski et al. (2004)) one has a critical data to empirically test evolution models (Liu et al., 2008). Observationally, detecting brown dwarf companions suitable for dynamical masses requires imaging with high contrast and angular separations close to the primary.

As discussed in the previous subsection, the technique of Non-Redundant Aperture Masking Interferometry provides a powerful, well-established method for ob-

taining high-contrast at very close angular separations. Binaries resolved with NRM also obtain higher precision photometry and relative astrometry, and dynamical masses up to an order of magnitude more precise (Figure 1.3).

Developing the technique of NRM on current and upcoming instruments will be invaluable for obtaining high precision mass measurements of brown dwarfs and giant exoplanets to advance evolution models.

### **1.3 The Organization of This Manuscript**

These considerations have motivated the research presented within this dissertation. Chapter 2 continues an overview of the current state of brown dwarf atmosphere and evolution models, and describes the challenges confronting the detection of brown dwarf binaries for dynamical mass measurements. Chapter 3 introduces Non-Redundancy Aperture Masking Interferometry (NRM), focusing on the difference between its application with and without adaptive optics and its relevance to resolving binaries. The chapter also includes a general purpose Monte Carlo simulation for determining the statistical significance of NRM detections. Chapter 5 presents previously published results of an NRM search using Laser Guide Star Adaptive Optics to detect companions to very low mass stars and brown dwarfs. The survey detected four candidate brown dwarf binaries at low to moderate confidence with projected physical separations favorable for dynamical mass measurements. Chapter 6 presents unpublished results of an experiment to increase the high contrast capabilities of aperture masking by spatially filtering the science wavefront. A detailed analytical description of the spatial structure of closure phase redundancy noise is also presented. Chapter 7 synthesizes the

results of this research and emphasizes their place in the ongoing developments of this field. The impact of this work for future high-contrast infrared imaging and for the study of brown dwarfs and exoplanets is discussed.

Dear Jamie, Ivan, Ira, Bruce, and Jeevak,

I am very happy to present to you the final draft of my dissertation. Upon your approval, I will submit this to the graduate school.

I would like to thank all of you for your time and effort these last several months, and for the guidance you have provided to me.

Sincerely, David Bernat

## CHAPTER 2

### BROWN DWARFS

#### 2.1 How does one identify a brown dwarf?

The early pursuits for brown dwarf were marked by spectroscopic searches for objects which could bridge the gap between the lowest known mass stars either just above or straddling the hydrogen burning mass limit (late-type M dwarfs,  $T_{eff} \sim 2600\text{K}$ ) and the spectrum of Jupiter, marked most notably by deep methane bands in the infrared ( $T_{eff} \sim 200\text{K}$ ). The dominant feature of the lowest mass stars are strong VO and TiO bands in the optical red.

Kirkpatrick (1992) identified GD 165B as an object much redder than the lowest mass stars and lacking VO and TiO, with unidentified absorption features but no methane absorption. Despite the lack of methane, the unique appearance of its spectrum and extreme red color suggested that GD 165B ought be classified beyond the Morgan-Keenan OBAFGKM spectral classifications (Morgan et al., 1943), and proposed as a candidate brown dwarf. Without adequate models to interpret the unidentified absorption features, the temperature was estimated to be  $\sim 2200\text{ K}$  from total luminosity. Later spectral analysis and atmospheric modeling of GD 165B identified features of metallic hydrides, and confirmed a substellar temperature of ( $T_{eff} \sim 1900\text{K}$ , Kirkpatrick et al. (1999)).

The successful confirmation of the first brown dwarf followed the detection of Gl 229B (Nakajima, 1994; Oppenheimer et al., 1995). The spectral analysis showed strong absorption of methane and water, similar to that of Jupiter. Moreso, almost all of the carbon was found in the form of methane rather than CO, offering an

independent estimation of its temperature based on purely chemical equilibrium considerations (Tsuji, 1995)( $T_{eff} \sim 900$  K, Oppenheimer et al. (1998)).

The discovery of these objects provoked the establishment of two new spectral types, L and T (Kirkpatrick et al., 1999), beyond the Morgan-Keenan OBAFGKM spectral classification (Morgan et al., 1943), with GD 165B and Gl 229B as the prototype members, respectively. Their discovery also led to quickly developing advances in the brown dwarf atmospheric models.

Most notable of the early discoveries into the brown dwarf atmospheres is the role metallic dust in the photosphere plays in shaping the spectra. Jones (1997) demonstrated that dust grains (mostly iron and magnesium silicates) begin forming in the atmospheres of the coolest stars, as well as GD 165B. Surprisingly, the spectrum of Gl 229B is *not* consistent with a dusty atmosphere (Oppenheimer et al., 1995).

For objects like GD 165B (L Dwarfs), dust grains drive the spectral features, in particular the absence of TiO and VO as these oxides are absorbed into micron and centamicron sized silicate grains (Kirkpatrick et al., 1999). This also allows the rise in prominence of the metallic hydrides Tsuji (1995). The size of dust grains that form is a function of temperature, pressure, and the particular chemical equilibrium of each species under consideration (Grossman (1972), and described elsewhere in Leggett et al. (1998); Allard et al. (2000)). These dust grains provide their own opacity (Alexander & Ferguson, 1994), but the predominant overall effect of dusty grains on opacity is by altering the composition of the photosphere gas (Lunine et al., 1989).

The transition from CO to methane as the dominant carbon feature marks the

boundary between L and T dwarfs, and occurs over a narrow range of temperatures: one expected equal parts CO and methane at about 1400 K, a factor of ten less at 1250 K, and virtually no CO at 900 K (Marley et al., 1996). Furthermore, the spectra and photometric colors are not consistent with dusty atmospheres, indicating that dust clouds grow thicker as temperatures cool through the L dwarf class but condense and "rain out" near the onset of the T dwarf class. This allows for the onset of non-metal absorbers, such as methane and water, in the spectra of T dwarf (Allard et al., 2003). The dominance of water opacity in the atmosphere of cool brown dwarfs forces flux emission to increase between the classic telluric bands which define the infrared bands; this results in dramatically enhanced J and H band ( $1.2\mu m$  and  $1.6\mu m$ ) fluxes relative to blackbody. (A similar enhancement in M band occurs for even cooler dwarfs. (Burrows et al., 1997)). This enhancement occurs in  $K_s$  band ( $2.2\mu m$ ) as well, but less so due to absorption by  $H_2$  and methane, driving infrared colors not redder but *bluer* with decreasing temperature (Leggett et al., 1998) (Figure 2.1).

## 2.2 The Current State of Brown Dwarf Atmosphere and Evolution Models

The discovery of GD 165B and Gl 229B and the classification of L and T dwarfs has allowed the development of models describing brown dwarf atmospheres and their evolution in tandem with empirically derived relations.

Spectra of hundreds of L dwarfs and more than sixty T dwarfs have been classified spectroscopically and photometrically (Cruz et al., 2003; Knapp et al., 2004; Golimowski et al., 2004). Both infrared and optical spectral features and

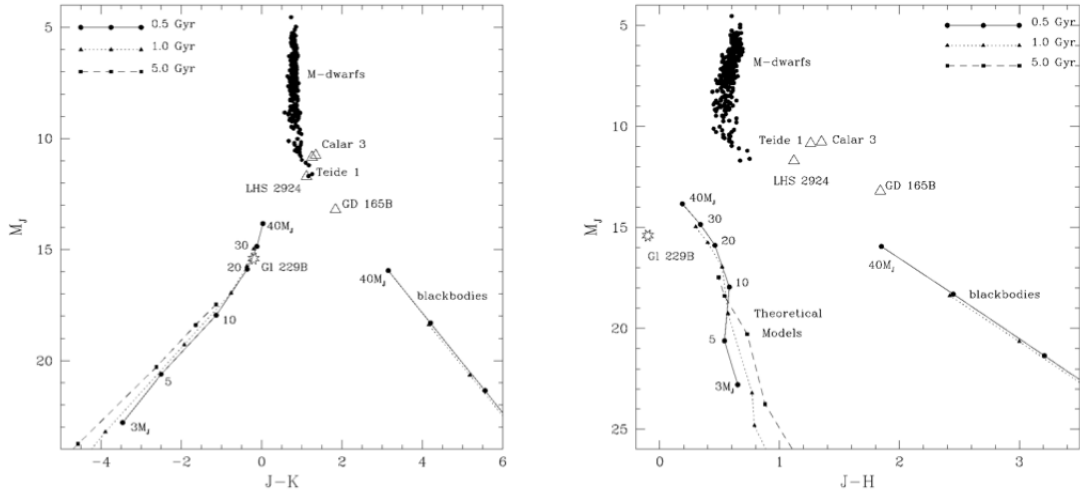


Figure 2.1: Color-magnitude diagrams of substellar objects plotted against modeled atmospheres and blackbody curves. (Left) Absolute J v. J-K color magnitude diagram. Curves indicate theoretical isochrones for substellar objects at ages of 0.5, 1.0, and 5.0 Gyr through a range of masses using the brown dwarf models of Burrows et al. (1997) and their blackbody counterpart. The difference between blackbody colors and model colors is immediately apparent. The prototype T dwarf, Gl 229B, and prototype L dwarf, GD 165B, are plotted for comparison. Notice that the L dwarf does not show an indication of particularly bluer-than-blackbody colors. (Right) Absolute J v. J-H color magnitude diagram. Figure from Burrows et al. (1997)

colors have been used to define subtypes from L1 through T9, all of which supply consistent empirical tests of atmospheric models across the entire span of brown dwarfs (Golimowski et al., 2004). These atmospheric models relate the photometric characteristics of a brown dwarf to its effective temperature ( $T_{eff}$ ) and total luminosity, as effective temperature is the primary driver of atmospheric chemistry, with gravity and metallicity playing lesser roles (Burrows et al., 2006)

Empirical and semi-empirical relations have also been created which relate total luminosity, effective temperature, spectral type, and infrared photometry. Golimowski et al. (2004) has derived bolometric corrections for converting infrared photometry to total luminosity,  $L_{bol}$ , using flux-calibrated optical and infrared spectra from several dozen brown dwarfs. This spectral type-luminosity relation has been shown to provide more accurate estimations of total luminosity than fitting atmospheric models to broad band photometry Konopacky et al. (2010) and is purely empirical.

Total luminosity is also related to effective temperature:

$$L_{bol} = \sigma(4\pi R^2)T_{eff}^4. \quad (2.1)$$

By making model-dependent assumptions of radius (Burrows et al., 1997; Chabrier et al., 2000), Golimowski et al. (2004) also derived effective temperature as a function of spectral type. These indicate the temperature ranges of L dwarfs ( $1400 \text{ K} \lesssim T_{eff} \lesssim 2200 \text{ K}$ ), and T dwarfs ( $400 \text{ K} \lesssim T_{eff} \lesssim 1300 \text{ K}$ ), also showing plateau of temperature between L7 and T4.5 (the so-called L/T Transition). This plateau of temperature is consistent with the chemical analysis by Marley et al. (1996) for Gl 229B indicating the sensitivity to temperature of the CO to methane transition. Additional analysis of changes in infrared colors across this transition are consistent with the onset of methane occurring with little temperature change,

but significant opacity changes in the near infrared, i.e., the condensation of dust out of the photosphere.

Likewise, Cruz et al. (2003) derived empirical relations between J band (1.2  $\mu m$ ) photometry and spectral type. Knapp et al. (2004) derived empirical relations between infrared photometry and spectral type using several dozen brown dwarf spectra ranging down to T9.

Currently, two suites of brown dwarf atmosphere and evolution models are widely used.

The set of models by Baraffe et al. (1998, 2003) and Chabrier et al. (2000) (sometimes referred to collectively as the LYON models) treat L and T dwarfs individually. The set of models appropriate for L dwarfs (the DUSTY model) assumes dust grain clouds form (in chemical equilibrium) and affect opacity by the scatter and absorption of flux, as well as by depleting the metallic and dust-forming elements from the photospheric gas. The second set of models appropriate for T dwarfs (the COND models) also assumes that dust grains forms, but that these grains large enough to condense out and only affect opacity by their depletion of metallic and dust forming elements. Neither of these models include any mechanism to drive grain growth and thus neither handle well brown dwarfs near the L-T transition. Likewise, out of equilibrium chemical species are not included.

Chabrier et al. (2000) stressed that although the variations in the treatment of dust could provoke large photometric and spectral changes, this had very little effect on the overall cooling rate used by evolution models. In other words, one need not derive evolution cooling curves for each set of atmospheric models (i.e., cooling curves are universal), and evolution models are fairly independent on the

finer details of atmospheric models (to about 10% in  $T_{eff}$  and 25% in  $L_{bol}$  at the extremes).

An alternative set of models by (Burrows et al., 2001) calculates the size of dust grains, their distribution, and cloud sizes as driven by vapor pressure levels within the atmosphere, following the model of Lunine et al. (1989). As such, there is no need to distinguish between dusty L dwarfs and depleted T dwarfs, as this is handled innately by the model; these models are sometimes referred to as the PHOENIX/TUCSON models.

## Atmosphere Models

Linking the observed features of the brown dwarf spectra to the underlying physical chemistry in the photosphere is the fundamental aim of atmospheric chemistry. The importance of obtaining accurate photometry across multiple wavebands and spectra of brown dwarfs were recognized early as the fundamental limitation to advancing the theory of brown dwarf atmospheres Stevenson (1986), and remain one of the most important considerations still (Konopacky et al., 2010; Dupuy et al., 2010).

Most of the trends and characteristics are understood in terms of general chemistry (Burrows & Sharp, 1999) which have put a premium on the calculation and inclusion of accurate molecular opacities. However, the most difficult challenge for the advance of atmospheric models is the accurate incorporation of a natural mechanism for the formation of dust grains (calcium aluminates, silicates, and iron) (Burrows et al., 2005). While a robust mechanism for grain condensation has not yet been formed, more recent models suggest that changes in surface gravity and metallicity, in addition to temperature, play an important role for driving the

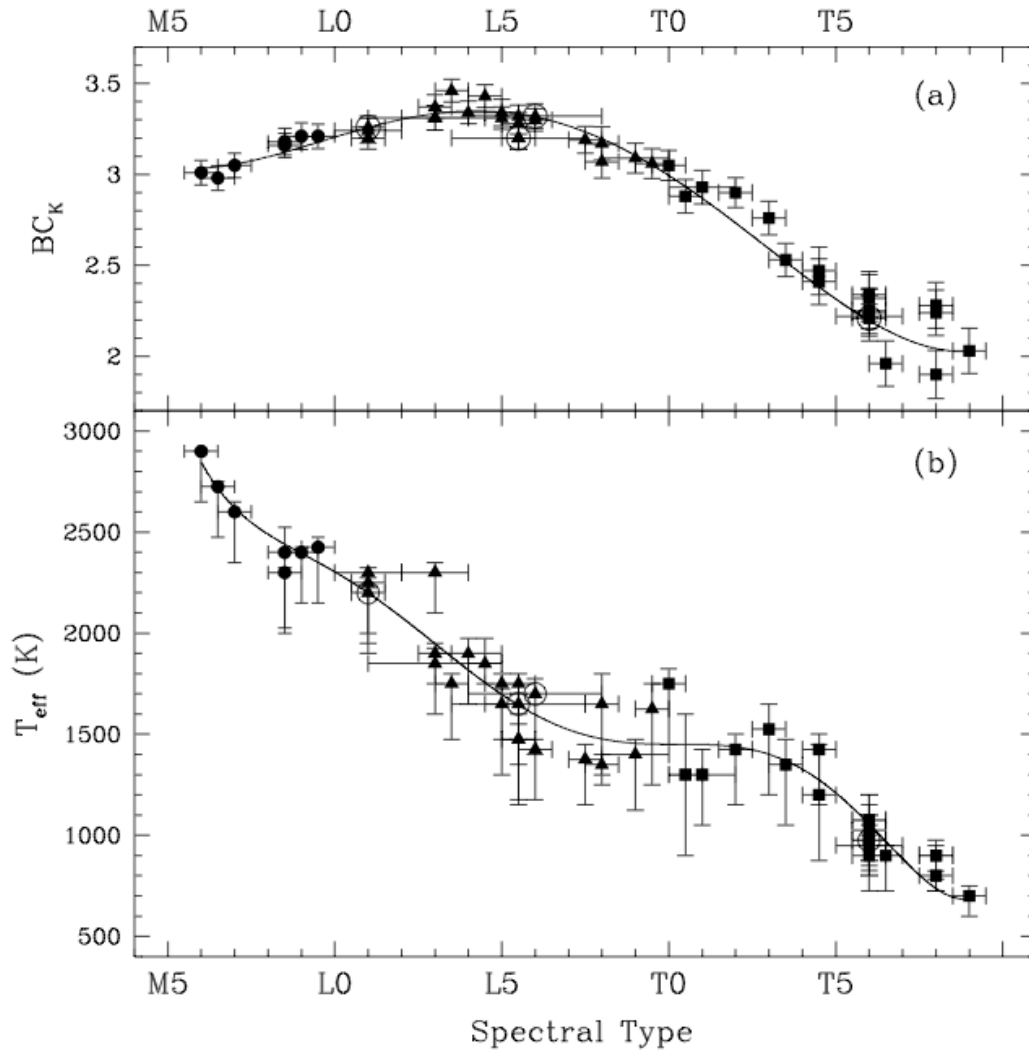


Figure 2.2: Bolometric correction for K band photometry and Effective temperature as functions of spectral type from Golimowski et al. (2004) (Top) Bolometric corrections can be used to obtain total luminosity,  $L_{bol}$ , from K band photometry. (Bottom) By making certain assumptions about the brown dwarf radius, effective temperature can be estimated from total luminosity. (See text.) Notice the plateau of temperature marking the transition from L and T dwarf classes

effect (Burrows et al., 2006).

Figure 2.3 shows the progression of infrared photometry through spectral type for solar mass stars, low mass stars, and brown dwarfs. Solar mass infrared photometry use the empirical mass-luminosity relations of Henry & McCarthy (1993). Low mass stars (M0 and later) and brown dwarfs use the photometry of Baraffe et al. (2003) and the spectral type- $M_J$  relation of Cruz et al. (2003). The infrared photometry of a blackbody is drawn for comparison; the infrared flux brightening of dusty stars (M6 and later) and brown dwarfs is readily apparent.

## Evolution Models

As stated previously, brown dwarfs shine by converting their gravitational energy into luminosity and slowly cool with age. In other words, the internal structure (i.e., radius, convection zone, etc.), temperature, and luminosity, of a brown dwarf of a particular mass evolves with time.

The evolution with age of total luminosity and effective temperature of very low mass stars, brown dwarfs, and planets through the lower spectral types are shown in Figures 2.4 and 2.5 using the evolution models of Burrows et al. (2001). Cooling during evolution results from the bulk luminosity output of brown dwarfs, and therefore is not particularly sensitive to the details of the atmospheric model used to describe the specific wavelengths of radiation emitted. These evolution curves can therefore be viewed as nearly universal and independent from atmospheric models.

Brown dwarfs form quite warm and bright ( $T_{eff} \sim 2500\text{-}3200$  K), and at temperatures on par with low-mass main sequence stars. This highlights the fundamen-

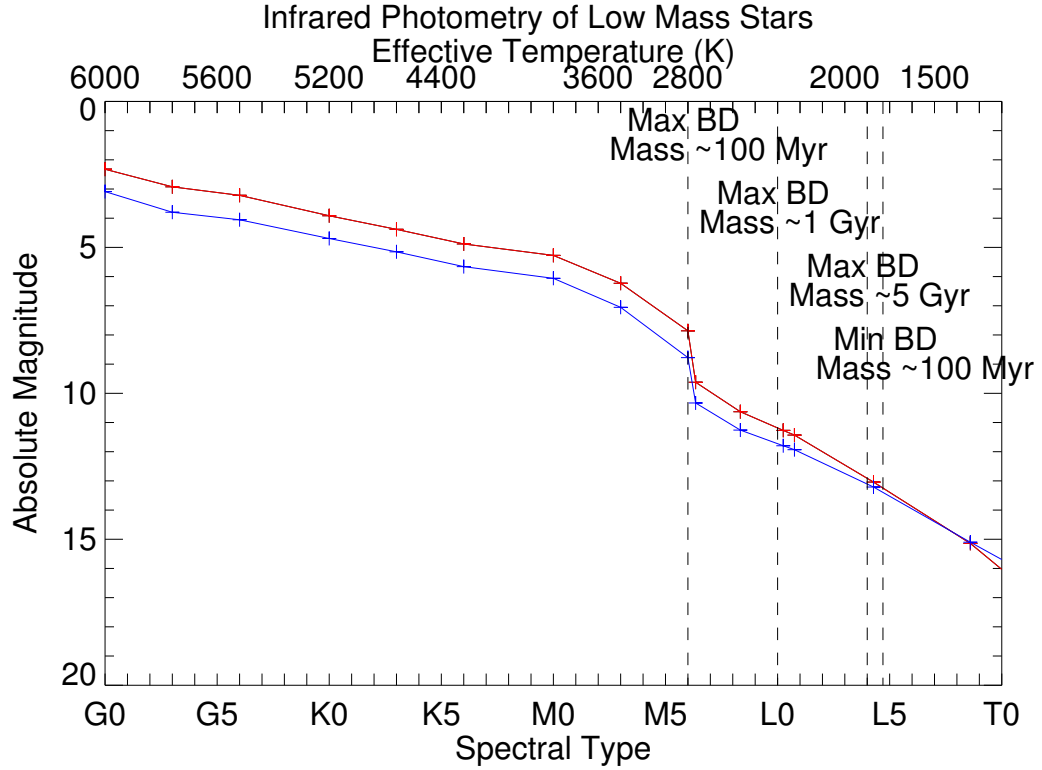


Figure 2.3: Infrared photometry of low mass stars as a function of effective temperature. Photometric colors are primarily a function of effective temperature and predominantly dependent on the physical chemistry of the brown dwarf atmospheres. In the absence of spectra, broadband photometric colors are a proxy for spectral type and temperature. Low mass curves (M0 and later) use photometry of Baraffe et al. (2003) and the spectral type- $M_J$  relation of Cruz et al. (2003). High mass curves use the mass-luminosity relations of Henry & McCarthy (1993). The infrared photometry of a blackbody is drawn for comparison; the infrared flux brightening of dusty stars (M6 and later) and brown dwarfs is readily apparent.

tal problem of using spectral type (or effective temperature) alone as a predictor of brown dwarf mass. That is, an object classified as a late-M dwarf may be either a young brown dwarf or an old-main sequence star. To accurately assess the brown dwarf mass, luminosity *and age* are necessary. In general regarding total luminosity, effective temperature, mass, and age, evolution models can be used with any two quantities to calculate the remaining two.

From these figures, it is clear that the lowest-mass hydrogen burning stars are in fact early L dwarfs, and brown dwarfs of all masses begin as M dwarfs for the first hundred million years of their life. But as expected from earlier investigations, brown dwarfs evolve predominantly through the L ( $1400 \text{ K} \lesssim T_{eff} \lesssim 2200 \text{ K}$ ) and T ( $400 \text{ K} \lesssim T_{eff} \lesssim 1300 \text{ K}$ ) spectral types.

The minimum hydrogen-burning mass is a clear demarcation between brown dwarfs and stars at  $0.072\text{-}0.075 M_{\odot}$ , below which hydrogen fusion is not ignited. However, brown dwarfs between  $13$  and  $80 M_J$  do undergo a brief period when young in which they fuse primordial deuterium. This onset of deuterium fusion can be seen in the brief shoulder of constant luminosity in tracks of Figure 2.4 before brown dwarfs reach an age of 50 million years. Because objects less massive than  $13 M_J$  never reach deuterium fusing temperatures, this is occasionally used to distinguish between brown dwarfs and planets.

Brown dwarfs more massive than  $65 M_J$  also undergo a brief period of primordial lithium fusion at an age of about 10 million years. This provides one method for placing an upper limit on the mass of an observed brown dwarf: the presence of lithium in the brown dwarf spectrum places the mass at below  $65 M_J$  (Rebolo et al., 1992)

Evolution models have limited effectiveness for brown dwarfs (and particularly massive exoplanets) at ages of less than tens of millions of years, as the specific characteristics of objects this young are still quite sensitive to the conditions of formation (Marley, 2007; Fortney et al., 2008). Most strikingly, models predict the total luminosity of young objects can span a factor of hundreds or thousands, depending on the method by which brown dwarfs and exoplanets expel their entropy during formation (i.e., 'hot start' versus 'cold start'). The specific formation mechanism can affect the observable properties of these objects out to an age of one billion years, depending on the mass of the object. Importantly, evolution models are least well constrained empirically at young ages, and the majority of directly imaged exoplanets will be youthful (because they are brighter). This speaks to the immediate need for empirical constraints on brown dwarf evolution models at young ages.

Because evolution models provide the mass-luminosity-age relation for brown dwarfs, one only needs two of the three to calculate the third. In particular, a measurement of the brown dwarf mass combined with luminosity (or photometry) allows one to place a constraint on the brown dwarf age. Constraints on age are more effective for young brown dwarfs, for which luminosity tracks are more widely spaced (See Figure 2.4).

Using the evolution model of Baraffe et al. (2003), we can explore the mass-temperature-age relation of very low mass stars and brown dwarfs. Figure 2.6 shows the relationship between mass and effective temperature for stellar and substellar objects for three isochrones (ages of 100 million years, 1 and 5 billion years). As can be seen, young ( $\sim 100$  million years old) brown dwarfs span temperatures of 1500-2500 K, cooling by as much as 1500 K over their lifetime. The oldest,

lowest mass brown dwarfs reach temperatures as low as 400 K. High mass curves use the empirical mass-luminosity relations of Henry & McCarthy (1993).

Using the evolution and atmospheric models of Baraffe et al. (2003) we can explore the mass-luminosity-age relation of very low mass stars and brown dwarfs. Figure 2.7 shows the relationship between mass and infrared photometry for stellar and substellar objects of the same isochrones as Figure 2.6. Despite the flux enhancement in the infrared, brown dwarfs are still much fainter than more massive objects in these wavebands. Eight magnitudes (1500:1 flux ratio) separate solar mass stars and the most massive brown dwarfs at an age of 1 billion years. This flux ratio improves at younger ages, but remains larger than 6 magnitudes (250:1) for younger objects. The onset of the T dwarf spectral class can be inferred from these curves by locating the point at which J band fluxes grows brighter than K band, at a mass of about  $0.030 M_{\odot}$  at 1 billion years.

### 2.3 Using Mass Measurements to Test Evolution Models

Brown dwarf atmospheric models are capable of reproducing the photometry and spectral features across the span of brown dwarf spectral types. As shown in Figure 2.2, these spectral types can be well characterized by their effective temperature and total luminosity. Spectra of hundreds of isolated brown dwarfs have been instrumental in advancing these models to their current state.

Brown dwarf evolution models relate the physical parameters of mass, age, and radius, to total luminosity and effective temperature, which can then be used by atmospheric models to determine photometry or spectra. Yet, the fundamental difficulty of measuring the mass, age, and/or radius of a brown dwarf has limited

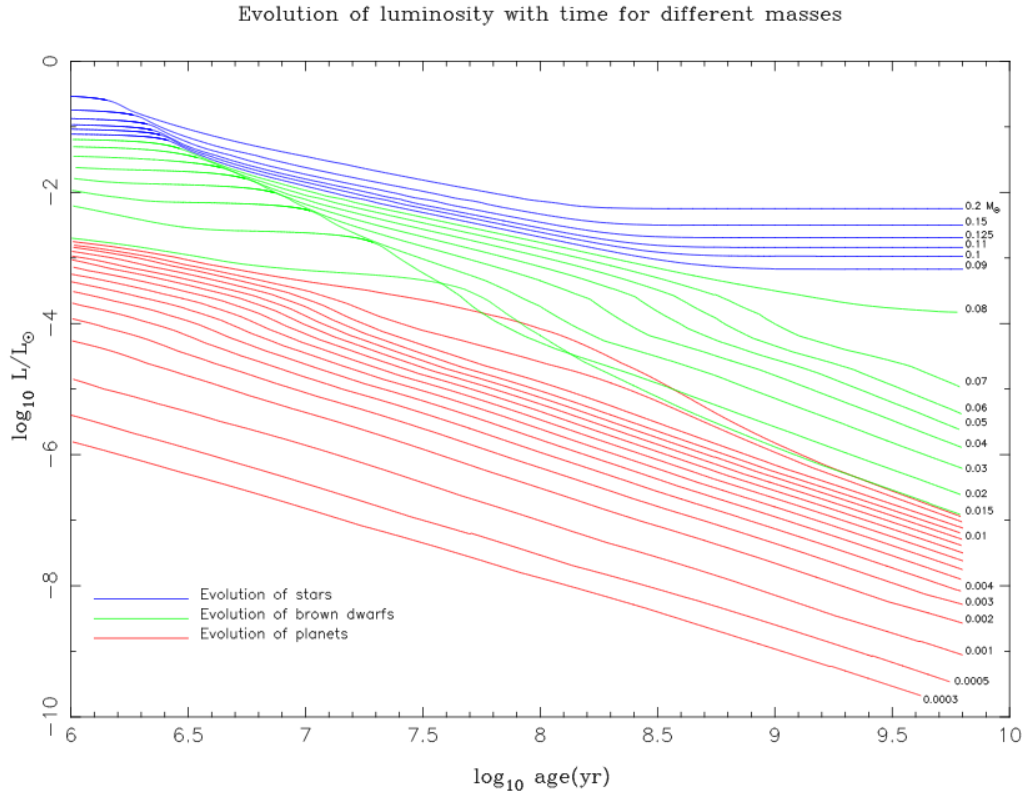


Figure 2.4: Evolution of luminosity tracks for low mass stars (blue), brown dwarfs (green), and planets (red) from Burrows et al. (1997). Object masses (in  $M_{sun}$ ) are marked at the right-side end of the tracks. The top set of lines (0.08-0.20  $M_{sun}$ ) trace out the evolution of low mass stars; note the onset of fusion at 0.5-1.0 Gyr and further stabilization of luminosity, while brown dwarfs continue to dim. The shoulder of brief, but constant luminosity early in the evolution of stars and brown dwarfs signals the brief fusion of primordial deuterium.

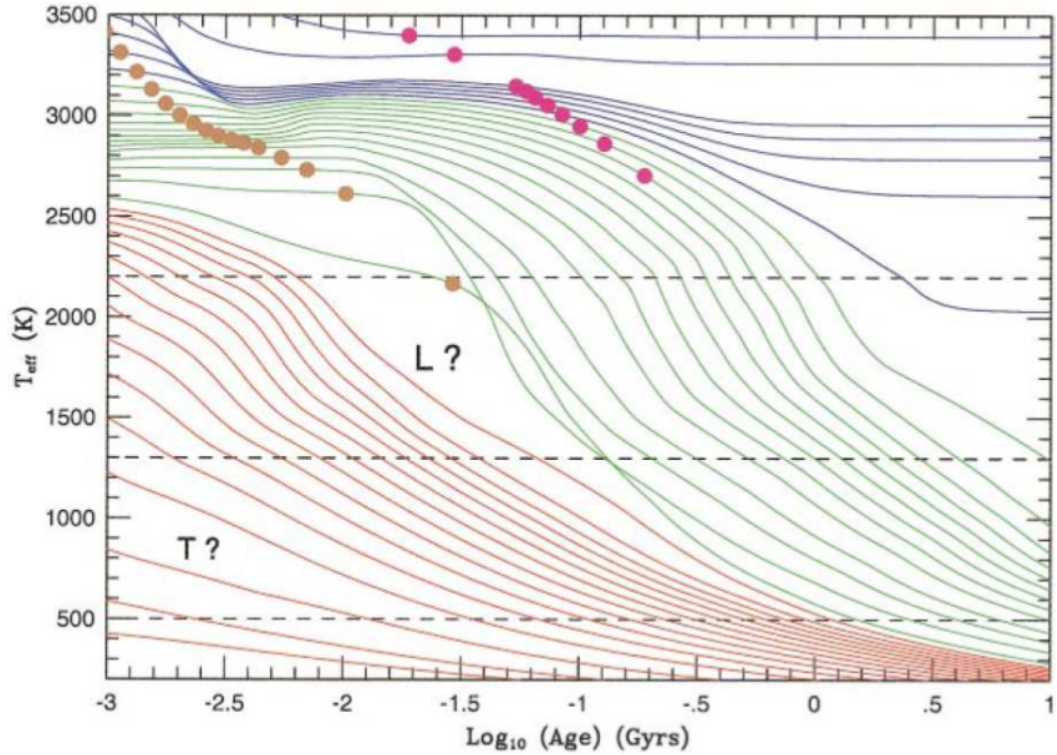


Figure 2.5: Evolution of effective temperature for low mass stars (blue), brown dwarfs (green), and planets (red) from Burrows et al. (2001). These sets of lines are the same as in Figure 2.4. Horizontal lines mark the evolution from spectra classes M to L and L to T. Note that the lowest mass hydrogen burning stars evolve into L dwarfs, and that all brown dwarfs start as M dwarfs. Because brown dwarfs evolve through to later spectral types for the entirety of their lifetime, unlike stars which stabilize after  $\sim 1$  Gyr, spectral type without age is a poor indicator of brown dwarf mass. The orange filled circles mark the 50% depletion of deuterium; the magenta circles mark the 50% depletion of lithium. Since brown dwarfs less massive than  $\sim 0.060 M_{\text{sun}}$  never deplete their primordial lithium, the presence of lithium in L dwarf spectra is an indicator that the object is a brown dwarf.

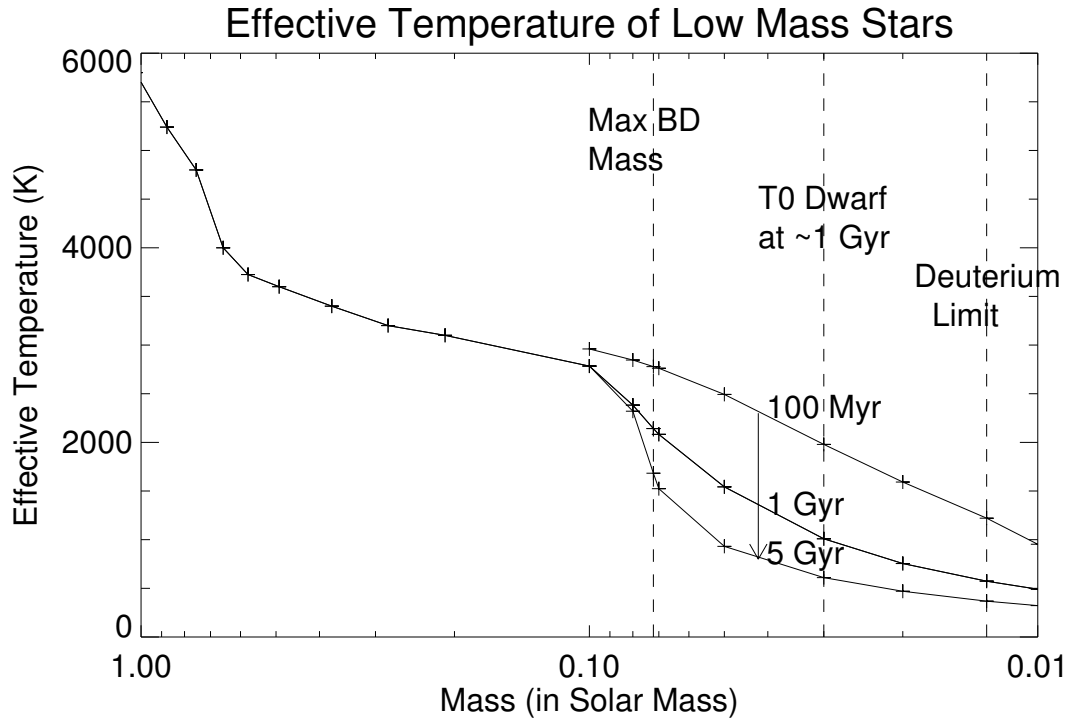


Figure 2.6: Effective Temperature as a function of mass for low mass stars and brown dwarfs using the evolutionary models of Baraffe et al. (2003). Unlike stellar objects, the temperatures of brown dwarfs cool significantly with age; for any temperature derived from photometry, nearly every brown dwarf mass may be possible if age is not constrained. Conversely, while temperature changes rapidly early, brown dwarfs cool more slowly after several billion years, and precisely measured masses ( $\sim 10\%$ ) give little constraint to age. Low mass curves (M0 and later) use photometry of Baraffe et al. (2003) and the spectral type- $M_J$  relation of Cruz et al. (2003). High mass curves use the mass-luminosity relations of Henry & McCarthy (1993).

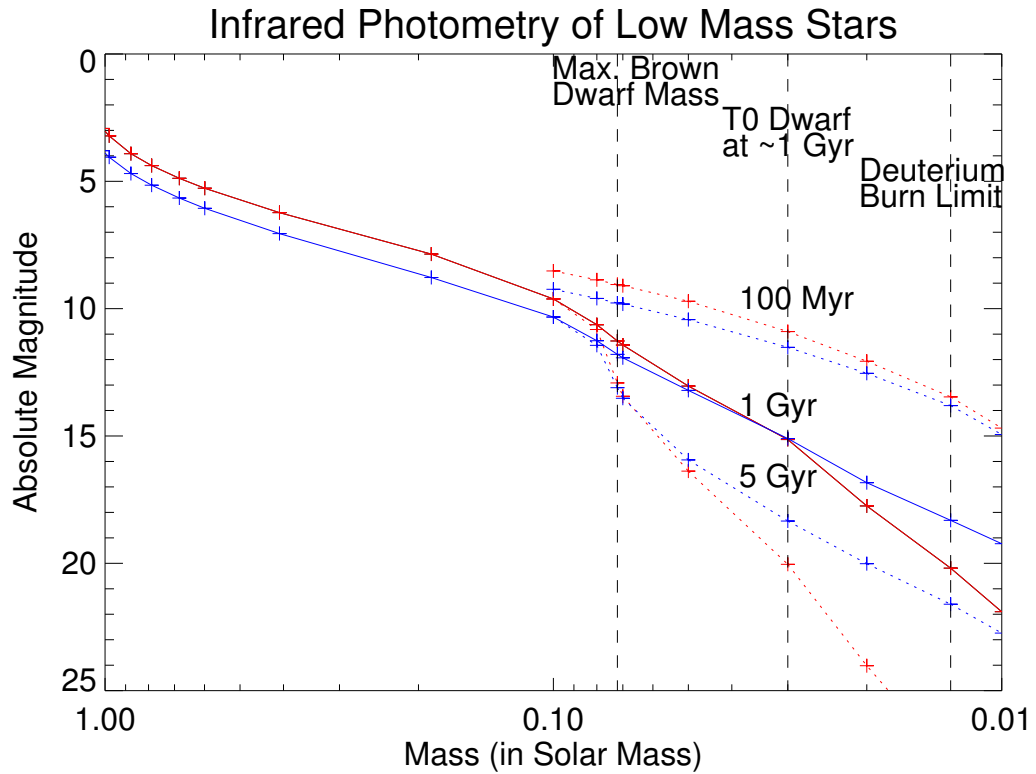


Figure 2.7: Infrared photometry of low mass stars and brown dwarfs (J band, blue; K band, red) using the models of Baraffe et al. (2003). Eight magnitudes (1500:1 Flux Ratio) separate solar mass stars and the most massive brown dwarfs at an age of 1 Gyr. Brown dwarfs dim with age, spanning roughly eight magnitudes between 100 Myr and 5 Gyr. Low mass stars and L dwarfs are red in infrared color, this changes rapidly at the onset of the T dwarf spectral class.

the number of empirical constraints used to confirm and progress these models.

Model-independent measurements of brown dwarf masses provide the strongest constraints on evolution models; i.e., "mass benchmarks" to which evolution predictions can be compared Liu et al. (2008). Fundamental properties such as effective temperature are about five times better constrained with dynamical mass measurements than with measurements of age.

Directly imaging a brown dwarf companion to another star and tracking its orbit provides the most readily available method for model-independent mass measurements. With relative astrometry provided by direct imaging, one is able to directly measure the total mass of the system. When combined with radial velocity, one obtains the masses of the individual components.

Companion detections through radial velocity alone give access to only to the quantity  $M \sin i$ , a combination of the companion mass and its orbital inclination, and requires direct imaging of the pair to break this degeneracy. Detections by transit give access to both the mass and radius of the brown dwarf (assuming the mass and radius of the host star can be accurately determined by stellar models), but are rare: only one brown dwarf is so far known by transit (Stassun et al., 2006).

Binary measurements give three constraints on the suite of models: mass; photometry, which can be used to obtain total luminosity from empirical relations; and the assumption that both objects are the same age, even if that age is unknown (co-evolution). As mentioned in the previous subsection, these three constraints allows one to calculate the system age using evolution models. For a given system age, one can directly calculate the mass and photometry (or luminosity) of each

component until the optimal age is found (Liu et al., 2008)

Likewise, effective temperature can be derived for the brown dwarfs because evolution models also provide the radius (c.f. Equation 2.1). These quantities have all been calculated using only evolution models and empirical relations.

Several approaches towards testing the evolution models can be used.

(1) On almost purely empirical bases, the evolution-derived effective temperature can be compared to temperatures for L and T dwarfs derived by Golimowski et al. (2004), by using the relations of Knapp et al. (2004) to obtain the spectral types of the binary components from their photometry. This comparison is reasonably accurate and limited only by model-dependent radii used by Golimowski et al. (2004), but these are predicted to vary by less than 30%.

(2) The atmospheric models can be used to fit photometric or spectral data to obtain an alternative measure of effective temperature. In this circumstance, it is not possible to discern whether the discrepancy arises from evolution or atmosphere models, although atmosphere models are quite uncertain in their determination of effective temperature (Liu et al., 2008).

(3) Measurements of the component masses can be compared directly to those predicted by atmosphere and evolution models. Using Golimowski et al. (2004) derived luminosities and atmospheric fits to photometry for effective temperature, evolution models can be used to make an estimate of the masses and age of the binary components. This approach is perhaps the most natural comparison for the purposes outlined in the introduction and has been used by Konopacky et al. (2010).

To date, mass measurements of "meaningful" precision ( $\lesssim 30\%$ ) have been made of only nine systems which contain brown dwarfs; several other systems have been measured with much less precision ( $\gtrsim 60\%$ ) (Konopacky et al., 2010; Dupuy et al., 2011). All but one of these brown dwarfs are M or L dwarfs.

Still, even this small subset shows systematic discrepancies when compared to models. Konopacky et al. (2010) and Liu et al. (2008) both show that temperatures derived with atmosphere models are generally inconsistent with those derived from evolutionary models. In particular, atmosphere models predict temperatures lower than evolution models by about 200-300 K for L dwarfs, although this systematic trend appears to reverse for the single T dwarf with measured masses. Alternatively, if atmosphere and evolution models are used to predict the brown dwarf masses from photometry, this method incorrectly yields masses too low by 50-70% for L dwarfs (and too high for the T dwarf).

Thus, one must exhibit caution when using these models to predict the masses of substellar objects. In particular, this indicates that imaged exoplanets, such as the planetary companions to HR 8799 (masses of 7, 10, and 10  $M_J$ ), are likely to also be systematically in error (Marois et al., 2008).

One must recognize that a large subset of much more precisely measured masses spanning the entire range of brown dwarf masses are necessary to begin challenging evolution models. This is particularly evident when one keeps in mind that inherent in the atmospheric models are assumptions of opacities, metallicities, cloud models, etc., all of which operate in tandem with evolution models to predict the mass or age of a binary system. Radius, for instance, may span a wide range (perhaps 25%) for a given mass and age for hot, evolving brown dwarfs depending on cloud formation and elemental composition (Burrows et al., 2011). To truly carve into

our understanding of brown dwarfs requires many additional benchmarks against which these models can be tested.

## 2.4 The Challenge of Resolving Brown Dwarf Binaries

A confluence of natural and technical challenges has prevented the brown dwarf community from amassing a larger database of precisely measured brown dwarf masses. Resolving brown dwarfs as companions to stellar and sub-stellar objects and the subsequent tracking of their orbits requires overcoming several challenges.

Four criteria must be satisfied to detect brown dwarf companions and acquire measurements of their dynamical masses:

1. The orbital period must be short enough to track the nearly full or full orbit in a reasonable length of time; this, equivalently, requires binaries with small primary-secondary separations.
2. Technology and/or techniques can be obtained that can achieve high enough levels of angular resolution to resolve the individual components of the binary, given the distortions introduced by the atmosphere.
3. Given the level of image contrast that technique is able to achieve (usually as a function of separation), the faint brown dwarf can be identified above photon noise, background noise, detector noise, or more usually, the glare of the primary star and/or systematic errors which distort image quality.
4. That such a potential system exist at a location in the sky which allows the above three constraints to be satisfied.

In other words, given the technical challenges at telescopes and the natural distribution of stars, what brown dwarf systems can we observe?

### 2.4.1 Angular Resolution for Brown Dwarf Dynamical Masses

To obtain precisely measured brown dwarf masses, one necessitates high-contrast *and* high-angular resolution capabilities.

The period,  $T$ , of a binary scales with Kepler's Third Law:

$$T^2 = (2\pi)^2 a^3 / GM_{total}$$

$$\left(\frac{T}{1 \text{ yr}}\right)^2 = \left(\frac{a}{1 \text{ AU}}\right)^3 \left(\frac{1 M_\odot}{M_{total}}\right) \quad (2.2)$$

where  $a$  is the semi-major axis of the orbit and  $M_{total}$  is the combined mass of the binary. Obtaining dynamical mass requires tracking a full or nearly full orbit; to track the orbit in reasonable amount of time (a few years) requires resolving very closely-separated ( $\lesssim$  a few AU) binaries.

This is shown quantitatively in Figure 2.8. The figure shows the period of a  $0.070 M_\odot$  brown dwarf in orbit around primaries of various spectral types and a range of semi-major axes. Orbital period clearly rises quickly with semi-major axis; to find a binary with periods shorter than 5 years requires the detection of brown dwarf companions at separations closer than about 3 AU.

Nearby field stars in the solar neighborhood span distances of  $\gtrsim$  10-100 parsecs. For binary systems at a given distance, the semi-major axis corresponds to an

angular separation of:

$$\theta_{bd} = 100 \text{ mas} \times \left( \frac{a}{1 \text{ AU}} \right) \left( \frac{d_{system}}{10 \text{ pc}} \right). \quad (2.3)$$

From this we conclude that dynamical mass measurements require a capability to resolve brown dwarf companions at separations closer than 300 mas ( $\sim 5. \times 10^{-4}$  degrees).

## 2.4.2 Primary-Secondary Contrasts for Brown Dwarf Companions

### Late-Type Primaries are Favorable

Despite the 'flux enhancement' in the infrared of brown dwarfs due to their opacity sources, the contrast between a solar type star and the most massive brown dwarfs at an age of 1 billion years is roughly eight magnitudes (1500:1 flux ratio). This contrast drops to six magnitude (200:1 flux ratio) when the primary is an M0 dwarf (Figures 2.7 and 2.9). Assuming that equal imaging performance can be achieved for both primaries, there is a large benefit to surveying late-type stars (M and K dwarfs).

### Youthful Systems are Favorable

Unlike stars, which retain their brightness throughout their lives, brown dwarfs dim by a factor of  $\sim 10$  while aging from 100 million to 1 billion years, and another factor of  $\sim 10$  by 5 billion years. Indeed, this signals another strategy for companion searches: young systems. These systems also yield insight into the early stages

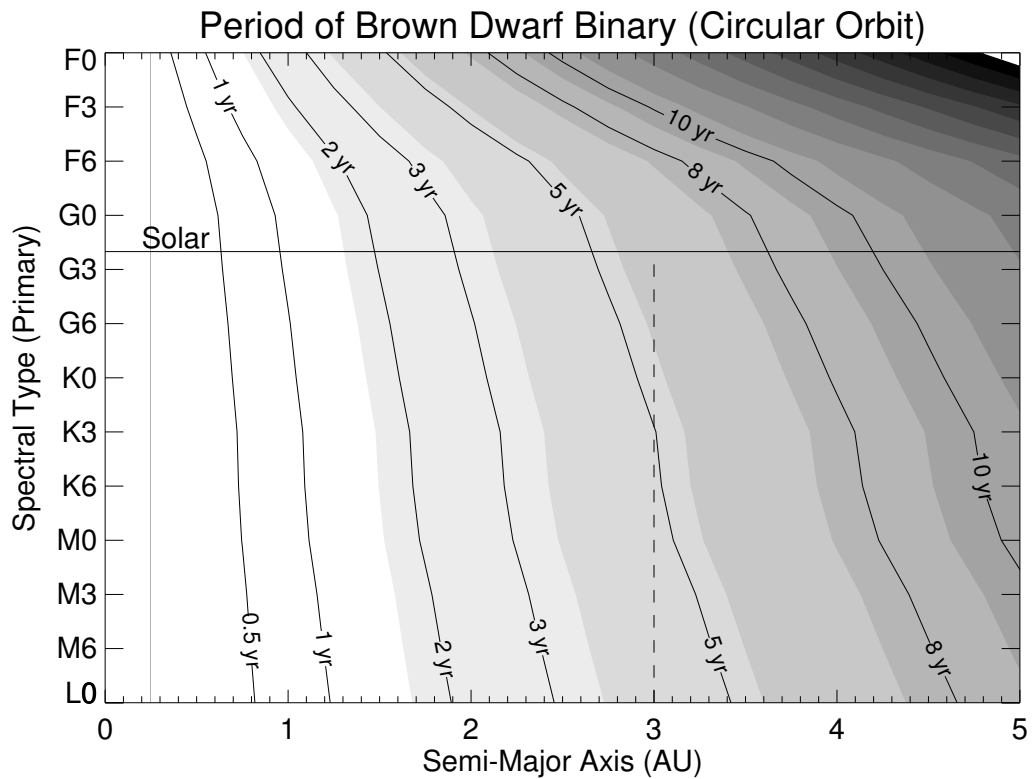


Figure 2.8: Orbital period for a  $0.070 M_{\odot}$  brown dwarf companion as a function of semi-major axis and primary spectral type. Wide-separated binaries orbit too slowly to track their orbits (and obtain dynamical masses) in a practical length of time. In order to obtain the system mass measurements in less than five years of observing, binaries with physical separations less than 3 AU need to be targeted.

of brown dwarf evolution and formation by exploring, for instance, the structure evolution of young brown dwarfs or their migration mechanism (Kraus et al., 2008, 2009).

Unfortunately, age is a difficult parameter to measure for individual stars and the distribution of stellar ages in the solar neighborhood is roughly flat. Correlations between age and activity have been successfully used to identify clusters of similarly youthful stars in the solar neighborhood. Several of these *young associations* and *moving groups* have been identified in the northern hemisphere (Zuckerman, 2004; Torres et al., 2006). To date, the youngest clusters are relatively far away (e.g., Upper Sco: roughly 5 million years and 140 parsecs). At such great distances, even higher resolution is needed for dynamical masses (e.g., diffraction limited H band observations correspond to physical separations of 1.1 AU at 140 parsecs). Alternatively, clusters of nearby, moderate age collections offer a potent compromise between youth and proximity (ages 10-150 million years at distances of 10-50 parsecs), while also providing insights into the evolution of brown dwarf systems with age. Several moving groups are known in the northern hemisphere and many more in the southern hemisphere. Moving group identification is an observationally intensive project and cataloging the late-type (M and K dwarf) members of these groups has only recently begun (Schlieder & Lepine, 2010). Both of these surveys will provide fertile grounds for upcoming brown dwarf and exoplanet imaging surveys and for the studies of young brown dwarfs.

### **Mid-Infrared Bands are Favorable**

Finally, one can consider the advantages of observing at the longer wavelengths of the mid-infrared (2-10 $\mu m$ ). Like the near infrared, brown dwarfs are flux enhanced

at mid-infrared wavelengths and the nominal blackbody contrasts are also more favorable at longer wavelengths. The impact of atmospheric turbulence is greatly reduced at longer wavelengths, in fact, 5-meter class telescopes are nearly diffraction limited at  $10\mu m$ , and turbulence evolves more slowly, allowing for slower run wavefront sensors and fainter natural guide stars. While direct imaging in the mid-infrared will certainly play a role in future exoplanet surveys, adaptive optics technologies have just recently begun to come online at these wavelengths (e.g., MMT Telescope, Wildi et al. (2003)).

### 2.4.3 Adaptive Optics: Resolution

Measuring the mass of brown dwarfs by orbit tracking in a few years requires resolution reaching approximately 300 mas or better. Resolving brown dwarfs requires contrasts of  $10^2$ - $10^3$ :1 in order to detect brown dwarf companions to solar type stars in the infrared. A far easier aim is to resolve companions in orbit around brown dwarf *primaries*. In this section, we explore the technical feasibility of these observations using current technology in the infrared.

An optically perfect telescope, observing a point source through a still and homogeneous atmosphere will image a spot of angular size  $1.22 \lambda/D$ , where  $D$  is the diameter of the telescope aperture and  $\lambda$  is the wavelength of the observation. As a point of reference, the 200" Hale Telescope at Palomar Observatory (5.08 m) observing in the infrared H band ( $1.6 \mu m$ ) images a spot size  $\sim 65$  milliarcseconds in radius.

Distinguishing two closely separated objects is the primary challenge of direct imaging for high angular resolution. The finite size of a point source provides

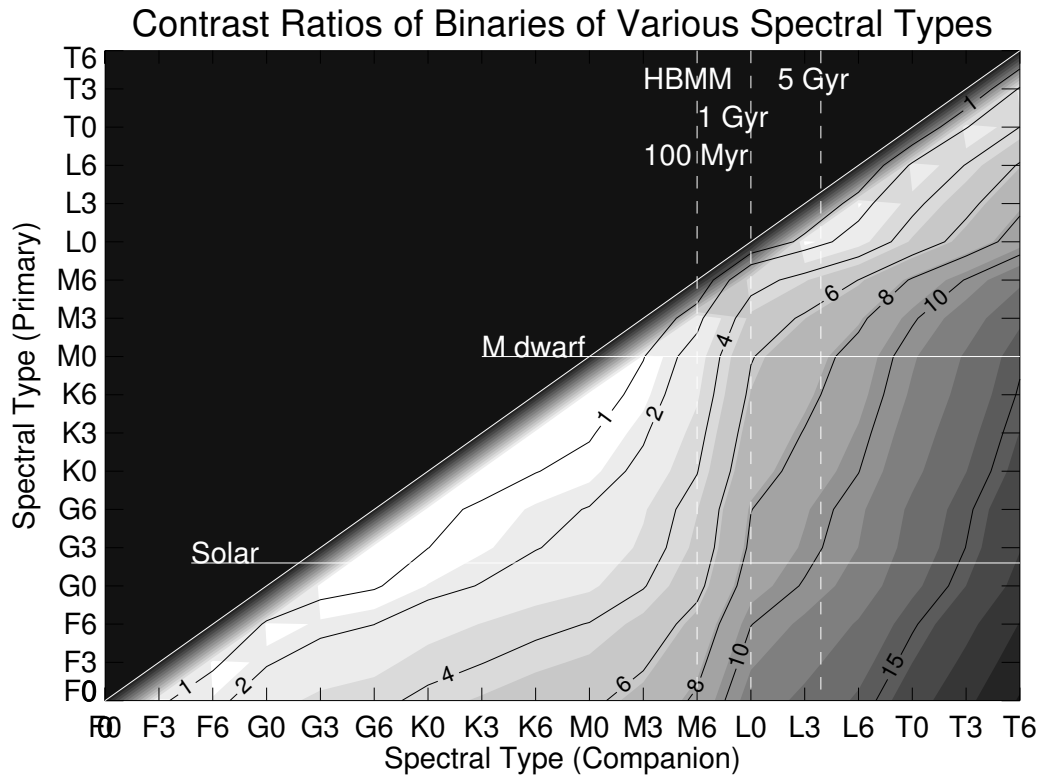


Figure 2.9: Primary-Secondary Contrast Ratio of Binary Systems. Clearly, late-type stars offer more favorable contrast ratios than solar type stars. Particularly noteworthy is the rapid drop in brightness (a factor of 100) moving from L0 dwarfs (massive brown dwarfs) to T5 dwarfs (lighter brown dwarfs). Probing the entire mass range of brown dwarfs requires very high contrasts in the most favorable of cases.

Table 2.1: Techniques For Resolving Closely Separated Brown Dwarf Companions

Technique	Contrast	Separations	Orbital Periods
Direct Imaging	30:1	200 mas	5+ years
Coronagraphy	10000:1	1000 mas	100+ years
Aperture Masking	200:1	50 mas	1+ year

Table 2.2: Pros and Cons of Primary Type

Binary Type	Contrast	Pros	Cons
Solar-BD Binary	100-1000:1	Great AO Correction	High Contrast; Rare
BD-BD Binary	10-100:1	Low Contrast	Requires LGSAO or Hierarchical Triple

Table 2.3: Survey Types For Brown Dwarf Companion Searches

Survey Sample	Pros	Cons
Field Stars	Nearby and Cataloged	Many Old Systems
Mid-IR	Contrast Better by 10x	Few mid-IR AO systems, Higher diffraction Limits
Young Stars	Contrast Better by 10-100x	Young Clusters Too Far To Probe Close
Moving Group Clusters	Moderate Age and Distance	Membership Unknown

an estimate for the smallest angle by which separate objects can be resolved, the so-called *diffraction limited resolution*:

$$\theta_{min} = \frac{1.22\lambda}{D}. \quad (2.4)$$

The criterion is only a rule-of-thumb; one can certainly imagine an experiment taking images so precisely that the overlap of two such spots could be distinguished by, for instance, the elongation of the spot in one direction.

However, the atmosphere is a turbulent, inhomogeneous window through which the stars are observed. Variations in the temperature and index of refraction deform the phase and amplitude of the incoming wavefront. These spatial and temporal variations of the wavefront distort the image and degrade image quality. Typically, these *seeing* effects blur out point sources in long exposures and prevent one from reaching angular resolution finer than about one arcsecond (1000 mas).

To minimize the effects of atmospheric turbulence, major efforts within the field aim to develop real-time optical components able to measure and counteract wavefront errors; these systems are generally referred to as *adaptive optics* or AO. A typical system consists of a feedback loop a system for measure real-time wavefront shape across the telescope pupil at a speed of about a thousand measurements per second and system between a deformable mirror without about a thousand actuators. Good adaptive optics systems can remove so much of the atmospheric turbulence that the resulting image approaches that of the diffraction limit. With deconvolution algorithms, one is often able to obtain diffraction limited resolution; although ones chances of seeing a particularly faint companion at these separations is not particularly high.

A diffraction-limited adaptive optics-corrected infrared image is shown in Figure 2.10. The image is a typical long exposure H band ( $1.6\mu m$ ) image taken by

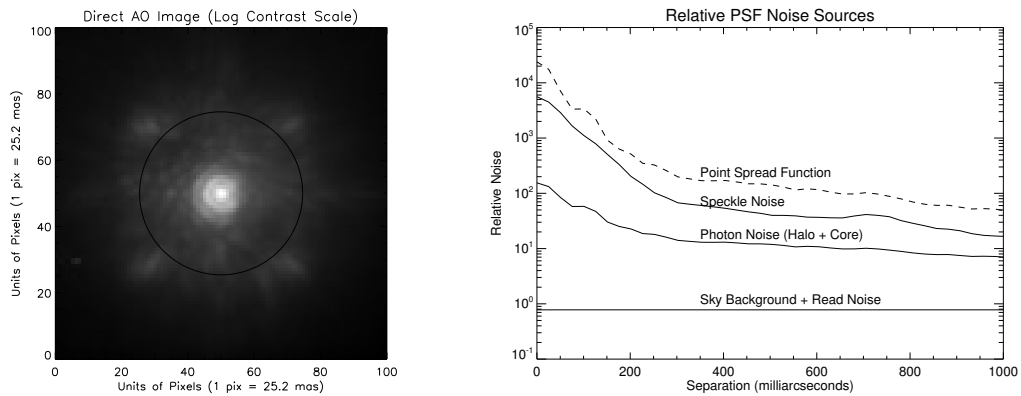


Figure 2.10: Contrast and Resolution of Direct AO Imaging is inhibited by *speckle* noise, a diffraction effect of wavefront errors, and not photon noise. (Left) Total of 150 one second exposures of HIP 52942 in H band on April 12, 2009 (Strehl  $\sim 20\%$ ). The first and second Airy ring can be clearly seen, as well as a diffuse halo peppered with speckles. A black circle is drawn at  $1.22\lambda/2r_a$  using the AO actuator spacing for  $r_a$ . This approximates the extent of the halo. (Right) The variance of each pixel is calculated as a function of distance from the primary and averaged azimuthally. The measured variance is compared to the calculated photon noise for the point spread function. As seen, speckle noise is a factor of  $\sim 30x$  higher than photon noise. NRM/Aperture masking leads to an increase in contrast precisely because closure phases are able to calibrate out the effect of these speckle-producing wavefront errors. This figure is an empirical analog to Racine et al. (1999), Fig. 2.

the PHARO infrared imaging instrument (Hayward et al., 2001) on the 200" Hale Telescope. The complex structure of an adaptively corrected image is immediately apparent:

1. *Diffraction Core*: At this level of correction, the bright *diffraction core* is evident at the center of the image, surrounded by the first two Airy rings. The strong presence of the diffraction core allows the extraction of diffraction limited resolution. The central location of the first two Airy rings are  $1.64\lambda/D$  and  $2.78\lambda/D$ , respectively.
2. *Halo*: A diffuse *halo* of flux encircles the diffraction core. This light is displaced from the core by the effect of small-scale inhomogeneities of the wavefront, perturbations which are on scales smaller than the adaptive optics actuator size and can't be measured or corrected. The surface intensity (the flux level) of this halo depends critically on the level of correction. However, if adaptive optics correction is consistent, deconvolution algorithms can remove some of the halo. The faintest object that can be detected within this halo depends on the success of these measures.
3. *AO Control Radius*: The finite spacing of the adaptive optics actuators prevents correction of the small-scale wavefront errors which develop the image far away from the diffraction core. The extent to which the AO system can impact image quality is about  $1.22\lambda/2r_a$ ; this is the approximate extend of the halo. Beyond this region, the image quality is no different than an uncorrected image.
4. *Speckles*: Near the first Airy ring and within the halo, one can observe a fine granular structure to the flux distribution. These grains are *speckles*, formed by large-scale wavefront errors not corrected by the adaptive optics system.

The last decade of high contrast imaging has shown that speckles set the ultimate limits for the contrast one can achieve with an imaging system.

The typical metric for measuring the quality of AO correction is the *Strehl ratio*,  $S$ , the ratio of the peak flux of the corrected point spread function to the ideal diffraction limited point spread function. Good correction in the infrared for current systems can achieve Strehl ratios of 10-30%. The percentage of the total flux contained within the diffraction core is also  $\sim S$ ; the percentage of flux within the halo is  $\sim 1 - S$ .

The level of correction is a sensitive function of the observing wavelength and brightness of the target. Shorter wavelengths experience more wavefront error and variance on shorter timescales, and are thusly more challenging to correct. Most importantly, the target must be bright enough to adequately illuminate the wavefront sensor (in the waveband in it uses to sense). The wavelength and the quality and timescale of atmospheric seeing set roughly the rate at which the AO system must run to effectively reduce the effects of turbulence.

The adaptive optics wavefront sensor requires a sufficiently bright 'guide' star to provide a reference; this can be the science target itself or a nearby object (usually less than 1 arcminute). The Palomar AO system achieves diffraction limited observing in the infrared (Strehl  $\sim 50\%$  in  $K_s$ ) using guide stars brighter than  $V \sim 10$  in typical seeing, with functionality down to  $V \sim 12$ . The celestial distribution of stars bright enough to drive adaptive optics covers less than about 1% of the total sky area. The brightness limit of adaptive optics system eliminates the prospect of observing confirmed, isolated brown dwarfs and other visually faint targets with adaptive optics.

Figure 2.11 shows the absolute visual magnitude of solar-mass and low mass stars. *Given the technical requirements of natural guide star adaptive optics, we conclude that companion searches for brown dwarfs aiming to make mass measurements must survey nearby stars of type earlier than about M3. As a rule-of-thumb, the resolution of brown dwarf companions to M3 dwarfs requires infrared contrasts of at least 100:1 or higher at separations closer than 300 mas.*

One exception which enables the exploration of even lower mass primaries for companions is the case in which this binary orbits another star which acts as a natural guide star, i.e., a hierarchical triple system. This has allowed detailed study of two nearby brown dwarf-brown dwarf binaries using the triplet primaries as natural guide stars: GJ 802b (Pravdo et al., 2005; Lloyd et al., 2006; Ireland et al., 2008) and GJ 569B (Lane et al., 2001; Osorio et al., 2004).

### **Laser Guide Star Adaptive Optics**

Another exception for exploring very low mass stars for companions with high resolution relies on the continued development of new Laser Guide Star Adaptive Optics systems (Palomar, Roberts et al. (2008); Keck, Wizinowich (2006)). These systems use a 589nm sodium laser to excite a patch of the sodium layer in the upper atmosphere. This excited path acts as the guide star to drive high order wavefront correction. This system still requires a bright star close to the science target for low order corrections, but with greatly relaxed constraints (as much as 60 arcminutes without loss of correction, down to visible magnitudes of 17.5).

Laser guide star adaptive optics systems allow diffraction limited imaging of faint targets, including companion searches using brown dwarfs as *primaries*. This greatly alleviates the difficulties of contrast ratios and enables mass measurements

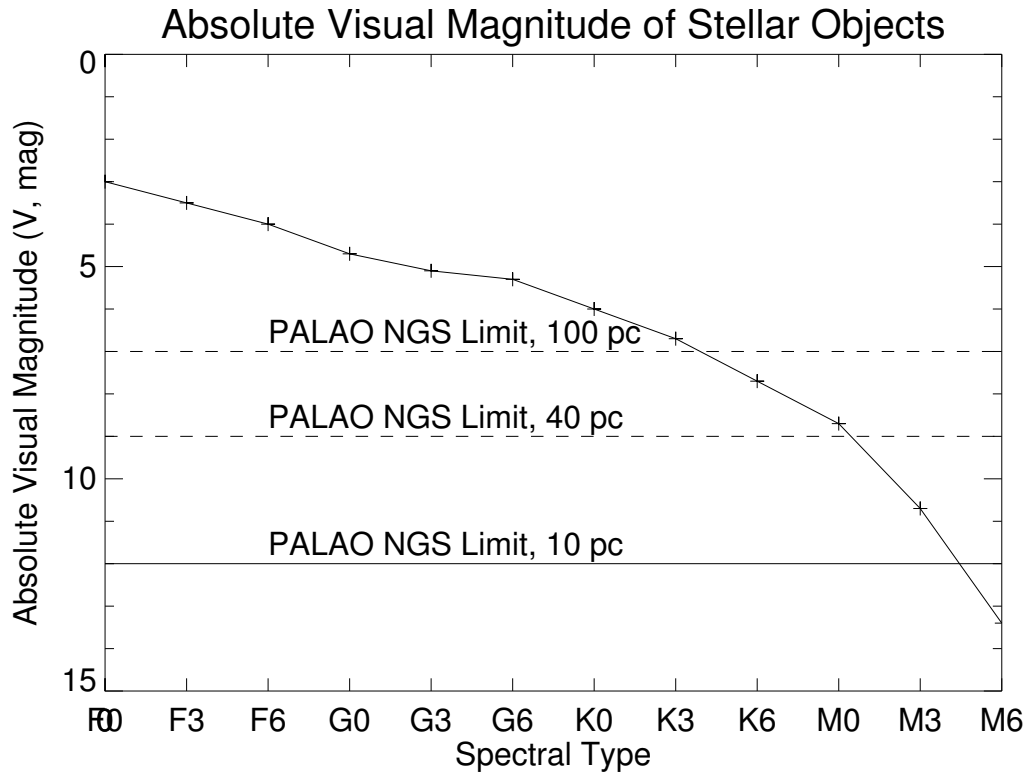


Figure 2.11: Absolute visual magnitude as a function of spectral type. Late type stars and brown dwarfs grow quickly faint in the visible and are too faint to drive adaptive optics systems. For this reason, companion searches which aim image with high angular-resolution (e.g. for dynamical mass measurements) must use primaries earlier (and brighter) than about M3 if natural guide stars are to be used.

of systems ensured to contain brown dwarfs.

The LGSAO system on Keck has been a boon for dynamical mass measurements of brown dwarfs. In fact, all but three of the dynamically measured brown dwarf masses have come from LGSAO programs (Konopacky et al., 2010; Dupuy et al., 2010): the two previously mentioned brown dwarf hierarchical systems and one system detected in transit (Stassun et al., 2006).

#### 2.4.4 Adaptive Optics: Contrast

The faintest companion one can detect (the *image contrast*) is most basically a simpler question: How faint can a companion source be before the observer can no longer distinguish the flux of the companion source from noise sources?

The obtainable contrast one achieves is a function of separation from the primary. As discussed in the previous section, close to the primary and within the halo, residual wavefront phase errors uncorrected by the AO system produce diffraction effects which litter the image with bright speckles. Speckles are not placed randomly throughout the halo, but are preferentially *pinned* to the first and second Airy rings (Bloemhof et al., 2000, 2001; Sivaramakrishnan et al., 2003). The precise location of the speckles shift on timescales of tens of seconds to tens of minutes (Figure 2.12). Speckles pinned to the first Airy ring introduced variations of as much as 10% the peak flux over ten minutes (2-5% on the second Airy ring) and changed locations irregularly. Because of the slowly varying nature of these speckles, they are referred to as *quasi-static speckles*.

As mentioned in the Perspective of this manuscript, the impact of wavefront errors arising from imperfect optics have been extensively explored in recent years,

mostly in the pursuit of high-contrast coronagraph observations (Lafrenière et al., 2007). Optical components of the telescope located after the wavefront sensor cannot be corrected by adaptive optics and produce *non-common path wavefront errors*. These wavefront errors evolve due to temperature or pressure changes, mechanical flexures, guiding errors, changing illumination of the primary mirror, or other phenomena (Marois et al., 2005, 2006).

Quasi-static speckles dominate long exposures within separations of 5-10 *arc-seconds* at the Keck and Palomar Hale Telescopes. They evolve too slowly to effectively average out over even hour long exposures (Hinkley et al., 2007; Macintosh et al., 2005; Metchev et al., 2003). With no mechanism to distinguish speckles from true companions, longer exposures will not yield any higher contrasts; it is not the stochastic variation of quasi-static speckles which cause them to hinder high contrast imaging. Thus, contrast limits are not set by the variation of the quasi-static speckles over a set of images, but by their mean brightness. Unequivocally, *quasi-static speckles set the ultimate noise floor of high contrast imaging, generating a slowly varying distribution of flux that can be mistaken for faint companions*.

Figure 2.13 shows typical 3-sigma contrast limits one can reach with direct imaging in H band using the Palomar AO system and PHARO camera. As evident, high contrast imaging is quite limited at close separations, and significantly less than what would be required to resolve brown dwarfs in orbit around even the lowest mass stars (100:1 or better).

Non-Redundant Aperture Masking Interferometry, through its use of closure phases, enables higher detection contrasts at close separations because closure phases are not affected by the wavefront errors which produce quasi-static speck-

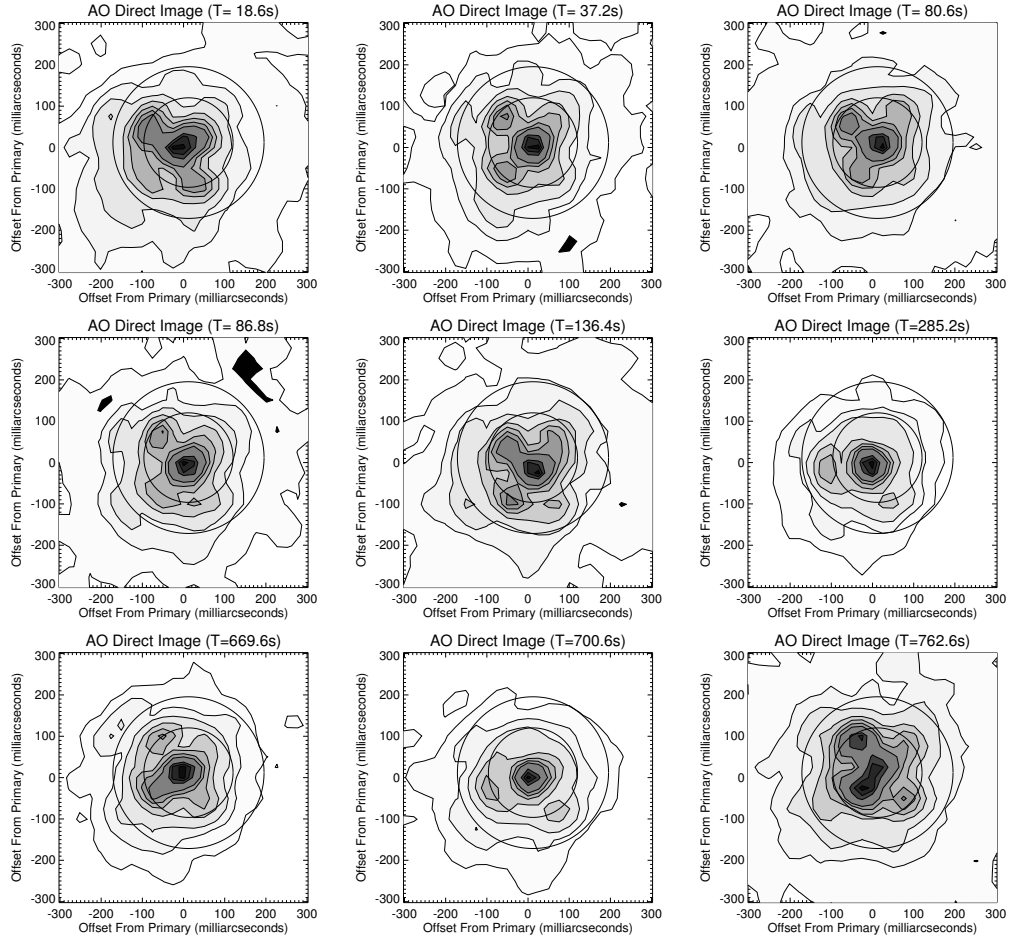


Figure 2.12: Close-up of the diffraction core and first and second Airy rings of 6 second exposures of HIP 52942, taken with the Palomar AO system and PHARO instrument. The field of view is 300 mas in radius, roughly that necessary to resolve binaries with periods short enough to measure brown dwarf masses. Contours are peak intensity divided by 1.05, 1.18, 1.33, 2., 2.5, 3.33, 5., 10., 20., and 50. Each row contains three images taken roughly ten seconds apart. The middle and bottom rows have sets of images taken 1 and 10 minutes after the first row, respectively. The tendency of speckles to pin to the Airy rings is readily apparent, as well as a three-fold and four-fold symmetry of the speckle locations on the first Airy ring which evolves on minute timescales. (Between, for instance, the first and second image of the first row.) These produce flux variations as much as 10% of the peak (seventh contour). Variations on the second Airy ring of as much as 2-5% are also observed. These *quasi-static* speckles limit the image contrast.

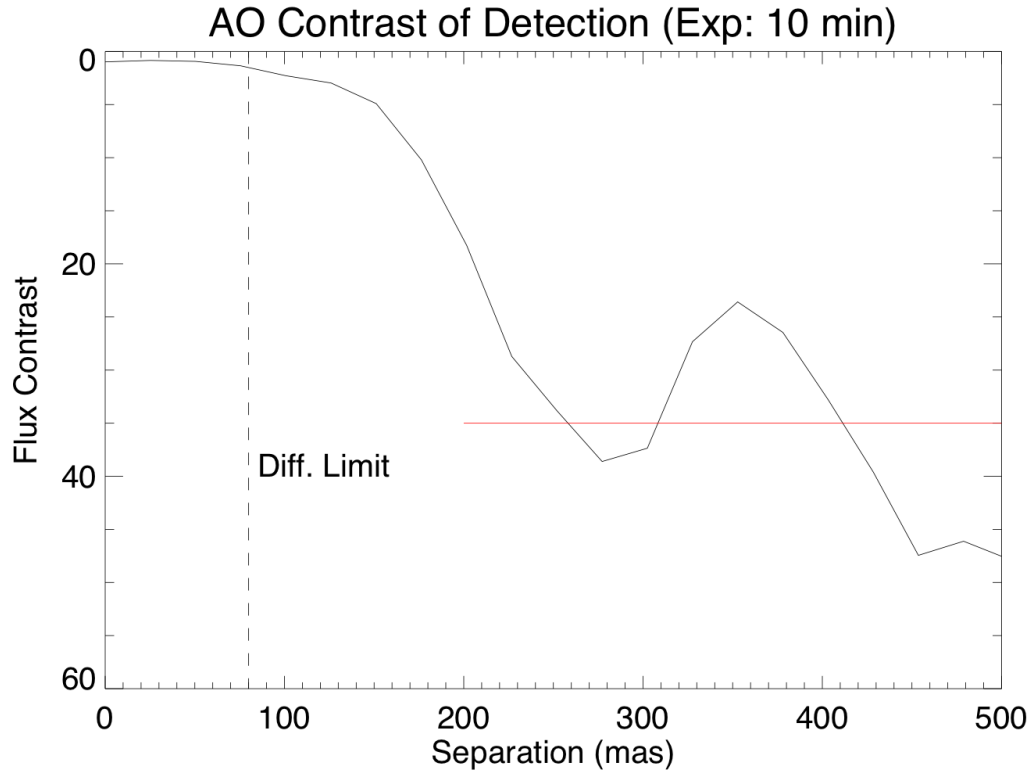


Figure 2.13: Primary-Secondary Contrast Ratio Detectable with Direct AO Imaging. The fundamental challenge of high contrast direct imaging at high angular resolution is to distinguish quasi-static speckles from true companions. Because quasi-static speckles vary too slowly to average out, it is their mean brightness that sets the companion detection limit. These speckles can be up to 10% peak brightness at the location of the first Airy ring. Above is the detection contrast limit imposed by quasi-static speckles for 10 minutes of direct imaging of HIP 52942 in H band. NRM achieves higher contrasts not by distinguishing companions from speckles, but by generating an observable that is not affected by the wavefront errors which produce the speckles (i.e, closure phases)

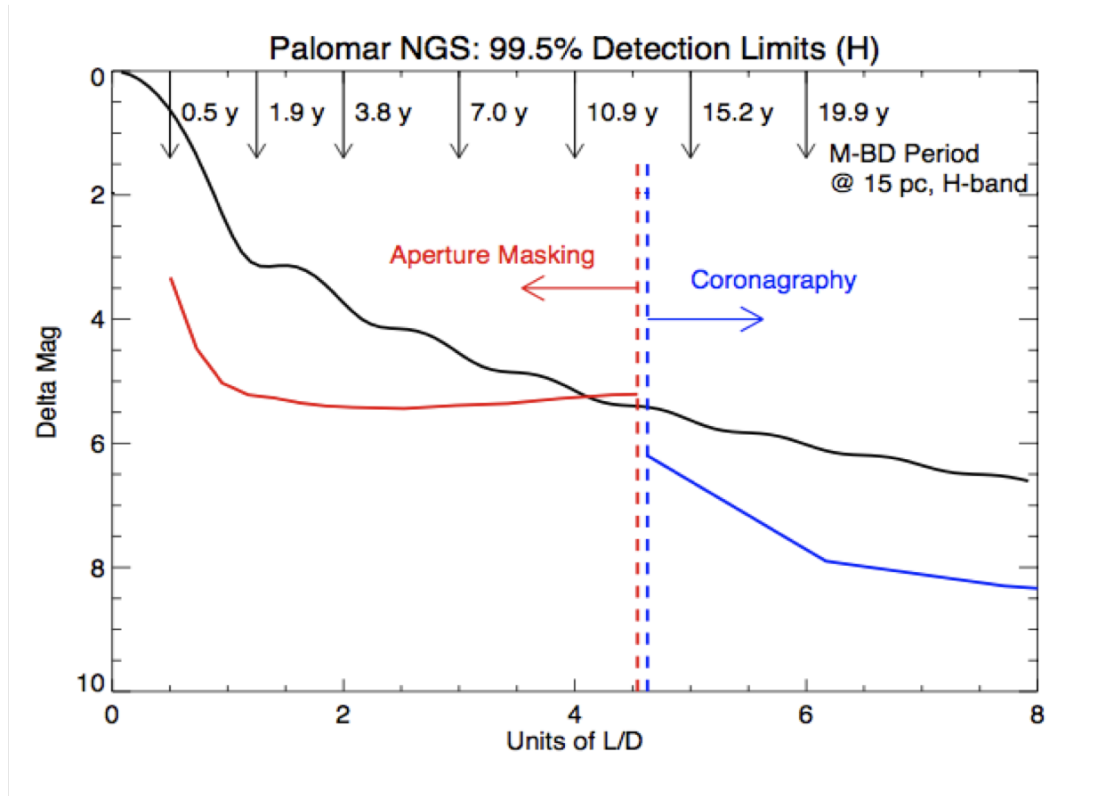


Figure 2.14: Comparison of imaging techniques in infrared H Band (Strehl  $\sim 20\%$ ) at Palomar Hale 200" Telescope. Aperture Masking (red) routinely achieves  $\Delta H \sim 5.5$  magnitudes (150:1) at the diffraction limit, much better than direct imaging alone (black). Coronagraphy (blue), although capable of providing very high contrast is obscured at close separations by its Lyot stop. High contrast at close separations is crucial for the detection of brown dwarfs for dynamical mass measurements. An M-Brown dwarf binary (Contrast  $\sim 4.0$ -5.0 magnitudes, 80-100:1) cannot be detected by direct imaging at a separation closer than about  $3 \lambda/D$ ; the system would have a period of at least 9 years. Aperture Masking can detect these binaries over a more expansive range, and with much shorter periods. Companions detected by coronagraphy are rarely able to provide dynamical masses.

les. NRM when combined with AO does not remove quasi-static speckles, per se. Instead, NRM closure phases are a dataset that are invariant to many pupil-plane phase errors. In effect, closure phases can mitigate the quasi-static problem in a single image.

Aperture masking with adaptive optics is well-established for resolving stellar companions at and within the formal diffraction limit (down to  $0.5\lambda/D$ ) and at high contrasts (200:1 at  $\lambda/D$ ) (Tuthill et al., 2000; Lloyd et al., 2006; Ireland et al., 2008; Martinache et al., 2007). This range of high-resolution and high-contrast make aperture ideal for close companion searches and dynamical mass measurements (Figure 2.14). Companions detected with aperture masking also have a similarly higher precision photometry and astrometry, providing much higher precision dynamical masses up to an order of magnitude higher.

The use of NRM with adaptive optics enables the detection of brown dwarf companions to K and M dwarfs for Strehls of 30% for typical field stars (i.e., ages of a few billion years). This level of adaptive optics correction is routinely achieved by most natural guide star adaptive optics systems.

When combined with laser guide star adaptive optics system (e.g., Keck, Wizinowich (2006)) at similar performance levels, NRM offers a method for measuring brown dwarf masses to much higher precision (less than 10%) than those currently available in the literature. If NRM with LGSAO is able to reach 200:1 contrasts using brown dwarf primaries, the technique may potentially be able to resolve companions through the entire mass range of brown dwarfs. This could provide much needed mass measurements of cool brown dwarfs and even young, massive exoplanets.

The development of a laser guide star adaptive optics program at Palomar (Roberts et al., 2008) motivated my high-angular resolution companion search to nearby brown dwarfs using NRM: Bernat et al. (2010), c.f. Chapter 5: A Close Companion Search Around L Dwarfs Using Aperture Masking Interferometry and Palomar Laser Guide Star Adaptive Optics.

## CHAPTER 3

# NON-REDUNDANT APERTURE MASKING INTERFEROMETRY WITH ADAPTIVE OPTICS

A substantial literature exists to detail the long heritage of seeing-limited aperture masking (Baldwin et al., 1986; Haniff et al., 1987; Roddier, 1986; Readhead et al., 1988; Cornwell, 1989; Tuthill et al., 2000), which itself draws on speckle interferometry (Noll (1976) showed that 87% of the spectral power of atmospheric (Kolmogorov) turbulence produces tip and tilt wavefront errors which only serve to move the image around the detector but not degrade its structure. Over long exposures (i.e., over several iterations of the atmosphere, roughly tens of milliseconds in the infrared), this movement smears the image, producing the blurry seeing-limited point spread function. Exposures short enough that the atmosphere can be treated as static offer an opportunity to retrieve images which are essentially unaffected by 7/8th of the atmospheric wavefront errors.

Positioning a non-redundant aperture mask in the pupil plane of the telescope or instrument transforms the full aperture into a sparsely populated set of sub-apertures (Figure 3.1). Provided the telescope instrument gives access to the pupil plane, such as the location of the Lyot stop within a coronagraph, then this is a convenient location to place the mask. Alternatively, the mask can be placed directly on the primary or secondary mirrors (e.g., Tuthill et al. (2000)). The resulting image produced is a set of over-lapping fringes called the *interferogram*. The amplitude and phase of each fringe corresponds to the measurement of one particular component of the target complex visibility, i.e., the Fourier Transform of the target brightness distribution. Multiplying the complex visibility of specific baseline triplets creates bispectra (Lohmann et al., 1983), the argument of which

is the closure phase (Jennison, 1958; Cornwell, 1989). Closure phases are robust against many forms of pupil-plane phase errors, and enables diffraction-limited imaging in seeing-limited conditions, provided that exposures are short. Closure phase errors arise only from atmospheric phase errors on scales smaller than a sub-aperture. In other words, closure phases rejects even more of the total spectral power of atmospheric turbulence. In its relation to direct imaging, closure phases are robust against precisely the wavefront phase errors that produce speckles close to the core, resulting in much improved image contrast close to the core. Provided that imaging is speckle or wavefront phase limited (Readhead et al., 1988; Racine et al., 1999), aperture masking provides higher fidelity imaging than direct imaging despite blocking a large percentage of the flux.

Adaptive optics systems, by design, aim to sharply reduce the spatial and temporal variation of the wavefront. Current systems on 5-10 meter class telescopes for infrared imaging provide stable and partially coherent wavefronts across the entire sub-aperture. As discussed in the Chapter 1, current adaptive optics systems can obtain near diffraction-limited resolution, but image contrast close to the core (within a few  $\lambda/D$ ) is hindered by quasi-static speckles arising from slowly varying instrumental phase errors. When combined with AO, NRM provides increased contrast at close separations ( $0.5-4.0\lambda/D$ ) by reducing the impact of AO residual phase errors (which produce the halo) and ultimately reaches deeper contrasts ( $10^2-10^3:1$ ) by mitigating the instrumental phase errors that produce quasi-static speckles (Lloyd et al., 2006; Kraus et al., 2008; Hinkley et al., 2010).

This Chapter and Chapter 5 aim to provide a technical underpinning for NRM with AO and to contribute to the growing body of investigation into limitations of the technique and its improvement. Reviews of seeing-limited NRM are available

elsewhere (e.g., Monnier (2000, 2003)) and this work does not wish to retrace their steps. Instead, this chapter revisits the basic premise of NRM to distinguish the seeing-limited and adaptive optics context. This chapter also discusses how one uses closure phases to resolve companions. To find a more detailed discussion of direct imaging, atmospheric turbulence, and adaptive optics the reader is invited to view the Appendix.

### 3.1 Non-Redundant Aperture Masking Interferometry

#### Two Sub-Aperture Mask: Imaging with an Interferometric Baseline

A simple mask that blocks the entire pupil except for two circular sub-apertures of size  $d_{sub}$  separated by a distance,  $\vec{b}$  is shown in Figure 3.2. Such an aperture is familiarly recognized as an interferometer, akin to the Young's double slit experiment. In the absence of wavefront errors, such a mask produces a intensity pattern on the detector that is a sinusoidal fringe with maximum-minimum spacing of  $\lambda/|\vec{b}|$  oriented in the direction of the hole separation, under an Airy pattern envelope of characteristic size  $\lambda/d_{sub}$ . The point spread function is:

$$M(\vec{x}) = \Pi[\vec{x}/d_{sub}] \star [\delta(\vec{x} - \vec{b}/2) + \delta(\vec{x} + \vec{b}/2)] \quad (3.1)$$

$$\tau(\vec{\theta}) = \text{Airy}[\pi\vec{\theta} \cdot d_{sub}] \cos^2[2\pi\vec{\theta} \cdot \vec{b}/\lambda] \quad (3.2)$$

$$T(\vec{f}) = A\Pi[\vec{x}/d_{sub}] \star [\delta(\vec{x} - b) + 2\delta(\vec{x}) + \delta(\vec{x} + b)] \quad (3.3)$$

Here,  $A\Pi$  is the autocorrelation of a single sub-aperture:  $A\Pi[\vec{f}] = \int \Pi[\vec{r}]\Pi^*[\vec{r} + \vec{f}]d\vec{r}$ . (See the Appendix, including Equation A.4 for a review.)

The mask, point spread function, and two-dimensional power spectrum are shown in Figure 3.2. The spot in the center of the power spectrum is the DC

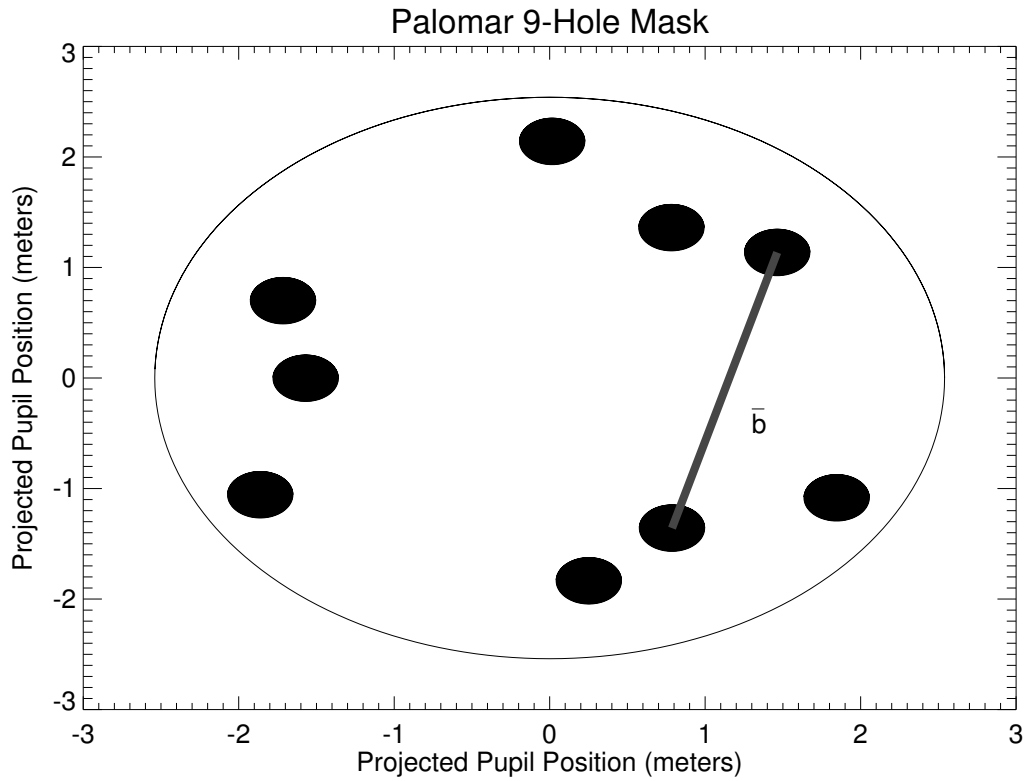


Figure 3.1: The sparse, non-redundant aperture mask used for observations at the Hale 200" Telescope at Palomar Observatory. Each pair of sub-apertures acts as an interferometer of a unique baseline length and orientation. Overdrawn is one such baseline. The 9-hole mask produces thirty-six baselines total; the point spread function of the mask is a set of thirty-six overlapping fringes underneath a large Airy envelope.

Fourier component, proportional to the square of the total flux in the image. We refer to the spots to the left or right of center as *splodges*; they show that the single baseline interferometer allows the transmission and measurement of two islands of spatial frequencies, centered at  $\vec{u} = \pm\vec{b}/\lambda$ . Because the source is a real valued function, the power spectrum is point symmetric and these two splodges contain the same information. Generally, we concern ourselves with the spatial frequency at the center of each splodge only, and only these must be non-redundant.

The van Cittert-Zernike theorem connects this measurement to a single Fourier component of the source brightness distribution, i.e., the complex visibility. More generally, the phase and amplitude of the fringe produced by an interferometer of baseline  $\vec{b}$  are equal to the amplitude and phase of complex visibility at spatial frequency  $\vec{u} = \vec{b}/\lambda$ . *In this way, imaging through an interferometry or aperture mask probes specific spatial frequencies of the image brightness.*

### **Pupil-Plane Wavefront Phase Errors Produce Visibility Phase Errors**

Consider an observation through a perturbed but static two-dimensional phase screen,  $\phi(\vec{x})$ . By design, the phase variance across each sub-aperture is generally small enough so that the sub-aperture wavefront can be considered partially coherent. The baseline extends up to the full diameter of the telescope and so the difference between the mean phase of each of the two sub-apertures may be quite large.

Pupil-plane phase errors cause the fringes to shift laterally in the image. A lateral shift, in turn, means that the *phase* of the fringe as measured relative to some reference point has shifted. The phase shift of the fringe matches the difference between the mean phases of each of the sub-apertures (Figure 3.3). This

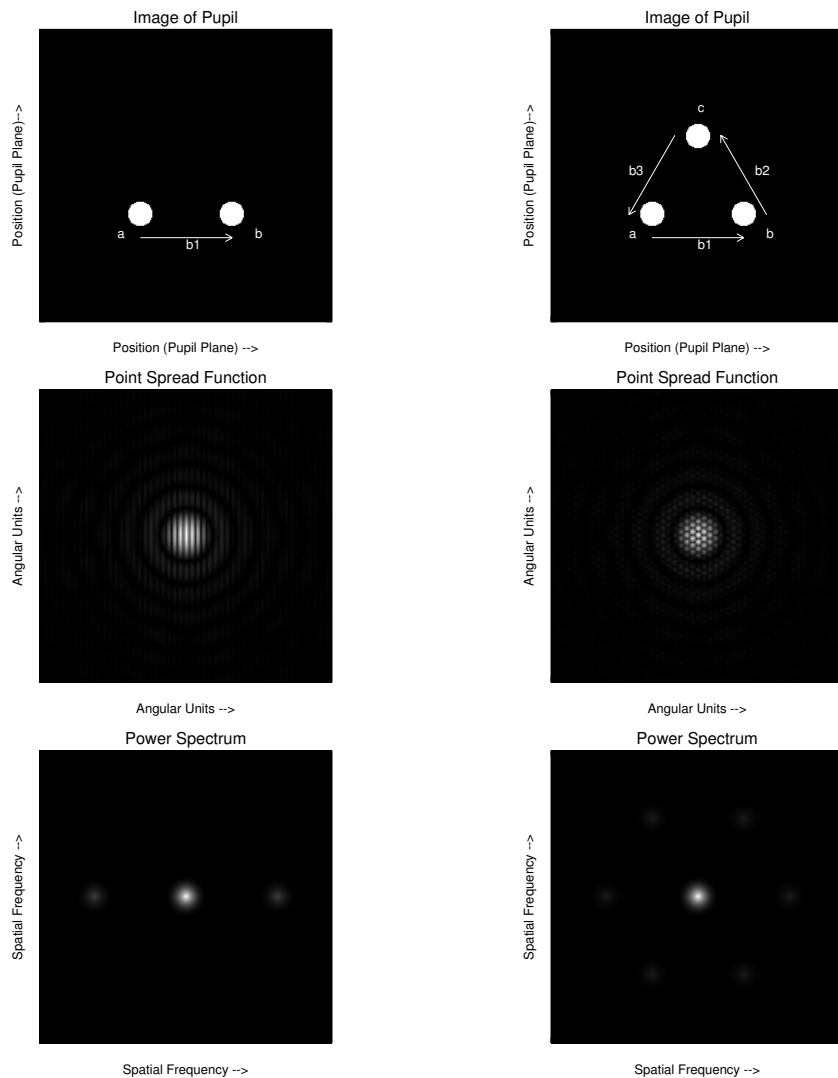


Figure 3.2: An example of a two and three hole aperture mask. For each, the mask, point spread function, and power spectrum are shown. (Left Middle) The pair of sub-apertures interfere to produce a fringe with spacing  $(\lambda/\vec{b}_1)$  underneath an Airy envelope of characteristic size  $\lambda/d_{sub}$ . Notice the fringes are oriented in the direction of the baseline. (Left Bottom) The power spectrum shows that such a mask allows the transmission of only two spatial frequencies  $(\pm\vec{b}_1/\lambda)$  which contain the same information; such a mask allows one to measure this Fourier component of the source brightness distribution. (Right Top) A three hole aperture mask. (Right Middle) Each pair of sub-apertures interfere to produce a fringe, three in total. This is reflected in the power spectrum, which shows the transmission of six frequencies (three unique). Additionally, closure phases can be used for a mask with three or more baselines to significantly reduce the effect of wavefront errors (see text).

also follows if directly apply Fourier Optics to calculate the complex visibility after the wavefront has propagated through a phase screen (See Equation A.10). The measured complex visibility after propagation through the phase screen,  $V'(\vec{b})$ , given the true complex visibility of the source,  $V(\vec{b})$ , is:

$$V'(\vec{b}) = V(\vec{b}) \int_{\substack{\text{sub-} \\ \text{aperture 1}}} d\vec{x} e^{i[\phi(\vec{x}+\vec{b})-\phi(\vec{x})]}. \quad (3.4)$$

The integral is carried out in the two-dimensional pupil plane. Taylor expanding the exponential in this equation yields:

$$V'(\vec{b}) = V(\vec{b}) \int d\vec{x} \left[ 1 + i[\phi(\vec{x} + \vec{b}) - \phi(\vec{x})] - \frac{1}{2}[\phi(\vec{x} + \vec{b}) - \phi(\vec{x})]^2 + O(i\phi^3) \right]. \quad (3.5)$$

where all integrals are assumed to be over sub-aperture one. The first order terms shift the phase of the complex visibility; performing the integral simply averages the phases above each of the sub-apertures. The measured visibility phase,  $\Phi'_b$  is:

$$\Phi'_b = \Phi_{\vec{b}} + \phi_2 - \phi_1 \quad \text{to first order in } \phi, \quad (3.6)$$

where that  $\phi_1$  and  $\phi_2$  are the average wavefront phase error above sub-apertures 1 and 2, respectively.

The second order terms reduce the visibility amplitude by a factor which depends on the variance of the phase difference between all points separated by a baseline length,  $\vec{b}$ :  $\sigma_\phi^2 = \langle [\phi(\vec{x} + \vec{b}) - \phi(\vec{x})]^2 \rangle$ . This is an interferometric analog to the Strehl ratio and the Marechal approximation (Born & Wolf, 1993), and a more detailed calculation reveals:

$$|\tilde{V}(\vec{b})| \sim e^{-\sigma_\phi^2/2} \sim 1 - \frac{1}{2}\sigma_\phi^2. \quad (3.7)$$

For the seeing-limited case, the wavefront phase errors arise from Kolmogorov turbulence. The quantity  $\phi(\vec{x} + \vec{b}) - \phi(\vec{x})$  is a Gaussian random variable with mean

zero and variance of  $D_\phi(|b|) = 6.88(b/r_0)^{5/3}$ . In particular, note that for baselines longer than  $b \gtrsim r_0$  the phase of  $V(\vec{b})$  now contains a noise term with a variance much larger than  $2\pi$  radians. These baselines correspond to the high-angular resolution content of the complex visibility.

One is unable to extract complex phase for such baselines. Consider the signal to noise one obtains from successive averaging of many measurements of the complex visibility quantity  $\exp(\Phi'_b) = \exp(\Phi_b) \exp(i\phi_1 - i\phi_2)$ . This expression is the averaging of a phasor  $\exp(ix)$  where  $x$  is mean zero Gaussian distributed with some large variance ( $\sigma \gtrsim \pi$  radians). Successive averaging of phasors with large variances never decreases measurement error and does not allow extraction of any useful information of the underlying signal (Figure 3.4). In other words, phase information is lost for all baselines longer than  $r_0$  in the seeing-limited case. This highlights the need for more sophisticated methods of extracting the visibility phase for long baselines. The reward for this diligence is higher resolution imaging.

Adaptive optics systems provide a mechanism for maintaining coherence across the full aperture, so that the variance  $D_\phi(|b|)$  asymptotes for long baselines. Diffraction-limited correction corresponds, roughly, to maintaining this asymptotic value below  $\pi$  radians. (See Section A.3.)

For both the seeing-limited and adaptive optics cases, using visibility amplitudes requires calibration against changes in wavefront phase variance. Note the difference between amplitude and phase. An increase in phase variance is reflected in larger measurement error of visibility phase but changes the measurement *mean* of visibility amplitude. Discerning this drop in visibility amplitude to either the intrinsic brightness distribution or the wavefront variance requires an observation of a known target under the same wavefront conditions. The level of seeing and

AO correction fluctuates on timescales of minutes, making precise calibration of amplitudes a challenge.

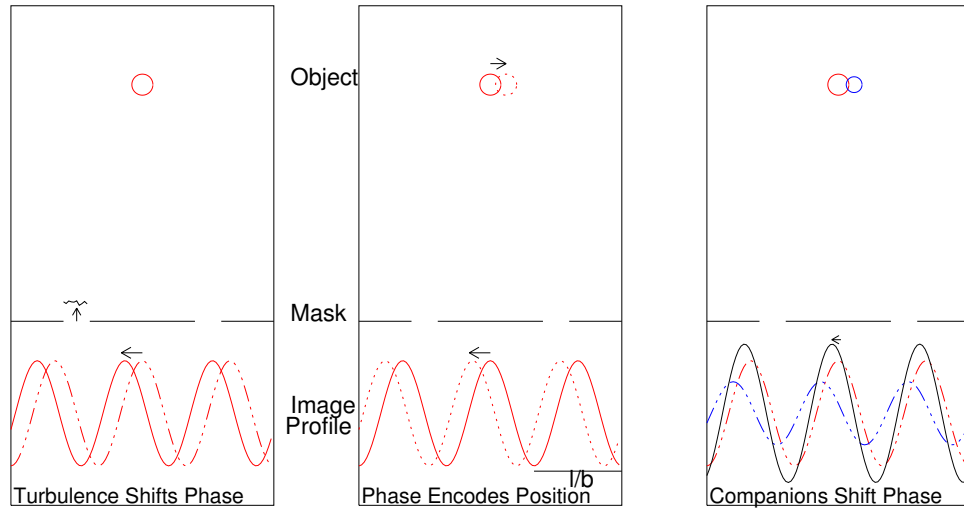


Figure 3.3: Factors which alter the baseline phase. (Left) Wavefront errors atop a sub-aperture will shift the baseline phase. The shift in the baseline phase will equal the wavefront phase error. This is the primary way in which turbulence and optical errors impact baseline (and closure) phase measurements. (Middle) The location of the target is encoded in the baseline phase. Determination of the position of a target on the sky has been transformed into a challenge to accurately measuring the baseline phase. (Right) Each object in a binary system produces a sinusoidal intensity pattern on the detector which add (in intensities) to produce a composite sinusoidal pattern with a different amplitude and phase; the resulting amplitude and phase will depend on the binary characteristics. The resolution of a companion has been transformed into a challenge to accurately measuring phase.

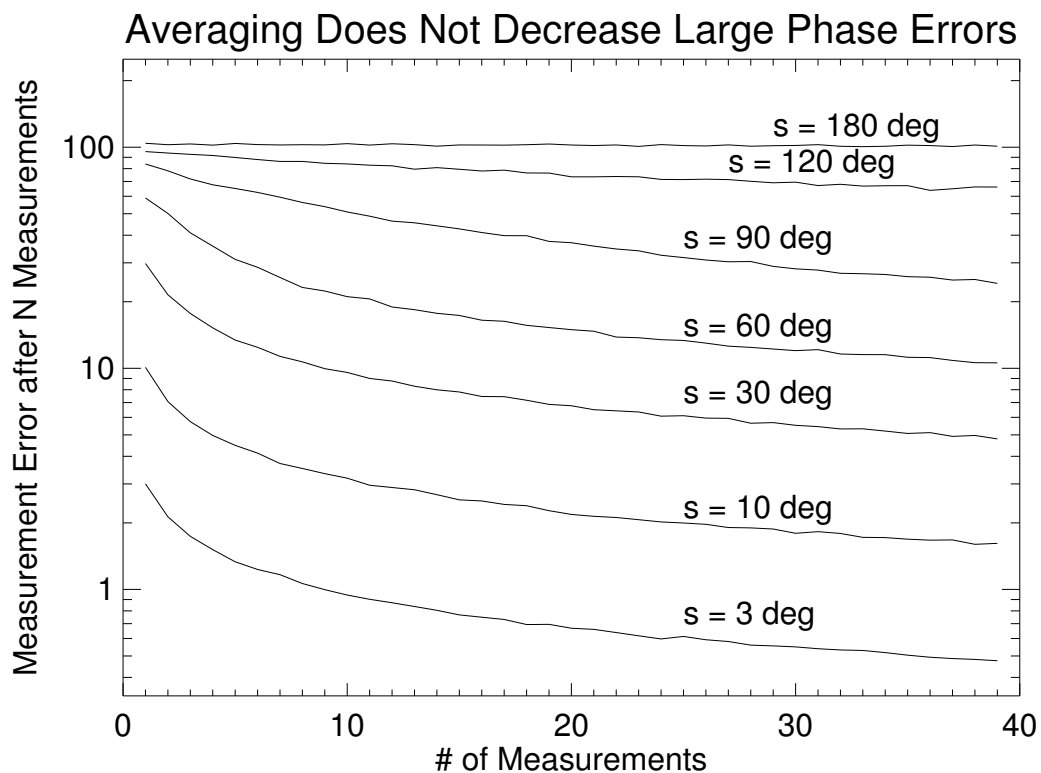


Figure 3.4: Monte Carlo simulation showing that all signal is virtually unrecoverable if phase noise is larger than about 150 degrees. Successive averaging of a Gaussian variable usually reduces its measurement error by  $N^{-1/2}$ ; this is not the case for successive averaging of phasors when phase variance is large. Each data point shows the measurement uncertainty of the phase of  $\sum_N \exp(ix)$ , if  $x$  is a mean-zero Gaussian variable with standard deviations ranging from 3 to 180 degrees. If the phase error of  $x$  is small, successive averaging leads to an  $N^{-1/2}$  improvement of error after  $N$  measurements. As the phase error approaches about 150 degrees, averaging is unable to recover that the mean phase is zero after any number of measurements by this approach.

### Three Sub-Apertures: Extracting Closure Phases

Consider the addition of a third sub-aperture in the aperture mask of Figure 3.2. Each pair of sub-aperture interferes, producing a set of three overlapping fringes underneath an Airy envelope. By design, the three baselines have been chosen to be unique vectors, so that each fringe is produced uniquely by the interference of a pair of sub-apertures; this is the constraint of *non-redundancy*. This allows the straightforward application of *closure phases*, and the extraction of higher fidelity phase information from the image.

One can imagine a cell of turbulence resting above the sub-aperture 'a' in Figure 3.2. Such a cell introduces a phase delay into the wavefront which passes through that sub-aperture, and introduces a shift in the fringe formed by baseline  $\vec{b}_1$ . The same cell introduces an equal but opposite shift in the fringe formed by baseline  $\vec{b}_3$ , opposite because of the orientation of the baseline vectors. The sum of the the two baseline phases is invariant to the wavefront phase errors (to first order). The closure phase is a generalization of this same idea, constructed by summing the fringe phase of three baselines which form a triangle (Baldwin et al., 1986; Haniff et al., 1987; Readhead et al., 1988; Cornwell, 1989). The closure phase is invariant to mean phase errors atop each sub-apertures:

$$\begin{aligned}
 \Phi'_{\vec{b}_1} &= \Phi_{\vec{b}_1} + \phi_1 - \phi_2 \\
 \Phi'_{\vec{b}_2} &= \Phi_{\vec{b}_2} + \phi_2 - \phi_3 \\
 \Phi'_{\vec{b}_3} &= \Phi_{\vec{b}_3} + \phi_3 - \phi_1 \\
 \Phi'_{\vec{b}_1} + \Phi'_{\vec{b}_2} + \Phi'_{\vec{b}_3} &= \Phi_{\vec{b}_1} + \Phi_{\vec{b}_2} + \Phi_{\vec{b}_3} \text{ to first order in } \phi. \quad (3.8)
 \end{aligned}$$

Another method for arriving at the closure phase is through the construction of the *bispectrum* or triple product (Weigelt, 1977), which is the product of three

complex visibilities:

$$\hat{B}_{123} = \hat{V}(\vec{b}_1)\hat{V}(\vec{b}_2)\hat{V}(\vec{b}_3) = |V_{\vec{b}_1}||V_{\vec{b}_2}||V_{\vec{b}_3}|e^{i(\Phi_{\vec{b}_1}+\Phi_{\vec{b}_2}+\Phi_{\vec{b}_3})} \quad (3.9)$$

The argument of the bispectrum is the closure phase (Roddier, 1986).

Regardless of the size of the sub-aperture, closure phases remove the first order term of wavefront noise; the error in closure phases is *third order in wavefront error*. This calculation is conducted in more depth and recast by decomposing the sub-aperture wavefronts into Zernike modes in Section 5.10. Its conclusion is that mean wavefront phase differences between sub-apertures have no impact on closure phases. Instead, only wavefront variation within a sub-aperture leads to closure phase errors. This is the key utility of closure phases. Last section discussed that phase variations grow for longer separations, and the phase variation across a baseline will always be larger than the phase variation within a sub-aperture.

In the seeing-limited case, closure phases allow extraction of phase information. The variance of closure phases (the argument of the bispectrum) is much smaller than the variance of visibility phases, and so successive measurement of the bispectrum allows meaningful extraction of the closure phase (c.f. Figure 3.4). With adaptive optics, closure phases still rejects a substantial portion of phase errors, and will be more precisely measured.

Closure phases have important consequences for calibration and quasi-static wavefront phase errors. The direct imaging point spread function changes shape significantly as seeing or adaptive optics performance changes and quasi-static speckle locations are sensitive to quasi-static wavefront errors across the entire pupil. By comparison, the transfer function for the closure phase does not depend on seeing or adaptive optics performance (except in the sense that they introduce phase errors), and so it is not necessary to calibration closure phases to seeing

effects (Weigelt, 1977). Closure phases also only lead to miscalibration if the quasi-static wavefront *within each sub-aperture* changes. The magnitude of quasi-static changes on sub-aperture scales is smaller and slower, and so closure phases are more robust to quasi-static errors as well.

Hence, closure phases are a powerful method for obtaining higher precision measurements of the Fourier content of the source brightness, particularly for the long baselines which are most important for high angular resolution. As an example, Figure 3.5, shows that the variation of closure phases from exposure to exposure is often an order of magnitude lower than the variance of each individual baseline phase, even when adaptive optics are providing diffraction-limited correction.

An array of  $N$  sub-apertures contains  $N(N-1)/2$  possible baselines. If the baselines are non-redundant, each probes the complex visibility at a different spatial frequency. Closure triangles can be constructed from any three sub-apertures, i.e., by drawing the triangle which connects them, of which there are  $N(N-1)(N-2)/3!$  possible triangles. However, the set of triangles is not linearly independent. (This must be so. Because the closure phases are derived from baseline phases, one cannot arrive at more independent information after constructing closure phases.) There are  $(N-1)(N-2)/2$  *linearly independent* closure phases (or bispectrum) (Readhead et al., 1988).

Because there are fewer closure phases than baselines, it is not possible to reverse this procedure. One cannot uniquely determine the baseline phases from the closure phases. The closure phase information cannot be uniquely inverted to an image (by conversion to baseline phases and inverse Fourier transform). Further assumptions are necessary, for instance, that the image is positive valued and of finite extent. (See, for example, the CLEAN algorithm (Högbom, 1974)

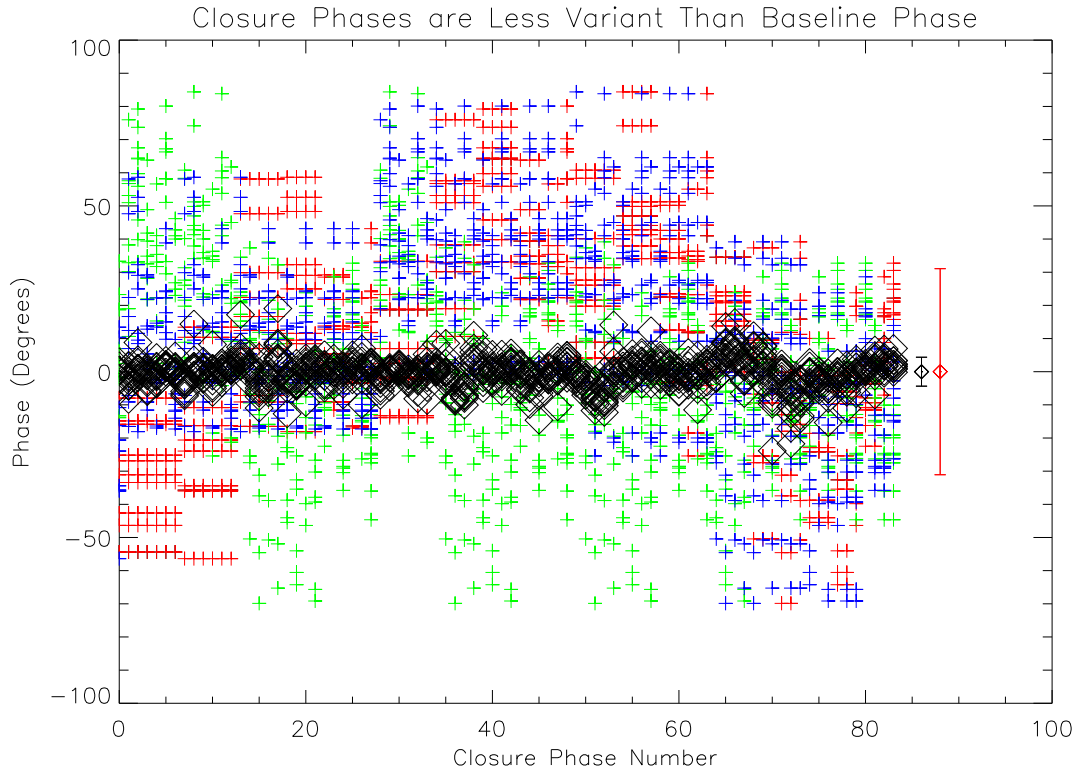


Figure 3.5: Closure phases increases the precision with which long-baseline Fourier content can be measured. The x-axis is the set of eighty-four closure phases that can be extracted from a single image of the Palomar 9-hole mask. Each closure phase is constructed from sets of three baselines. Here we compare the variation of these baseline phases to the variation of the closure phase. Plotted in black are the closure phases obtained from twenty aperture masking images; for each closure phase, the individual baseline phases are overplotted (red, blue, green). As can be seen, the the closure phases (black) vary by about  $\sim 3.3$  degrees across the twenty separated exposures. Compare this to the individual baseline phases (red, blue, green), which vary by 30-35 degrees. This is a tenfold increase in fidelity by using closure phases.

and the Maximum Entropy Method (Gull & Skilling, 1984)). Alternatively, by parameterizing the image structure - such as describing a binary target only by separation, orientation, and contrast - one can make tractable inferences of the source distribution without producing an image.

### **Baseline and Sub-Aperture Redundancy**

A critical requirement of the non-redundant aperture masking design is that each pair of sub-aperture creates a unique interferometric baseline (Haniff et al., 1987; Roddier, 1986). Readhead et al. (1988) provides an extensive treatment of the impact of redundant baselines for seeing-limited aperture masking. When two or more baselines contribute to the same spatial frequency, the power adds partially incoherently depending on the phase difference of each contributing baselines. A random phase component will be introduced into the resulting spatial frequency phase which cannot be removed by closure phases; this component is termed *redundancy noise*. In completely analogous fashion, temporal variations of the non-redundant baseline phase during a single exposure create *temporal redundancy* which also give rise to closure phases errors.

The mask cannot be entirely non-redundant. The finite sub-aperture size means that baselines are redundant at least within a sub-aperture. The terminology of Readhead et al. (1988) defines redundant baselines slightly more critically, referring specifically to any two pairs sub-apertures (i.e., any two baselines) which differ in phase by more than one radian r.m.s., in other words, any two baselines which are totally incoherent. Given the properties of Kolmogorov turbulence, atmospheric phase screens decorrelate on length scales larger than the Fried parameter and timescales longer than the atmospheric coherence time. With uncorrected ob-

serving, forbidding incoherent baseline redundancy restricts sub-aperture sizes to smaller than the Fried parameter and exposure times shorter than the atmospheric coherence time.

Adaptive optics removes both constraints since good correction supplies a stable, mostly coherent wavefront across the full aperture. Since each baseline is redundant within the sub-aperture, closure phase errors still arise due to the remaining spatial incoherence within the sub-aperture. This lends itself to a definition of redundant baselines which includes any partially coherent baselines, not just those which are fully incoherent. In short, with sub-aperture scale correction provided by the AO system, sub-aperture redundancy noise is largely, but not entirely, removed (Tuthill et al., 2006). The interplay between quasi-static wavefront errors and sub-aperture redundancy almost certainly sets the ultimate limits one can achieve with current NRM experiments. In particular, a study of sub-aperture redundancy noise necessitates a mathematical treatment more exact than the useful models of Readhead et al. (1988). Such models are provided, as well as a detailed treatment of sub-aperture redundancy noise for NRM with adaptive optics in Section 5.10 of Chapter 5.

## **3.2 Observing Binaries with an Aperture Mask**

### **3.2.1 Closure Phase Signal**

Aperture masking observations sample Fourier components of the source brightness. Closure phases are constructed because they permit higher fidelity measurements of this Fourier information. While various techniques exist to revert closure

phases back into an image, it is advantageous to use the inherent structure of the binary to build a parameterized model that can be fit directly to the closure phase data.

Consider two different source distributions: a single, unresolved star and a resolvable binary of two unresolved stars. The binary can be described by three parameters: separation,  $|\vec{\rho}|$  (typically measured in milli-arcseconds); position angle,  $\theta$ , the azimuthal angle measured from celestial north; and contrast ratio,  $r(\lambda)$ , the wavelength dependent ratio of secondary brightness to primary brightness with  $r < 1$ . We may also include the (off-axis) position of the target on the sky,  $\vec{\alpha}$ , measured in the same angular units as the binary separation. Closure phase (and visibility amplitude) are invariant to absolute target position, but baseline phases are not. Given the known brightness distribution of each source, we can calculate the complex visibility directly:

$$\begin{aligned}
I_{single}(\vec{r}) &= \delta(\vec{r} - \vec{\alpha}) & I_{binary}(\vec{r}) &= \delta(\vec{r} + \vec{\rho}/2 - \vec{\alpha}) + r \delta(\vec{r} - \vec{\rho}/2 - \vec{\alpha}) \\
\tilde{V}_{single}(\vec{b}) &= e^{\pi i \vec{b} \cdot \vec{\alpha} / \lambda} & \tilde{V}_{binary}(\vec{b}) &= \frac{e^{\pi i \vec{b} \cdot \vec{\alpha} / \lambda} e^{\pi i \vec{b} \cdot \vec{\rho} / \lambda} + r e^{-\pi i \vec{b} \cdot \vec{\rho} / \lambda}}{1 + r} \\
|\tilde{V}_{single}| &= 1.0 & |\tilde{V}_{binary}| &= \frac{1 + r^2 + 2r \cos(2\pi \vec{b} \cdot \vec{\rho} / \lambda)}{1 + r} \\
\phi_v &= \pi \vec{b} \cdot \vec{\alpha} / \lambda & \phi_v &= \pi \vec{b} \cdot \vec{\alpha} / \lambda + \arctan \left[ \frac{r \sin(2\pi \vec{b} \cdot \vec{\rho} / \lambda)}{1 + r \cos(2\pi \vec{b} \cdot \vec{\rho} / \lambda)} \right]
\end{aligned}$$

Closure phases are constructed using baseline triplets which form closed triangles. This constrains the three baselines such that  $\vec{b}_1 + \vec{b}_2 + \vec{b}_3 = 0$ . Equivalently, each closure triangle can be specified by two baselines, with  $\vec{b}_3 = -\vec{b}_1 - \vec{b}_2$ . Using this constraint, we can derive an analytic expression for the closure phases of single

and binary systems:

$$\begin{aligned}
\Phi(\vec{b}_1, \vec{b}_2) &= \phi_v(\vec{b}_1) + \phi_v(\vec{b}_2) + \phi_v(-\vec{b}_1 - \vec{b}_2) \\
\Phi_{single}(\vec{b}_1, \vec{b}_2) &= 0 \\
\Phi_{binary}(\vec{b}_1, \vec{b}_2) &= \arctan \left[ \frac{r \sin(2\pi \vec{b}_1 \cdot \vec{\rho}/\lambda)}{1 + r \cos(2\pi \vec{b}_1 \cdot \vec{\rho}/\lambda)} \right] + \arctan \left[ \frac{r \sin(2\pi \vec{b}_2 \cdot \vec{\rho}/\lambda)}{1 + r \cos(2\pi \vec{b}_2 \cdot \vec{\rho}/\lambda)} \right] \\
&\quad - \arctan \left[ \frac{r \sin(2\pi (\vec{b}_1 + \vec{b}_2) \cdot \vec{\rho}/\lambda)}{1 + r \cos(2\pi (\vec{b}_1 + \vec{b}_2) \cdot \vec{\rho}/\lambda)} \right] \tag{3.10}
\end{aligned}$$

From Equation 3.10 it is clear that by measuring the deviations of the closure phases from zero one can infer the presence of a companion. Thus, instead of inverting the closure phases to form an image, we can similarly complete a parameter search to find the modeled binary that best fits the measured closure phases. This approach of forward-modeling can be extended for any target whose brightness distribution can be modeled by a small number of parameters (e.g., imaging of debris disks or multiple systems).

By the dot product in Equation 3.10,  $\vec{b} \cdot \vec{\rho}$ , we see that baselines are insensitive to binaries oriented perpendicular to the baseline. For this reason, aperture masks must be constructed to sample many spatial frequencies spanning all orientations and a wide range of separations.

Figure 3.6 illustrates the phases one would measure as a function of baseline for the detection of a 2:1 contrast binary separated by 150 mas using the Palomar 9-hole aperture mask. The middle rows show the target phase as a function of baseline, overplotted by the thirty-six spatial frequencies sampled by the Palomar mask. The uniform coverage of the Palomar mask at a full range of orientations and separations ensures sensitivity to companions at all separations and orientations. The bottom row shows the baseline-phase relation collapsed to one dimension. The companion induces a phase offset of up to 30 degrees; with typical measurement

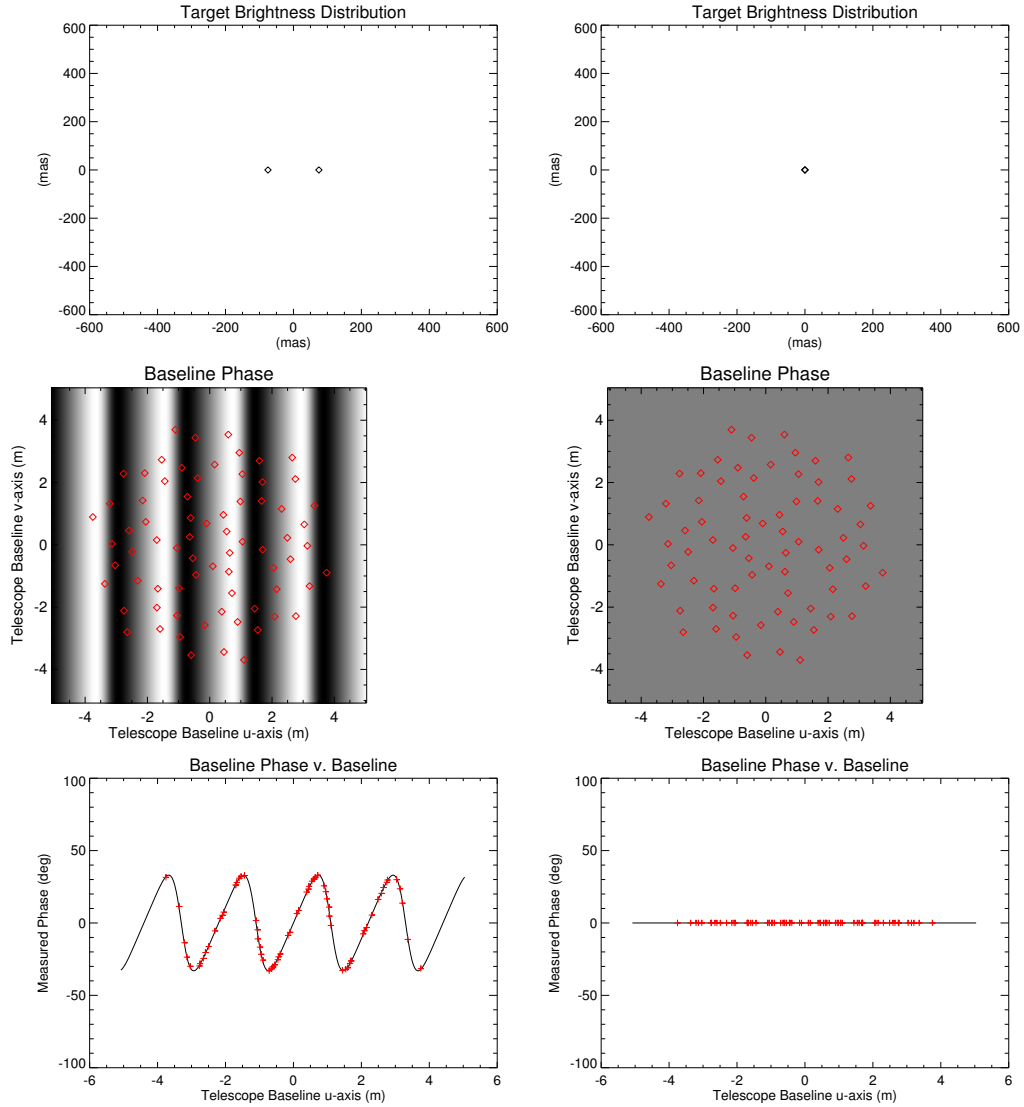


Figure 3.6: Illustration of the phases as a function of baseline induced by a 2:1 contrast binary separated by 150 mas using the Palomar 9-hole aperture mask. The phase signal of an unresolved single star is shown for comparison. (Middle) Showing the target phase as a function of baseline, overplotted by the thirty-six spatial frequencies sampled by the Palomar mask. The uniform spatial frequency (or uv-coverage) coverage of the Palomar mask ensures sensitivity to companions at all separations and orientations. (Bottom) Showing the baseline-phase relation collapsed to one dimension. The companion induces a phase offset of up to 30 degrees for many baselines; with typical measurement precisions of a few degrees *per closure phase*, this companion is readily detected at very high confidence.

precisions of a few degrees *per closure phase*, this companion is readily detected at very high confidence.

### 3.2.2 Robust Measurement of Binary Parameters and Confidence Intervals

Unlike the detection of a companion by traditional direct imaging, in which the companion can be resolved by visual inspection of the image, the detection of a faint or close companion by aperture masking rests purely on achieving a statistically significant fit of a model to data. In many of the most interesting cases, this detection cannot be corroborated by other methods.

In this chapter we present the basic method for calibrating and fitting closure phase data, which motivates the creation of a new Monte Carlo method for determining the strength of these fits.

For concreteness, we will consider data obtained with the Palomar 9-hole mask, although the method can easily be generalized. As described previously, each image produced by the Palomar 9-hole mask consists of thirty-six overlapping fringes which, when Fourier transformed yields the amplitude and phase of each transmitted spatial frequency. The amplitudes are usually discarded because they are highly variable due to seeing variations between target and calibrator observations. Eighty-four closure phases (or bispectrum) can be constructed from each image, which are then averaged over the set of images and standard deviations are calculated. Finally, these averaged are compared to model closure phases of various binary configurations to determine the likelihood that the target is binary.

## Determination of Best Fit

Each closure phase measured from each image is the composite of three sources: the intrinsic signal of the target, which is zero for a single star and non-zero for a binary; a non-stochastic systematic error component, which may vary from target to target (e.g. quasi-static wavefront errors, flexure of the primary mirror after slewing, etc.), but not during the observation of a single target; and stochastic noise from various sources such as time-varying wavefront errors, read noise, etc. We denote the intrinsic signal by  $\Phi_{binary}$ , the systematic component by  $\beta_{system(t)}$ , and the stochastic noise by  $\xi_{noise(t,i)}$ . The closure phase,  $k$ , extracted from a single image,  $i$ , during a single set of images,  $t$ ,  $\hat{\Phi}_{k,t,i}$ , is:

$$\hat{\Phi}_{k,t,i} = \Phi_{k,binary} + \beta_{k,system(t)} + \xi_{k,noise(i,t)}. \quad (3.11)$$

Averaging over the set of images yields

$$\mu_{\Phi_{k,t}} = \Phi_{k,binary} + \beta_{k,system(t)}, \quad (3.12)$$

$$\sigma_{\Phi_{k,t}}^2 = \langle \xi_{k,noise(i)}^2 \rangle. \quad (3.13)$$

In other words, the systematic contribute introduces an offset from the true value, and the stochastic noise describes the measurement variance. The systematic component  $\beta_{k,system(t)}$  may change from one acquisition to another but is assumed constant during the observation of a single target.

Typically, one uses the measurement of calibrator (single) stars, with zero intrinsic signal (i.e.,  $\Phi_{k,binary} = 0$ ), to estimate the underlying distribution of systematic noise. The typical observing mode is to obtain several observations of the science target, interspersed with observations of calibrator stars. Although the systematic component cannot be determined exactly because it is itself a random

variable, we can compile a composite distribution of  $\beta_{k,system}$  from the several sets of calibrator observations:

$$\mu_{\beta_{k,system}} = \langle \beta_{k,system(c)} \rangle \quad (3.14)$$

$$\sigma_{\beta_{k,system}}^2 = \langle \beta_{k,system(c)}^2 \rangle - \mu_{\beta_{k,system}}^2 \quad (3.15)$$

Here the averages are over the sets of calibrator observations;  $\sigma_{\beta_{k,system}}^2$  reflects the variation of the systematic effects as the telescope is moved from one star to another, etc. For instance, the evolution of quasi-static wavefront errors will cause the systematic component to vary from one calibrator to the next.

Subtracting the systematic component from the measured closure phases leaves remaining the intrinsic signal of the target,  $\Phi_{k,binary}$ :

$$\Phi_{k,binary} = \mu_{\Phi_{k,t}} - \mu_{\beta_{k,system}} \quad (3.16)$$

$$\sigma_{\Phi_{k,t}}^2 = \langle \xi_{k,noise(i)}^2 \rangle + \sigma_{\beta_{k,system}}^2 \quad (3.17)$$

In short, the calibrator closure phases are subtracted from the science target closure phases, and their errors are added in quadrature. This calibration step is important for obtaining high contrasts during high signal to noise observations, when the contribution from systematic noise is on the order of the stochastic noise.

We wish find the three-parameter model binary (separation  $\rho$ , orientation  $\theta$ , and contrast ratio  $r$ ) which best fits the calibrated signal,  $\Phi_{k,binary}$ . This is most readily approached as a  $\chi^2$  minimization problem by finding the set of noiseless, modeled binary closure phases  $\Phi_m(\rho, \theta, r)$  which minimize the quantity:

$$\chi^2 = \sum_k \frac{(\Phi_{k,binary} - \Phi_{k,m}(\rho, \theta, r))^2}{\sigma_{\Phi_{k,t}}^2} \quad (3.18)$$

There are many alternatives to this approach. For instance, one could use bootstrapping methods to calculate measurement errors (or measurement likelihood

curves) that don't assume Gaussianity. There could easily be incorporated into a Monte Carlo algorithm to determine the distribution of best fits. For simplicity, we will consider the problem as a  $\chi^2$  minimization problem.

The best-fitting model is that which minimizes the  $\chi^2$ , which we determine by a combination of gradient search and visual inspection. The parameter errors are calculated from the curvature of the  $\chi^2$  surface at the minimum. Calculating the confidence of this fit, i.e. that this model represents the true target configuration, is detailed in the next subsection.

Experience has shown that the reduced- $\chi^2$  of best fits to even benchmark (i.e., known) binaries are typically larger than unity by a factor of one to a few. We take this as an indication of an unknown systematic error that is not properly accounted for by our estimate of the systematic component from calibrator measurements, nor the measurement scatter across the set of images. In these cases, it is typical for us to artificially scale the closure phase until the reduced  $\chi^2$  of the best fitting binary is unity. Further development of the closure phase extraction pipeline may also indicate a bias towards underestimated errors, but this has not yet been explored.

### Binary Detection Confidence

Our null hypothesis, which we wish to test against the binary fit, is that the observed target is a single star, with intrinsic binary phase zero. Following Equation 3.18, the probability of the null model is

$$\chi_{null}^2 = \sum_k \frac{\Phi_{k,m}(\rho, \theta, r)^2}{\sigma_{\Phi_{k,t}}^2}. \quad (3.19)$$

A natural goodness-of-test statistic is to compare the ratio of the data and null  $\chi^2$ . This is particularly useful for our aperture masking data because its value will

not change if errors are scaled (see previous section). This ratio is similar to an 'F-statistic,' which is the ratio of two reduced  $\chi^2$  variables and we adopt the same name:

$$F = \chi^2 / \chi_{null}^2 \quad (3.20)$$

The F statistic ranges from 0 to 1; a low F value signifies a strong fit.

Systematic and stochastic noise may at times conspire to mimic a binary signal, as expressed by a well fitting a binary model, even though the target is a single star. This is a false alarm event. We, therefore, classify the target fit as statistically significant only if its F-value small compared to a distribution of F-values obtained by fitting single stars.

To obtain this probability of false alarm we simulate ten thousand measurements of single stars with identical  $(u,v)$ -coverage and noise properties of the candidate binary target data. The intrinsic phase of a single star,  $\Phi_{binary}$ , is zero. For one measurement, the contribution due to statistical noise is drawn from the measured distribution of  $\xi_{k,noise}$ , which typically can be approximated by a Gaussian distribution with mean zero and its measured standard deviation ( $\sigma_{\Phi_{k,t}}^2$ ). The systematic contribution, if included, is drawn from a distribution  $\beta_{k,system}$ , compiled from observations of calibrator (single) stars. An alternative to this method is to employ bootstrapping for generating simulated datasets using the original data. Without justification to assume noises are Gaussian, bootstrapping is less biased, and will automatically preserve all correlations between the data (which are known to be large for closure phase data).

We then fit the simulated single star data with a three-parameter binary model, record its  $\Delta\chi^2$  or  $F$  statistic, and build a distribution of these variables. The probability of false alarm, then, is the probability that the goodness-of-fit of a

single star is higher than the target data’s goodness-of-fit. The percentage of single star fits which yield a *better* fit than the data yields the probability of false alarm, that claim our data reveals a phantom binary:

$$p_{false\ alarm}(\Phi_m) = p(F_{best\ fit\ to\ data} > F_{fits\ to\ single\ stars}) \quad (3.21)$$

and

$$detection\ confidence = 1 - p_{false\ alarm}. \quad (3.22)$$

We consider the target data to reveal a definitive 3-sigma binary detection if the best-fitting model produces a detection confidence greater than 99.7% (false alarm probability less than 0.3%). Note that this empirical method is more conservative than comparing the measured  $\Delta\chi^2$  statistic to an analytical distribution with three degrees of freedom (Fig. 3.7).

### 3.2.3 Calculation of Contrast Limits

Whether or not the target is identified as a single star or binary, we are also able to quantitatively state the highest contrast (dimmiest) companion that our technique *would have* been capable of identifying with high confidence (99.7%) as a function of separation. This is, in essence, a statement on the noise characteristics of the data and the *uv*-coverage of our mask.

This amounts to asking the following question: Given simulated binary observations (separation  $\rho$ , orientation  $\theta$ , and contrast ratio  $r$ ), at what contrast does our detection confidence drop below 99.7% (or false alarm probability rise above 0.3%)?

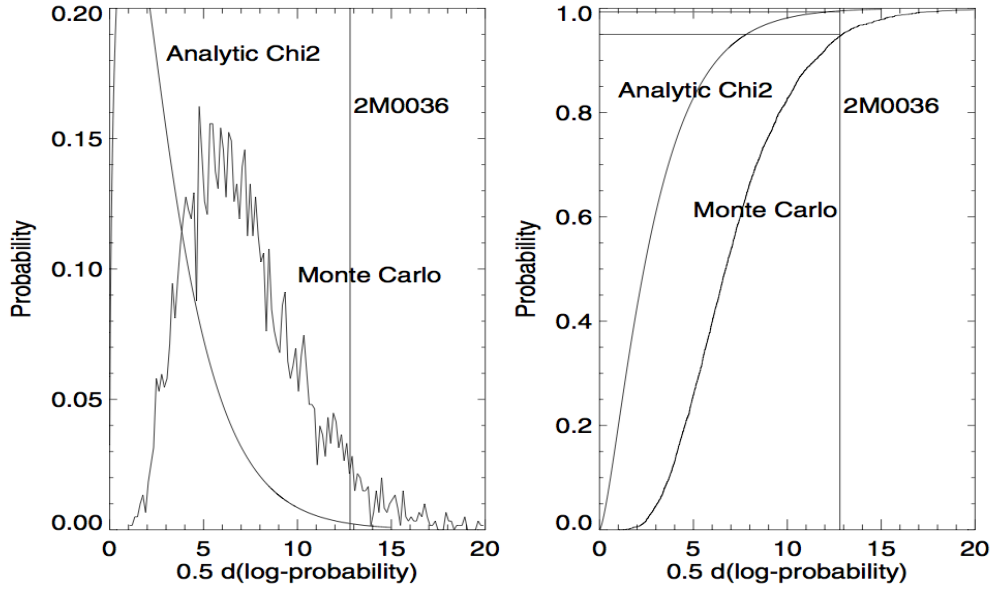


Figure 3.7: Determination of fit confidence with Monte Carlo is more conservative. Data is drawn from NRM observations of L-dwarf binary 2M 0036+1806 (Bernat et al., 2010). The goodness-of-fit statistic here is  $\Delta\chi^2=6.55$  and is compared to a distribution generated from fits to simulated single stars, resulting in a fit confidence of 96% (Monte Carlo). Notice that comparing this value to a  $\chi^2$  distribution with three degrees of freedom (Analytic) results in a much higher confidence of fit.

Simulated binary data is the composite of the same noise contributions to single star data plus an intrinsic signal due to the presence of a companion. That is, the  $n$ th simulated binary data is:

$$\Phi_{k,binary}^n = \Phi_{k,single}^n + \Phi_{k,model}(\rho, \theta, r) \quad (3.23)$$

For a binary model of a given separation, orientation, and contrast ratio, we can generate ten thousand mock binary signals of each by adding the intrinsic binary signal to the mock noise simulations described in the previous subsection. We fit each, record the fit confidence, and determine the average confidence that that binary can be detected. This yields the false alarm probability for detecting this particular binary.

We construct a grid of false alarm probabilities across a range of separations,

orientations, and contrast ratios. For each separation we average over the orientations, and determine the highest contrast ratio i.e., dimmest companion) that would be detected with 99.7% confidence.

Ideally, we would determine the confidence of each mock binary by searching for its best fit, recording its  $F$  or  $\Delta\chi^2$ , and comparing it to the false alarm distribution of the previous subsection. In practice, using a fitting routine to fit each of these simulated binaries is computationally slow.

Instead we approximate this process by modifying the false alarm distribution. We make the assumption that the inserted binary model yields the best fit. Because we effectively restrict the fitting search to the range of separation, orientations, and contrast ratios used to generate the mock binaries, we apply the same restriction to the fitting search that generates the false alarm distribution. We then use this modified false alarm distribution to determine the confidence of the mock binary fits. In practice, this approximation produces contrast limits slightly more conservative than full fitting by about 5-10%.

## CHAPTER 4

# A CLOSE COMPANION SEARCH AROUND L DWARFS USING APERTURE MASKING INTERFEROMETRY AND PALOMAR LASER GUIDE STAR ADAPTIVE OPTICS<sup>1</sup>

### 4.1 Abstract

We present a close companion search around sixteen known early-L dwarfs using aperture masking interferometry with Palomar laser guide star adaptive optics. The use of aperture masking allows the detection of close binaries, corresponding to projected physical separations of 0.6-10.0 AU for the targets of our survey. This survey achieved median contrast limits of  $\Delta K \sim 2.3$  for separations between  $1.2 - 4 \lambda/D$ , and  $\Delta K \sim 1.4$  at  $\frac{2}{3}\lambda/D$ .

We present four candidate binaries detected with moderate to high confidence (90-98%). Two have projected physical separations less than 1.5 AU. This may indicate that tight-separation binaries contribute more significantly to the binary fraction than currently assumed, consistent with spectroscopic and photometric overluminosity studies.

Ten targets of this survey have previously been observed with the Hubble Space Telescope as part of companion searches. We use the increased resolution of aperture masking to search for close or dim companions that would be obscured by full aperture imaging, finding two candidate binaries.

This survey is the first application of aperture masking with laser guide star adaptive optics at Palomar. Several new techniques for the analysis of aperture

---

<sup>1</sup>Previously published as Bernat et al. (2010)

masking data in the low signal to noise regime are explored.

## 4.2 Introduction

The mass determinations of stars through binary studies have provided numerous mass-luminosity benchmarks for the testing and calibration of stellar models. Such studies have only recently begun for the regime of brown dwarfs.

The empirical calibration of brown dwarf models is generally made more difficult by the added dependency on age in the mass-luminosity relationship. For example, an object spectroscopically classified as a late-M dwarf may be a young brown dwarf or an old star just above the hydrogen burning limit. This broadens the range of potential physical properties (mass, age, composition) that generate the same observable spectrum. Conversely, photometry can only very generally reveal the objects' physical properties. Measurements of brown dwarf masses through the tracking of binary orbits provide the strongest constraints on stellar models, "mass benchmarks" that reduce the degeneracy of photometric studies even for targets with unknown ages (Liu et al., 2008). Mass measurements of brown dwarfs by Konopacky et al. (2010) show systematic discrepancies between models and measurements; late-M through mid-L systems tended to be more massive than models predict, while one T dwarf system was less massive than its model prediction. This collection of mass benchmarks grows even more important as brown dwarf models are extended to infer the masses of directly imaged planets, such system HR 8799 (Marois et al., 2008).

Binary surveys have also begun to turn up interesting statistical results that may suggest the brown dwarf binary formation mechanism is different than that for

solar type binaries (see Burgasser et al. (2007) for a summary of results from low mass surveys, including many results presented in this section). Few surveys, however, have produced results for very low mass binaries, especially those with very tight separations ( $\lesssim 3.0$  AU). This regime of short period binaries is particularly challenging to achieve with ground-based direct imaging.

While the companion fraction of brown dwarfs is proposed to be low ( $\approx 15\%$ ) and peaked within a narrow separation range, 3-10 AU (Burgasser et al., 2008), little conclusive results are known for separations less than 3 AU despite preliminary evidence that many additional companions are likely to reside at very close distances (Jeffries & Maxted (2005); Pinfield et al. (2003); Chappelle et al. (2005)).

Over 90% of known very low mass binaries have less than 20 AU (Burgasser et al., 2007). Competing theories of stellar formation aim to explain the observed companion statistics of brown dwarfs. As a general trend, stars appear to have a binary fraction that decreases with mass. This can partly be explained by the decreased binding energy of lower mass primaries, and thus a maximum binary separation that decreases as a function of total mass (Reid et al. (2001); Close et al. (2003)). For very low mass stars, the companion fraction peaks near 3-10 AU, and exhibits a significant (and statistically significant) drop at separations beyond 20 AU separation. Slightly more than half of known very low mass binaries lay within this narrow separation range (Burgasser et al., 2007). On the near side of this peak, the data collected is very likely incomplete, where the necessary resolution (300 mas) stretches the limitations of HST/NICMOS and ground-telescopes with AO alone. What data has been collected suggests direct imaging may have missed companions at very close separations.

Spectroscopic, spectral morphology, and Laser Guide Star AO surveys suggest

that very tight binaries within 3 AU may be as plentiful as binaries of moderate separation. Burgasser et al. (2007) has used spectral features of unresolved sources to indicate composite spectra, implying multiplicity. This technique has suggested numerous early/mid-L dwarfs with potential mid-T dwarf secondaries and systems of equal-mass L/T transition objects. Jeffries & Maxted (2005) used sparse radial velocity data-sets of very low mass systems to predict an additional 17-30% binaries at separations less than 2.6 AU. Photometric overluminosity studies by Pinfield et al. (2003) and Chappelle et al. (2005) have also hinted at surprisingly larger binary fractions (up to 50%) in the Pleiades and Praesepe, though concerns over membership contamination and the influence of variability limit the conclusiveness of the results. In each study, with the exception of the Burgasser mid-L/mid-T systems, very low mass binaries tend towards equal mass pairs ( $q \sim 1$ ) at close separations, just as is the case at moderate separation.

These preliminary results contrast those of previous, observationally complete surveys that focused on moderate and wide separation binaries. Those surveys predict that fewer than 3% of very low mass companions sit at separations closer than 3 AU (Allen, 2007). This discrepancy speaks to the importance of additional, observationally complete surveys searching for binaries at close separations.

Non-Redundant Aperture Masking (NRM) on 5-10m class telescopes, combined with LGS AO, allows sub-diffraction limit resolution observations at contrasts high enough to search for most binaries in this potentially fertile, unresolved region. The detection of close brown dwarf binaries, with a typical period of 1-2 years, also allows mass measurements of late-L or T dwarfs, providing particularly valuable empirical benchmarks for the study of low mass stellar models. To put into perspective the dearth of benchmarks, the mass measurements of fifteen very low

mass systems (including six with L or T dwarf components) using LGS AO alone by Konopacky et al. (2010) has tripled the number of very low mass systems with mass measurements.

In Section 4.3 we describe the sixteen field L-dwarf targets imaged at Palomar using aperture masking with laser guide star adaptive optics and outline the data analysis techniques used to determine the binarity of the targets. In Section 4.4, we present the results of our survey, which operated in the range of 60-320 mas (1.1-8.4 AU @ 18.4 pc, the median distance of our targets). We identify four new candidate L dwarf-brown dwarf binaries at moderate or high (90-98%) confidence. This survey achieved median contrast limits of  $\Delta K \sim 2.3$  between  $1.2 \lambda/D$  and  $4 \lambda/D$ , ruling out companions down to approximately  $.06 M_{\odot}$  for old (5 Gyr) systems and  $.03 M_{\odot}$  for young (1 Gyr) systems. In Section 5.8, we discuss the aperture masking techniques employed in this paper and present recommendations for future faint target observations. In Section 4.6, we summarize the results of this survey and discuss its implications for future companion searches around brown dwarfs.

## 4.3 Observations and Data Analysis

### 4.3.1 Observations

We observed our target sample of sixteen field L dwarfs in September and October 2008 with the Palomar Hale 200" telescope (refer to Table 4.1).

Ten of the sixteen targets in this survey have been observed previously as part of various companion searches using the Hubble Space Telescope (Reid et al.,

2006; Bouy et al., 2003). These previous observations were capable of resolving low contrast or distant (beyond about 300 mas) companions. Aperture masking complements these previous surveys, extending the detection limits around these targets to dimmer and closer companions.

Aperture masking observations were obtained using the PHARO instrument (Hayward et al., 2001), with a 9-hole aperture mask installed in the pupil plane of the Lyot-stop wheel (Figure 4.1). The longest and shortest baselines, which set the approximate inner and outer working angle, are 3.94m and 0.71m respectively (58 and 320 mas in K band). We operate to minimize atmospheric and AO variation during a single image, using PHARO in 256 x 256 sub-array mode with a total of 16 reads (sub-frames) per array reset and 431 ms exposures. Every read was saved to disk. In post-processing, we discard the first three sub-frames of each exposure (usually corrupted by detector reset), and combine the remaining sub-frames by a Fowler sampling algorithm in which later sub-frames are weighed more heavily. Approximately 300 images (each with 16 sub-reads) were taken in  $K_s$  for each target, for a total integration time of roughly 60-70 minutes per target.

The Palomar laser guide star adaptive optics system (Roberts et al., 2008) provided the wavefront reference for high order AO correction, while nearby (a few arc-minutes) field stars were observed contemporaneous to provide tip-tilt correction.

Aperture masking operates most effectively when exposure times are as short as possible, but long enough to observe fringes over read noise. The optimal exposure time depends on the brightness of the targets and the level of correction provided by the AO system. Poor correction favors shorter exposure times, where variation of the incoming wavefront quickly degrades the average transmission of

long baseline frequencies. For targets brighter than about tenth magnitude, the read out limited exposure time of the PHARO detector, 431 ms for the 256 x 256 array, is sufficient to observe long baseline fringes. The targets of this survey are approximately twelfth magnitude, and initial experimentation showed that short exposures did not consistently provide long baseline fringes. Longer exposure times (1 minute) fared poorly because variations in correction over the exposure degraded the average transmission of long baselines below background levels. We opted to use short exposures and to weigh more heavily in post-analysis those observations in which long baseline fringes could be seen (see additional discussion later in this section).

Background subtraction is necessary for targets as faint as L Dwarfs and background levels were often comparable to the signal levels. In many instances our observations were background limited. To remove the background in post-processing, each target was dithered on the 256 x 256 sub-array.

A requirement for obtaining good contrast limits around bright targets is the contemporaneous observation of calibrator sources: single stars which are nearby in the sky and similar in near-infrared magnitudes and colors. This calibration is necessary to remove non-stochastic phase errors introduced by primary mirror imperfections and other non-equal path length errors. This error can be on the order of one to a few degrees, comparable to the measurement scatter of the closure phases for bright targets. For brighter targets, the typical observing mode is to obtain several observations of the science target, interspersed with observations of calibrator stars. However, the lengthy time of acquisition for the laser guide star AO system made this method inefficient for this survey. Furthermore, the measurement scatter for the faint targets of this survey were much larger than the

expected systematic error. Therefore, we did not use calibrator stars. We note that calibrator stars have also not been used for similar reasons in Dupuy et al. (2009).

### 4.3.2 Aperture Masking Analysis and Detection Limits

#### Extracting Closure Phases from Raw Images

The core aperture masking pipeline implemented in this paper is similar to that discussed in previous work (Lloyd et al., 2006; Pravdo et al., 2006; Kraus et al., 2008), with additions to handle low signal to noise data and calculate confidence intervals and contrast limits.

Raw images are first dark subtracted and flat-fielded, bad pixels are removed, and the data is windowed by a super-Gaussian (a function of the form  $\exp(-kx^4)$ ). This window limits sensitivity to read noise and acts as a spatial filter. A per-pixel sky background map is then constructed from the set of target data and subtracted. The background map is generated by masking out the target from each image within a set, then, for each pixel, using the median value of the pixel flux from those images that were not masked.

The point spread function of the nine hole mask consists of thirty-six interfering fringes, called the *interferogram*. Because the mask is non-redundant, each fringe is produced uniquely by the pairing of two holes; the amplitude and phase of this fringe translates directly to the complex visibility of the corresponding spatial frequency.

Fourier-transforming each image reveals seventy-two patches of transmitted

power we call *splodges* (thirty-six frequencies transmitted, positive and negative)(Figure 4.2). The complex visibilities are extracted by weighted averaging of the central nine pixels of each splodge. Optical telescope aberrations, AO residuals, and detector read-noise contribute noise to the complex visibilities. Under the best conditions, visibility amplitudes suffer large ( $> 100\%$ ) calibration errors and are not used for the analysis in this survey.

Visibility phase suffers less from these variations, but the use of the complex triple product and *closure phase* (Lohmann et al., 1983) yields an observable that reduces the effect of wavefront-degradations from baseline-length independent sources such as low-order AO residuals. For an interferometric array (or aperture mask), closure phases are built by adding the visibility phases of 'closure triangles': sets of three baseline vectors that form a closed triangle (see Figure 4.2). The set of closure phases have lower noise than visibility phases, allowing precise photometric measurements despite the loss of photons imposed by the mask.

Thirty-six baselines are present with the 9-hole mask, from which 84 closure phases can be constructed. However, these closure phases are not all linearly independent, and the 36 baseline phases cannot be uniquely determined. The phase information cannot be uniquely inverted (by inverse Fourier transform) into an image without further assumptions (see, for example, the CLEAN algorithm (Högbom, 1974) and the Maximum Entropy Method (Gull & Skilling, 1984)).

As our survey is a search for binaries, the closure phase signal of such a target can be modeled easily. Thus, instead of inverting the closure phases to form an image, we search for the modeled binary configuration that best fits the measured closure phases.

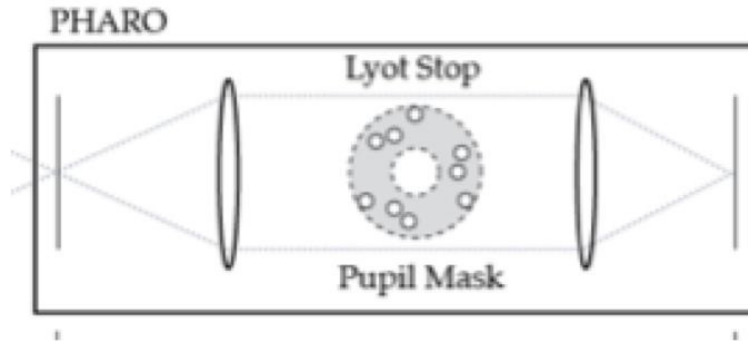


Figure 4.1: The aperture mask inserted at the Lyot Stop in the PHARO detector. Insertion of the mask at this location is equivalent to masking the primary mirror.

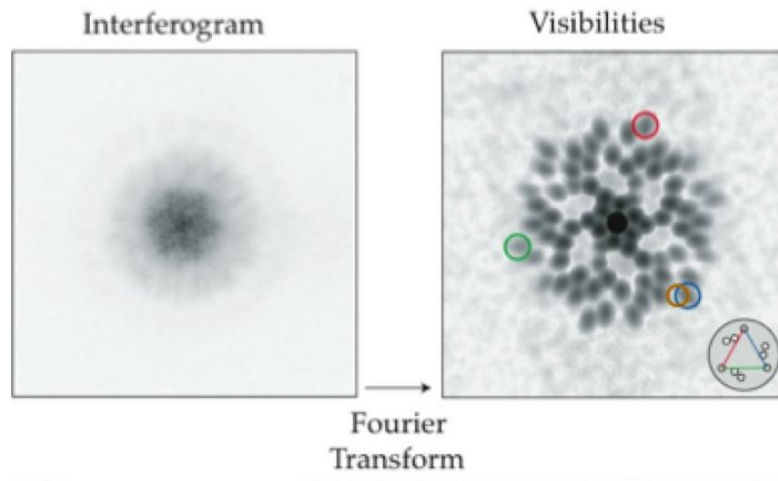


Figure 4.2: Interferogram and power spectrum generated by the aperture mask. (Left) The interferogram image is comprised of thirty-six overlapping fringes, one from each pair of holes in the aperture mask. (Right) The Fourier transform of the image shows the thirty-six (positive and negative) transmitted frequencies. (Right, inset and overlay) Closure phases are built by adding the phases of 'closure triangles': sets of three baseline vectors that form a closed triangle.

## Typical Results on Bright Targets

Aperture masking with natural guide star adaptive optics has been employed during numerous near infrared surveys on the Palomar and Keck telescopes. (For mass determinations made through orbit tracking see Lloyd et al. (2006); Ireland et al. (2008); Martinache et al. (2007, 2009) and Dupuy et al. (2009), and Kraus et al. (2008) for an extensive survey of Upper Scorpius.) Aperture masking has also recently begun usage in conjunction with Keck laser guide star adaptive optics (Dupuy et al., 2009)).

The observation of bright targets ( $K_s \lesssim 9$ ), such as nearby early-M dwarfs, with an aperture mask enables the detection of companions of contrast up to 150:1 ( $\Delta K_s \sim 5.5$ ) at the formal diffraction limit and 20:1 ( $\Delta K_s \sim 3.3$ ) at  $\frac{2}{3}\lambda/D$  in at Palomar.

In this regime, non-stochastic phase errors introduced by the optical pipeline dominate closure phase errors, as well as background flux, wavefront residuals of the adaptive optics system, and achromatic smearing of the fringes. Typically, these sources contribute errors on the order of one degree after calibration.

## Noise Properties of Dim Targets

For each star image, of which we have approximately 300 for each star, we extract closure phases.

Because our targets are faint and exposure times are short, detector read-outs contribute significant noise in the phase and amplitude of the complex visibilities and bispectrum. Amplitudes are particularly susceptible to calibration errors.

Even during high signal to noise conditions, amplitudes have been seen to fluctuate by up to 100%, and are not directly used for fitting to model binaries. However, closure phase data show a clear improvement in per-measurement signal to noise for increasing amplitude. That is, bispectrum with the largest amplitude tend to have the highest fidelity closure phases. In order to pare off bad data and weigh higher signal to noise measurements more heavily, we empirically estimate the relationship between amplitude and closure phase fidelity (Figure 4.3).

This relationship is estimated by binning the set of closure phase data by amplitude and calculating the standard deviation of each bin. As already described, as the average amplitude within a bin increased, the standard deviation within the bin decreased. To first approximation, this estimates the relationship between amplitude and closure phase fidelity.

The noisiest bins often show closure phase errors approaching  $180^\circ$ . Because the closure phase is inherently a measurement of the bispectrum phasor, there is a  $360^\circ$  ambiguity in the measurement of closure phase. Furthermore, even if the underlying noise source is Gaussian distributed, the distribution of measured closure phases approaches a uniform distribution when the standard deviation of the noise source is larger than about  $180^\circ$ . Direct calculation of the root mean squared deviation under represents the variance of the underlying noise source; the calculation of the mean depends on the choice of angle zero-point. The variation within one bin was at times large enough to motivate alternative methods for averaging bispectrum data.

We adopt a maximum likelihood method to calculate the standard deviations of bins and overall closure phase mean. We presume the closure phases in each bin are drawn from a wrapped normal distribution<sup>1</sup>. The standard deviation is varied

to maximize the likelihood of the data in the bin. The same mean is used for every bin, and the mean which maximizes the likelihood of the entire data set is data set's overall mean. This allows bins to take arbitrarily large standard deviations; a wrapped normal distribution with large standard deviation converges towards a uniform distribution. For bins dominated by read-noise or very low signal to noise, this method accurately estimates very large standard deviations and translate that into very low weighting for the bin. The overall errors of closure phase sets ranged between 6-15 degrees. In addition, this method of paring off bad data typically reduced errors by a factor of two over other methods.

Even after employing this data paring, some sets of closure phase data contained so much noise that no reliable signal could be discerned. In this case, the closure phase was removed from the set of eighty-four closure phases further analyzed. For some targets, up to half of the closure phases triangles were removed. In these circumstances, the  $uv$ -coverage of the data drop allowed the possibility of model aliasing: i.e., that multiple binary configurations yield similar closure phase sets and each fit the data equally well. When previous observations of the target were available, we used this information to rule out unlikely fits. When not, we list all fits to the data.

Finally, non-stochastic errors are typically on the order of one to a few degrees. This contribution is much smaller than the statistical error, and as such overall best fits of our data changed very little whether or not we attempted to calibrate out this component.

---

<sup>1</sup>The wrapped normal distribution is the probability distribution function of the wrapped variable  $\theta \equiv x \pmod{2\pi}$ , given by  $p_w(\theta) = \sum p(\theta + 2\pi k)$ , where  $p$  is the unwrapped probability of the unwrapped variable  $x$ . The sum is over integer values of  $k$  from  $-\infty$  to  $\infty$ . The wrapped normal distribution, denoted by  $WN$  is,  $WN(\theta) \equiv \frac{1}{\sqrt{2\pi\sigma^2}} \sum \exp[\frac{-(\theta-\mu-2\pi k)^2}{2\sigma^2}]$ , with the same summation limits.

## Modeling the Binary Fit, and the Calculation of Confidence and Contrast Limits

For each target, we attempted to fit the observed closure phases with a three-parameter binary model (separation  $\rho$ , orientation  $\theta$ , and contrast ratio  $r > 1$ ). The best fitting model is the one which maximized the overall likelihood of the data. Errors in the parameters are calculated from the curvature of the log-likelihood surface at its maximum.

The strength of our fits were determined by comparing the increase in log-likelihood,  $\Delta \log \mathcal{L}$ , between a single star fit and a binary star fit for our real data set as compared to many simulated data sets of single stars. If the real data set has a much higher value of  $\Delta \log \mathcal{L}$  than the simulated data sets, we regard the real data set to be indicative of a binary star. (For purely Gaussian noise,  $\Delta \log \mathcal{L}$  is equivalent to  $\Delta \chi^2$ .)

We simulate measurements of single stars with identical noise properties and  $uv$ -coverage of the candidate binary target. The measured closure phases of a single star is the sum of three sources: the intrinsic signal of the target, which is zero for a single star; noise fluctuations from various sources which are described by the standard deviations measured on the target; and a non-stochastic systematic error component, which we assume is negligible compared to the stochastic noise of these targets. (As a check, we also estimated the typical systematic contribution from the measured signal of eight survey targets whose best fits indicated high likelihood for being single stars. Including this component to simulate single stars had little effect on the overall confidence measurements.)

From this information, we generate ten thousand mock measurements of single

stars. To each, we fit the three-parameter binary model, record the  $\Delta \log \mathcal{L}$ , and build a distribution of  $\Delta \log \mathcal{L}$  that result from single star observations.

Comparing the value of  $\Delta \log \mathcal{L}$  of the data's fit to the simulated distribution yields the probability of false alarm: the probability that our apparent binary fit is an observation of a single star co-mingled with noise. The confidence that our target is binary is one minus this false alarm probability.

To calculate our contrast limits, we first add model binary signals to the simulated single star data. These mock binary signals span a range of separations, orientations, and contrast ratios. We fit each, determine the fit confidence, and determine, for a given separation, the highest contrast ratio (i.e. dimmest companion) that would be detected with 99.5% confidence (false alarm probability of .005). These calculations are discussed in more detail in the Section ?? of the previous Chapter.

### **Calculation of Bayes' Factors**

As an alternative to confidence measure presented in the previous subsection, our group also applied bayesian methods to calculate the Bayes' Factor of each fit, i.e, the odds by which our data favors binary models.

Using Bayesian comparison, the binary hypothesis is tested by contrasting two probabilities: that the data set would arise from a binary target observation, and that the set would arise from a single star observation. Expressed mathematically, this is:

$$\frac{Pr(\text{ binary } | \text{ data } )}{Pr(\text{ single } | \text{ data } )} = \frac{Pr(\text{ star is binary } ) Pr(\text{ data } | \text{ binary } )}{Pr(\text{ star is single } ) Pr(\text{ data } | \text{ single } )}. \quad (4.1)$$

The first term on the right hand side is an attribute of the survey population – it is the ratio of the companion fraction to one minus the companion fraction – and is independent on the data.

The second term is the *Bayes' Factor*, representing the odds by which the data favors one hypothesis over the other. These probabilities are marginalized (and integrated) over the binary parameters. Whereas the maximum likelihood method searches out the set of parameters that maximizes the likelihood of the data, the Bayesian approach *averages* over the parameters.

$$Bayes' Factor = \frac{Pr(\text{ binary } | \text{ data } )}{Pr(\text{ single } | \text{ data } )} \quad (4.2)$$

$$= \frac{\int Pr(\rho | \text{ bin.}) Pr(\theta | \text{ bin.}) Pr(r | \text{ bin.}) \mathcal{L}(\text{data} | \rho, \theta, r)}{\mathcal{L}(\text{data} | \text{ single})} \quad (4.3)$$

The quantities  $Pr(\rho | \text{binary})$ ,  $Pr(\theta | \text{binary})$ ,  $Pr(r | \text{binary})$  refer to distributions of the companion separation, orientation, and contrast ratio as they are presumed known prior to our observation. These distributions for very low mass primaries are themselves ongoing topics of debate and limited by observational incompleteness, particularly in the separation regime of our survey. (For a current review of separation and mass ratio distributions derived through observational studies, the reader is invited to view Burgasser et al. (2007).) Allen (2007) quantifies the underlying companion distributions from the currently available data. We ultimately chose to use blind prior distributions (known as Jeffreys' priors). These

distributions are uniform for separation and log-uniform for contrast ratio. We compare this choice to the Allen priors and discuss its implications.

Our survey focuses on close binaries; our observations probe between roughly 1 and 8 AU for seventy five percent of our L dwarf targets. Allen (2007) concludes that the (physical) separation of companions can be characterized by a log-normal distribution which peaks at  $7.2_{-1.7}^{+1.1}$  AU with a  $1\sigma$  width of roughly  $11_{-3}^{+2}$  AU. This uncertainty in the peak and width contributes noticeable variability of the resulting distribution at the separations we consider (see Figure 4.4). One characteristic unifying the span of distributions, however, is that companions closer than  $\sim 2$  AU are less likely by up to an order of magnitude. This is due in part to describing the distribution as a log-normal functional. This choice is motivated by the sharp drop in companion fraction observed outward of about 10 AU, and by assuming a similar drop shortward of a few AU, where observational data is incomplete. As Allen states, this result is derived without well-defined searches for companions at close separations, and the preliminary results of the Jeffries & Maxted (2005) and Basri & Reiners (2006) surveys potentially indicate the presence of a larger number of close binaries. We use a uniform prior to avoid the bias of the Allen priors, keeping in mind that companions with high Bayes' factor at less than 2 AU could indicate observational evidence of close companions yet may also be biased towards undue significance.

Observational surveys of very low mass systems show a tendency towards equal mass binaries ( $q \sim 1$ ) (Burgasser et al., 2007; Reid et al., 2006; Allen, 2007). The distribution of mass ratios has been roughly characterized by a power law,  $p(q) \propto q^\gamma$ , with  $\gamma \sim 2 - 4$  depending on the survey. The large exponent of this distribution indicates that low mass ratio (low  $q$ ) systems are highly unlikely (and

rare). Transforming this to a distribution of *broad-band contrast ratios* ( $r$ , with  $r > 1$ ) requires assumptions about target age distributions, bolometric luminosity corrections, and mass-luminosity models (see Allen et al. (2005, 2003) for these assumptions applied to field stars). We wish our prior distribution not depend so highly on these assumptions and rather rely on a few basic assumptions.

The rapid drop of the L dwarf mass-luminosity relation (i.e., halve the mass of the star and its luminosity drops by much more) implies that ratios of contrast are larger than ratios of mass, and that contrast ratios still favor unity (i.e.,  $p(r) \propto (1/r)^\gamma$  with  $0 < \gamma \lesssim 2 - 4$ ). The blind prior for a scale independent quantity like contrast ratios is  $p(r) \propto 1/r$  which, conveniently, has the desired properties. It is worth noting that Allen (2007, Fig. 14) carries out the transformation from mass ratio to contrast ratio, finding a distribution that follows roughly  $p(r) \propto 1/(r \log r)$  for contrasts down to below 100:1.

Finally, the same methods can be applied to calculate posterior distributions for  $\rho$ ,  $\theta$ , and  $r$  for each data set. For a data set with a single best fit, this distribution yields a p.d.f. describing the best fitting parameters. The parameter values and errors quoted in this paper are those derived from maximum fit likelihood, as discussed in the previous subsection, and are not drawn from Bayesian posteriors. However, we calculate the posterior distributions to assure both methods give comparable results.

Table 4.1: The Sixteen Very Low Mass Survey Targets

Name	R.A. (J2000.0)	Decl. (J2000.0)	Spectral Type	Distance (pc)	J (mag)	H (mag)	K (mag)	5 Gyr 65-105/105-450 mas	$q$ ( $m_s/m_p$ ) <sup>b</sup> 65-105/105-450 mas	1 Gyr
2M 0015+3516.....	00 15 44.76	+35 16 02.6	L2	20.7 ± 3.2 <sup>a</sup>	13.88	12.89	12.26	0.87 / 0.84	0.68 / 0.60	
2M 0036+1821 <sup>s1</sup> ...	00 36 16.17	+18 21 10.4	L3.5	8.76 ± 0.06	12.47	11.59	11.06	0.86 / 0.83	0.61 / 0.58	
2M 0045+1634 <sup>s1</sup> ...	00 45 21.43	+16 34 44.6	L3.5	10.9 ± 2.1 <sup>a</sup>	13.06	12.06	11.37	0.83 / 0.82	0.57 / 0.54	
2M 0046+0715.....	00 46 48.41	+07 15 17.7	M9	30.5 ± 4.1 <sup>a</sup>	13.89	13.18	12.55	0.86 / 0.83	0.80 / 0.73	
2M 0131+3801.....	01 31 18.38	+38 01 55.4	L4	20.9 ± 4.2 <sup>a</sup>	14.68	13.70	13.05	0.92 / 0.91	0.74 / 0.70	
2M 0141+1804.....	01 41 03.21	+18 04 50.2	L4.5	12.6 ± 2.7	13.88	13.03	12.50	0.87 / 0.84	0.66 / 0.63	
2M 0208+2542 <sup>s2</sup> ...	02 08 18.33	+25 42 53.3	L1	25.3 ± 1.7	13.99	13.11	12.59	0.84 / 0.82	0.62 / 0.56	
2M 0213+4444 <sup>s1</sup> ...	02 13 28.80	+44 44 45.3	L1.5	18.7 ± 1.4	13.50	12.76	12.21	0.83 / 0.82	0.56 / 0.53	
2M 0230+2704.....	02 30 15.51	+27 04 06.1	L0	32.5 ± 4.0 <sup>a</sup>	14.29	13.48	12.99	0.88 / 0.87	0.78 / 0.75	
2M 0251-0352 <sup>s1</sup> .....	02 51 14.90	-03 52 45.9	L3	12.1 ± 1.1	13.06	12.25	11.66	0.92 / 0.91	0.75 / 0.71	
2M 0314+1603 <sup>s1</sup> ...	03 14 03.44	+16 03 05.6	L0	14.5 ± 1.8 <sup>a</sup>	12.53	11.82	11.24	0.82 / 0.80	0.60 / 0.54	
2M 0345+2540 <sup>s2</sup> ...	03 45 43.16	+25 40 23.3	L1	26.9 ± 0.36	14.00	13.21	12.67	0.83 / 0.81	0.57 / 0.53	
2M 0355+1133 <sup>s1</sup> ...	03 55 23.37	+11 33 43.7	L5	12.6 ± 2.7 <sup>a</sup>	14.05	12.53	11.53	0.91 / 0.90	0.77 / 0.72	
2M 0500+0330 <sup>s1</sup> ...	05 00 21.00	+03 30 50.1	L4	13.1 ± 2.6 <sup>a</sup>	13.67	12.68	12.06	0.91 / 0.89	0.72 / 0.65	
2M 2036+1051 <sup>s1</sup> ...	20 36 03.16	+10 51 29.5	L3	18.1 ± 3.2 <sup>a</sup>	13.95	13.02	12.45	0.87 / 0.85	0.63 / 0.58	
2M 2238+4353.....	22 38 07.42	+43 53 17.9	L1.5	21.8 ± 1.6	13.84	13.05	12.52	0.84 / 0.82	0.57 / 0.54	

Table 4.2: Coordinates and characteristics of the sixteen very low mass targets observed in this sample. Photometry is taken from the 2MASS catalog. Spectral types (spectroscopic) and distances are taken from DwarfArchives.org, unless otherwise noted. <sup>a</sup>Distance measurements derived from J-band photometry and  $M_J$ /SpT calibration data of Cruz et al. (2003) assuming a spectral type uncertainty of  $\pm 1$  subclass. <sup>b</sup>Survey detection limits of Table 4.3 given in terms of secondary-primary mass ratio, assuming a co-eval system (same age and metallicity). Masses ratios are derived from the 5-Gyr (first row) and 1-Gyr (second row), solar-metallicity substellar DUSTY models of Chabrier et al. (2000), using J and K band photometry. <sup>s1</sup>Target previously observed by Reid et al. (2006). <sup>s2</sup>Target previously observed by Bouy et al. (2003)

Table 4.3: Survey Contrast Limits ( $\Delta K$ ) at 99.5% Confidence

Primary	$\Delta K^a$															
	65.0	85.0	105.0	125.0	145.0	165.0	185.0	225.0	265.0	305.0	345.0	385.0	425.0			
2M 0015+3516	0.92	1.52	1.73	1.88	2.07	2.25	2.27	2.18	2.03	1.82	2.06	2.06	1.79			
2M 0036+1821	1.77	2.30	2.52	2.57	2.63	2.74	2.77	2.79	2.71	2.70	2.62	2.67	2.56			
2M 0045+1634	2.06	2.61	2.82	2.87	2.90	2.96	3.01	3.02	2.94	2.93	2.80	2.86	2.84			
2M 0046+0715	0.62	1.01	1.16	1.29	1.48	1.58	1.66	1.60	1.38	1.27	1.28	1.35	1.22			
2M 0131+3801	0.74	1.26	1.30	1.30	1.35	1.47	1.52	1.55	1.45	1.28	1.25	1.41	1.25			
2M 0141+1804	1.52	2.13	2.37	2.51	2.55	2.61	2.65	2.59	2.58	2.58	2.41	2.51	2.42			
2M 0208+2542	1.29	1.93	2.16	2.28	2.35	2.48	2.52	2.47	2.34	2.28	2.29	2.32	2.25			
2M 0213+4444	1.84	2.40	2.59	2.64	2.72	2.77	2.79	2.81	2.76	2.73	2.59	2.69	2.58			
2M 0230+2704	0.72	1.11	1.20	1.18	1.23	1.27	1.30	1.32	1.27	1.09	1.03	1.26	1.08			
2M 0251-0352	0.69	1.07	1.24	1.26	1.32	1.39	1.48	1.38	1.36	1.28	1.24	1.37	1.34			
2M 0314+1603	1.52	2.08	2.32	2.47	2.54	2.60	2.65	2.61	2.54	2.50	2.51	2.52	2.39			
2M 0345+2540	1.75	2.28	2.51	2.56	2.61	2.70	2.76	2.75	2.61	2.57	2.55	2.58	2.51			
2M 0355+1133	0.69	1.15	1.21	1.05	1.04	1.22	1.27	1.25	1.29	1.32	1.24	1.27	1.12			
2M 0500+0330	0.79	1.35	1.53	1.64	1.81	1.97	2.02	1.99	1.80	1.57	1.80	1.83	1.57			
2M 2036+1051	1.30	1.90	2.10	2.26	2.31	2.41	2.50	2.40	2.31	2.24	2.26	2.30	2.18			
2M 2238+4353	1.77	2.29	2.51	2.53	2.57	2.63	2.71	2.69	2.57	2.54	2.52	2.56	2.50			

Table 4.4: Detection contrast limits around primaries: <sup>a</sup>Primary-Secondary separations are given in units of mas, and the corresponding detection limits are in  $\Delta K$  magnitudes.

Table 4.5: Model Fits to Candidate Binaries

Primary	J. Date (+245000)	Separation (mas)	Az. Ang. (deg)	Contrast Ratio	Bayes Factor	Conf.	Separation (AU)
2M 0036+1821	4731	89.5 ± 11.4	114.1 ± 5.5	13.14 ± 3.14	7.9	96%	0.78 ± 0.10
2M 0345+2540	4731	217.4 ± 9.1 352.7 ± 10.5	258.8 ± 2.8 87.6 ± 2.0	26.44 ± 4.22 30.79 ± 9.08	7.6	98% 96%	5.85 ± 0.26 9.49 ± 0.31
2M 2238+4353	4732	128.2 ± 10.3 228.5 ± 9.1	209.9 ± 5.3 251.8 ± 3.5	17.76 ± 4.25 23.79 ± 5.92	7.1	97% 95%	2.79 ± 0.30 4.98 ± 0.42
2M 0355+1133	4757	395.5 ± 9.7 82.5 ± 13.0	19.5 ± 1.2 276.2 ± 4.1	17.63 ± 4.22 2.10 ± 0.40	6.3	97% 90%	8.62 ± 0.66 1.03 ± 0.27

## 4.4 Sixteen Brown Dwarf Targets - Four Candidate Binaries

Aperture masking is most sensitive to companions between  $\lambda/2D$  and  $4\lambda/D$ , corresponding to angular separations of 60-450 mas in  $K_s$  at Palomar and physical projected separations ranging from 0.6-10 AU for the targets in our survey.

Our achieved detection limits for all sixteen targets are summarized in Table 4.3. Our limits remain relatively flat at separations beyond  $\lambda/D$ , plateauing near  $\Delta K \sim 2.3$  for more than half our targets, and decline to roughly 1.4 magnitude shortward of  $\lambda/D$  (See figure 4.5).

We infer the (companion) stellar properties and mass ratios to the corresponding magnitude limits using the DUSTY models for target ages of 5 Gyr and 1 Gyr (Table 4.1). At the formal diffraction limit (about 110 mas in  $K_s$ ), companions with mass ratios of .83 for 5 Gyr systems and .55 for 1 Gyr systems would be resolved for 50% of our targets at a 99.5% confidence of detection (Fig. 4.6).

Our survey found four candidate binary systems with detections at 90-99% confidence and Bayes' Factors favoring the binary model (Table 4.5). We summarize and discuss these detections below.

For some targets in our survey, closure phase measurements constructed from the longest baselines had too much noise to extract a useable signal. The resulting drop in  $uv$ -coverage can give rise to aliasing of the model fits: i.e., multiple binary configurations fit the data equally well. When possible, we used previous observations of the target to rule out certain aliased fits; when not possible, all model fits are listed.

**2M 0036+1821:** A companion at separation 89.5 mas and 13.1:1 contrast was detected with 96% confidence and a Bayes' Factor of 7.8:1. The data also fits an alternative (alias) binary configuration ( $\rho \sim 243$  mas and 25:1 contrast) with 96% confidence that we rule out by a previous observations. Reid et al. (2006) observed this target in November 2005 with the NICMOS imager on the Hubble Space Telescope in the F170M and F110W bands. At or near this separation, this alternative configuration would have likely been detectable in the F110W bands.

**2M 0355+1133:** A companion at separation 82.5 mas and 2.1:1 contrast was detected with 90% confidence and a Bayes' Factor of 6.3:1. Reid et al. (2006) also observed this target in the F110W band and found no companion. As a proxy for the F110W bandpass, we estimate a J band contrast of 2.5:1 using the J-K color-magnitude relations of Dahn et al. (2002). Their program achieved a contrast limit of 2.5:1 beyond approximately 100 mas in F110W, suggesting that this candidate binary sat at the edge of their detection limits.

**2M 2238+4353:** Thirty-five percent of the closure phase triangles showed very high noise and were removed from analysis. As a result, aliasing of the signal was particularly problematic. Three distinct binary configurations were detected at 95-97% confidence. These range in separations between 100 and 400 mas and contrasts between 17:1 and 28:1.

**2M 0345+2540:** Like 2M 2238+4353, a large percentage of the closure phases were removed from analysis. Two distinct configurations, both with contrasts  $\sim 28:1$  ( $\Delta K \sim 3.5$ ) were determined with high confidence. Bouy et al. (2003) observed this target with the Wide Field Planetary Camera 2 (WFPC2) on the Hubble Space Telescope in March 2001, but we estimate these companions to be below their detection limits. Their survey reached background limitations at

contrasts between  $\Delta M \sim 3-5$  in the F814W band. Using the I band as a proxy for F814W, we estimate the companion of 2M 0345+2540 to have a contrast of  $\Delta I \gtrsim 5$  and to have been undetectable in the Bouy survey.

**2M0213+4444:** We observed target 2M0213+4444 three times over two nights in September 2008 (two sets in  $K_s$ , one in H) and once one month later (in  $K_s$ ). Two data sets from September were of poor quality and were not used for analysis. The remaining set from September found one binary fit ( $\rho \sim 81$  mas,  $\theta \sim 290^\circ$ , 5.2:1 contrast in  $K_s$ ) at 89% confidence. The target was observed again in  $K_s$  in October under poor seeing and much of the data was unusable. This data set could not be fit well by the September results, and implied a different configuration with 90% confidence ( $\rho \sim 234$  mas,  $\theta \sim 135^\circ$ , 11:1 contrast in  $K_s$ ). Given the low confidences of fits and the unreproducibility of these results, we conclude that this target is unlikely to be binary.

## 4.5 Discussion: Aperture Masking of Faint Targets

The use of non-redundant masking removes many types of spatial perturbations to the incoming wavefront. During high signal to noise observations, when read and background noise are minimal, the largest contributor to measurement noise is the temporal and spatial atmospheric fluctuations of the wavefront, even after adaptive optics correction. Short exposure times, roughly less than the coherence time of atmosphere, freezes the tip-tilt and low-order perturbations to the wavefront, which can be removed by combining fringe phases into closure phases. This advantage is lost when exposures extend over multiple coherence times. For this reason, aperture masking flourishes with short exposures.

Behind laser guide star adaptive optics systems, although the structure of the corrected wavefront may be different, the functionality of aperture masking is the same. However, targets requiring laser guide star AO tend to be fainter, and thus require either longer exposure times (permitting sufficient correction) or techniques for dealing directly with noise from read outs and background flux.

This survey opted for maintaining short exposure times. The signal to noise of fringe amplitudes decline rapidly for longer baselines, as the transmission function for these baselines is lower and turbulence variations are larger. Just as, for instance, Stehl ratio depends on the variance of the incoming wavefront, so does the fringe amplitude, also dropping as  $\exp(-\sigma_{baseline}^2)$ . For faint targets, long baseline fringes often linger undetectable below the background and read noise, making difficult measurements of long baseline phases.

The capture of a large number of short exposure images allows us to select out the best fringe measurements, during the serenditous moments of very good correction or still atmospheres, and discard those dwarfed by read noise. This technique, analogous to *lucky imaging*, effectively selects high signal to noise measurements of closure phase. In most cases, these lucky closure phases were sufficient to obtain measurements of the target closure phase, even at long baselines. We contrast this method to two measurements of targets observed with long (1 minute) exposures. These exposures did often have long baseline fringes detectable at or just above background. But this method resulted in poor measurements of the target closure phase, even at shorter baselines. The multiple-coherence time exposures means that low order perturbations are not effectively removed by closure phases, resulting in large phase errors, and the fewer overall number of data points removes the statistical advantage. The measured closure phase is not a good measurement of

the true target phase.

Long exposures, with adequate correction, do allow longer baseline fringes to grow in amplitude above the read noise or background limit. Exposures for aperture masking should be limited to the effective coherence time of the adaptive optics system – the interval over which the phase variance of the longest baselines reaches about one radian.

The quality of measurements from both sets of exposure data suggests a slight modification of technique for the next application of aperture masking with laser guide star adaptive optics. The higher noise content of the one-minute exposures suggests that these exposures are too long for the level of correction obtained in this survey. The short exposure method fared much better, but a large percentage of images failed to observe fringe amplitudes above read noise. This suggests that slightly longer exposures would have benefited the observations. It is worthwhile to note that the low transmission of the long baselines, even at Strehl ratios of 15% typically reached in this survey, indicates that direct imaging would not have been able to obtain  $\lambda/D$  resolution.

## 4.6 Conclusion

We present the results of a close companion search around nearby L dwarfs using aperture masking interferometry and Palomar laser guide star adaptive optics. The combination of these techniques yielded typical detection limits of  $\Delta K_s = 1.5$ -2.5 between  $1$ - $4\lambda/D$  and limits of  $\Delta K_s = 1.0$ -1.7 at  $0.6 \lambda/D$ . Our survey revealed four candidate binaries with moderate to high confidence (90-99%) and favorable Bayes' Factors.

Ten of the targets have previously been observed with the Hubble Space Telescope as part of companion searches. As such, we did not expect to find bright or distant companions around these targets which would have been identified in the previous surveys. But as demonstrated in this paper, the detection profile of aperture masking is capable of revealing close or dim companions which are obscured by the point spread function of full aperture imaging. Aperture masking demonstrates an increase in formal resolution and detectable contrast at close separations over laser guide star adaptive optics alone.

Our survey indicated two previously observed targets as candidate binaries. Our survey indicated one companion around 2M 0355+1133 within the formal diffraction limit of the HST and one companion around 2M 0345+2540 below the background detection threshold of the previous survey. Two other targets, 2M 0345+2540 and 2M 2238+4354, also indicated the presence of companions, both with contrast ratios greater than 15:1.

Aperture masking is most sensitive to companions between  $\lambda/2D$  and  $4\lambda/D$ , corresponding to angular separations of 60-450 mas in  $K_s$  at Palomar and physical projected separations ranging from 0.6-10 AU for the targets in our survey. Two candidate binaries presented in this paper have projected separations less than 1.5 AU. The results suggest a favorable target set for future companion searches. Their candidacy is consistent with the conjecture that tight binaries are underrepresented in the current tally of low mass binaries. Spectroscopic surveys, which focus on separations within 3 AU, are necessary to conclusively answer this question. Extending the use of aperture masking with laser guide star AO is a rewarding approach for detecting companions within this range, and facilitating the measurements of their masses.

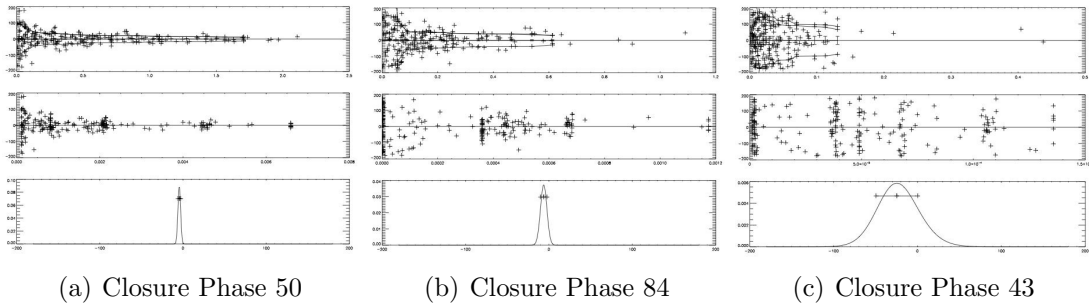


Figure 4.3: Estimating per-measurement weights for three closure phase data sets for target 2M 2238+4353. The data sets have comparatively high- (left), moderate- (center) and very low- (right) signal to noises. (Top) Plot of bispectrum (closure) phase vs. bispectrum amplitude. Note that larger amplitude data have smaller phase spreads, and a clear asymptotic mean can be identified in the high and moderate signal to noise cases. (Closure phase 43 contains no discernible signal, and would be removed from further analysis.) Low amplitude bispectra are swamped by read noise, introducing phase errors which are nearly uniformly distributed. The solid line estimates the relationship between per-measurement standard deviation and bispectrum amplitude. (Middle) Closure phase vs. approximate weighting. Note that the higher weighted points have lower per-measurement standard deviation. (Bottom) Resulting p.d.f. of the closure phase.

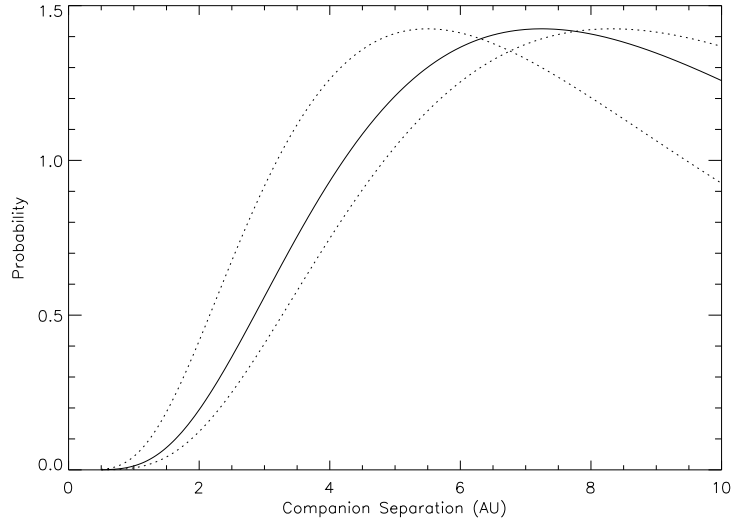


Figure 4.4: Proposed log-normal distribution of companion separation around L dwarf primaries from Allen (2007). The peak and width of the distribution have been constrained by previous surveys. The most likely distribution (solid line) and one sigma distributions (dashed lines) are shown. Despite the constraints, the distribution is noticeably uncertain in the region of separations searched by our survey. We opt to use a uniform prior for our Bayesian analysis, noting that such a prior may over signify companions closer than roughly 2 AU as compared to the Allen prior. Similarly, a confirmed detection of a close companion could indicate this distribution has been incorrectly described as log-normal (see text).

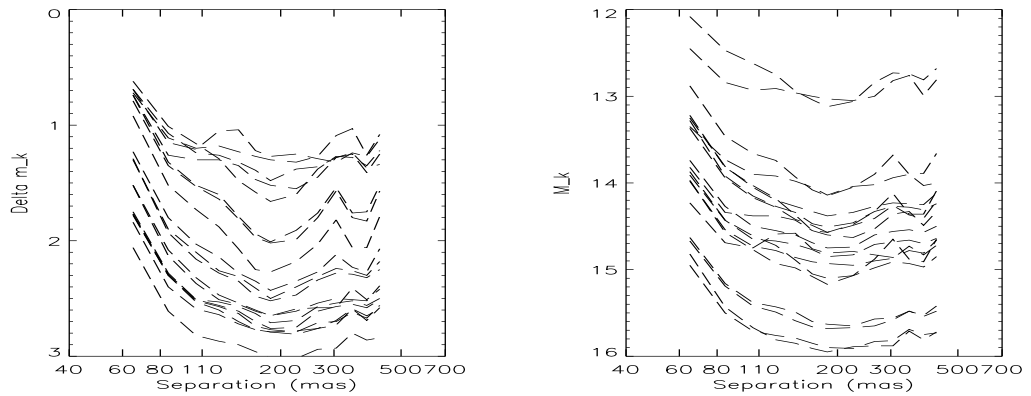


Figure 4.5: Contrast limits at 99.5% detection as a function of primary-companion separation: (left) The primary-secondary magnitude difference in  $K_s$  detectable at 99.5% confidence. (right) The same detection limits in terms of the absolute magnitude of the companion.

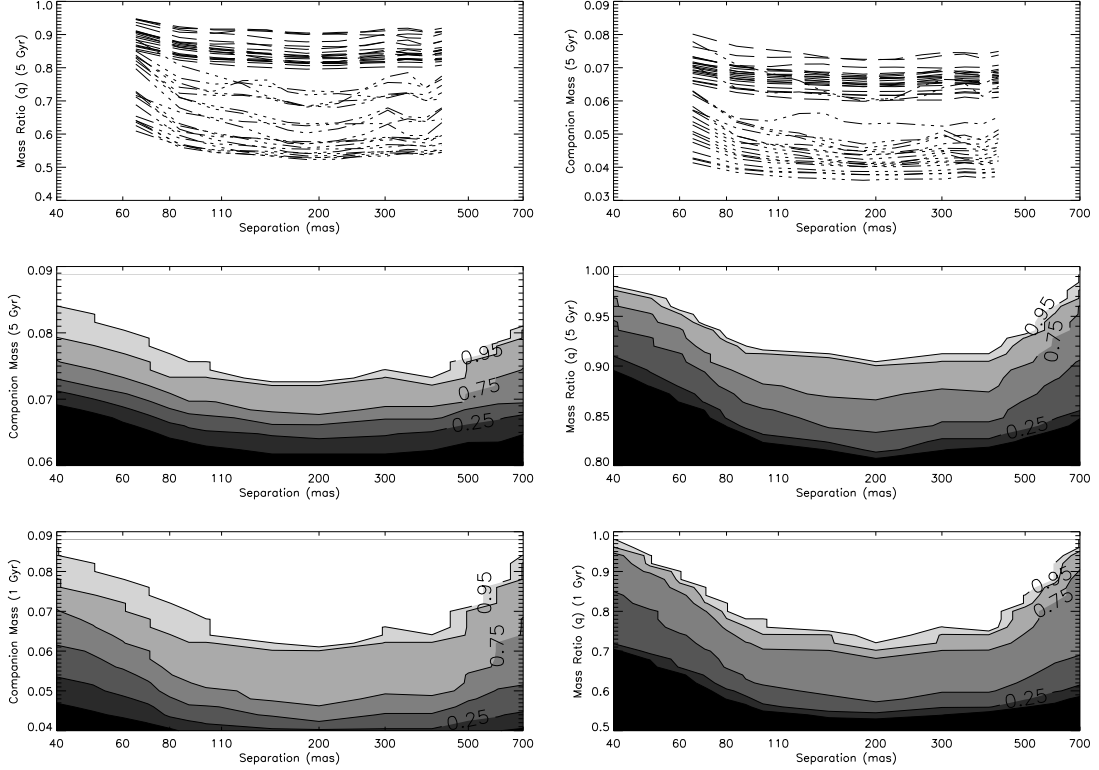


Figure 4.6: Companion mass and mass ratio limits at 99.5% detection as a function of primary-companion separation: (top left) The primary-companion mass ratio detectable at 99.5% confidence. *Dashed* lines are for systems aged 5 Gyr; *Dot-dashed* lines are systems ages 1 Gyr. (top right) The same data in terms of companion mass. (middle/bottom left) As a function of separation and companion mass, this plot reveals the percentage of 5 Gyr (middle) and 1 Gyr (bottom) companions detectable at 99.5% given the data quality of the survey. Binaries in the white area would have been detected for 100% of the survey targets, followed by contour bands of 95%, 90%, 75%, 50%, 25%, and 10%. At the diffraction limit (110 mas), companions of mass  $0.65 M_{\odot}$  would be resolved for 50% of our targets. (middle/bottom right) The same plot in terms of mass ratio. Diffraction limit sensitivity: 5 Gyr companions of mass  $0.65 M_{\odot}$  ( $.038 M_{\odot}$  for 1 Gyr) would be resolved for 50% of our targets. Equivalently, our survey reached mass ratios of .83 (5 Gyr) and .55 (1 Gyr) for 50% of our targets at the diffraction limit.

## CHAPTER 5

# THE USE OF SPATIAL FILTERING WITH APERTURE MASKING INTERFEROMETRY AND ADAPTIVE OPTICS<sup>1</sup>

### 5.1 Abstract

Non-redundant aperture masking interferometry with adaptive optics is a powerful technique for high contrast at the diffraction limit with high-precision astrometry and photometry. A limitation to the achievable contrast can be attributed to spatial fluctuations of the wavefront - those within a sub-aperture and across sub-apertures - and temporal fluctuations within a single-exposure. Spatial filtering addresses spatial fluctuations within a sub-aperture. An optimized pinhole in the focal place preceding the aperture mask is one approach for reducing the variation of the wavefront within a sub-aperture. Similarly, a weak spatial filtering effect is shown to be provided by post-processing the images with an apodized window function, typically used to minimize detector read noise and contamination from wide-separated sources. We explore the effects of spatial filtering through calculation, simulation, and observational tests conducted with a pinhole and aperture mask in the PHARO instrument at the Hale 200" Telescope at Palomar Observatory. We find that a pinhole decreases stochastic closure phase errors and calibration errors, but that tight restrictions are placed onto the alignment of binary targets within the pinhole. We propose an observation strategy to relax these restrictions. If implemented the pinhole could potentially yield an increase in achievable contrast by up to 10-25% in H and K<sub>s</sub> bands, and more at very high Strehl ( $\gtrsim 80\%$ ). We also conclude that correcting low-order wavefront modes within the sub-apertures will

---

<sup>1</sup>This work has been under review for publication by the *The Astrophysical Journal* as of August 1, 2011.

be key for reaching high contrasts with extreme-AO systems such as the Gemini Planet Imager and PALM3K to search for planets.

## 5.2 Introduction

Current planetary searches using a coronagraph (e.g., Hinkley et al. (2011)), excel at obtaining very high contrast ( $10^5:1$ ) but are unable to probe at close separations ( $\lesssim 300\text{-}500$  mas) where the field of view is blocked by the occulting spot. This separation rules out the observation at physical separations  $\lesssim 10$  AU for many host stars. The detection of planetary companions with techniques providing both high-contrast and high-resolution will play a key role in identifying the full distribution of Jupiter-class planets and for investigating the mechanisms of planetary formation (Kraus et al., 2009), migration, and stability (Veras et al. (2009); Raymond et al. (2009) and e.g. HR 8799, Fabrycky & Murray-Clay (2010)).

Non-Redundant Aperture Masking Interferometry (*NRM* or *aperture masking*), in conjunction with adaptive optics (AO) is well established for yielding much more precise astrometry and photometry than adaptive optics alone at close separations (e.g., Kraus et al. (2008, 2011)) and for the detection of high contrast companions (Lloyd et al., 2006). The application of aperture masking with AO on 5-10 meter class telescopes achieves contrasts of  $10^2\text{-}10^3:1$  at and outward of  $\lambda/D$  and nicely complements companion searches with a coronagraph. The increased contrast and resolution of NRM has been used with great effect for stellar multiplicity studies (Kraus et al., 2008, 2011), the detection of short period brown dwarfs for dynamical mass measurements (Lloyd et al., 2006; Bernat et al., 2010), and a high-contrast search for inner planetary companions to HR 8799 (Hinkley et al.,

2011). With the Gemini Planet Imager (Macintosh et al., 2008) and Project 1640 IFS (Hinkley et al., 2009) equipped with non-redundant masks, aperture masking interferometry from the ground will play a key role in the detection of exoplanets at close separations.

NRM observations use a mask to transform the full telescope aperture into a sparsely populated set of sub-apertures, constructed so that no two pairs of sub-apertures share the same baseline direction and length (i.e., are non-redundant). The strength of this technique draws on its measurement of the closure phase quantity (e.g., Jennison (1958); Readhead et al. (1988); Cornwell (1989)), an observable which naturally mitigates the effect of wavefront errors on scales larger than a sub-aperture. These same wavefront errors produce the speckles of direct imaging, which dominate the image noise by orders of magnitude whether arising from atmospheric variation (Racine et al., 1999) or quasi-static instrumental effects (Hinkley et al., 2007). Their mitigation by closure phases enables higher contrast despite the blocking of 90-95% of the flux by the aperture mask.

The achievable contrast of the technique is limited by its own calibration challenges, one of which arises from quasi-static spatial variation of the wavefront within the sub-aperture. Such wavefront errors erode the effectiveness of using closure phases (resulting in *redundancy noise* in the language of Readhead et al. (1988) and others). Similarly, decreasing the wavefront variation within the sub-aperture can increase the contrast of NRM observations further.

Optical and infrared long-baseline interferometers have implemented single-mode fibers and pinholes which spatially filter (i.e., smooth) aperture wavefront errors to improve measurements of complex visibility (Shaklan & Roddier, 1987; du Foresto et al., 1997). Poyneer & Macintosh (2004) have studied the use of a

pinhole to develop an AO wavefront sensor which more accurately measures of the wavefront above a sub-aperture. Likewise, spatially filtering the wavefront errors with a pinhole placed in the image (focal) plane before the aperture mask may provide a means for substantially increasing the achievable contrast of NRM observations.

This paper provides a comprehensive analysis of NRM with pinhole spatial filtering. To establish its theoretical foundation, we present an analytic description of the combined technique (Section 2). Using an accurate simulation of an aperture masking equipped telescope, we derive the optimal pinhole size and estimate its expected performance, limitations, and restrictions. We also derive several results applicable to general aperture masking observations. (Sections 3 and 4). We have also installed a pinhole in the PHARO instrument of the Hale 200" Telescope at Palomar Observatory. To study how spatial filtering improves the sensitivity of NRM observations and influences the astrometric and photometric characterization of discovered binary systems, we observed twenty-six single stars and four known binaries with and without the pinhole (Section 5). This paper further develops the understanding of NRM as a technique for detecting high-contrast companions and provides several new findings to guide the design of NRM experiments for next generation adaptive optics systems and instruments dedicated to exoplanet detection.

## 5.3 Aperture Masking with Spatial Filtering

### 5.3.1 Aperture Masking: Current Technique

An aperture mask is positioned in the pupil plane behind the adaptive optics system and transforms the full aperture into a sparsely populated set of sub-apertures (Fig. 5.1(a)). The resulting image of the target is a set of overlapping fringes called the *interferogram*. The amplitude and phase of each fringe corresponds to the measurement of one particular component of the complex visibility with spatial frequency  $\vec{b}/\lambda$ , where  $\vec{b}$  is the baseline vector and  $\lambda$  is the observing wavelength. Multiplying the complex visibility of specific baseline triplets formed by three sub-apertures creates bispectra (Lohmann et al., 1983), the argument of which is the closure phase (Jennison, 1958; Cornwell, 1989). Closure phases are robust against pupil-plane phase errors, which are a source of direct imaging PSF calibration errors and speckle noise, and provide the mechanism for obtaining more precise astrometry and photometry with the aperture masking technique.

Typical observations (including those in this paper) are conducted by taking one or more sets of target images interspersed with sets of one or more calibrators (unresolved stars near in the sky and of similar magnitude and color.) After the basic processing the raw images (see, for example, Lloyd et al. (2006); Martinache et al. (2007); Bernat et al. (2010)), the phase and log-amplitude of each fringe is extracted from the images and used to construct bispectra and closure phases. Mean values are obtained by averaging the quantities over a single set, and error estimates are derived from the scatter. Multiple sets are combined by weighted average. Calibration is performed by subtracting the closure phase and log-amplitude of the reference stars. Amplitudes are generally not used in com-

panion searches because calibration is subject to stable atmospheric seeing and often is measurable to only 10-50% (Tuthill et al., 2006). A binary model is fit to the closure phase data to minimize  $\chi^2$ ; a positive detection results in measurement of the binary parameters (separation, orientation, and wavelength-dependent contrast ratio). Errors in binary parameters are often taken from the curvature of the  $\chi^2$  space at minimum. Many examples of this implementation for the detection of stellar companions can be found in the literature (Kraus et al., 2008; Bernat et al., 2010; Kraus et al., 2011).

For targets in which the adaptive optics system provides stable and mostly coherent ( $\sigma_{rms}^2 \lesssim 0.1 \text{ rad}^2$ ) correction of the wavefront on sub-aperture scales, this observing mode typically measured closure phases with an error scatter of 1-2 degrees in H band ( $1.6\mu m$ ) after a few minutes on a bright target, equivalent to a contrast of detection of about 100-200:1 at  $\lambda/D$ . This technique is calibration limited by a systematic closure phase component of one to several degrees which likely arises from quasi-static instrumental wavefront errors. Additional calibrators usually decrease, but do not fully eliminate, this component. To account for this, an addition error term is added in quadrature to the closure phase errors until the best fitting model yields a  $\chi^2$  of unity.

### **5.3.2 Aperture Masking: Why Spatial Filter? Calibration Errors.**

A critical requirement of the aperture masking design is that each pair of sub-aperture creates a unique interferometric baseline. The lack of baseline redundancy ensures that any spatial frequency measured can be traced back to the interfer-

ence of a unique pair of sub-apertures (Haniff et al., 1987; Roddier, 1986). Closure phases constructed by non-redundant baselines will be less affected by pupil-plane phase which would otherwise distort measurements of the spatial frequency phase. When two or more baselines contribute to the same spatial frequency, the power adds partially incoherently depending on the phase difference of each contributing baselines (e.g., Figure 5.1(b)). A random component will be introduced into the resulting spatial frequency phase which cannot be removed by closure phases (yielding a so-called non-zero closure phase). This component, termed *redundancy noise*, is largest when the redundant baselines are incoherent and zero when they are coherent. Readhead et al. (1988) provides an extensive treatment of redundancy noise for seeing-limited imaging.

The mask cannot be entirely non-redundant. The finite sub-aperture size means that baselines are redundant at least within a sub-aperture (Figure 5.1(c)). With sub-aperture scale correction provided by the AO system, this *sub-aperture redundancy* noise is largely removed (Tuthill et al., 2006), as compared to the uncorrected case, but still gives rise to closure phase measurement errors due to the remaining spatial incoherence within the sub-aperture. In completely analogous fashion, temporal variations to the baseline phase during a single exposure create *temporal redundancy* which also give rise to closure phases errors (again, see Readhead et al. (1988)).

It may be illuminating to contrast the uncorrected and corrected cases. With uncorrected observing, redundancy restricts sub-aperture sizes to smaller than the characteristic size of atmospheric turbulence and exposure times shorter than the atmospheric coherence time. Adaptive optics removes both constraints since good correction supplies a stable, mostly coherent wavefront across the full aperture.

Current NRM masks are designed with sub-apertures on the order of the AO actuator spacing; this need not be the case and will likely not be so in upcoming extreme-AO aperture masking experiments. Atmospheric and adaptive optics residuals decorrelate on timescales much shorter than the exposure length and thus likely only contribute to the stochastic variation of closure phases from one image to the next. Changes in seeing between target and calibrator observations change the magnitude of the stochastic variability of closure phases (the signal to noise of the measurement), but do not introduce calibration offsets (Roddier, 1986), and can thus be minimized by additional exposures. This is precisely why closure phases provide a robust measurable unlike visibility amplitudes, which are poorly calibrated if seeing changes (Tuthill et al., 2006).

Quasi-static instrumental wavefront errors contribute to all spatial scales and vary on timescales of tens of minutes (e.g., Bloemhof et al. (2001); Hinkley et al. (2007)), or with movement of the telescope (Marois et al., 2005). As long as these errors remain static over a single exposure, large-scale wavefront changes (those larger than a sub-aperture) are removed by closure phases. One of the great advantages of using non-redundant masking to mitigate the quasi-static imaging problem is that closure phases require only a single image (they 'self-calibrate', Cornwell (1989)). Instrumental errors change between observations of the target and calibrator, but only those smaller scale than a sub-aperture contribute to aperture masking calibration errors.

We propose that spatial filtering the wavefront before its propagation through the aperture mask can be used to reduce the inhomogeneity of the wavefront phase within the sub-aperture and, by virtue of being more coherent, reduce sub-aperture redundancy noise. Figure 5.2 illustrates the effect of an optimized pinhole

spatial filter (discussed in the next subsection) to smooth the phase of a simulated adaptive optics corrected wavefront (Strehl ratio  $\sim 50\%$  in  $K_s$ ). The portion of the wavefront sampled by each sub-aperture is much more uniform after spatial filtering.

We anticipate that spatial filtering can lead to several measurable improvements of the closure phases, including decreases in systematic calibration error and stochastic variation from one image to the next. Measured visibility amplitudes, by virtue of their dependence on sub-aperture inhomogeneity, can show less degradation and be more robust to changes in seeing.

### 5.3.3 Pinhole Filtering

One possible implementation of the pinhole spatial filter, reminiscent of the four planes of a coronagraph (see Ferrari (2007) for a review), is shown in Figure 5.3. The pinhole, positioned at the center of the field and in what is usually referred to as the coronagraphic plane, blocks light beyond its inner transmission region. This acts to spatially filter the wavefront before entering the non-redundant aperture mask, located in a re-imaged pupil plane. (The mask location is equivalent to the Lyot-plane of coronagraphy).

The transmission profile of the pinhole is a top-hat function, with diameter  $d_{spf}$  which will be expressed for convenience in units of  $\lambda/D$ , with  $D$  the diameter of the telescope. At the location of the aperture mask, this is equivalent to the wavefront convolved by a Jinc function (c.f. Footnote <sup>1</sup>) of characteristic diameter  $\lambda/d_{spf}$ .

---

<sup>1</sup>The Jinc function is defined as  $Jinc(x) \equiv \frac{J_1(x)}{x}$ . It is the two-dimensional Fourier Transform of a circular aperture, and is related to the Airy function by  $Airy(x) = 4 Jinc(x)^2$ .

Efficient spatial filtering aims to make the wavefront uniform within one sub-aperture of the non-redundant mask, and so one wants the characteristic diameter to be matched to the diameter of a sub-aperture, suggesting

$$d_{spf} \approx \frac{D}{d_{sub}} \quad (\text{in units of } \lambda/D). \quad (5.1)$$

A larger pinhole decreases the impact of the spatial filtering; a smaller pinhole restricts the field of view and begins to impinge on the signal we wish to measure.

This technique differs from the form of spatial filtering implemented in optical and infrared long baseline interferometers, where the signal from each telescope is injected into a single mode fiber or pinhole before beam combination and extraction of the interferometric signals (du Foresto et al., 1997). The use of single mode fibers on long baseline interferometers has shown increases in phase estimations by a factor of two, or more in bad seeing, despite the loss of flux (Tatulli et al., 2010). The implementation of this approach with non-redundant aperture masking would require the injection of light from each sub-aperture into a single mode fiber or pinhole before recording the interferogram. Given the simplification of the single pinhole implementation, it offers, a priori, an appealing alternative (Keen et al., 2001).

### **Aperture Masking Through a Pinhole**

Given that the aperture mask is located in a pupil plane, the point spread function (PSF) of masking interferometry is invariant to target position over a wide field of view (several arc seconds). With the pinhole filter in place (in an image plane), the PSF and system response varies with target position relative to the pinhole, a

smaller effective field of view.

Section 5.9 shows that the use of the pinhole filter alters the measured complex visibility of a point source:

$$V_{spf}(\vec{b}) = T(\vec{b}) \int d\vec{\theta} \Pi[\vec{\theta}/d_{spf}] \times e^{2\pi i \vec{\theta} \cdot \vec{b}/D} \times PSF[\theta - \vec{\alpha}], \quad (5.2)$$

where  $\vec{\alpha}$  is the location of the point source on the sky (measured in angular units of  $\lambda/D$ ), and  $\vec{\alpha} = 0$  corresponds to perfect alignment of the source in the pinhole. The baseline being measured is  $\vec{b}$ , corresponding to a spatial frequency  $\vec{u} = \vec{b}/\lambda$ . The complex visibility is usually expressed as a function of the spatial frequency; here we present it as a function of baseline and wavelength for clarity. The telescope transfer function,  $T(\vec{b})$ , gives the spatial frequency response of the aperture or aperture mask in terms of the baseline. It is defined explicitly in Section 5.9. The top-hat function,  $\Pi[\frac{|\vec{\theta}|}{d_{spf}}]$ , is equal to one for  $\frac{|\vec{\theta}|}{d_{spf}} < \frac{1}{2}$  and zero otherwise.

From three baselines vectors,  $\vec{b}_1$ ,  $\vec{b}_2$ , and  $-\vec{b}_1 - \vec{b}_2$ , a closure phase is the argument the product of the complex visibilities:

$$\phi_{cp} = \arg \left[ V(\vec{b}_1) V(\vec{b}_2) V(-\vec{b}_1 - \vec{b}_2) \right] \quad (5.3)$$

The observed visibility amplitudes and closure phase change by an amount which depends on the position of the target with respect to the pinhole (its alignment) and the point spread function. (e.g., Figure 5.4). The transmission of the pinhole blocks high spatial frequency content of the wavefront, even in the absence of wavefront errors. In this way, removal of the higher spatial frequencies can alias into changes in lower, baseline frequencies, similar to the effect observed by Poyneer & Macintosh (2004). Those on sub-aperture scales compete with closure phase measurements.

As the point spread function varies, so too will the aliased phase errors. This introduces a stochastic component to the closure phase errors which appears to undercut the effectiveness of the pinhole. A portion of the phase errors will also remain fixed and be strictly a function of the asymmetrical truncation of the target and its mean point spread function. The latter we term misalignment error, to distinguish it from other calibration components. Generally speaking, both will increase as the target is positioned further from the pinhole center.

Qualitatively, we can illustrate that the asymmetrical truncation of the target shifts the visibility and closure phase. Consider Figure 5.4c. The visibility phase is influenced by the position of the target on the sky; the asymmetrical truncation of the target shifts its center of light, and so too the visibility phase. While closure phases are normally invariant to the position of the target normally, the pinhole breaks this invariance. The overall isotropy of the point spread function and circular pinhole shape suggests that the misalignment error is symmetric about the origin. That is, just as aligning the target at two diametrically opposed positions will induce equal and opposite shifts in the center of light, the overall symmetry suggests equal and opposite phase errors as well.

The aliased phase errors are small as long as the majority of the flux resides within the pinhole and only competes with the closure phase measurements if the power aliases back into sub-aperture scale wavefront deviations. For this reason shorter wavelength observations will be preferentially advantaged with this approach. More generally this suggests, that to minimize aliasing, the pinhole could be optimized to filter only frequencies that are not corrected by the AO system; in that case the pinhole size would be matched the the AO actuator size instead of the masking sub-aperture size.

Each target of a binary will be truncated differently. The misalignment error can be calculated directly by replacing the single star point spread function in Equation 5.2 or Figure 5.4 with the binary image. This will be approximately the same as the error of each component individually. In other words, the misalignment error of the primary added to the misalignment error of the secondary multiplied by the secondary-primary contrast ratio. Assuming that the misalignment error is point symmetric about the origin, aligning the binary center of light near the pinhole center appears to be a viable strategy for minimizing the misalignment error.

If the misalignment component is large enough as to become the limiting component in closure phase noise, there are three approaches which can be employed for removing the component from science data. Empirically, the component can be calibrated by observing a single star aligned at the same location as the primary under similar AO performance. In practice, this may be limited by the accuracy with which one can repeatedly (visually) align a target within the pinhole, and the component arising from the (unknown) companion remains. Computationally, if the location of the primary is known along with an estimate of the point spread function, then the misalignment component can be included in the mathematical closure phase model which is fit to data. This approach requires a direct image of the primary within the pinhole to determine its location and estimate its point spread function. Both may detract from the overall efficiency of observing. Finally, a third option is to take several sets of aperture masking data with the target (center of light) at various alignments. Specifically, if diametrically opposed alignments have misalignment errors opposite in sign, then the component could be averaged out.

### 5.3.4 Post-Processing with a Window Function

In this course of our investigation of the pinhole filter, we also characterize the use of a tapered window function on masking images to reduce the impact of various noise sources and small-scale wavefront errors on closure phases. For example, we use a super-Gaussian function,  $\exp(-kx^4)$ , with our experiments for its flat-top and quickly tapering Fourier Transform. For concreteness, we will use this same function as an illustrative example here (Figure 5.5). The window function is described by the size of its half width at half max measured in pixels on the detector or in units of  $\lambda/D$ .

Multiplying the images by a window function that retains the intensity of the interferogram core but tapers at its edges greatly reduces the contamination of detector read noise and dark current, or scattered light from nearby targets not of scientific interest. Per-pixel Gaussian-distributed read noise, when Fourier Transformed, results in a per-baseline Gaussian-distributed uncertainty. The per-baseline noise has a magnitude that is directly related to the total transmission of the window function. Therefore, a tighter window function removes more read noise.

However, complex visibilities are extracted from the Fourier Transform of the image, so the application of a window function is identical to the convolution of the complex visibilities with the Fourier Transform of the window function. This mixes the complex visibilities of the baselines and, ultimately, restricts the minimum window function size.

The aperture mask is designed to be non-redundant for baselines extending between the centers of sub-apertures; the finite size of the sub-apertures give rise

to islands of transmitted power in the power spectrum, which we call *splodges* (see Figure 5.5, Bottom Left). The splodges of a completely non-redundant mask do not overlap, and hence the separation between neighboring splodge peaks is about  $2 d_{sub}$ . (In practice, some overlap at the splodge edges may be exchanged for better coverage or larger sub-apertures.) Furthermore, neighboring splodges may arise from completely separate pairs of sub-apertures (i.e., separate baselines), and one would not assume any coherence between the baseline phases. For this reason, window functions narrower than about  $\lambda/2d_{sub}$ , or those without quickly tapered Fourier Transforms, will mix the incoherent baselines of neighboring splodges and rapidly increase the error of closure phases, similar to redundancy noise.

The optimally sized window function will balance the reduction of read noise with the increase of redundancy noise.

Post processing with a window function also reduces the impact of small-scale wavefront errors. This is most readily recognized by noting that the outer rings of the point spread function encapsulate the high spatial frequency content of the wavefront; removing this flux also removes the high spatial frequency content of the wavefront.

## 5.4 Simulated Observations

We have developed an accurate simulation of the Palomar aperture masking interferometry experiment in order to explore the effect of spatial filtering on wide band data and to optimize the pinhole for implementation on the telescope.

The Palomar 9-hole aperture mask has been described previously in Lloyd

et al. (2006) and is shown in Figure 5.1(a). Placed in the pupil plane, the mask has baselines ranging from 0.71m to 3.94m and sub-apertures that are 0.42m in diameter.

As discussed in Pravdo et al. (2006) and Bernat et al. (2010), aperture masking and the implementation of closure phases works most effectively using the short exposure times, when large scale wavefront errors (be they atmospheric or instrumental) can be regarded as approximately static. The typical aperture masking operation at Palomar uses exposure lengths of 431 ms. Over this time scale, the evolution of the atmosphere produces a highly dynamic wavefront on sub-aperture scales.

#### **5.4.1 Characterization and Simulation of Palomar's Atmosphere**

Studies by Ziad et al. (2004) and Linfield et al. (2001) conducted with the Palomar Testbed Interferometer (PTI) and Hale 200" Telescope confirm that the atmospheric turbulence power spectrum is approximately Kolmogorov with an outer scale most often within the range 10 - 50 meters. The median-seeing Fried parameter ( $r_0$ ) has been measured to be 9.0 cm at 550 nm, dropping to 3.8 cm during bad, but regularly observed seeing (Dekany et al., 2007).

Advection (wind) speeds drive the evolution of atmospheric structure within the sub-aperture on intervals between 0.1 and 1.0 seconds. Using measurements of the Palomar atmospheric temporal structure function over four nights, Linfield et al. (2001) derive wind speeds typically less than 4 m/s. For shorter time scales, the temporal structure function decays exponentially. The characteristic decay

time, which scales with  $\lambda^{6/5}$ , has been measured in two surveys to vary between 15-80 ms (Ziad et al., 2004) and 60-150 msec (Linfield et al., 2001) in  $K_s$ .

Our simulations assume an outer scale of 50 meters and Fried parameter value 9.0 cm, which corresponds to 48 cm in  $K_s$  and 32 cm in H. We use wind speeds of 5 m/s and temporal decay time of 60 ms.

### 5.4.2 Numerical Simulation

We generate time-evolved Kolmogorov phase screens following the procedures of Lane et al. (1992) and Glindemann et al. (1993). These phase screens are characterized by three parameters: the Fried parameter of an instantaneous phase screen; the wind velocity which blows the static phase screen across the aperture; and an additional parameter driving the decorrelation of high spatial frequencies between time steps. From this last parameter emerges the exponentially decreasing temporal structure function for short time scales.

A single 431 ms exposure image is constructed by adding 24 sub-images, each of which is an instantaneous snapshot separated in time by 18 ms. We chose this time step to sufficiently sample the atmospheric evolution over relevant time scales: the wind sub-aperture crossing time is 84 ms; the coherence decay time is 60 ms.

The generated images are 512 x 512 pixels, designed to preserve the pixel scale of the PHARO detector. In frequency space, the 5.08-meter aperture spans slightly less than 256 x 256 pixels in  $K_s$  band. Phase screens of this size are generated; this corresponds to an inner scale of approximately 2 cm, and sub-apertures approximately 450 pixels in area. We repeated several simulations with four times as many pixels and arrived at similar results; from these results we

conclude our simulation is well-sampled.

The simulation generates one sub-image for each phase screen using an incoming monochromatic wavefront perturbed by the screen. After passing through the telescope aperture, the wavefront is corrected by adaptive optics, then propagates through the spatial filter, the aperture mask, and, finally, forms an image on the detector. We ignore read noise and photon noise. This simulation is similar to that used by Sivaramakrishnan et al. (2001).

We model the adaptive optics system as an instantaneous high-pass filter of the form  $A(k) = 1/(1 + (k_c/k)^2)$ , with a cutoff imposed by the Nyquist frequency of the actuator spacing,  $k_c = N_{act}/2D$  (about 1.4 cycles/m at Palomar). This filter is applied to the Fourier Transform of the phase screens and accurately reproduces the wavefront residuals observed under optimal operation at Palomar (Dekany et al., 2007). This overestimates the typical AO performance on faint targets, particularly the performance of tip-tilt suppression. To account for this, we apply the following modified AO filter function, which degrades the low spatial frequency AO response:

$$A(k) = \min \left[ \frac{1}{1 + (k_c/k)^2}, 0.05 \right], \quad (5.4)$$

$$k_c = N_{act}/2D.$$

To include the polychromatic effects, each wide band transmission filter is divided into a number of subintervals (generally 4). A monochromatic image is generated for each sub-interval (taking into account wavelength dependent effects), and these images are added to form the a single polychromatic sub-image. The sub-images are co-added to create a single 431 ms exposure.

This produces direct imaging Strehl ratios of 40-50% in H band and 60-70% in  $K_s$ .

## 5.5 The Palomar Pinhole Experiment

### 5.5.1 Pinhole Implementation on PHARO

The PHARO instrument (Hayward et al., 2001) is especially suited to a pinhole implementation. PHARO has been designed with coronagraphic capabilities, giving access to both a focal plane and a pupil plane before the final focal plane (Figure 5.3).

The pinhole is placed in the focal plane before the aperture mask. Based on our simulations from the next subsection, a pinhole of angular diameter 0.779 arc-second was installed at the Lyot Stop in PHARO in June 2008. This pinhole was chosen for optimal use at  $1.6\mu m$  (H band), corresponding to an angular size of  $12 \lambda/D$ . The pinhole is of size  $8.7 \lambda/D$  at  $2.2\mu m$  ( $K_s$  band).

### 5.5.2 Pinhole Size Optimization

With sub-aperture sizes of 0.42 m, the estimate from Section 5.3.3 suggests the optimal pinhole size to be  $D/d_{sub} \approx 12\lambda/D$ . Using the simulation of the Palomar aperture masking experiment described in Section 5.4.2, we can determine the optimal pinhole size under typical observing conditions.

For various pinhole sizes, we simulated one hundred H band images of a 10:1

binary with companion separation 150 mas under typical Palomar observing conditions, without read noise, and with the primary aligned at the center of the pinhole. Images of a single star were simulated to be used as a calibrator. We analyzed these images both with and without a window function, and calculated the R.M.S. residuals of the simulated closure phases fit to a model binary. Figure 5.6 shows these results for each pinhole size (with window function, solid line; without window function, dashed line). For reference, the RMS obtained with no pinhole in place is included as a horizontal line.

The spatial filter performance can be broken into three classes:

- A small pinhole ( $\lesssim 10 \lambda/D$ ) impinges on the field of view, rejecting enough of the light coming from the off-axis companion that the closure phases will not match the model. (See also Section 5.3.3.)
- A very large pinhole ( $\gtrsim 20 \lambda/D$ ) provides very little filtering and the data is statistically similar to the unfiltered case.
- The operational pinhole range (10-20  $\lambda/D$ ) reduces the image to image variation of closure phases and produces data that better fits its model. The range 11-14  $\lambda/D$  is most effective, reducing the fit residuals by roughly 25%.

These results agree with the estimate at the top of this sub-section.

Finally, we note that because the window function itself provides some spatial filtering, the inclusion of the pinhole provides slightly less improvement if compared to the case in which no window function is used.

### 5.5.3 How Important Is Target Placement?

In Section 5.3.3, we showed that the asymmetrical truncation of the target by the pinhole alters the measured closure phases, even in the absence of wavefront errors, an effect we called misalignment error.

Equation 5.2 can be directly integrated to determine the misalignment error when a target is observed through the pinhole. Alternatively, we chose to simulate the effect to more accurately reflect the details of our analysis pipeline. For clarity, we present the R.M.S. closure phase deviation between the pinhole and non-pinhole values with the Palomar 9-hole mask (averaged over the set of 84 closure phases) in Figure 5.7.

By inspection, we see that in H band and at high levels of correction (Strehl  $\gtrsim 40\%$ ), the pinhole introduces less than  $0.3^\circ$  R.M.S. closure phase error at nearly any alignment within the 440 mas diameter pinhole. At a diameter of  $12\lambda/D$ , less than 2% of the total flux resides outside the pinhole and very little aliases back into the baseline frequencies. The misalignment deviation is also insensitive to the orientation of the misalignment; the aperture mask is three-fold symmetric in physical space, but provides a uniform coverage of spatial frequencies. At moderate Strehl ratios, the misalignment deviation increases, but observationally, this increase is balanced by a larger benefit of spatial filtering.

The alignment requirements are tighter in  $K_s$ . Because the pinhole is designed for H band, its size is only  $8.9\lambda/D$  in  $K_s$ . Good positioning is even more important given that AO residuals and closure phase errors are usually smaller. Alignment can introduce up to  $1.0^\circ$  of closure phase errors if misaligned by 200-300 mas, or roughly  $2-3\lambda/D$ .

The presence of a companion adds an additional misalignment error, although this error will be attenuated by the secondary-primary contrast ratio. Therefore, particularly for high contrast binaries, the misalignment errors provided here give good rule-of-thumb indications of how well a target must be positioned within the pinhole. Given that aperture masking observations at Palomar typically yield 1-2 degrees of closure phase, targets must be positioned close to the pinhole center during  $K_s$  band observations.

Finally, we note that the percentage of blocked flux is a weak function of the target alignment, and a strong function of the AO performance and size of the direct imaging halo (Figure 5.2, right panel). In the observations of Section 5.6 which compare pinhole and non-pinhole observations, the percent loss of flux is a measurable quantity. From the results of this plot, it is clear that large flux drops can be attributed to momentary drops in AO performance or very large shifts in alignment. Astrometric jitter on the scale of hundreds of mas is never seen. Practically, if a series of images contains one or a few with large flux drops, and the target was initially well aligned, then identifying large flux drops is a useful proxy for excluding frames taken with poor AO performance.

#### 5.5.4 Window Function: Optimal Size and the Palomar 9-Hole Mask

For our experiment, we use a super-Gaussian function,  $\exp(-kx^4)$ , for its flat-top and quickly tapering Fourier Transform. We describe the window function by the size of its half width at half max,  $w_{pix}$ , measured in pixels on the detector.

The optimal window function size finds the balance between eliminating read

noise and increasing redundancy noise. We present a measure of the effectiveness of various window function sizes in the presence of various levels of read noise in Figure 5.8.

We simulated one hundred images (256 x 256 in size) of a 10:1 binary with companion separation 150 mas and of a calibrator in the same fashion as described in Section 5.5.2 but without a pinhole in place. To each set of images we added gaussian read noise with a per-pixel noise level ranging from 0.2% to 5.0% of the peak intensity. (This corresponds to targets of 7th to 10th magnitude when taking 6 second exposures on the PHARO detector.) The images were processed with window functions of various sizes and we calculated the root mean squared (RMS) residuals of fits to a model binary. In Figure 5.8 we plot the ratio of the measured RMS with a window function to the same set of images without the window function. For all levels of read noise an optimally sized window function improves the model fits. We caution that, because the effect of read noise on closure phases scales with image size, and the choice of default image size is arbitrary, the results can only be evaluated qualitatively.

Several features are apparent.

First, the optimal window function is approximately  $\lambda/d_{sub}$ , or  $\sim 12\lambda/D$  for the Palomar aperture mask, with tighter windows for the high noise cases; one expects the optimal window size to be a function of the aperture mask. This makes qualitative sense: The interferogram image is a set of interference fringes under an Airy function envelope of characteristic size  $\lambda/d_{sub}$ . One would expect the optimal window function to crop out those pixels with signal to noise less than one. Beyond  $\lambda/d_{sub}$ , the intensity of the interferogram drops below a few percent of its peak value, comparable to the read noise.

Second, too small a window function quickly adds redundancy noise into the measurements. This turning point is near  $0.5 \lambda/d_{sub}$ .

Third, even in the absence of read noise, a window function decreases closure phase noise (solid curve). This demonstrates the capacity of the window function to spatial filter the wavefront phase noise, even though the improvement is only about 3-4%.

To emphasize the utility of the window function as a spatial filter of wavefront errors we simulated another set of images in which the wavefront is static over the exposure. With only spatial variation of the wavefront, the window function reduces closure phase errors by nearly 20% (Figure 5.9).

Misaligning the peaks of the window function and interferogram introduces a tiny amount of closure phase error. Even an unrealistic misplacement of  $10\lambda/D$  (about 26 pixels on PHARO at  $1.6\mu m$ ) with a tight window of size  $0.7 \lambda/d_{sub}$  produces an error below  $0.06^\circ$ . This will likely on be relevant for observations taken by space telescopes.

## 5.6 Observations

Between June 2008 and September 2009, we observed twenty-six single star targets and four known binaries spanning infrared magnitudes between 6.0 and 9.0 using the PHARO instrument on the Hale 200" Telescope at Palomar Observatory.

Each aperture masking observation was conducted with and without the pinhole in place to compare the effectiveness and practicality of using the pinhole filter during ground observing. An observing sequence consisted of sets of twenty images

(six second exposures) with the Palomar 9-hole aperture mask in several standard infrared bands. Typically images were taken in a particular band with the pinhole in place, then again with the pinhole removed, until the sequence of bands had been taken. Similar observations of a calibrator were then taken. This was done to minimize changes in seeing between comparison observations and to minimize the effect of instrumental wavefront changes from slewing the telescope on calibration. Care was taken to use identical detector configurations (position, etc) and to align the target center of light at the center of the pinhole. This alignment procedure added approximately two to five minutes additional overhead to each observation set.

The aperture mask, data taking procedure, and custom IDL pipeline to analyze aperture masking images have been previously described by Lloyd et al. (2006), Kraus et al. (2008), and Bernat et al. (2010). The mean and variance of the closure phases and amplitudes were calculated (across the set of images) and calibrated. The calibrated closure phases were found by subtracting the calibrator closure phases from those of the target; their errors were estimated by adding in quadrature the errors of the targets and calibrator. The closure phase signal of a single star is zero; deviations from zero may indicate the presence of a companion or result from wavefront errors. The log-amplitudes are calibrated identically and are included to determine if spatial filtering improves measurement of the amplitudes, but are not used for the analysis of the binary candidates. Companions are located by fitting the closure phase data set with a three parameter binary closure phase model (separation distance, position angle, and contrast ratio) to minimize  $\chi^2$ .

The targets are bright enough that the per-pixel read noise is at or below a few percent. For the analysis that follows, we use the results of Section 5.5.4 and use a

window function with half-width at half-max of  $1.0 \lambda/d_{sub}$  (30.9 pixels in H band, 41.5 in  $K_s$  band).

### 5.6.1 Pinhole Stability and Target Alignment

Images of the pinhole were taken at several periods throughout the run, from which its location on the detector can be measured. The location of the pinhole remained accurate to less than two pixels for the entire run, with the exception of two instances in which the Slit wheel appeared to lodge the pinhole at an alternative location. This was easily repaired by putting the Slit wheel into its 'HOME' position.

Explicit (direct) images of the target within the pinhole were taken only rarely. However, the locations of the interferogram centers provided an accurate location of the binary targets on the detector. Drift of the target was typically less than one-half pixel during a set of twenty images (about two minutes). Comparison of the target and pinhole locations indicate that our alignment was accurate to within four pixels of the measured pinhole center. We conclude that the largest potential source of misalignment error arises from the initial pointing accuracy within the pinhole, and not jitter of the target or pinhole during data taking.

The effect of the pinhole was seen to alter several observables. Most directly, when observing reference stars, the pinhole induced a drop of target flux by roughly 35% in H and 15% in  $K_s$ . The pinhole is located after the adaptive optics system in the focal plane, hence these values reflect the percentage of the direct imaging point spread function which falls outside the pinhole. These percentages are consistent with the pinhole size and the level of AO performance (Strehl ratios of

approximately 10% in H and 30% in  $K_s$ ). Binary targets show a similar drop in flux despite their larger size, which we can take as an indication that their center of light is well aligned.

Simulations and calculations using a sample of direct images show that the percentage of blocked flux is a weak function of the target alignment, and so large flux variations do not indicate a high level of astrometric jitter. Instead, this percentage is a strong function of the AO performance (and size of direct imaging halo). Low transmission (below 40%) well identified individual images blurred by temporary drops in AO correction. High flux transmission well predicted good fits to models (e.g. Figure 5.10).

### **5.6.2 Calibrators: Pinhole Filtering Produces Lower Closure Phase Variance and Higher Amplitudes**

The use of the pinhole generally reduced the variance of closure phases and increased the amplitudes for the observed single stars. These results are compared to a set of simulated observations in Figure 5.11.

The closure phase standard deviation is reduced by 10 and 19 percent in H band ( $1.6\mu m$ ) and  $K_s$  band ( $2.2\mu m$ ), respectively. A larger reduction is expected at the longer wavelength, as the pinhole is relatively smaller and provides more aggressive spatial filtering. Although not displayed, the root mean squared residuals of the data fit to their model values also reduced by 10-20% indicating better calibrated data. The pinhole filtering increases the visibility log-amplitude by 14 and 18 percent on the longest baselines at H band and  $K_s$  band, respectively. Each of these confirm the spatial filter is reducing closure phase noise from sub-aperture

redundancy.

In both cases the simulation predicts a larger reduction in variance, although the results across wavelengths are consistent. The simulation does not include the time-variation of AO residuals during a single exposure, particularly slow tip-tilt correction of the PALAO system (Bloemhof et al., 2001). This can produce several interferograms in a dataset with large closure phase errors which cannot be improved by spatial filtering.

### 5.6.3 Binaries: Lower Closure Phase Variance

We observed four previously characterized binaries with well defined orbits with and without the pinhole in several bandpasses: GJ 164 (Martinache et al., 2009); G 78-28 (Pravdo et al., 2006); GJ 623 (Martinache et al., 2007); and GJ 802B (Ireland et al., 2008). The characterized orbits were used to predict the location of each companion on the observing date using a Monte Carlo simulation to account for the uncertainty of the orbital parameters. Each target was observed to obtain twenty images (six second exposures) in several bandpasses in September 2009. Three of the four known binaries were successfully resolved (Table 5.1). The high contrast companion to GJ 802B could not be resolved at the correct separation and contrast ratio.

GJ 164 was imaged for three sets near dawn with the pinhole and one set without. All but the first sets of data suffered poor AO correction, were visibly less sharp, and had flux levels drop by nearly 75%. The binary could be well resolved in all three sets with the pinhole, but the later sets yield much worse fits and larger systematic errors and are not used in the analysis. The fit parameters

to GJ 164 share a degeneracy with a spurious set of parameters ( $\Delta H = 0.030$ , at nearly the same location), and limit the quality of parameter errors which can be derived from the fit. Instead, the magnitude contrast was held fixed to the values determined by Martinache et al. (2007). The observations of reference stars to calibrate GJ 623 varied in AO correction and quality between pinhole and non-pinhole measurements, and so this target is presented without calibration in order to compare the two performances.

The median closure phase scatter (stochastic errors) decreased for each observation by roughly 20-25%, which indicates that the pinhole operated effectively to minimize closure phase errors from AO residuals. However, the data fits to binary models showed no decrease in R.M.S. residuals, whereas the fits to single star data decreased by 10-20%. Of the eight total measurements, four showed an increase in R.M.S., although only two  $K_s$  band observations increased by more than 10%. The observations which increased in R.M.S. are those in which either the companions was aligned far from the pinhole center, or the companion is comparatively bright. We prefer to discuss this measurement in terms of the amount of unattributed systematic error that needs to be added in quadrature to the stochastic errors to yield the R.M.S. values, i.e.,  $(R.M.S.)^2 = \langle \sigma_\phi^2 + \sigma_{sys}^2 \rangle$ . This is listed in the next to last column of Table 5.1. A systematic component of  $1.0^\circ$  specific to binary targets would account for the discrepancy of performance.

Misalignment of the target within the pinhole contributes to the increased residuals. Because each binary system could be resolved by direct imaging, the targets were aligned with their center of light as close to the pinhole center as could be accurately judged by eye. This necessarily placed each star off-center of the pinhole. The astrometric alignment of each component can be inferred from

the center of the interferograms and is listed in Table 5.3. As discussed earlier, the alignment of the components is determined by the original placement of the observer and moves comparatively little during a set of images.

We simulated each binary with and within the pinhole displaced by the amounts in Table 5.3. The atmospheric seeing was tuned to fit Strehl ratio estimates from direct images taken throughout the night: 40% in  $K_s$  and  $Br\gamma$  bands, 15% in H and  $CH4_s$  bands, and 10% in J band. The astrometric jitter of the simulated images was consistent to those observed (and less than 20 mas per twenty images for most targets). Each simulation produced enough images until all errors reached a steady state; the estimates of the misalignment error are included in the last column of Table 5.1. Additional contributions from misaligned calibrators are not included.

Our calculation of the misalignment error requires knowledge of the absolute positions of the pinhole and target components, and an accurate measure of the point spread function. Given the small jitter of targets, our calculation is limited by imperfect knowledge of the point spread function. Even still, the quality of correction can fluctuate in timescales of minutes, as can be observed by viewing successive direct images or other observables such as pinhole transmission (Figure 5.10). Given these assumptions, misalignment contributes systematic components of  $0.4\text{-}0.8^\circ$  to the H and  $K_s$  band binary observations. We also note that simulations demonstrate large  $\gtrsim 1.0^\circ$  alignment errors for slightly lower Strehl ratios ( $\lesssim 10\%$  in H and  $\lesssim 20\%$  in  $K_s$ ). These challenges instead warrant the development of an observing strategy to calibrate alignment errors empirically.

The binary parameters measured with and without the pinhole, and those predicted by the system orbits, are in good agreement. In each case, the spatial filter data fit to slightly higher contrasts ratios ( $\approx 5\%$ ). This may indicate that the

Table 5.1: Observation of Known Binaries With and Without Spatial Filter

Binary	Band	Separation (mas)	Pos. Ang. (deg)	Contrast $\Delta$ Mag	Best Fit R.M.S (°)	Median $\sigma_\phi$ (°)	Cal	Est'd $\phi_{sys}$ (°)	Est'd $\sigma_{align}$ (°)
GJ 164	H	$48.7 \pm 1.9$	$346.5 \pm 1.7$	$d$	4.03	2.11	Y	3.4	
	H (SPF)	$48.8 \pm 1.5$	$343.9 \pm 0.9$	$d$	3.33	1.99	Y	2.7	0.61
	Predicted <sup>a</sup>	$49.4 \pm 2.2$	$348.1 \pm 10.1$	$1.835 \pm 0.006$					
	K <sub>s</sub>	$46.8 \pm 1.2$	$340.3 \pm 1.0$	$d$	3.46	1.20	Y	3.2	
	K <sub>s</sub> (SPF)	$46.3 \pm 0.7$	$341.2 \pm 1.2$	$d$	2.16	0.70	Y	2.9	0.42
	Predicted <sup>a</sup>	$49.4 \pm 2.2$	$348.1 \pm 10.1$	$1.721 \pm 0.097$					
G 78-28	H	$101.7 \pm 0.3$	$359.2 \pm 0.2$	$1.275 \pm 0.010$	2.78	1.16	Y	2.5	
	H (SPF)	$102.6 \pm 1.4$	$359.6 \pm 0.2$	$1.323 \pm 0.015$	3.00	1.09	Y	2.8	0.68
	Predicted <sup>b</sup>	$105.0 \pm 5.7$	$359.3 \pm 1.8$	$1.24 \pm 0.07$					
	K <sub>s</sub>	$103.4 \pm 0.3$	$359.0 \pm 0.1$	$1.221 \pm 0.007$	2.68	0.72	Y	2.6	
	K <sub>s</sub> (SPF)	$104.5 \pm 0.2$	$359.3 \pm 0.1$	$1.221 \pm 0.005$	3.60	0.56	Y	3.6	0.75
	Predicted <sup>b</sup>	$105.0 \pm 5.7$	$359.3 \pm 1.8$	$1.14 \pm 0.06$					
	J	$101.4 \pm 0.6$	$358.7 \pm 1.3$	$1.257 \pm 0.021$	7.60	3.12	Y	6.9	
	J (SPF)	$100.8 \pm 0.6$	$358.5 \pm 0.2$	$1.263 \pm 0.011$	5.80	2.55	Y	5.2	0.24
	Predicted <sup>b</sup>	$105.0 \pm 5.7$	$359.3 \pm 1.8$	$1.24 \pm 0.07$					
GJ 623	CH4 <sub>s</sub>	$282.3 \pm 1.4$	$176.3 \pm 0.4$	$2.798 \pm 0.050$	3.38	1.90	N	2.8	
	CH4 <sub>s</sub> (SPF)	$277.3 \pm 3.0$	$176.2 \pm 0.2$	$2.829 \pm 0.51$	3.43	1.65	N	3.0	0.75
	Predicted <sup>c</sup>	$279.1 \pm 1.2$	$177.4 \pm 0.7$	$2.860 \pm 0.039$					
	K <sub>s</sub>	$277.1 \pm 0.4$	$176.5 \pm 0.1$	$2.675 \pm 0.014$	2.35	0.45	N	2.3	
	K <sub>s</sub> (SPF)	$280.7 \pm 0.2$	$176.6 \pm 0.7$	$2.780 \pm 0.10$	1.9	0.30	N	1.9	0.46
	Predicted <sup>c</sup>	$279.1 \pm 1.2$	$177.4 \pm 0.7$	$2.720 \pm 0.014$					
	Br $\gamma$	$279.1 \pm 0.3$	$176.2 \pm 0.7$	$2.664 \pm 0.012$	0.94	0.42	N	0.8	
	Br $\gamma$ (SPF)	$279.4 \pm 0.4$	$176.5 \pm 0.1$	$2.778 \pm 0.009$	1.28	0.33	N	1.2	0.63
	Predicted <sup>c</sup>	$279.1 \pm 1.2$	$177.4 \pm 0.7$	$2.720 \pm 0.014$					

Measurements of three known binary systems with and without the pinhole filter (SPF). <sup>a</sup>Spatial filtering reduces the median scatter of closure phase measurements in all cases. <sup>b</sup>The median residual between the data and best fitting model does not increase when using the pinhole. <sup>c</sup>An estimate of the systematic error due to a misalignment of 3 pixels. See text for discussion. Note: Target GJ 802 is excluded from this table.

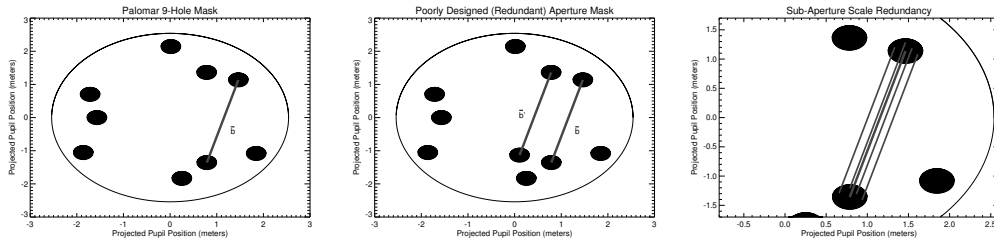
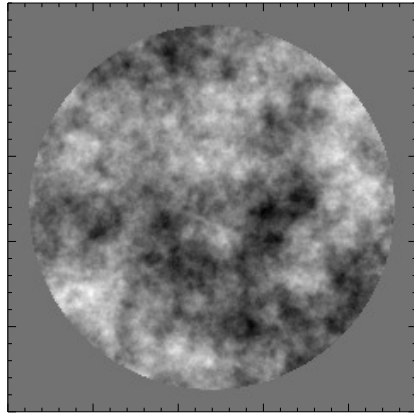


Figure 5.1: Aperture masks are designed to be non-redundant, but some redundancy persists because of the finite sub-aperture size. (Left) The Palomar 9-hole Mask. Each pair of sub-apertures acts as an interferometer. (Center) A redundant mask. Two pairs of sub-apertures transmit the same baseline. As a result, the baseline carries redundancy noise into its closure phase. (Right) Because of the finite hole size, every baseline is redundant on sub-aperture scales. Spatially filtering the wavefront smooths the wavefront phase, reducing noise from the sub-aperture redundancy.

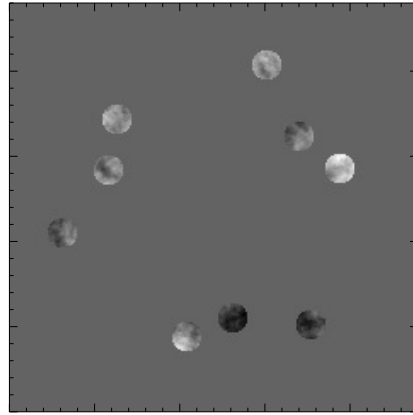
Table 5.2: Astrometry and Alignment of Targets within Pinhole

Binary	Band	Distance From Center (mas)		Est'd
		Primary	Secondary	$\sigma_{align}$
GJ 164	H	$90 \pm 50$ (60)	$140 \pm 50$ (60)	0.61
	$K_s$	$50 \pm 15$ (40)	$90 \pm 15$ (40)	0.42
G 78-28	H	$90 \pm 35$ (50)	$110 \pm 35$ (50)	0.68
	$K_s$	$80 \pm 10$ (40)	$70 \pm 10$ (40)	0.75
	J	$100 \pm 25$ (45)	$170 \pm 23$ (45)	0.24
GJ 623	$CH4_s$	$130 \pm 10$ (35)	$200 \pm 10$ (35)	0.75
	$K_s$	$90 \pm 10$ (40)	$200 \pm 10$ (40)	0.46
	$Br\gamma$	$150 \pm 10$ (40)	$190 \pm 10$ (40)	0.63

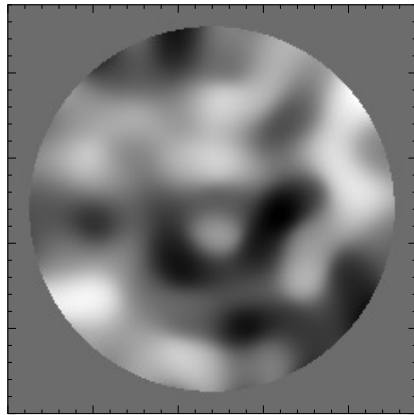
Table 5.3: Alignment of Targets Within Pinhole and Estimated Closure Phase Misalignment Error. Position determined by center of interferograms, errors estimated from spread over twenty images. Values in parentheses include 40 mas uncertainty of the absolute pinhole position. Misalignment errors are calculated using the simulation of Section 5.5.3, assuming a Strehl of 15% in H and  $CH4_s$ , 45% in  $K_s$  and  $Br\gamma$ , and 10% in J band.



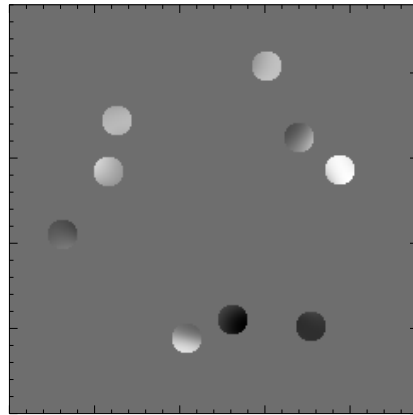
(a) AO Corrected Phase



(b) Overlay of Aperture Mask



(c) AO + Spatial Filter Phase



(d) Overlay of Aperture Mask

Figure 5.2: Effect of the pinhole filter on sub-aperture scale phase variation. a) AO corrected wavefront phase. Small scale spatial inhomogeneities are apparent. b) The AO corrected wavefront with an overlay of the aperture mask. Notice that the wavefront phase is inhomogeneous within the sub-aperture. c) AO corrected wavefront after spatial filtering. The small scale features are smoothed out; the wavefront exhibits structure with a characteristic scale close to that of the sub-apertures. d) Within each sub-aperture, the spatially filtered phase is much more uniform.

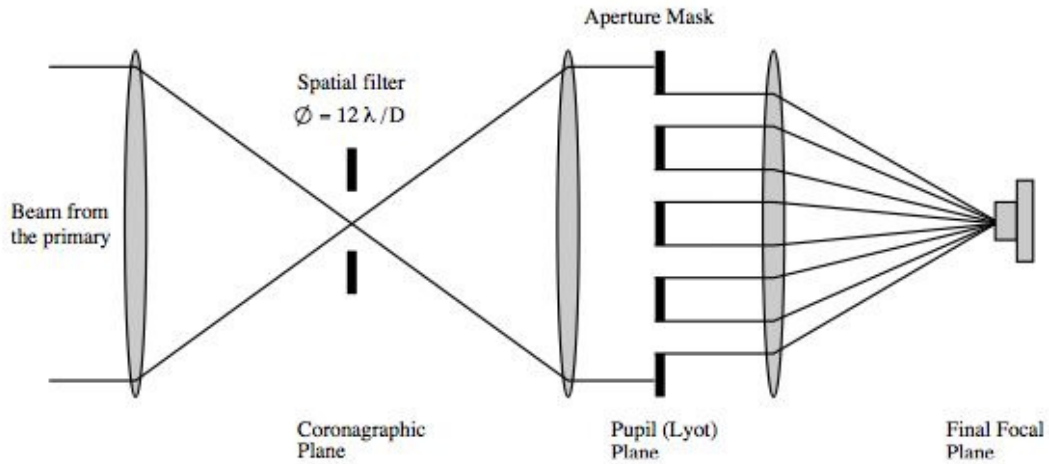


Figure 5.3: Optical setup for pinhole filtered aperture masking interferometry at Palomar. One takes advantage of the coronagraphic capabilities of PHARO by inserting the aperture mask in the Lyot wheel and the spatial filter in the Slit wheel.

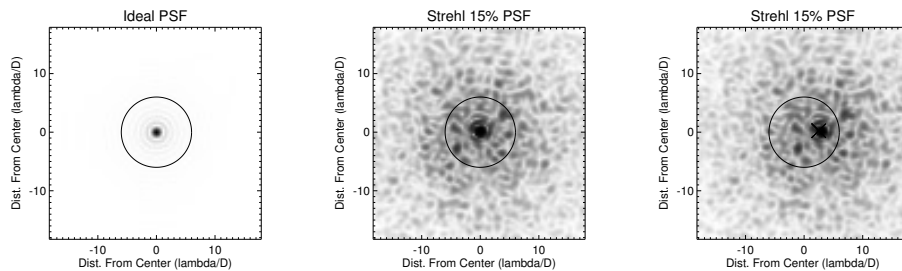


Figure 5.4: Imaging An Unresolved Targets Through a Pinhole. The point spread function of three targets is shown with a pinhole of size  $6\lambda/D$  overlaid. Square root contrast scaling is used to highlight the truncated flux. (Left) The pinhole, located in an image plane, truncated the portion of electric field which forms the outer rings of the point spread function. In perfect seeing, the total flux blocked is very low. (Center) Wavefront errors disperse flux outward creating a diffuse halo around the target. The blocked flux increases, and more power aliases back into sub-aperture scales, resulting in closure phase errors. (Right) When asymmetrically truncated, the center of light shifts towards the pinhole center (black x). Each component of a binary is truncated differently, leading to errors in astrometry or contrast.

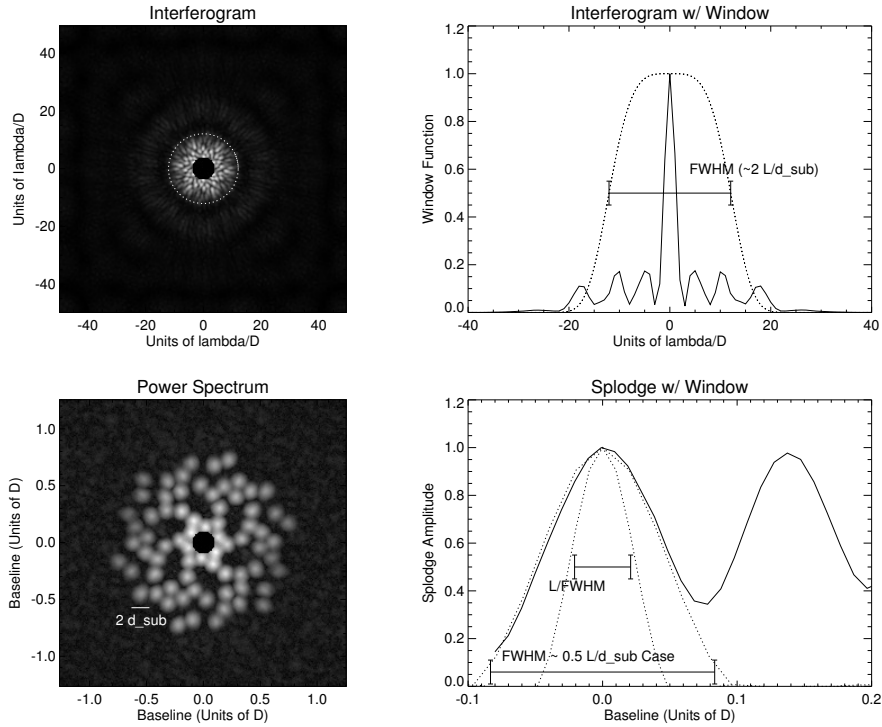


Figure 5.5: Effect of a Window Function. (Top Left) The aperture mask produces a set of interference fringes beneath an envelope of size  $\lambda/d_{sub}$ , as seen in this Palomar 9-hole masking image. The central peak has been zeroed to highlight the envelope and outer rings. The radius of the white ring is  $\lambda/d_{sub}$ . (Bottom Left) The power spectrum of the same interferogram, presented in units of baseline/D rather than spatial frequency. Each island of transmitted power (or *splodge*) is of size  $2d_{sub}$ . This is expected, as the transmission function is related to the autocorrelation of the mask. (Top Right) Using a window function of characteristic HWHM  $\lambda/d_{sub}$  (here, a super-Gaussian) removes the interferogram wings and its associated read and wavefront noise. (Bottom Right) The window function produces a convolution kernel of size  $\lambda/2\text{HWHM}$ . Notice that a window function larger than  $0.5 \lambda/d_{sub}$  creates a kernel larger than  $2d_{sub}$  and mixes neighboring splodges, adding redundancy noise. (see text)

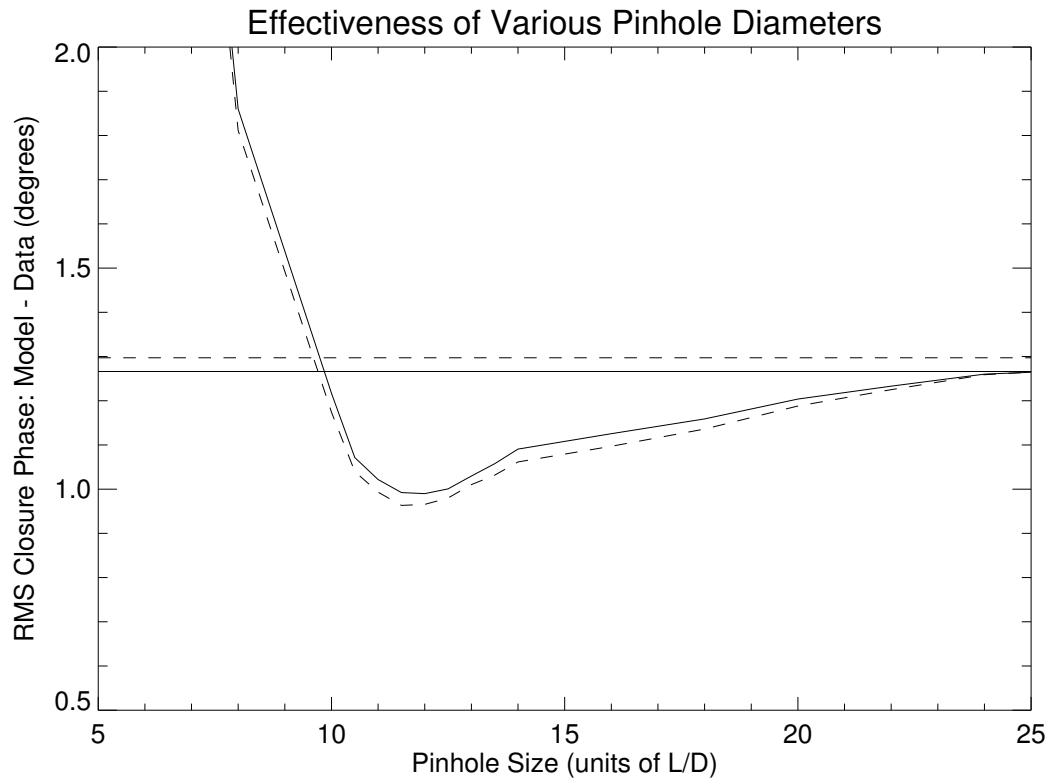


Figure 5.6: The RMS fit residuals of simulated data (H-band, no read noise) with pinholes of various size, analyzed with (solid line) and without (dashed line) a window function. The horizontal line is the measurement level without any pinhole in place. The pinhole filter is most effective within the range 11-14  $\lambda/D$ .

companion flux was skewed closer to the pinhole edge and its flux truncated by a few percent more, which is consistent with the measured locations of the objects within the pinhole (Table 5.3). No bias was found in the relative astrometry.

Binary parameter errors decrease in proportional to the closure phase errors, and indicate that one can use a pinhole to measure binary parameters more precisely. Detection contrast also scales with closure phase errors, and indicate pinhole measurements can provide an increase of contrast by 20-25%. However, it must be noted that our practice of scaling the closure phase errors until the  $\chi^2$  of the best fit is unity, because the data residuals did not improve, will partially counteract the other gains in precision.

## 5.7 Summary of Results and Conclusions

In this text, we discussed spatial wavefront variation on the scale of NRM sub-apertures, which contributes to closure phase errors we called sub-aperture redundancy noise. We proposed that quasi-static wavefront errors on the scale of the sub-aperture, which evolve over hundreds of seconds or with telescope movement, give rise to the limitations of aperture masking calibration. Through simulations and direct observation we have shown that the use of a pinhole filter effectively reduces sub-aperture spatial variation and can reduce closure phase errors, increase visibility amplitudes, and lead to better calibration and higher detection contrasts.

With a simple premise, we estimate the optimal pinhole size to be  $d_{spf} \approx D/d_{sub}$  in units of  $\lambda/D$ , or about  $12\lambda/D$  for the Palomar 9-hole mask. We confirm this result using a detailed simulation of the Palomar aperture masking experiment and show that the operational pinhole size ranges from 11 to  $14\lambda/D$ . Smaller pinholes

reject enough light from off-axis companions to alter the measured closure phases. Larger pinholes provide little spatial filtering.

Because the pinhole is not a perfect low-pass filter, the truncation of off-axis targets aliases power back into phase at sub-aperture scales. This introduces closure phase errors of its own, both systematic and stochastic. Using simulated observations over a wide range of correction (Strehl ratio of 10-100%), we show that a misalignment of the target by 200 mas introduces 0.3-1.0° degrees of systematic closure phase, which we have termed misalignment error. We propose several methods for the calibration of this component although none are undertaken in this experiment. As a result, the effectiveness of pinhole technique is limited by the accuracy with which targets can be aligned within the center of the pinhole.

We installed a pinhole of size 0.779 arcsec ( $12\lambda/D$  at  $1.6\mu m$ ) in the Slit wheel focal plane of the PHARO instrument on the Hale 200" Telescope at Palomar Observatory. Using this pinhole we observed twenty single unresolved stars and three well characterized binaries with and without the pinhole in a selection of standard near infrared bands. The AO system provided moderate correction: Strehl  $\sim$ 5-15% in H band and  $\sim$ 20-40% in  $K_s$  band.

Observations of unresolved stars showed that the pinhole reduced the stochastic variation of closure phases by 10-25% from one image to the next, and visibility amplitudes increased. R.M.S. residuals to model fits decreased by a similar factor. Each shows that increasing sub-aperture coherence decreases closure phase redundancy noise. Lower fit residuals indicate that calibration improved, and that the aperture masking calibration limit is partially attributable to small scale quasi-static wavefront errors. Furthermore, detection contrasts scales proportional to fit residuals, indicating an increase in detection contrast of 10-25%.

The modest increase in closure phase signal to noise when the pinhole is used suggests that the spectrum of wavefront errors contains relatively little power on the smallest spatial-scales within the sub-aperture. Additionally, the smallest scale variations which cycle multiple times within a single sub-aperture tend to produce redundancy noise that averages out. The leading source of spatial redundancy noise, both quasi-static instrumental and residual atmospheric wavefront errors, is more likely low-order Zernike modes (i.e, 'phase slopes') across the sub-apertures. Section 5.10 presents a more detailed derivation of sub-aperture spatial redundancy in terms of the spatial structure of the sub-aperture wavefront.

Simulations of these observations, when compared, predict a slightly larger benefit from the pinhole filtering. As discussed in Section 5.3.2, temporal variations of the baseline phase within a single exposure leads to a sort of temporal redundancy noise which cannot be removed by closure phases of the pinhole filter. Furthermore, the slow response of the Palomar AO tip-tilt mirror (5 Hz) gives rise to full aperture scale wavefront residuals which evolve on the order of a fraction of an exposure. The baseline phase changes these residuals induce contribute to the overall variation of the closure phases from one image to the next (though not calibration errors). The simulation did not include temporal variations of the AO residuals, and as a result gives the impression that the pinhole is more effective at reducing stochastic closure phase noise (50% vs. 20%). Indeed, these results imply that temporal variation of the wavefront phase is a large source of closure phase variance with the current PALAO system.

We observed three well characterized binary systems to determine how the pinhole influences the astrometric and photometric characterizations of discovered systems. The measured binary parameters were consistent with those acquired

without the pinhole, and those predicted by the measured orbital parameters of the system. No bias was found in the astrometry (i.e., binaries did not tend towards shorter separations with the pinhole), however contrast ratios with the pinhole tended to be a few percent fainter. Our alignment technique placed the system center of light near the pinhole center, and the light of the companion is preferentially blocked by this arrangement. Better positioning of the target would likely remedy this bias.

Although closure phase stochastic errors decreased by 20-25%, binary data acquired with the pinhole provided no better fits to data, and suggest that binary targets observed with the pinhole contain an additional  $1.0^\circ$  systematic error. After simulating these observations with and without the pinhole, we conclude that the systematic component arises from the off-center alignment of a resolved target. Simulations demonstrate large  $\gtrsim 1.0^\circ$  alignment errors at low Strehl ratios ( $\lesssim 10\%$  in H band and  $\lesssim 20\%$  in  $K_s$ ).

Binary parameter errors and detection contrast both decrease in proportion to the closure phase errors, and indicate that one can achieve more precisely measured binary parameters and higher contrasts (20-25%) with the pinhole. However, our practice of scaling closure phase errors to account for data residuals will partially counteract the other gains in precision and requires calibration of the misalignment error in the high contrast or high precision regime.

Finally, we showed that multiplying the images by an apodized window function acts to reduce the effects of wavefront error similar to a spatial filter. We found that the optimal window function has a half-width at half-max of about  $\lambda/d_{sub}$ , with smaller window functions favored for targets in which read noise is higher.

## 5.8 Discussion

### 5.8.1 A Strategy for Future Pinhole Observations

In light of this investigation, the pinhole can prove effective in two scenarios. When seeing or correction is poor, and closure phase observations do not reach the calibration limit, a pinhole filter will clearly provide higher signal to noise closure phases and more efficient data taking.

At the other extreme, the pinhole may be valuable for improving very-high Strehl ratio ( $\gtrsim 80\%$ ) observations with extreme-AO systems. The high spatial frequencies filtered by the pinhole contribute a larger proportion of the overall wavefront errors in this scenario. The pinhole could be optimally tuned to the AO actuator size, much larger, and alignment requirements would be substantially relaxed. Most importantly, the aliasing of high spatial frequency content into sub-aperture scale phase errors is a higher order effect of the wavefront (Poyneer & Macintosh, 2004). At very high levels of correction, the aliased power is a smaller component of closure phase errors.

We can arrive at a rough estimate of a pinhole performance on extreme-AO systems by simulating a higher-order AO system, such as the 3368-actuator Palomar 3000 system (P3K, Dekany et al. (2007)). As mentioned earlier, our simulation does not account for the sluggish tip-tilt correct of the current Palomar system and over predicted the pinhole performance as a result. The P3K system will have upgraded response by using the current 241 actuator system to perform low-order correction, and thus provide more stable correction. Using the specifications of this system, we simulated a 10:1 binary separated by 150 mas in H band under

typical conditions (c.f., Section 5.5.2). A pinhole of size  $12\lambda/D$  decreased stochastic closure phase errors to 20% nominal values, i.e., a fivefold increase in signal to noise. When compared to our simulations of the current AO system (a twofold increase), the pinhole can impact extreme-AO observations favorably.

For very-high Strehl ratio observations, misalignment error will be lower and less sensitive to changes in correction ( $0.19^\circ$  in this example). Empirically calibrating misalignment by observing a reference star at the same position as the primary is only a partial solution (as it does not take into account the companion), likely limited by the pointing accuracy of the observer, and decreases the overall efficiency of the observations. Instead, dithering the center of light around the pinhole center will likely be an effective way to minimize this systematic component. Using diametrically opposed target placements successfully reduced the misalignment component to  $0.11^\circ$  in simulation, a reduction of nearly half.

Finally, one must also consider the optimal pinhole size to survey across the near infrared bands. For example, if the effective range of pinhole sizes is narrow enough (e.g., 11-14  $\lambda/D$  for this experiment) a single pinhole may not accommodate multiple wide band infrared filters. In those cases, multiple pinholes tuned to specific observation bands will be most effective.

### 5.8.2 Extreme-AO Aperture Masking Experiments

Next generation adaptive optics systems with aperture masks, such as Palomar 3000 (Dekany et al., 2007) and Gemini Planet Imager (Macintosh et al., 2008), provide actuator densities high enough to correct wavefront errors on sub-aperture scales. Design and optimization of these aperture masking experiments which bal-

ance sub-aperture size and number against adaptive optics correction and the limitations of systematics requires a more detailed understanding of how sub-aperture wavefront errors impact closure phases, and where resources should be focused. This work provides one such investigation, and Section 5.10 presents a formalism for this optimization. Extreme-AO systems are anticipated to provide highly stable correction down to scales of 8 cm and thus may motivate smaller and additional sub-apertures, providing more spatial frequency coverage and resolution. This balance will depend on the spatial and temporal power spectra of the corrected wavefront residuals, and this data should be accumulated.

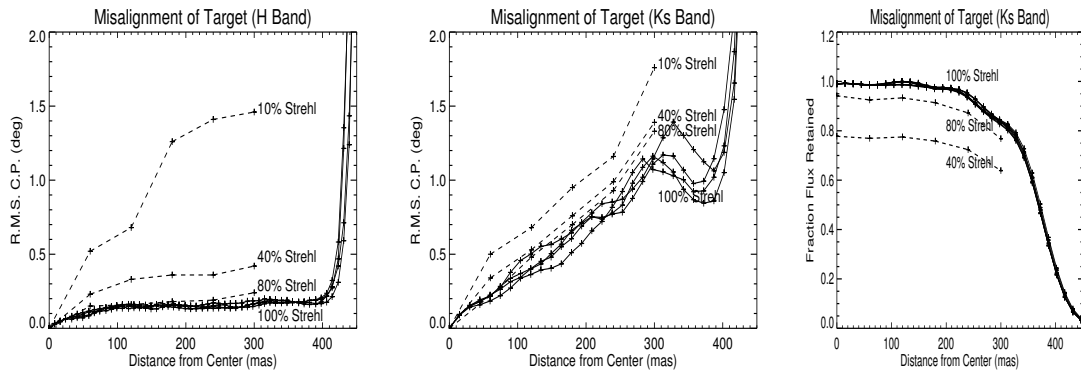


Figure 5.7: Misalignment of a single star within the pinhole introduces closure phase errors. (a) The Palomar 9-hole mask, overlaid with three closure triangles for which the misalignment errors are calculated. (b) Error due to misalignment at  $1.6 \mu\text{m}$  (H band) as a function of target distance from the pinhole center. (Several azimuthal orientations are plotted for each separation.) (c) Closure phase errors at  $2.2 \mu\text{m}$  ( $K_s$  band), in which the pinhole is smaller. In both cases, errors in visibility amplitude errors below .005 for the same ranges.

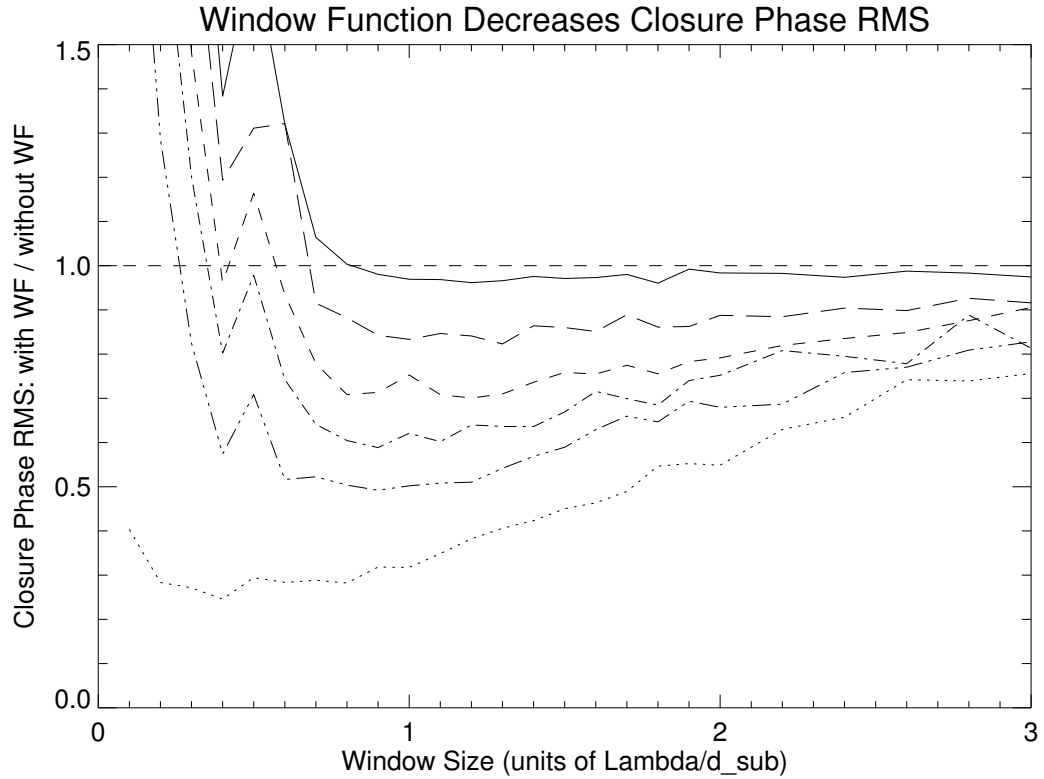


Figure 5.8: Window functions reduce closure phase error from read noise. These curves, from top to bottom, display the reduction in RMS closure phase error when read noise is 0% (top, solid), 0.2%, 0.4%, 0.6%, 1.0%, and 5.0% (bottom, dotted) of the peak image intensity. The optimal window function is typically of size  $\sim \lambda/d_{sub}$ , or  $\sim 12\lambda/D$  for the Palomar aperture mask, with higher read noise favoring tighter window functions. Smaller window functions quickly add large amounts of redundancy noise. (See text.) Note: Even with no read noise (solid curve), a window function reduces closure phase errors, indicating that the window function provides an effect similar to spatially filtering the wavefront.

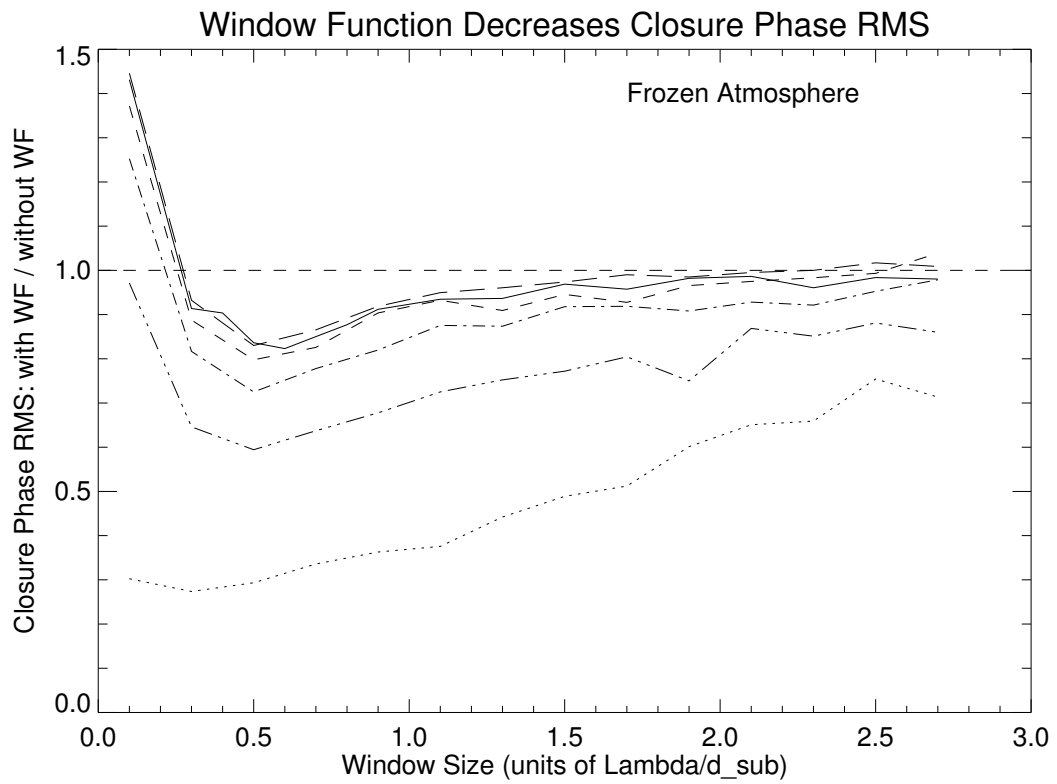


Figure 5.9: Curves showing the effectiveness of the window function as in Figure 5.8, except the wavefront is static over an exposure. Most notably, a window function provides better spatial filtering when the wavefront is static (solid line).

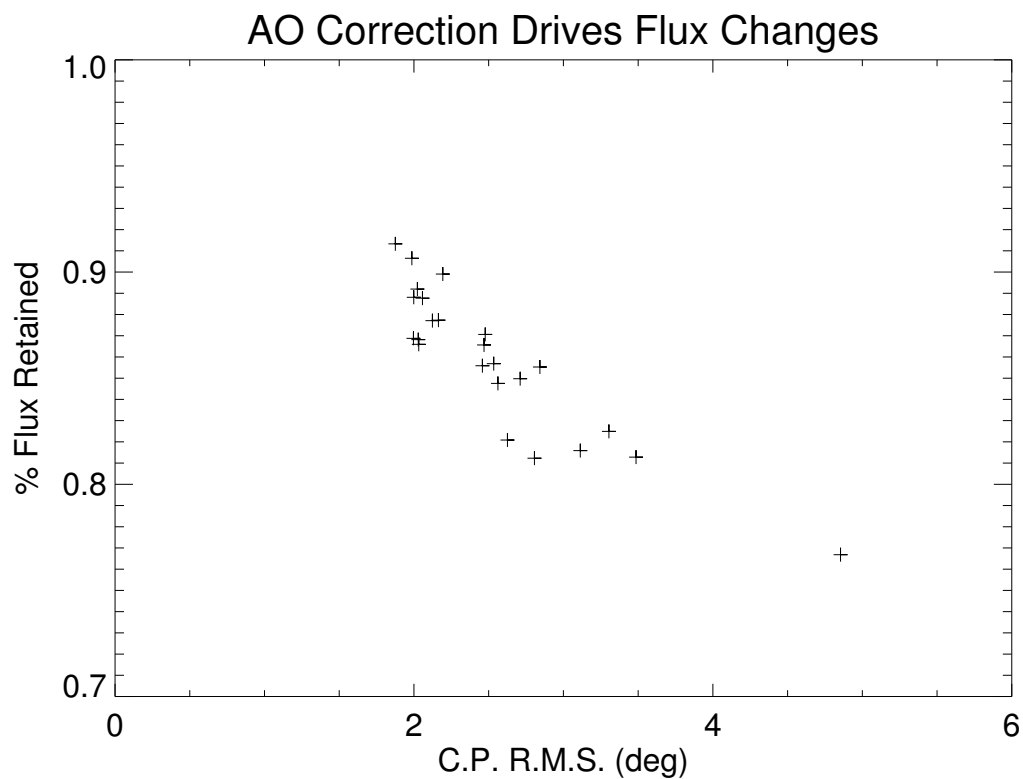


Figure 5.10: Drops in flux transmission through the pinhole are driven by changes in AO performance. The binary GJ 623 was resolved in  $K_s$  using twenty five masking images through the pinhole. The images which produced the best fitting closure phases (as measured by R.M.S. deviation from the model) also had the least flux blocked by the mask. Poor correction displaces more flux into the outer halo of the PSF, which is then blocked by the pinhole. Poor correction also leads to larger closure phase errors. This trend is not caused by misalignment or movement of the target within the pinhole (see text), but rather changes in AO correction.

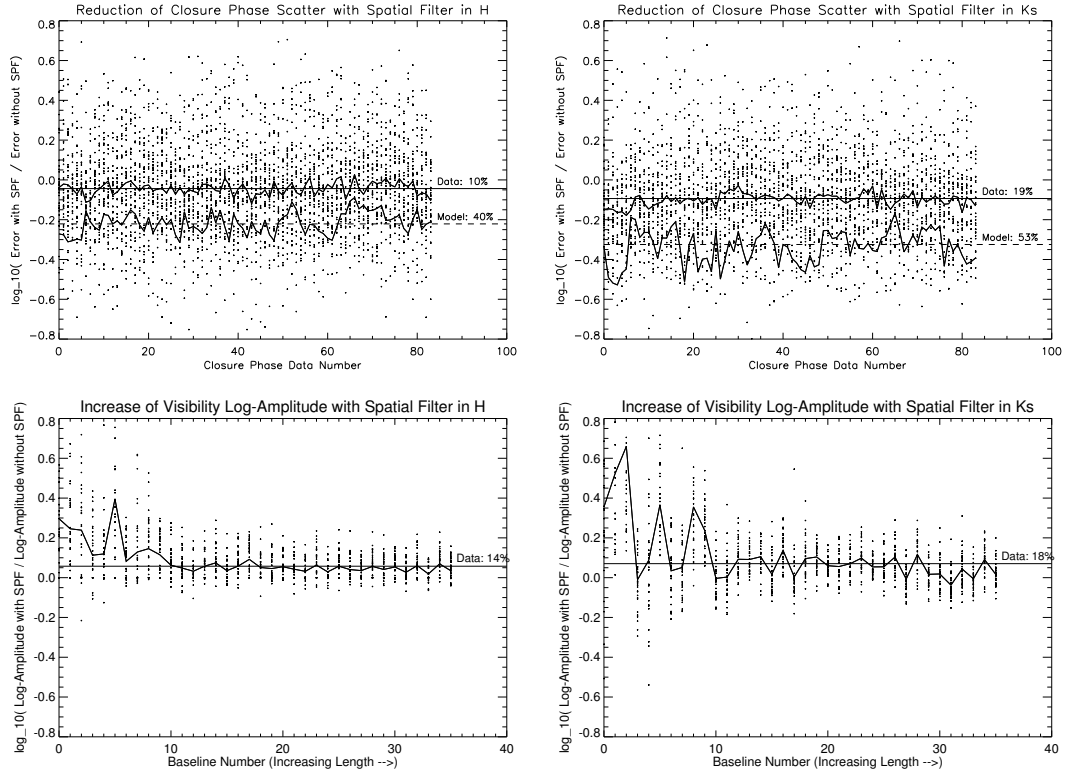


Figure 5.11: Closure phase standard deviation (scatter) is reduced and baseline visibility amplitude is increased when observed through the pinhole filter. Data points are drawn from observations of 26 single stars. Horizontal lines are the median of the data (solid) and the simulated experiment (dashed). (Top Row) Closure phase scatter is reduced by 10 and 19 percent in H and K<sub>s</sub> band measurements, respectively. (Bottom Row) Visibility amplitude is increased by 14 and 18 percent in H and K<sub>s</sub> bands, respectively. In all cases, the simulation (model) predicts a larger reduction in noise (see Discussion).

## ACKNOWLEDGEMENTS

We thank the staff and telescope operators of Palomar Observatory for their support and many nights of assistance at the Hale Telescope. The authors appreciate the effort of the reviewers, who provided valuable advice on the clarity and depth of this text. This material is based upon work supported by the National Science Foundation under Grant No. AST-0705085. The Hale Telescope at Palomar Observatory is operated as part of a collaborative agreement between Caltech, JPL, and Cornell University. This publication makes use of data products from the Two Micron All Sky Survey, which is a joint project of the University of Massachusetts and the Infrared Processing and Analysis Center/California Institute of Technology, and is funded by the National Aeronautics and Space Administration and the National Science Foundation.

### 5.9 Pinhole Filtering: Inteferometry

Observing through a pinhole alters the measured complex visibility of a point source even in the absence of any wavefront aberrations. This analysis assumes that the Fraunhofer approximation applies, i.e., that the electric field in the image plane is the Fourier Transform of the phasor of the wavefront phase in the pupil frame. We assume no wavefront aberrations, including those from optical errors and central obscurations.

The optical path is shown in Figure 5.3. We denote the electric field at the telescope aperture with the subscript  $a$  and the electric field after spatially filtering with the subscript  $spf$ . The coordinates in the image plane are  $\vec{\theta}$ ; all angles are measured in units of  $\lambda/D$ . We assume the pinhole has angular diameter  $d_{spf}$  and

is positioned at  $\vec{\theta} = 0$ . The point source is located at an angular position  $\vec{\alpha}$  on the sky and  $\vec{\alpha} = 0$  corresponds to perfect alignment of the source in the pinhole.

The wavefront phasor at the entrance of the aperture is:

$$E_a(\vec{x}) = \Pi(\vec{x}/D)e^{2\pi i\vec{\alpha}\cdot\vec{x}/D}, \text{ with } \begin{cases} \Pi(\vec{x}/D) = 1 & \text{for } |\vec{x}/D| < \frac{1}{2}, \\ \Pi(\vec{x}/D) = 0 & \text{elsewhere.} \end{cases} \quad (5.5)$$

The optics of the spatial filter truncate the electric field in the focal plane, which results in a convolution when the field is transformed back at a pupil plane. The spatially filtered electric field is then:

$$E_{spf}(\vec{x}) = [\Pi(\vec{x}/D)e^{2\pi i\vec{\alpha}\cdot\vec{x}/D}] \star \left[ \frac{2J_1(\pi\vec{x}d_{spf}/D)}{(\pi\vec{x}d_{spf}/D)} \right], \quad (5.6)$$

where the star represents convolution.

The use of an aperture mask,  $M(\vec{x})$ , containing a baseline  $\vec{b}$  ultimately measures the spatial frequency  $\vec{u} = \vec{b}/\lambda$  of the complex visibility. For clarity, we present this as a function of baseline:

$$V(\vec{b}) = \int d\vec{x} \left[ M(\vec{x})M^*(\vec{x} + \vec{b}) \right] \left[ E(\vec{x})E^*(\vec{x} + \vec{b}) \right], \quad (5.7)$$

where  $E(\vec{x})$  is the electric field sampled by the mask.

Without the spatial filter, substitution for the field from Equation 5.5 gives

$$V(\vec{b}) = T(\vec{b})e^{2\pi i\vec{\alpha}\cdot\vec{b}/D}, \text{ with } T(\vec{b}) = \int d\vec{x} M(\vec{x})M^*(\vec{x} + \vec{b}). \quad (5.8)$$

With the spatial filter, the aperture mask samples  $E_{spf}(\vec{x})$  of Equation 5.6. By

recognizing that convolution with  $e^{2\pi i \vec{\alpha} \cdot \vec{x}/D}$  leads to a Fourier Transform, doing so before substitution yields:

$$V_{spf}(\vec{b}) = T(\vec{b}) \int d\vec{\theta} \Pi[\vec{\theta}/d_{spf}] \times e^{2\pi i \vec{\theta} \cdot \vec{b}/D} \times \left[ \frac{2J_1(\pi|\vec{\theta} - \vec{\alpha}|)}{\pi|\vec{\theta} - \vec{\alpha}|} \right]^2 \quad (5.9)$$

In the limit of an infinite pinhole, the integral converges to the value  $T(\vec{b})e^{2\pi i \vec{\alpha} \cdot \vec{b}/D}$ .

We can extend use this approach to include arbitrary pupil-plane phase errors which arise prior to propagation through the pinhole system. In the presence of inhomogeneous phase in the pupil plane,  $e^{i\phi(x)}$ , Equation 5.6 becomes

$$E_{spf}(\vec{x}) = [\Pi(\vec{x}/D)e^{2\pi i \vec{\alpha} \cdot \vec{x}/D} e^{i\phi(\vec{x})}] \star \left[ \frac{2J_1(\pi \vec{x} d_{spf}/D)}{(\pi \vec{x} d_{spf}/D)} \right], \quad (5.10)$$

Repeating the steps above, the complex visibility is written as:

$$V_{spf}(\vec{b}) = T(\vec{b}) \int d\vec{\theta} \Pi[\vec{\theta}/d_{spf}] \times e^{2\pi i \vec{\theta} \cdot \vec{b}/D} \times PSF[\vec{\theta} - \vec{\alpha}], \quad (5.11)$$

with

$$PSF[\vec{\theta}] = \left| \int d\vec{x} e^{2\pi i \vec{\theta} \cdot \vec{x}/D} \Pi(\vec{x}/D) e^{i\phi(\vec{x})} \right|^2. \quad (5.12)$$

## 5.10 Spatial Structure of Closure Phase Redundancy Noise

Within this work it has been stated that non-zero closure phases can be introduced by sub-aperture phase inhomogeneities, and that producing a more coherent phase across a sub-aperture will lead to better measurements. While this statement has been studied at length for the seeing limited case (see, e.g., Readhead et al. (1988) and Nakajima et al. (1989)), no approach has been put forward tailored for NRM observations with adaptive optics.

Spatially filtering the smallest scale structure of wavefront inhomogeneities is one approach for producing a more coherent sub-aperture wavefront. Next generation adaptive optics systems, such as Palomar 3000 and Gemini Planet Imager, provide actuator densities high enough to correct wavefront errors on sub-aperture scales. Additionally, pupil-reimaging techniques, such as Serabyn et al. (2006) have successfully concentrated the set of actuators onto a subset of the pupil, thus providing increased actuator densities and achieving very high Strehl ratios ( $\gtrsim 92\%$ ) with conventional adaptive optics systems on a smaller aperture. Sparse NRM techniques generally cover less than 10% of the full aperture; one can conceive of future experiments which concentrate adaptive optics correction to sub-aperture wavefront modes.

Design and optimization of new aperture masking experiments, which balance sub-aperture size and number against adaptive optice correction and the limitations of systematics, requires a more detailed understanding of how sub-aperture wavefront errors impact closure phases, and where resources should be focused.

This section presents a formalism for this optimization, and establishes redundancy noise in the semi-coherent sub-aperture case. We also find that decomposing the sub-aperture wavefronts in Zernike modes is convenient for accommodating the conventions used in adaptive optics.

## **Zernike Modes**

By describing the inhomogeneities of a static wavefront with Zernike modes, we will investigate the spatial noise sources of aperture masking interferometry and show that the primary noise source for closure phases comes from only the structure of the wavefront within the sub-aperture.

A static wavefront can be decomposed into Zernike modes,  $Z_n^m(x)$ , a set of orthonormal functions which naturally describe perturbations to spherical wavefronts. The polynomials are defined on a unit circle, and must be scaled to fit the aperture. We use the definitions of Noll (1976) which normalize the polynomials such that they are orthonormal, i.e.,

$$\int d^2x Z_0^0(x) = 1 \quad (5.13)$$

$$\int d^2x Z_{\neq 0}^m(x) = 0 \quad (5.14)$$

$$\int d^2x Z_n^m(x) Z_r^s(x) = \delta_{nr} \delta_{ms} \quad (5.15)$$

Although Kolmogorov turbulence distributes power into even very high order Zernike modes, most of the power falls into the low order modes. To facilitate discussion of these modes, we present their names:  $Z_0$ , piston;  $Z_1^{\pm 1}$ , tip/tilt;  $Z_2^0$ , defocus; and  $Z_2^{\pm 2}$  astigmatism.

### 5.10.1 Baseline Visibility Measurement

The measured visibility of the incoming wavefront,  $e^{i\phi(\vec{x})}$ , through an aperture  $M(\vec{x})$  is:

$$V(\vec{r}) = \int_0^{t_{exp}} dt \int d\vec{x} e^{i[\phi(\vec{x}+\vec{r},t)-\phi(\vec{x},t)]} M(\vec{x} + \vec{r}) M(\vec{x}). \quad (5.16)$$

If the aperture,  $M(\vec{x})$ , is a two-hole mask with unit area circular sub-apertures separated by a distance  $\vec{b}$ , then the visibility of the corresponding baseline simplifies to

$$V(\vec{b}) = \int_0^{t_{exp}} dt \int_{\text{sub-aperture } 1} d\vec{x} e^{i[\phi(\vec{x}+\vec{b},t)-\phi(\vec{x},t)]}. \quad (5.17)$$

In the limit of zero exposure time, the *instantaneous* baseline visibility is

$$V(\vec{b}) = \int_{\text{sub-aperture } 1} d\vec{x} e^{i[\phi(\vec{x}+\vec{b})-\phi(\vec{x})]}. \quad (5.18)$$

Notice that the integral is carried out over the set of redundant baselines. For a so called non-redundant mask, the baselines stretching between sub-aperture centers are redundant only within the sub-aperture. The baseline phasors, not phases, add.

One could decompose the wavefront over *each sub-aperture* into Zernike modes. We define a sub-aperture at  $\vec{x} = 0$  by  $\phi_1(\vec{x}) = \sum_{n,m} a_n^m Z_n^m(\vec{x})$ , with  $a_n^m = \int d\vec{x} \phi_1(\vec{x}) Z_n^m(\vec{x})$ . The wavefront over the sub-aperture at  $\vec{x} = \vec{b}$ ,  $\phi_2(\vec{x})$ , is decomposed into Zernike coefficients  $b_n^m$ .

Referring to Equation 5.18, we note that the quantity  $\phi(\vec{x} + \vec{b}) - \phi(\vec{x})$  is itself, then, a sum of Zernike terms. We denote the coefficients of this difference by  $\alpha_n^m \equiv a_n^m - b_n^m$ .

We also note that if the apertures are far separated (with respect to the adaptive optics decorrelation length), then we can assume the Zernike coefficients of the two sub-apertures are uncorrelated. This implies, then, that the coefficient  $\alpha_n^m$  has the same statistics as the single aperture coefficients, with a standard deviation increased by  $\sqrt{2}$ .

This allows us to represent the visibility by

$$V(\vec{b}) = \int_{\substack{\text{sub-} \\ \text{aperture 1}}} d\vec{x} \exp \left[ i \sum_{n,m} \alpha_n^m Z_n^m(\vec{x}) \right]. \quad (5.19)$$

Taylor expanding the exponential the sub-aperture yields

$$V(\vec{b}) = \int_{\substack{\text{sub-} \\ \text{aperture 1}}} d\vec{x} \delta(\vec{x}) + \left[ i \sum_{n,m} \alpha_n^m Z_n^m(\vec{x}) \right] - \frac{1}{2} \left[ \sum_{n,m} \alpha_n^m Z_n^m(\vec{x}) \right]^2 + O(\alpha^3) \quad (5.20)$$

and integrating the Zernike polynomials yields

$$V(\vec{b}) = 1 + i\alpha_0^0 - \frac{1}{2} \sum_{n,m} (\alpha_n^m)^2 + O(\alpha^3). \quad (5.21)$$

The leading order error in the visibility phase is  $\alpha_0^0 = a_0^0 - b_0^0$ , the difference of the sub-aperture  $Z_0^0$  (piston) modes. The piston mode is the average phase above the sub-aperture. However, the second and third order terms are not generally zero: *the visibility phase is not generally equal to the average phase above one sub-aperture minus the average phase of the other sub-aperture.* This is the source of redundancy noise.

The leading order term that affects the amplitude of  $V(\vec{b})$  is equivalent to the mean wavefront variance over the sub-aperture.

### 5.10.2 Instantaneous Closure Phase

In this sub-section we show that closure phases remove sub-aperture piston, but that high order terms persist.

We define the *bispectrum*,  $B(\vec{b}_1, \vec{b}_2)$ , as

$$B(\vec{b}_1, \vec{b}_2) \equiv V(\vec{b}_1) V(\vec{b}_2) V^*(\vec{b}_1 + \vec{b}_2). \quad (5.22)$$

The argument (complex phase) of the bispectrum is the closure phase.

For three sub-apertures centered at  $\vec{x} = 0$ ,  $\vec{b}_1$ , and  $\vec{b}_1 + \vec{b}_2$ , we can follow the same progression that lead to equation 5.21 for the bispectrum

$$B(\vec{b}_1, \vec{b}_2) = \int_{\substack{\text{sub-} \\ \text{aperture 1}}} d\vec{x} d\vec{x}' d\vec{x}'' e^{i[\phi(\vec{x}+\vec{b}_1)-\phi(\vec{x})]} e^{i[\phi(\vec{x}'+\vec{b}_1+\vec{b}_2)-\phi(\vec{x}'+\vec{b}_1)]} e^{i[\phi(\vec{x}'')-\phi(\vec{x}''+\vec{b}_1+\vec{b}_2)]}, \quad (5.23)$$

where each integral occurs over the domain of the sub-aperture centered at  $\vec{x} = 0$  only.

We cast the bispectrum in terms of the sub-aperture Zernike modes of the three sub-apertures. We define the three sets of Zernike coefficients over the apertures centered at  $\vec{x} = 0$ ,  $\vec{x} = \vec{b}_1$ , and  $\vec{x} = \vec{b}_1 + \vec{b}_2$  as  $a_n^m$ ,  $b_n^m$ , and  $c_n^m$ , respectively.

Again, we recognize that the bispectrum is the difference between Zernike decompositions, and denote the difference coefficients as  $\alpha_n^m \equiv b_n^m - a_n^m$ ,  $\beta_n^m \equiv c_n^m - b_n^m$ , and  $\gamma_n^m \equiv a_n^m - c_n^m$ . Their definitions lead to the identity:  $\alpha_n^m + \beta_n^m + \gamma_n^m = 0$ .

$$B(\vec{b}_1, \vec{b}_2) = \int_{\substack{\text{sub-} \\ \text{aperture 1}}} d\vec{x} \exp \left[ i \sum_{n,m} \alpha_n^m Z_n^m(\vec{x}) + \beta_n^m Z_n^m(\vec{x}') + \gamma_n^m Z_n^m(\vec{x}'') \right]. \quad (5.24)$$

Taylor expanding the exponential yields the following terms:

$$0^{th} \text{ Order} : \quad 1 \quad (5.25)$$

$$1^{st} \text{ Order} : \quad i \sum_{n,m} \int \alpha_n^m Z_n^m(\vec{x}) + \beta_n^m Z_n^m(\vec{x}') + \gamma_n^m Z_n^m(\vec{x}') \\ = \alpha_0^0 + \beta_0^0 + \gamma_0^0 = 0 \quad (5.26)$$

$$2^{nd} \text{ Order} : \quad -\frac{1}{2} \sum_{n,m,r,s} \int \alpha_n^m \alpha_r^s Z_n^m(\vec{x}) Z_r^s(\vec{x}) + \alpha_n^m \beta_r^s Z_n^m(\vec{x}) Z_r^s(\vec{x}') + \alpha_n^m \gamma_r^s Z_n^m(\vec{x}) Z_r^s(\vec{x}'') \\ + \beta_n^m \alpha_r^s Z_n^m(\vec{x}') Z_r^s(\vec{x}) + \beta_n^m \beta_r^s Z_n^m(\vec{x}') Z_r^s(\vec{x}') + \beta_n^m \gamma_r^s Z_n^m(\vec{x}') Z_r^s(\vec{x}'') \\ + \gamma_n^m \alpha_r^s Z_n^m(\vec{x}'') Z_r^s(\vec{x}) + \gamma_n^m \beta_r^s Z_n^m(\vec{x}'') Z_r^s(\vec{x}') + \gamma_n^m \gamma_r^s Z_n^m(\vec{x}'') Z_r^s(\vec{x}'') \\ = -\alpha_0^0 \beta_0^0 - \alpha_0^0 \gamma_0^0 - \beta_0^0 \gamma_0^0 - \frac{1}{2} \sum_{n,m} [(\alpha_n^m)^2 + (\beta_n^m)^2 + (\gamma_n^m)^2] \quad (5.28)$$

$$= -\frac{1}{2} \sum_{n \neq 0, m} [(\alpha_n^m)^2 + (\beta_n^m)^2 + (\gamma_n^m)^2] \quad (5.29)$$

Equation 5.28 is obtained by directly integrating the Zernike terms over  $x, x'$ , and  $x''$ . The last line pulls the  $n = 0$  terms out of the sum and uses the identity  $\frac{1}{2}(\alpha_0^0 + \beta_0^0 + \gamma_0^0)^2 = 0$  to remove these terms. We see that to second order of  $\alpha_n^m$ ,  $\beta_n^m$ , and  $\gamma_n^m$ , the error in the closure phase is zero. The bispectrum amplitude and phase are both unaffected by sub-aperture piston.

To account for the errors in closure phase, we must go to third order. In a similar process of integrating over Zernike terms, regrouping piston terms outside the summation, and application of the identity  $\alpha_0^0 + \beta_0^0 + \gamma_0^0 = 0$ , we find the third order term to be

$$Third \text{ Order} : \quad -\frac{i}{6} \sum_{\substack{n \neq 0, m, \\ r \neq 0, s, \\ v \neq 0, w}} \int d\vec{x} \alpha_n^m \alpha_r^s \alpha_v^w Z_n^m(\vec{x}) Z_r^s(\vec{x}) Z_v^w(\vec{x}) + \beta_n^m \beta_r^s \beta_v^w \text{ \& } \gamma_n^m \gamma_r^s \gamma_v^w \text{ terms,} \quad (5.30)$$

Piston terms again drop out, as do cross terms such as  $\alpha_n^m \beta_r^s \beta_v^w Z_n^m(\vec{x}) Z_r^s(\vec{x}') Z_v^w(\vec{x}'')$ .

Although this integral is difficult to solve analytically, we can use several relations to restrict the set of Zernike indices which produce non-zero integrals. We recognize that, when integrated over the unit circle, the angular part of the Zernike polynomials restricts either one or three of the azimuthal indices to be even. This implies the leading term of the sequence to be  $\alpha_1^{\pm 1} \alpha_1^{\pm 1} \alpha_2^{0, \pm 2}$ . If we assume the long baseline approximation such that  $\alpha$  has the same statistical behavior as the sub-aperture coefficients, then the leading term of closure phase noise is the product of *two sub-apertures' tip/tilts and one sub-aperture's defocus/astigmatism*.

Equation 5.30 provides a valuable avenue for estimating the impact of sub-aperture adaptive optics. For example, the PALM3K extreme-AO system actuator spacing is 8.1 centimeters (Dekany et al., 2007). Using the current 9-hole NRM mask with 42 cm sub-apertures, corresponding to roughly 21 actuators per sub-aperture, the PALM3K system will be able to actively control the first twenty one terms of the expression above (see, for example Nakajima & Haniff (1993)). This provides a useful metric for balancing sub-aperture size against other considerations, such as calibration and quasi-static wavefront limitations, photon noise, and trade-offs between smaller sub-apertures and increasing the number of sub-apertures.

## CHAPTER 6

### SYNTHESIS AND CONCLUSIONS

This body of work provides the technical underpinnings of Non-Redundant Aperture Masking Interferometry with Adaptive Optics and contributes to a young but growing literature on this subject. By enabling high-contrast infrared imaging at diffraction-limited separations, the combined technique allows for the resolution of brown dwarfs and exoplanet systems that cannot be observed by any other method. One of the most valuable uses of this technique is in the detection of short period brown dwarf binary systems, which lead to model-independent measurements of brown dwarf masses. These, in turn, can be used to empirically test and refine current brown dwarf evolution and atmospheric models which also set the foundation for our understanding of massive Jupiter exoplanets.

Enhancing the precision of NRM with AO by upgraded AO systems and refined analysis techniques will enable even higher contrasts and the resolution of exoplanets directly. The scientific potential of NRM exoplanet imaging includes the mass measurement of exoplanets and the full-characterization of planetary systems imaged by coronagraphic surveys (e.g., Hinkley et al. (2011)). For nearby stars, the NRM working angle corresponds to planet-star separations of much less than 5 AU, and provides a unique method to image exoplanets formed in situ by core accretion (Kraus et al., 2009).

The goal of this final chapter is to review and synthesize the results of the presented studies. Section 1 reviews the new methods that have been developed in this work, Section 2 reviews the major results, Section 3 explores the possible future work that could be motivated by these studies, and Section 4 concludes with the broader implications of this work.

## 6.1 Refinement of the NRM with AO Technique: Results

Completing this work required several new numerical and statistical methods for using NRM with AO to detect faint companions. The early successes of NRM with AO imaging were driven by the immediate effectiveness of the closure phase method for producing observations uninhibited by quasi-static wavefront errors. The detection of moderate-contrast companion can be readily identified (e.g., Martinache et al. (2007); Pravdo et al. (2006), and NRM provides much higher precision than direct imaging alone. But the forward model approach (see Chapter 3), when employed before this work, often produced spurious detections of faint companions, sometimes even at the many-sigma level. This over confidence arose in part because of inherent correlations of the closure phase signals that were not taken into account (c.f. Kulkarni (1989)); this is not to be confused by correlations of measurement error, which can be handled by a covariant matrix. By developing a simple Monte Carlo simulation that tests the forward model fits against simulated observations bootstrapped directly from the data, we now have tools to confidently search for unknown, high-contrast companions. The simulation also inherently incorporates measurement noise and calibration errors (and their correlations), which makes the the simulation a more robust choice for calculating contrast detection limitations (Chapter 4). The simulation has also been used by Zimmerman et al. (2011) (of which I am a contributing author), which will publish the first NRM images taken by an Integral Field Spectrograph and dedicated exoplanet instrument.

More broadly, my studies in this work aim to mix empirical analysis tools with theoretical foundations to extract more precise information from current NRM images, and to reach higher contrast. Chapter 4 described a novel, intuitive, empirical

method for averaging closure phases that resulted a 2-4 fold increase in measurement precision over what would have been derived by conventional averaging of closure phases of bispectra.

Chapter 5 asserts that NRM is calibration-limited by quasi-static wavefront errors on the sub-aperture scale, and describes precisely how these errors alter closure phases and bispectra. Upcoming extreme-AO systems will push observations far enough into the calibration limit that individual modes of sub-aperture wavefront errors may be discernible in the closure phase data. Developing higher-order calibration methods may enable closure phases to be calculated that remove the impact of some sub-aperture scale wavefront errors, in much the same way that current radial velocity surveys extend to lower velocities by accurately parameterizing the point spread function response to telescope flexure. These same tools will aid in the design of future aperture masking experiments that optimally alleviate noise from AO residuals and instrumental effects. These new masks will balance sub-aperture size and number against adaptive optics stability and actuator density. This balance will depend on the spatial and temporal power spectra of the corrected wavefront residuals, and a formalism for doing so is presented.

## **6.2 Refinement of the NRM with AO Technique: Future Work**

By far, the greatest advances in NRM for the near term will arise from new NRM-equipped exoplanet imagers with extreme-AO systems, e.g., Project 1640 at Palomar (Hinkley et al., 2009), the Gemini Planet Imager (Macintosh et al., 2008), and SPHERE on VLT (Beuzit et al., 2006). These instruments also feature In-

tegral Field Spectrographs capable of taking narrow-band images across multiple wavelengths simultaneously. As discussed in Chapter 1, the inherent dependence of quasi-static speckles behavior on wavelength allows one to distinguish true companions from quasi-static speckles.

Much of the focus in the high-contrast imaging community is currently directed toward obtaining higher contrast with coronagraphs behind extreme-AO and by invoking speckle deconvolution algorithms that eliminate many of the quasi-static speckles at wide separations (beyond 0.5 arcseconds; e.g., Crepp et al. (2010)). Early speckle deconvolution algorithms anticipate to increase detection contrast by a factor of 20 (Hinkley et al., 2010).

Narrow-band IFS NRM images, also allows one to construct algorithms analogous to speckle deconvolution that deconvolve closure phase errors, e.g., *differential* closure phases or differential spatial frequency phases. In the case of NRM phase deconvolution, one aims to exploit the linear relationship between baseline phase errors and inverse wavelength that one would expect to arise from physically induced pupil-plane phase errors (i.e.,  $\Delta\phi = \Delta x/\lambda$ ). In order to develop a relationship between *closure phase*, pupil-plane phase errors, and wavelength, one needs a more sophisticated understanding of how higher mode wavefront phase errors affect closure phases (i.e., Section 5.10 to Chapter 5). The joint effort of closure phases and deconvolution algorithms are *complementary* methods for mitigating the effect of quasi-static wavefront errors.

Zimmerman et al. (2010), of which I am a contributing author, will publish the first IFS NRM data, acquired by the Project 1640 instrument. Our analysis reveals strong, positive correlations ( $\rho \approx 0.80$ ) between closure phase errors of various channels, on par with those found by Crepp et al. (2010) for coronagraphic images.

This indicates that deconvolution algorithms can reduce closure phase errors. We estimate a reduction by 5-10x per channel and a corresponding increase in detection contrast. While the AO correction provided by the PALAO system is not high enough to produce the simple, linear relationship just discussed, the recently commissioned extreme-AO system PALM3K is likely to do so. (It is important to stress that developing more exacting algorithms to extract closure phases from NRM images is *crucial* for these techniques to be effective. In my analysis of the Zimmerman et al. (2010) data, redesigned extractions methods and diligent awareness of systematic errors enabled clean deconvolution.)

Additionally, the spatial frequencies measured by an NRM are a function of wavelength; hence, each channel of an IFS measures unique signals, increase the total spatial frequency coverage by a factor of roughly twenty in the wavelength limit, without considering chromatic techniques. The technique of IFS NRM, when used with the current AO system and the Project 1640 instrument, has achieved an estimated detection contrast of 1000:1 ( $\Delta M \sim 7.5$ ) or higher at the diffraction limit. The Project 1640 coronagraph performance is anticipated to increase by more than tenfold after upgrading to the Palomar extreme-AO system and enabling the precision wavefront control device of the instrument (Hinkley et al., 2010). Based on these specifications, NRM with the Project 1640 instrument may reach as high as  $10^4$ :1 contrasts ( $\Delta M \sim 10.0$ ).

Finally, one consequence of IFS NRM imaging is that it makes an excellent tool for diagnosing instrumental misalignments and wavelength dependent errors, which can, in turn, aid coronagraphic observations. For example, my analysis of the Zimmerman et al. (2010) NRM images found evidence of a small tilt of the mask in the Lyot wheel. Also, the dependence of the mask transmission function

on wavelength allows for a robust, independent determination of the central wavelength of each channel with a single image. This scaling relation is a necessary parameter of speckle deconvolution algorithms (e.g., Crepp et al. (2010), Figure 5) and crucial for extracting precise spectra from IFS images (E. Rice, private communication). It is worth noting that the scaling relation may change as the telescope moves, since the IFS lenslets alters the point spread function reaching the detector. In other words, the scaling relation may be change from target to target, and NRM provides an efficient way to calibrate this concurrent with coronagraph observations.

For these reasons, this is a very exciting time for high-contrast NRM imaging, and certainly deserves further attention in subsequent studies with more advanced equipment.

### 6.3 Study of Brown Dwarf Binaries using LGSAO: Results

NRM is most sensitive to companions between  $\lambda/2D$  and  $4\lambda/D$ , corresponding to angular separations of 50 to 400 mas in the  $K_s$  infrared band ( $2.2\mu m$ ). When providing good correction, NRM with LGSAO has been shown to reach  $10^2:1$  ( $\Delta K_s=5.0$ ) contrasts at the diffraction limit (Dupuy et al., 2009). The enhanced contrast and resolution of NRM with LGSAO makes the technique a formidable tool for resolving low mass brown dwarf (T dwarfs) companions to nearby field brown dwarfs, particularly to enable high precision mass measurements (Chapter 2).

In Chapter 4, I used NRM in conjunction with the Palomar Laser Guide Star Adaptive Optics system (LGSAO, Roberts et al. (2008)) to survey sixteen nearby

field brown dwarfs for companions. Due to the proximity of nearby field brown dwarfs, the combined technique reached physical projected separations ranging from 0.6-8.0 AU for most of the survey targets; this was the first imaging survey to probe for companions to brown dwarfs shortward of 3 AU and the first NRM with LGSAO survey at Palomar. Setbacks with the LGSAO system hampered the observing, but despite the setbacks the survey reached contrasts of  $\Delta K_s=1.5-2.5$  outward of 100 mas. These results benefited greatly from the enhanced closure phase averaging mentioned in the previous subsection.

In addition to seeking a subset of brown dwarf companions suitable for dynamical mass measurements, the imaging survey can glean insights into the formation process of brown dwarfs. The companion fraction of brown dwarfs is proposed to be low ( $\approx 15\%$ ) and peaked within a narrow separation range, 3-10 AU (Burgasser et al., 2008), little conclusive results are known for separations less than 3 AU. Using preliminary evidence compiled from irregular and sparse radial velocity datasets, several authors suggested that at least as many brown dwarfs may reside shortward of 3 AU (Jeffries & Maxted, 2005; Pinfield et al., 2003; Chappelle et al., 2005). Such interesting statistical results may suggest that the brown dwarf binary formation mechanism is different than that for solar type binaries (Burgasser et al., 2007). The NRM with LGSAO imaging survey is one of the first observationally complete surveys of the brown dwarf companion fraction at these separations.

The survey detected four candidate binaries with moderate to high confidence (90-98%), including two with projected physical separations less than 1.5 AU. This may indicate that tight-separation binaries contribute more significantly to the binary fraction than currently assumed, consistent with the preliminary radial velocity results. One companion resides within the formal diffraction limit,

and one companion orbits a target previously imaged as part of a Hubble Space Telescope companion search. All four candidates suggest brown dwarf masses and the candidate status of all four targets can be immediately resolved by NRM with LGSAO imaging on the Keck Telescope. The short projected separations of the systems indicate a favorable likelihood that masses of the brown dwarfs can be obtained within a few years.

## **6.4 Study of Brown Dwarf Binaries using LGSAO: Future Work**

Concurrent with the NRM with LGSAO for brown dwarf binaries were the LGSAO direct imaging surveys of Konopacky et al. (2010) and Dupuy et al. (2010) (and references within). Taken together, the set has more than tripled the number of late-M, L, and T dwarf binaries with dynamical mass measurements. was the dynamical mass measurement survey of several authors.

Based on direct measurements of their luminosities and total masses, evolution model radii give effective temperatures that are inconsistent with those from model atmosphere fitting of observed spectra by 100-300 K (the 'temperature problem'). Evolutionary models also underpredict the luminosities for the only binary with an independent age measurement by a factor of  $\sim 2$  (the 'luminosity problem'), which implies that model-predicted substellar masses may be systematically too large. Evolutionary models are also still untested at early ages ( $\lesssim 100$  Myr).

To tackle the 'temperature problem,' it must first be determined whether the discrepancy arises from systematic errors within the atmospheric models or incor-

rect estimated radii in the evolutionary models. This can be directly tested with future discoveries of late-M and brown dwarf eclipsing binaries, as the temperature offset corresponds to a substantial radius difference (15-20%) (Dupuy et al., 2010). Furthermore, infrared photometry has been shown to be a poor proxy for effective temperature, particularly when visible photometry or a partial SED is unavailable (Konopacky et al., 2010). In this respect, the low-resolution infrared spectra of brown dwarfs obtained by Integral Field Spectrographs, combined with dynamical mass measurements, will be valuable. Currently, no IFS instruments are commissioned for telescopes with LGSAO systems. However, observations of the two brown dwarfs resolvable with NGS AO, GJ 802b and GJ 581B (both from Palomar), can be pursued.

Additionally, campaigns to image brown dwarfs in young systems (i.e., favorable contrasts between brown dwarfs and stellar primaries) can be pursued with new high-contrast and IFS instruments, this would also move forward the test of evolutionary models at young ages. Furthermore, because young systems have constrained ages, comparisons of dynamical masses and model-implied masses will begin to identify the nature of the 'luminosity problem'

Finally, continued observing of the currently known brown dwarf binaries with LGSAO will increase the precision of the mass measurements. These binaries have typical uncertainties larger than 30% (larger for the smallest mass brown dwarfs) and are limited by relative astronomy of their orbits (as opposed to parallax distance). Continued observation, *especially* with the improved relative astronomy and photometry of NRM and LGSAO at Keck Telescope, can lead to truly high precision mass and photometry measurements.

## **6.5 Future Explorations: Probing Evolution and Formation of Brown Dwarfs and Massive Jupiter Exoplanets**

Within this work, the uncertainty of brown dwarfs atmospheric and evolution models (and by extension, giant exoplanets) have been discussed at length, and empirical tests have been discussed, proposed, and carried out. Dynamical mass measurements, along with precise photometry, has been regularly discussed as a major empirical test. The extensions of these models to planetary masses, in concert with observations, will provide insights into the mass, radius, structure, temperature, and metallicity of the exoplanets. In this section, I discuss how these soon to be discovered massive Jupiter exoplanets can form and arrive at their observed location, and I propose a method and survey for testing theories of planetary formation.

### **6.5.1 New Paradigms of Planet Formation Driven by Direct Imaging**

The Jupiter-sized planets detected so far are radically different than the gas giant planets in our solar system. Radial velocity and transit surveys detect hot Jupiters with orbital periods of a few days; directly imaged planet-like companions have been found out beyond even 50 AU, e.g., HR 8799 (Marois et al., 2010). These detections have motivated sweeping changes to the paradigms of planet formation and migration (Ida & Lin, 2004; Boss, 2001). More broadly, dozens of newly discovered planetary systems outward 5-10 AU are anticipated after first light of dedicated exoplanet imagers begin coronagraphic surveys (Beichman et al., 2010).

*Core accretion* occurs most rapidly at the ice line (2-8 AU), and characteristically produces metal-enriched planets  $\lesssim 5M_J$  (Marcy et al., 2005). Subsequent migration inward explains the short period hot-Jupiters, including the planet densities measured by transits. At large separations, the timescales of formation are too slow. Thus, wide-separated planets must be formed in situ by an alternative method, such as *gravitation instability* (most prominent beyond 10 AU), or migrate outward after formation near the ice line. Migration outward, either by planetesimals in the disk or massive inner planets, occurs on timescales of 50-100 Myrs (Reipurth et al., 2007). The two mechanisms are predicted to yield different distributions of planetary mass, star-planet separation, luminosity, and metallicity. Testing these theories has not yet been possible because of a lack of observable data. *The detection of well-characterized planetary systems around youthful stars, including massive inner planets, before migration can occur, will be a key to testing formation mechanisms* (Hinkley et al. (2010), and references within).

### 6.5.2 A Growing Population of Nearby, Young Stars

Recently, great effort has been put into extending the membership of nearby, young moving group associations in both the Northern and Southern hemisphere, including several with median distances closer than 40 pc and ages less than 50 Myr. Additionally, efforts are underway to identify new GK-type members, with a new-membership rate of dozens per year (Zuckerman, 2004; Schlieder & Lepine, 2010). The detection of full planetary systems around these stars provides a unique way to test formation predictions.

With an inner working angle of 0.300" (10 AU @ 35 pc), the Gemini Planet Imager and Project 1640 coronagraphs are unable to probe planets formed within

about 10 AU, including those formed in situ by core accretion. NRM provides a complement to coronagraph observations. The working angle of NRM at shortward infrared wavelengths is 0.040-0.400" (1-13 AU), and both exoplanet instruments will be equipped with NRM masks. Used jointly, NRM and Coronagraphs explore the full planetary architecture outward of roughly 1 AU.

This combination of targets and techniques opens up exoplanet searches to massive inner planets, planets near the ice line, and planets formed in situ by bona fide core accretion. Probing at these separations is not possible by radial velocity because of stellar variability of youthful targets. It should be noted that such a survey complements ongoing NRM companion searches in the Upper Scorpius star-forming region. At an age of 5 Myrs, the region is ideal for planet searches, but its distance (140 pc) limits detections to beyond 7 AU even with NRM (Kraus et al., 2008).

### **6.5.3 Feasibility of the Survey with Exoplanet Instruments and NRM**

NRM provides the highest contrast of any technique at the diffraction-limited, and one of the core motivations of this dissertation has been to refine the technique of NRM to reach contrasts high enough to detect massive Jupiter exoplanets with these next generation instruments.

The foremost factor influencing the detection of massive Jupiter planets at close separations with NRM is that the host star must be bright enough to function as a natural guide star. Currently, the Gemini Planet Imager and Project 1640 require I band magnitudes  $\leq 8-9$  in order to use extreme-AO (Macintosh et al., 2008;

Hinkley et al., 2009). The performance drops sharply after this limit. Second, the distance determines the physical star-planet separations probed by NRM. The working angle of NRM at shortward infrared wavelengths (40-400 mas) corresponds to roughly 1-10 AU at 20 parsecs. Finally, the host star is preferred to be of late-type, i.e., intrinsically faint.

Both hemispheres have nearby, young moving group associations with median distances closer than 40 pc and ages less than 50 Myr. As mentioned previously, great effort has been put into extending their membership, particularly adding late-type members. Additionally, moderate to high resolution spectra exist to characterize these stars.

These targets make an ideal survey for planet detection. Imposing  $I_j > 9$  yields 91 targets of median distance 45 pc observable from Gemini Observatory and about 35 targets observable from Palomar Observatory. Figure 6.1 shows the anticipated detection limits for a median object; Figure 6.2 shows the brightness and distance distribution for the Gemini sample. Roughly half of the objects are sensitive to 5-10  $M_J$  objects between 2.0-8.0 AU with the upgraded instrumentation. Assuming that the Jupiter fraction of solar-type stars is 20% (Beichman et al., 2010) and that they are evenly distributed in mass between 1-10  $M_J$ , one can expect to discovery 4-6 planetary systems.

## 6.6 Conclusions

This dissertation has provided the first thorough treatment of Non-Redundant Aperture Masking Interferometry with Adaptive Optics, and outlines its use as an observational tool for detecting brown dwarf and exoplanet companions at close-

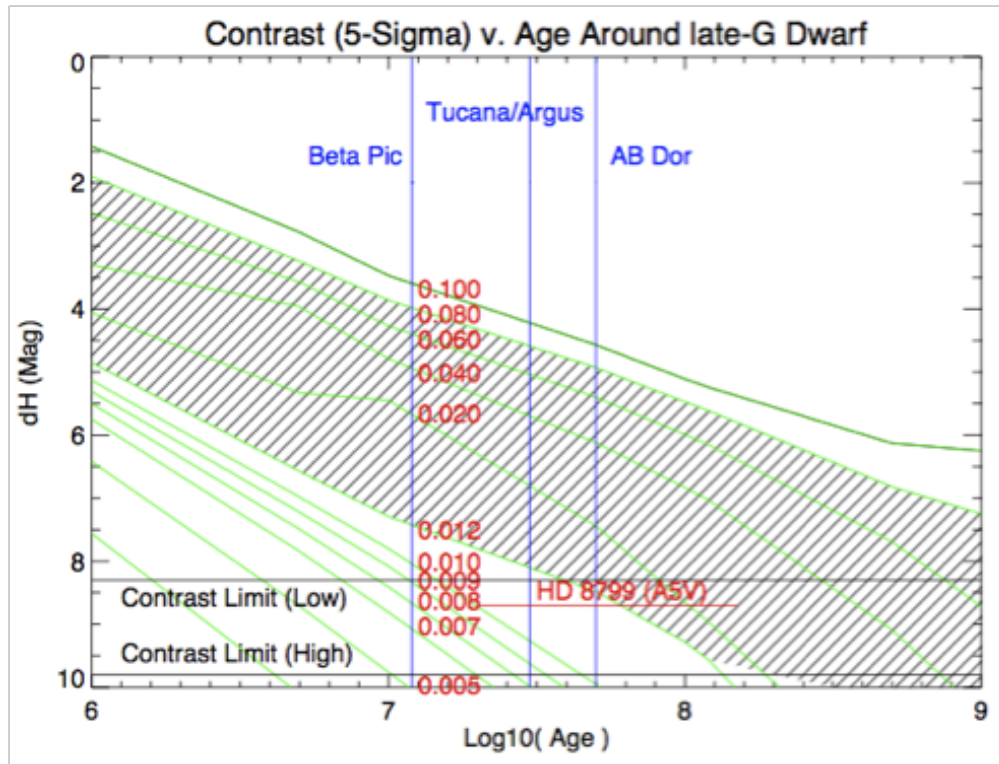


Figure 6.1: Star-Planet Contrast of brown dwarfs and massive Jupiters (green tracks) orbiting a late-G star, plotted against anticipated P1640 NRM contrast limits (black lines). Youthful brown dwarfs and exoplanets are bright enough to be detected by NRM on P1640 and Gemini Planet Imager. Vertical lines (blue) plot the age of known, nearby moving groups. Note that planets of mass 6-9  $M_J$  are consistently detectable with the estimated performance using extreme-AO and precision wavefront control (see text). A brown dwarf of *any* mass can be detected most targets.

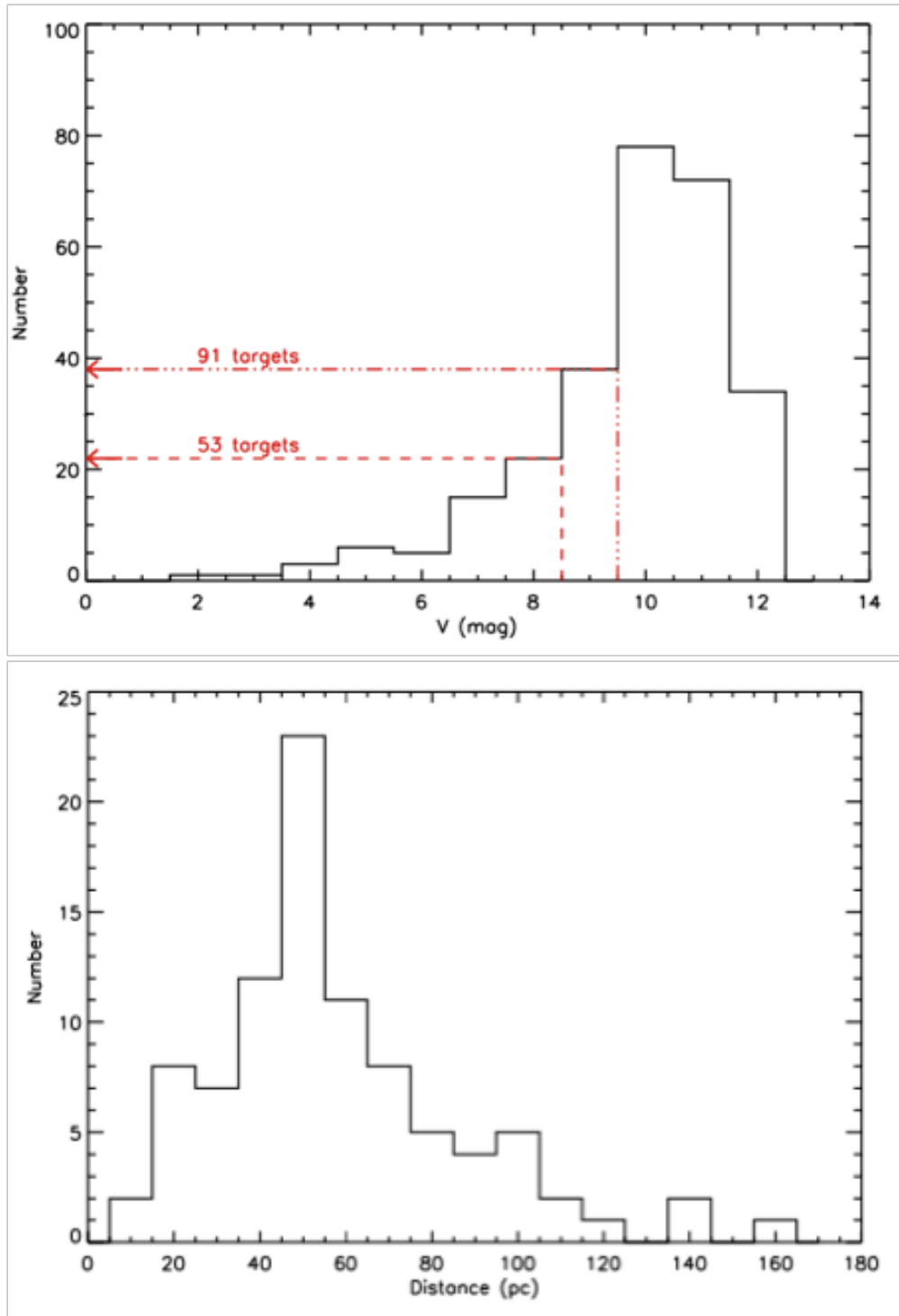


Figure 6.2: (Top) Histogram of visual magnitudes for all currently known moving group objects observable from Gemini Observatory. Fifty-three targets are  $V < 8.5$  and ninety-one targets are  $V < 9.5$ . I band magnitudes are 0.5 lower (i.e.,  $V-I=0.5$ ) for these targets. These sets represent  $I < 8$  and  $I < 9$ , respectively, in the AO sensing wavelength of the Palomar AO system. (Bottom) Histogram of distances for the 91 targets with  $I < 9$ . The median distance is 45 pc, corresponding to physical separations of 1.8 - 7.2 AU for the Palomar NRM working angles.

separations and testing models of their astrophysical evolution.

I presented results of a detection search for companions to sixteen nearby, known brown dwarfs using NRM with LGSAO on the Palomar 200" Hale Telescope. The four candidate brown dwarf companions detected with this survey, if confirmed, these brown dwarfs make excellent candidates for dynamical mass measurement. (Chapter 4)

I investigated the impact of small-scale wavefront errors (those smaller than a sub-aperture) on NRM using a technique known as spatial filtering through calculation, simulation, and observational tests conducted with an optimized pinhole and aperture mask in the PHARO instrument at the 200" Hale Telescope. I find that spatially filtered NRM can increase observation contrasts by 10-25% on current AO systems and by a factor of 2-4 on higher-order AO systems.

Completing this work required several new numerical and statistical methods for using NRM with AO to detect faint companions. The improved analysis tools allow for confident detection of faint targets by NRM, robust calculation of contrast limits, and empirical averaging techniques that yield lower closure phase noise. I also developed a formalism for detailing the impact of sub-aperture quasi-static wavefront errors on closure phases that will be valuable for improving higher order calibration techniques for NRM with exoplanet imaging instruments.

Combined, the evidence presented in this dissertation leads to the conclusion that NRM with AO is rapidly developing into a fully mature high-contrast technique. With further attention and subsequent studies with more advanced instrumentation, the exoplanets resolved by NRM will contribute key scientific discoveries to the burgeoning population of directly imaged planetary systems.

## APPENDIX A

### PRIMER: IMAGING THROUGH A TURBULENT ATMOSPHERE WITH ADAPTIVE OPTICS

#### A.1 The Point Spread Function

The image intensity pattern incident on the telescope detector,  $I(\vec{\theta})$ , can be represented as the convolution of the object (or source) intensity distribution on the sky,  $S(\vec{\theta})$ , with the point spread function of the atmosphere and telescope,  $\tau(\vec{\theta})$ :

$$I(\vec{\theta}) = S(\vec{\theta}) \star \tau(\vec{\theta}), \quad (\text{A.1})$$

where the star,  $\star$ , denotes convolution. This representation is valid when the object under consideration is small enough that its emitted light is perturbed by essentially identical optical aberrations, i.e., *isoplanatic*. When this condition is valid is dependent on the the quality of seeing but is typically on the order of a few arcseconds in the infrared.

The source, located far enough to be considered at infinity, imparts a electric field plane wave upon the telescope aperture ( $E_a$ ) which is the Fourier Transform of the electric field emitted by the source ( $E_s$ ).

$$E_a(\vec{x}) = \int E_s(\vec{\theta}) \exp(2\pi i \vec{\theta} \cdot \vec{x} / \lambda) d\vec{\theta} \quad (\text{A.2})$$

Throughout this text we will denote this form of the Fourier Transform by  $E_a(\vec{x}) = \mathcal{F}[E_s(\vec{\theta})]$ .

Equation A.1 can be derived directly by considering the truncation of the incoming wavefront at the telescope pupil. We represent the transmission of the pupil by a two dimensional function,  $P(\vec{x})$ , valued zero where light is blocked and

one where light is fully transmitted. Apodized pupils can be represented by giving the function a value between zero and one.

The electric field distribution incident upon the *detector* ( $E_d$ ) is directly related to the Fourier Transform of the wavefront incident on the telescope aperture. The detector is located at the so-called *image* (or *focal*) plane, and measured in angular units  $\vec{\theta}$ ; the telescope aperture is in the *pupil* plane, and measured in physical units (i.e., meters),  $\vec{x}$ .

$$\begin{aligned}
E_d &= \mathcal{F}[E_a(\vec{x})P(\vec{x})] \\
&= E_s(\vec{\theta}) \star \mathcal{F}[P(\vec{x})] \\
I_d(\vec{\theta}) &= \langle |E_d(\vec{x})|^2 \rangle \\
&= S(\vec{\theta}) \star |\mathcal{F}[P(\vec{x})]|^2.
\end{aligned} \tag{A.3}$$

In the equations above, the brackets denote a time average over many cycles of the emitted electric field. Inherent in this derivation is the assumption that the source is spatially incoherent, i.e.,  $\langle E_s(\vec{\theta}_1)E_s^*(\vec{\theta}_2) \rangle = S(\vec{\theta})\delta(\vec{\theta}_2 - \vec{\theta}_1)$ .

In analog to Equation A.1, the point spread function is

$$\tau(\vec{\theta}) = |\mathcal{F}[P(\vec{x})]|^2. \tag{A.4}$$

For an idealized telescope (i.e., a circular top-hat function of diameter D), this leads to the familiar Airy function point spread function.

Atmospheric turbulence introduces perturbations to the wavefront incident on the telescope aperture and imperfect optics further perturb the wavefront during its propagation to the detector. To a good approximation, these errors can be considered as pupil-plane phase errors; scintillation by the atmosphere produces amplitude changes on the order of  $10^{-4}$ , optical errors impart phase errors in both

the pupil plane and image plane but can be approximated as only the former. Thus, the wavefront is modified by aberrations of the form  $A(x) = e^{i\phi(x)}$ , where  $\phi(x)$  is the phase error introduced across the pupil plane. If we treat the aberrations as a modification to the pupil function, the distorted point spread function is

$$\tau[\vec{\theta}] = |\mathcal{F}[e^{i\phi(\vec{x})}P(\vec{x})]|^2. \quad (\text{A.5})$$

The structure of the wavefront aberrations drive the form of the short and long exposure aberrated point spread function. While uncorrected atmospheric turbulence perturbs the point spread function in an unknown way at every instant, its long exposure average value is a well-determinable function of the aperture and atmospheric seeing. On short times (defined by timescales shorter than the timescale by which the wavefront aberrations,  $\tau_0$ ), the phase aberrations can be approximated as static; the resulting image is composed largely of the granular structure of speckles. As the exposure extends over several coherence lengths, many instances of speckles ultimately smear the image. Flux is displaced from the core of the perfect point spread function core into a larger diffuse area. For typical uncorrected atmospheric seeing in the infrared, the coherence time of the atmosphere is tens of milliseconds and the long exposure image has a full width half max of approximately one arc second.

## Fourier Domain

Taking the Fourier Transform of the image in Equation A.3 yields

$$i(\vec{f}) = \int P(\vec{x} + \vec{f})P^*(\vec{x}) < E_a(\vec{x} + \vec{f})E_a^*(\vec{x}) > d\vec{x}. \quad (\text{A.6})$$

The term  $< E_a(\vec{x} + \vec{f})E_a^*(\vec{x}) >$  is the *spatial coherence function* of the electric field incident on the aperture or, alternatively, referred to as the (*complex*) *visibility*

$\tilde{V}(\vec{f})$  when normalized so that  $\tilde{V}(0) = 1$ . Importantly, the complex visibility is fundamentally related to the source intensity distribution, a relationship known as the van Cittert-Zernike theorem (Thompson, 2001):

$$\tilde{V}(\vec{f}) = \langle E_a(\vec{x} + \vec{f}) E_a^*(\vec{x}) \rangle / \langle |E_a(0)|^2 \rangle \quad \text{and} \quad (\text{A.7})$$

$$\tilde{V}(\vec{f}) = \left[ \int S(\vec{\theta}) \exp(2\pi i \vec{\theta} \cdot \vec{f} / \lambda) d\vec{\theta} \right] / \left[ \int S(\vec{\theta}) d\vec{\theta} \right]. \quad (\text{A.8})$$

Likewise, the Fourier Transform of the image reduces to

$$i(\vec{f}) = \tilde{V}(\vec{f}) T(\vec{f}) \quad \text{with} \quad (\text{A.9})$$

$$T(\vec{f}) = \int d\vec{x} P(\vec{x} + \vec{f}) P^*(\vec{x}) e^{i\phi(\vec{x} + \vec{f}) - i\phi(\vec{x})}. \quad (\text{A.10})$$

where  $T(\vec{f})$  is the *optical transmission function*, representing the amount by which a given spatial frequency,  $\vec{f}$ , is transmitted by the atmosphere and telescope.

This recasts the direct imaging problem as a challenge to obtain precision measurements of the complex visibility. The complex visibility, by Equation A.8, is a direct measure of one Fourier component the source brightness distribution.

## A.2 Atmospheric Turbulence and Adaptive Optics

### A.2.1 Kolmogorov Turbulence

#### Spatial Structure of Atmospheric Turbulence

The wavefront phase fluctuations imparted by the atmosphere arise because the wavefront propagates through a large number of small index of refraction variations of various physical sizes on its path to the telescope aperture. By the law of

large numbers, this aggregate deformation is Gaussian, and the variation of the wavefront phase at any one point in space and time is a Gaussian random variable. The wavefront variation has a spatial structure dependent on the mechanism which drives the fluctuations, and this can most easily be facilitated by discussing the *phase structure function*,  $D_\phi(\vec{r}_1, \vec{r}_2)$ , describing the mean-squared phase variations between two points in space separated by a distance vector,  $\vec{r} = \vec{r}_1 - \vec{r}_2$ , at a given instant in time.

$$D_\phi(\vec{r}_1, \vec{r}_2) = \langle [\phi(\vec{r}_1) - \phi(\vec{r}_2)]^2 \rangle . \quad (\text{A.11})$$

The brackets imply averaging over the spatial extent of the turbulence.

Turbulence arises by velocity fields mixing different layers of air in pressure equilibrium, but with different temperatures, densities, and indices of refraction; these small differences in local velocities move pockets of high and low temperature (and density) around in a random fashion. Kolmogorov (1941) first studied the spatial structure of these velocity differences. In principle, the structure function varies at each point due to its local instantaneous conditions, but with a few assumptions the problem is greatly simplified. If the atmosphere is assumed to be homogenous, isotopic, and incompressible, a single structure function can be applied to every point of origin and depends only on the total displacement between two points, i.e,  $r = |\vec{r}_1 - \vec{r}_2|$  and  $D_v(\vec{r}_1, \vec{r}_2) = f(|\vec{r}_1 - \vec{r}_2|)$  (Batchelor, 1953).

Furthermore, Kolmogorov showed that, for the spatial scales in which these eddies more by turbulent flow, a scale generally ranging from millimeters to kilometers for typical wind speeds ( $\sim 5$  m/s), the structure function reduces to a single power law function:  $D(r) = C_v^2 r^{2/3}$ . The constant  $C_v^2$  is a measure of the energy in the turbulence.

Tatarskii (1961) later related the random motions of these pockets of temper-

ature variation to index of refraction inhomogeneities, finding that the index of refraction structure function also follows a 2/3 power law:  $D_n(r) = C_n^2 r^{2/3}$ . Given a measure of the turbulence strength,  $C_n^2$ , this equation completely describes the statistical nature of index of refraction (and phase) fluctuations. The structure constant  $C_n^2$  varies with broadly over seasons, as well as daily and hourly.

The structure constant also varies with height in the atmosphere, and the wavefront propagates through many individual turbulence cells. The total deformation of the wavefront is found by integrating over the depth of the atmosphere, leading to the *phase structure function*,  $D(r) = \langle [\phi(x+r) - \phi(x)]^2 \rangle$  expressed as:

$$D_\phi(r) = 2.91 r^{5/3} \sec(z) \left( \frac{2\pi}{\lambda} \right)^2 \int dh C_n^2(h) \quad (\text{A.12})$$

$$= 6.88 \left( \frac{r}{r_0} \right)^{5/3} \quad (\text{A.13})$$

with

$$r_0 = \left[ 0.423 \sec(z) \left( \frac{2\pi}{\lambda} \right)^2 \int_0^L C_n^2(h) dh \right]^{-3/5}. \quad (\text{A.14})$$

Thus the nature of atmospheric phase variation across an aperture reduces to a fairly simple expression, i.e, phase variations are gaussian distributed at each point with a variance which follows the structure function expression. Despite the complex mechanisms driving atmospheric turbulence, its statistical nature can be characterized by a single parameter, the Fried parameter  $r_0$ , which is a function of the turbulence strength, zenith angle, cumulative path length through the atmosphere, and wavelength.

## Significance of the Fried Parameter, $r_0$

While the Fried parameter has been introduced here as a matter of convenient bookkeeping, the parameter naturally lends itself to a deeper significance. Indeed, Fried (1966) introduced the parameter as the maximum diameter of an aperture before atmospheric distortion seriously limits its resolving performance. That is, the seeing-limited resolution of a large telescope obtained through an atmosphere characterized by a Fried parameter,  $r_0$ , is no better than the resolution of a diffraction limited telescope of diameter  $r_0$ . Both circumstances lead to a point spread function of full width at half max  $\sim \lambda/r_0$ .

In particular, despite the dependence of the Fried parameter on the turbulence strength constant (and each layer of the atmosphere) and the zenith angle, an estimate of  $r_0$  can be obtained by measuring the full-width half-max of a long-exposure uncorrected image.

Furthermore, Noll (1976) showed that the wavefront variance averaged across an aperture of size  $r_0$  is  $\sigma^2 = 1.03\text{rad}^2$ , or more generally  $\sigma^2 = 1.03(D/r_0)^{5/3}$  for an aperture of diameter  $D$ . Two points separated by more than  $r_0$  are essentially incoherent. This result leads to the adoption of a simple picture of turbulence as a collection of cells of  $r_0$  with constant phase, but random phase between individual cells.

From its definition in Equation A.14,  $r_0$  can be seen to vary as a function of  $\lambda^{6/5}$ . With  $r_0 \sim 30$  cm in H band ( $1.6\mu\text{m}$ ), this scaling implies that even 5-10 meter class telescopes are diffraction limited in the mid-infrared ( $\lambda > 10\mu\text{m}$ ). Diffraction limited performance of adaptive optics systems is easier to achieve at longer wavelengths and fewer actuators are necessary.

## Turbulence in the Fourier Domain

Additionally, one can calculate the power spectral density of the structure function, detailing the strength of phase fluctuations to a given spatial frequency. As we will see in later sections, aperture masking interferometry measures specific spatial frequencies of the incoming wavefront, and such, this description of turbulence is in some ways more natural to this task. This calculation results in the *Kolmogorov Power Spectrum*:

$$\Phi_n(k) = \frac{0.023}{r_0^{5/3}} k^{-11/3}. \quad (\text{A.15})$$

Thus, the phase variation across an aperture can be decomposed to independent (Fourier) spatial frequencies. The phase of these spatial frequencies, in turn, are subject to random Gaussian fluctuations with a variance which follows the Kolmogorov Power Spectrum. The steep negative slope of the Kolmogorov spectrum implies that power preferentially resides in low-spatial frequency (i.e., large scale) perturbations to the wavefront (Noll, 1976). Large scale wavefront errors result in diffraction speckles in the image, indicating that speckles ought to determine the structure of short exposure images and dominate the image noise.

## Temporal Variation of the Wavefront

Turbulence is a time-varying phenomena, as local inhomogeneities are driven by winds and eddies. The simplest model of this effect, the *Taylor hypothesis of frozen turbulence* treats the atmosphere as a static, spatial phase structure that is blown across the aperture by some wind with velocity,  $v$ . (If multiple levels contribute to the total turbulence, the temporal behavior can still be treated by assuming the turbulence weighted wind velocity.) Under this assumption, the temporal variation

of the phase over a time interval,  $\tau$ , is equivalent to the spatial variation of the phase over distance  $v\tau$ .

$$D_{\phi,Taylor}(\delta t = \tau, \delta r = 0) \iff D_{\phi,Frozen}(\delta t = 0, \delta r = v\tau). \quad (\text{A.16})$$

Under these assumptions, the wavefront becomes decoherent over timescales of  $\tau_0 = r_0/v$ . With typical wind speeds on the order of 5-10 m/s,  $t_0 \sim 30\text{-}60$  ms. By its definition,  $\tau_0$  also scales as  $\lambda^{6/5}$ .

This timescale provides a natural length of time to separate long exposures from short exposures. Short exposures,  $t \ll \tau_0$ , are perturbed, essentially, by a single instantaneous realization of the atmosphere. In these circumstances, the high spatial frequency information of the image is retained. This forms the basis of *speckle interferometry*. Long exposures, alternatively, quickly lose high spatial frequency information. The granular structure of speckles smooth away and the halo forms.

A more in depth treatment of turbulence recognizes that the truncation of turbulence cells at the aperture edge results in rapid fluctuation of the high spatial frequencies as these cells are blown across the aperture edge. Greenwood (1976) calculated that the characteristic frequency of turbulence variations to be

$$f_g = 2.31\lambda^{-6/5} \left[ \sec(z) \int_0^L dh C_n^2(h) v^{5/3}(h) \right]^{3/5}. \quad (\text{A.17})$$

For the constant wind case, the Greenwood frequency can be approximated as

$$f_g \approx 0.43 \frac{v}{r_0} \approx 0.43 \frac{1}{\tau_0}. \quad (\text{A.18})$$

For typical observing the Greenwood frequency is tens of hertz. To effectively reduce most of the phase fluctuations, adaptive optics systems must be capable of correcting the wavefront at a rate much faster than this frequency.

### A.3 Adaptive Optics

Adaptive optics systems function on the basis of *phase conjugation*, noting that phase deformations can be corrected by reflecting the incoming wavefront off a deformed mirror in which the path length difference created along the mirror matches the conjugate of the deformed wavefront. Sensing the wavefront distortions of the incoming wavefront is often done by picking off a particular wavelength band of the incoming flux that will not be used for science observations.

Typically, the pupil plane aperture is subdivided into a number of sub-apertures by a wavefront sensor which utilizes a method for measuring the phase across each sub-aperture. For instance, a Shack-Hartmann wavefront sensor uses a lenslet array to focus each sub-aperture onto a CCD, and the displacement of the spots from a reference position indicate the slope of the wavefront across each sub-aperture. These wavefront slopes are then used to reconstruct the overall shape of the wavefront.

The steep negative slope of the turbulence power spectrum ( $k^{-11/3}$ ) indicates that the overwhelming power of the turbulence arises at large scales (low spatial frequencies). Noll (1976) showed that  $\sim 85\%$  of the spatial variance of the phase across an aperture arises from variations of the tip and tilt of the wavefront. These wavefront errors do not degrade the overall structure of the instantaneous point spread function but rather shift the image about on the science camera (giving rise to an image wander in successive short exposures and smearing in long exposures). For this reason, many adaptive optics systems implement an additional component to control the translational motion of the image.

The deformable mirror receives the measurements from the wavefront sensor

and implements phase conjugation. A zonal approach of phase conjugation positions each actuator to minimize a least squared fit between the deformable mirror surface and the turbulent wavefront. Or alternatively, a modal approach decomposes the wavefront into Zernike modes and introduces conjugate modes into the deformable mirror to remove some subset of Zernike modes from the turbulent wavefront (see, for example, Nakajima & Haniff (1993)).

Current generation adaptive optics systems dramatically reduce the effects of atmospheric turbulence and alter the spatial and temporal power spectrum of the wavefront phase. The characteristics of the adaptive optics corrected wavefront and the limitations to correction are discussed here.

The finite spacing of the actuators limit the smallest wavefront features which can be corrected (i.e., the highest frequency variation that happens within the scale of the actuator size). This limits the field of view which can be corrected by adaptive optics. The outer field of view of an image is formed by the high-spatial frequency content of the wavefront; since the adaptive optics system cannot correct the wavefront on scales smaller than  $r < r_a$ , where  $r_a$  is the actuator spacing, the adaptive optics cannot correct the field of view beyond  $\lambda/r_a$ . Beyond this *outer control radius*, the region is essentially identical to the seeing limited case.

The length of time required for the wavefront sensor to gather enough photons to measure the wavefront and the finite response lag between measurement and implementation both introduce an error between the atmospheric wavefront and the phase conjugation. Because the wavefront sensor is photon limited, the rate at which the adaptive optics control system can be run is a function of the guide star brightness.

In addition to atmospheric turbulence, imperfections of the optics introduce wavefront errors as well. Wavefront optical elements which occur before the wavefront sensor (for instance, the primary mirror) can be corrected by the adaptive optics system, up to the limitations of the actuator spacing. Smaller scale (higher frequency) components remain in the wavefront. Optical elements which occur *after* the wavefront sensor cannot be corrected. These *non-common path* errors have become a focus of the high-contrast imaging community, as these errors generally set the ultimate limitation of contrast one can achieve with a system.

The performance of current adaptive optics systems are primarily characterized in terms of the residual phase variance across the telescope aperture. This phase variance can be reasonably well estimated by summing the individual error terms described above. The estimated performance of a generic adaptive optics system is given below, along with the specific performance of the Palomar Adaptive Optics systems with the PHARO infrared imager on the Hale 200" Telescope (Troy et al., 2000).

### **Adaptive Optics Spatial Errors**

The finite spacing of the actuators ( $r_a$ ,  $N_a$  actuators total) limit the smallest features of the wavefront which can be corrected. Zonal methods aim to minimize the overall wavefront variance over the aperture after correction; Modal methods decompose the wavefront structure into a set of linearly independent components (usually Zernike modes) and configure the actuators to remove the lowest modes. Both methods produce similar correction. It is generally assumed that an adaptive optics system can remove spatial wavefront errors on scales larger than  $2r_a$  (frequencies lower than  $\lambda/2r_a$ ), or alternatively the  $N_a$  lowest Zernike modes.

The residual atmospheric wavefront error after zonal correcting scales are

$$\sigma_{fit}^2 = \kappa \left( \frac{r_s}{r_0} \right)^{5/3}, \quad (\text{A.19})$$

where  $\kappa$  depends on the various basis functions and influence properties of the actuators. For PALAO,  $\kappa = 0.28$ . Noll (1976) developed an approximate relation for the residual wavefront error after modal correction:

$$\sigma_{fit}^2 = 0.2944 N_a^{\sqrt{3}/2} \left( \frac{D}{r_0} \right)^{5/3}. \quad (\text{A.20})$$

The similarity of the two equations can be seen when  $r_a \sim D/\sqrt{N_a}$  is substituted into the former.

The PALAO system at Palomar utilizes  $N_a = 241$  actuators, with an actuator spacing of  $r_a = 31.2$  cm. For typical H band ( $1.6 \mu m$ ) seeing of 30 cm, this yields atmospheric residual error of  $\sigma_{fit} \sim 142$  nm. The residual wavefront error due to optical imperfections depends on the telescope and instrument and are estimated to be  $\sim 100$  nm.

### Adaptive Optics Temporal Errors

Greenwood (1979) showed the residual phase errors which result from the finite rate at which the adaptive optics system measure and apply correction is

$$\sigma_{temp}^2 = \kappa_t \left( \frac{f_g}{f_s} \right)^{5/3}, \quad (\text{A.21})$$

where,  $f_g$  is the Greenwood frequency (Eq. A.18) and  $f_s$  is the control loop frequency. The constant  $\kappa_t$  depends on the servo algorithm; it is approximately 1 for the PALAO system. Note that these errors arise even if the adaptive optics system were able to perfectly conjugate the atmospheric wavefront, and instead result due

to the lag between the wavefront sensor measurement and implementation of the wavefront conjugate on the mirror.

The dynamical control loop of the adaptive optics system will also alter the temporal power spectrum of the wavefront phase, and with it the temporal structure function. Indeed, the Taylor hypothesis now only applies to those time intervals shorter than the control loop period,  $t_s = 1/f_s$ . For time intervals longer than the servo period the wavefront at a specific point can be regarded as uncorrelated, and the structure function asymptotes to the Greenwood time-delay residuals.

$$D_{AO}(t, \delta r = 0) = 6.88 (f_g t)^{5/3}, \quad t \lesssim 2t_s \quad (\text{A.22})$$

$$= 2\sigma_{temp}^2, \quad t \gtrsim 2t_s \quad (\text{A.23})$$

and  $\langle \phi(t + \delta t)\phi^*(t) \rangle = 0$  when  $t \gtrsim 2t_s$ .

Figure A.1 shows the temporal power spectrum of the residuals obtained with the PALAO high-order deformable mirror during observations of a bright star. The "open loop" residuals show the temporal power spectrum of the atmospheric turbulence; a clear  $t^{-5/3}$  power spectrum can be seen, consistent with the Kolmogorov model and the Taylor hypothesis. Operating with "closed loop" (i.e., the deformable mirror control loop activated), the adaptive optics system effectively removed turbulence power at frequencies slower than  $f_s \sim 15\text{Hz}$  (timescales longer than  $t_s \sim 65\text{ msec}$ ). From these results, one can conclude that the corrected wavefront decorrelates after 65 msec.

The PALAO system also uses an additional mirror to stabilize the image, i.e. correct for tip-tilt wavefront errors. The finite time of implementation introduces

an additional residual wavefront error of

$$\sigma_{temp,TT}^2 = \left( \frac{f_T}{f_{s,TT}} \right)^{1/6} \left( \frac{\lambda_T}{D} \right) \quad (\text{A.24})$$

$$f_T \sim 0.0811 \left( \frac{r_0}{D} \right) \left( \frac{v}{r_0} \right) \quad (\text{A.25})$$

where  $f_T$  is the atmospheric tilt frequency. Figure A.1 shows the temporal power spectrum of the tip-tilt residuals opened with the PALAO tip/tilt mirror during observations of a bright star. The "open loop" residuals show the natural temporal spectrum of tip-tilt phase errors; "closed loop" operation of the tip-tilt effectively reduces the turbulence power at frequencies slower than  $f_{s,TT} \sim 5\text{Hz}$ . From this expression we can estimate the residual tip/tilt errors, which are expected to decorrelate after 200 msec.

One should recognize that control servo rate and wavefront sensor rate are related but separated quantities. As an informal rule of thumb, the servo frequency – the frequency with which the deformable mirror can apply effective correction – can be approximated as one-tenth the wavefront sensor measurement rate.

Importantly, the rate at which the wavefront sensor depends on the brightness of the target. Likewise, the level of wavefront residuals after correction is also a function of target brightness. We can arrive at a rough scaling law for the residual variance as a function of target magnitude (in the AO wavefront sensor waveband) by requiring a uniform level of signal to noise by the wavefront sensor.

The number of photons per sub-aperture per cycle is  $N_{photons} \sim r_a^2 t_{wfs}$ . Assuming the servo rate is decreased to keep the number of photons constant, the temporal wavefront residuals increase by  $\sigma_{temp}^2 \sim 10^{M_{AO}/3}$ . It follows that a drop in target brightness of one magnitude leads to an increase of phase variance by approximately 2.15x (and a precipitous drop in Strehl ratio). The residual wavefront

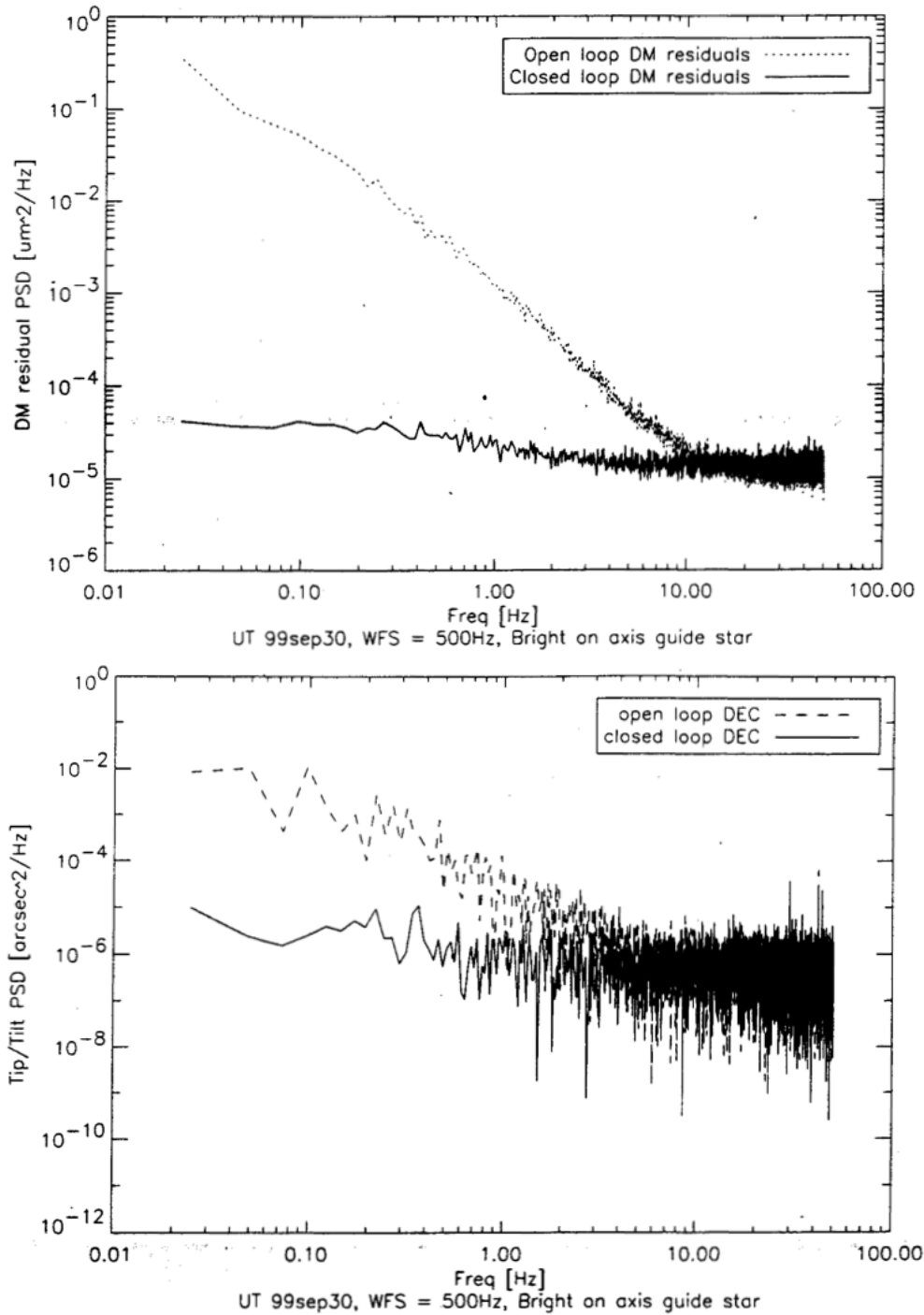


Figure A.1: The sparse, non-redundant aperture mask used for observations at the Hale 200" Telescope at Palomar Observatory. Each pair of sub-apertures acts as an interferometer of a unique baseline length and orientation. Overdrawn is one such baseline. The 9-hole mask produces thirty-six baselines total; the point spread function of the mask is a set of thirty-six overlapping fringes underneath a large Airy envelope.

tip-tilt errors vary less dramatically due to the lower order exponent in Equation A.24.

Given typical wind speeds at Palomar of about 5 m/s and servo control frequencies of  $f_s \sim 15$  Hz and  $f_{s,tt} \sim 5$  Hz (valid for bright stars), temporal residual errors are  $\sigma_{temp} \sim 140$  nm and  $\sigma_{temp,TT}$ .

### Adaptive Optics Structure Function

These results motivate the adaptive optics corrected structure function given by Greenwood (1979):

$$D_{AO}(r) = 6.88(r/r_0)^{5/3}, \quad r \lesssim r_s \quad (\text{A.26})$$

$$= 2\sigma_{fit}^2, \quad r \gtrsim r_s \quad (\text{A.27})$$

with the implicit conclusion that wavefront residuals are not spatially correlated at separations larger than  $r_s$ :  $\langle \phi(\vec{x} + \vec{r})\phi^*(\vec{x}) \rangle = 0$  when  $|\vec{r}| \gtrsim r_s$ .

Likewise, adaptive optics provides a high pass filter to the Kolmogorov Power Spectrum, effectively eliminating power at spatial frequencies below  $k_{AO} < 2\pi/2r_s$ .

## BIBLIOGRAPHY

- Alexander, D. R. & Ferguson, J. W. 1994, *Astrophysical Journal*, 437, 879
- Allard, F., Guillot, T., Ludwig, H.-G., Hauschildt, P. H., Schweitzer, A., Alexander, D. R., & Ferguson, J. W. 2003, *Brown Dwarfs*, 211, 325
- Allard, F., Hauschildt, P. H., Alexander, D. R., Ferguson, J. W., & Tamanai, A. 2000, *From Giant Planets to Cool Stars*, 212, 127, ISBN: 1-58381-041-2
- Allen, P. 2007, *The Astrophysical Journal*
- Allen, P. R., Koerner, D. W., Reid, I. N., & Trilling, D. E. 2005, *The Astrophysical Journal*, 625, 385
- Allen, P. R., Trilling, D. E., Koerner, D. W., & Reid, I. N. 2003, *The Astrophysical Journal*, 595, 1222
- Baldwin, J. E., Haniff, C. A., Mackay, C. D., & Warner, P. J. 1986, *Nature* (ISSN 0028-0836), 320, 595
- Baraffe, I., Chabrier, G., Allard, F., & Hauschildt, P. 1998, arXiv, astro-ph
- Baraffe, I., Chabrier, G., Barman, T. S., Allard, F., & Hauschildt, P. H. 2003, *Astronomy and Astrophysics*, 402, 701
- Basri, G. & Reiners, A. 2006, *The Astronomical Journal*, 132, 663
- Batchelor, G. K. 1953, *The Theory of Homogeneous Turbulence*
- Beichman, C. A., Krist, J., Trauger, J. T., Greene, T. P., Oppenheimer, B., Sivaramakrishnan, A., Doyon, R., Boccaletti, A., Barman, T. S., & Rieke, M. 2010, arXiv, astro-ph.IM

- Bernat, D., Bouchez, A. H., Ireland, M., Tuthill, P., Martinache, F., Angione, J., Burruss, R. S., Cromer, J. L., Dekany, R. G., Guiwits, S. R., Henning, J. R., Hickey, J., Kibblewhite, E., McKenna, D. L., Moore, A. M., Petrie, H. L., Roberts, J., Shelton, J. C., Thicksten, R. P., Trinh, T., Tripathi, R., Troy, M., Truong, T., Velur, V., & Lloyd, J. P. 2010, *The Astrophysical Journal*, 715, 724
- Beuzit, J.-L., Feldt, M., Dohlen, K., Mouillet, D., Puget, P., Antichi, J., Baruffolo, A., Baudoz, P., Berton, A., Boccaletti, A., Carbillet, M., Charton, J., Claudi, R., Downing, M., Feautrier, P., Fedrigo, E., Fusco, T., Gratton, R., Hubin, N., Kasper, M., Langlois, M., Moutou, C., Mugnier, L., Pragt, J., Rabou, P., Saisse, M., Schmid, H. M., Stadler, E., Turrato, M., Udry, S., Waters, R., & Wildi, F. 2006, *The Messenger*, 125, 29
- Bloemhof, E., Marsh, K., Dekany, R., & Troy. . . , M. 2000, [spie.org](http://spie.org)
- Bloemhof, E. E., Dekany, R. G., Troy, M., & Oppenheimer, B. R. 2001, *The Astrophysical Journal*, 558, L71
- Boss, A. P. 2001, *The Astrophysical Journal*, 551, L167
- Bouy, H., Brandner, W., Martín, E., & Delfosse, X. 2003, *The Astronomical Journal*
- Burgasser, A. J., Liu, M. C., Ireland, M. J., Cruz, K. L., & Dupuy, T. J. 2008, *The Astrophysical Journal*, 681, 579, (c) 2008: The American Astronomical Society
- Burgasser, A. J., Reid, I. N., Siegler, N., Close, L., Allen, P., Lowrance, P., & Gizis, J. 2007, *Protostars and Planets V*, 427
- Burrows, A., Heng, K., & Nampaisarn, T. 2011, *The Astrophysical Journal*, 736, 47

- Burrows, A., Hubbard, W. B., Lunine, J. I., Guillot, M. M. T., Saumon, D., & Freedman, R. S. 1997, arXiv, astro-ph
- Burrows, A., Hubbard, W. B., Lunine, J. I., & Liebert, J. 2001, arXiv, astro-ph
- Burrows, A. & Sharp, C. M. 1999, *The Astrophysical Journal*, 512, 843
- Burrows, A., Sudarsky, D., & Hubeny, I. 2005, arXiv, astro-ph
- . 2006, *The Astrophysical Journal*, 640, 1063
- Chabrier, G., Baraffe, I., Allard, F., & Hauschildt, P. 2000, *The Astrophysical Journal*, 542, 464, (c) 2000: The American Astronomical Society
- Chappelle, R. J., Pinfield, D. J., Steele, I. A., Dobbie, P. D., & Magazzù, A. 2005, *Monthly Notices of the Royal Astronomical Society*, 361, 1323
- Close, L. M., Siegler, N., Freed, M., & Biller, B. 2003, *The Astrophysical Journal*, 587, 407
- Cornwell, T. J. 1989, *Science (ISSN 0036-8075)*, 245, 263
- Crepp, J. R., Pueyo, L., Brenner, D., Oppenheimer, B. R., Zimmerman, N., Hinkley, S., Parry, I., King, D., Vasisht, G., Beichman, C., Hillenbrand, L., Dekany, R., Shao, M., Burruss, R., Jr., L. C. R., Bouchez, A., Roberts, J., & Soummer, R. 2010, arXiv, astro-ph.IM, accepted to ApJ
- Cruz, K. L., Reid, I. N., Liebert, J., Kirkpatrick, J. D., & Lowrance, P. J. 2003, *The Astronomical Journal*, 126, 2421
- Dahn, C. C., Harris, H. C., Vrba, F. J., Guetter, H. H., Canzian, B., Henden, A. A., Levine, S. E., Luginbuhl, C. B., Monet, A. K. B., Monet, D. G., Pier, J. R., Stone, R. C., Walker, R. L., Burgasser, A. J., Gizis, J. E., Kirkpatrick, J. D., Liebert, J., & Reid, I. N. 2002, *The Astronomical Journal*, 124, 1170

- Dekany, R., Bouchez, A., Roberts, J., Troy, M., Kibblewhite, E., Oppenheimer, B., Moore, A., Shelton, C., Smith, R., Trinh, T., & Velur, V. 2007, Proceedings of the Advanced Maui Optical and Space Surveillance Technologies Conference, 64
- du Foresto, V. C., Ridgway, S., & Mariotti, J.-M. 1997, A & A Supplement series, 121, 379
- Dupuy, T., Liu, M., Bowler, B., Cushing, M., Helling, C., Witte, S., & Hauschildt, P. 2010, arXiv, astro-ph.SR, 53 pages, 12 figures, accepted to ApJ
- Dupuy, T. J., Liu, M. C., & Ireland, M. J. 2009, The Astrophysical Journal, 699, 168, apJ, in press
- . 2011, eprint arXiv, 1103, 5747
- Fabrycky, D. C. & Murray-Clay, R. A. 2010, The Astrophysical Journal, 710, 1408
- Ferrari, A. 2007, The Astrophysical Journal, 657, 1201
- Fortney, J. J., Marley, M. S., Saumon, D., & Lodders, K. 2008, The Astrophysical Journal, 683, 1104
- Fried, D. 1966, JOSA
- Glindemann, A., Lane, R. G., & Dainty, J. C. 1993, Journal of Modern Optics, 40, 2381
- Golimowski, D., Leggett, S., & Marley... , M. 2004, The Astronomical ...
- Greenwood, D. 1976, Atmosphere
- Greenwood, D. P. 1979, Journal of the Optical Society of America, 69, 549
- Grossman, L. 1972, Geochimica et Cosmochimica Acta

- Gull, S. F. & Skilling, J. 1984, *Indirect Imaging: Measurement and Processing for Indirect Imaging*. Proceedings of an International Symposium held in Sydney, 267, ISBN: 0-521-26282-8
- Haniff, C. A., Mackay, C. D., Titterton, D. J., Sivia, D., & Baldwin, J. E. 1987, *Nature* (ISSN 0028-0836), 328, 694
- Hayashi, C. & Nakano, T. 1963, *Progress of Theoretical Physics*, 30, 460
- Hayward, T. L., Brandl, B., Pirger, B., Blacken, C., Gull, G. E., Schoenwald, J., & Houck, J. R. 2001, *The Publications of the Astronomical Society of the Pacific*, 113, 105, (c) 2001: The Astronomical Society of the Pacific
- Henry, T. J. & McCarthy, D. W. 1993, *Astronomical Journal* (ISSN 0004-6256), 106, 773
- Hinkley, S. 2009, *ProQuest Dissertations And Theses; Thesis (Ph.D.)—Columbia University*, 226
- Hinkley, S., Oppenheimer, B. R., Brenner, D., Zimmerman, N., Roberts, L. C., Parry, I. R., Soummer, R., Sivaramakrishnan, A., Simon, M., Perrin, M. D., King, D. L., Lloyd, J. P., Bouchez, A., Roberts, J. E., Dekany, R., Beichman, C., Hillenbrand, L., Burruss, R., Shao, M., & Vasisht, G. 2010, *The Astrophysical Journal*, 712, 421
- Hinkley, S., Oppenheimer, B. R., Soummer, R., Brenner, D., Graham, J. R., Perrin, M. D., Sivaramakrishnan, A., Lloyd, J. P., Roberts, L. C., & Kuhn, J. 2009, *The Astrophysical Journal*, 701, 804
- Hinkley, S., Oppenheimer, B. R., Soummer, R., Sivaramakrishnan, A., Roberts, L. C., Kuhn, J., Makidon, R. B., Perrin, M. D., Lloyd, J. P., Kratter, K., & Brenner, D. 2007, *The Astrophysical Journal*, 654, 633

- Hinkley, S., Oppenheimer, B. R., Zimmerman, N., Brenner, D., Parry, I. R., Crepp, J. R., Vasisht, G., Ligon, E., King, D., Soummer, R., Sivaramakrishnan, A., Beichman, C., Shao, M., Roberts, L. C., Bouchez, A., Dekany, R., Pueyo, L., Roberts, J. E., Lockhart, T., Zhai, C., Shelton, C., & Burruss, R. 2011, *Publications of the Astronomical Society of the Pacific*, 123, 74
- Högbom, J. A. 1974, *Astronomy and Astrophysics Supplement*, 15, 417, a&AA ID. AAA011.033.031
- Ida, S. & Lin, D. N. C. 2004, *The Astrophysical Journal*, 616, 567, (c) 2004: The American Astronomical Society
- Ireland, M. J., Kraus, A., Martinache, F., Lloyd, J. P., & Tuthill, P. G. 2008, *The Astrophysical Journal*, 678, 463, 10 pages, 6 figures, accepted for ApJ
- Jeffries, R. D. & Maxted, P. F. L. 2005, *Protostars and Planets V*, 8154
- Jennison, R. C. 1958, *Monthly Notices of the Royal Astronomical Society*, 118, 276
- Jones, H. R. A. 1997, *The Astrophysical Journal Letters*
- Keen, J., Buscher, D., & Warner, P. 2001, Arxiv preprint astro-ph
- Kirkpatrick, J. 1992, adsabs.harvard.edu
- Kirkpatrick, J. D., Reid, I. N., Liebert, J., Cutri, R. M., Nelson, B., Beichman, C. A., Dahn, C. C., Monet, D. G., Gizis, J. E., & Skrutskie, M. F. 1999, *The Astrophysical Journal*, 519, 802
- Knapp, G., Leggett, S., & Fan... , X. 2004, *The Astronomical ...*
- Kolmogorov, A. 1941, *Dokl. Akad. Nauk SSSR*, 30, 301

- Konopacky, Q. M., Ghez, A. M., Barman, T. S., Rice, E. L., Bailey, J. I., White, R. J., McLean, I. S., & Duchêne, G. 2010, *The Astrophysical Journal*, 711, 1087
- Kraus, A., Covey, K., Liu, M., Metchev, S., White, R., Prato, L., Lin, D., & Marley, M. 2009, *Astro2010: The Astronomy and Astrophysics Decadal Survey*, 2010, 163
- Kraus, A., Ireland, M., Martinache, F., & Lloyd, J. 2008, *The Astrophysical Journal*
- Kraus, A. L., Ireland, M. J., Martinache, F., & Hillenbrand, L. A. 2011, *The Astrophysical Journal*, 731, 8
- Kulkarni, S. 1989, *The Astronomical Journal*
- Kumar, S. S. 1963, *Astrophysical Journal*, 137, 1121
- Lafrenière, D., Marois, C., Doyon, R., Nadeau, D., & Artigau, É. 2007, *The Astrophysical Journal*, 660, 770
- Lane, B. F., Osorio, M. R. Z., Britton, M. C., Martin, E. L., & Kulkarni, S. R. 2001, arXiv, astro-ph
- Lane, R. G., Glindemann, A., & Dainty, J. C. 1992, *Waves in Random Media*, 2, 209
- Leggett, S. K., Allard, F., & Hauschildt, P. H. 1998, *The Astrophysical Journal*, 509, 836
- Lenzen, R., Close, L., Brandner, W., Biller, B., & Hartung, M. 2004, *Ground-based Instrumentation for Astronomy*. Edited by Alan F. M. Moorwood and Iye Masanori. *Proceedings of the SPIE*, 5492, 970

- Linfield, R. P., Colavita, M. M., & Lane, B. F. 2001, *The Astrophysical Journal*, 554, 505
- Liu, M. C., Dupuy, T. J., & Ireland, M. J. 2008, *The Astrophysical Journal*, 689, 436, apJ, in press. Typo in Eqn. 6 corrected in v2
- Lloyd, J. P., Martinache, F., Ireland, M. J., Monnier, J. D., Pravdo, S. H., Shaklan, S. B., & Tuthill, P. G. 2006, *The Astrophysical Journal*, 650, L131
- Lohmann, A. W., Weigelt, G., & Wirtitzer, B. 1983, *Applied Optics* (ISSN 0003-6935), 22, 4028
- Lunine, J., Hubbard, W., & Burrows. . . , A. 1989, *The Astrophysical . . .*
- Macintosh, B., Poyneer, L., Sivaramakrishnan, A., & Marois, C. 2005, *Astronomical Adaptive Optics Systems and Applications II*. Edited by Tyson, 5903, 170
- Macintosh, B. A., Graham, J. R., Palmer, D. W., Doyon, R., Dunn, J., Gavel, D. T., Larkin, J., Oppenheimer, B., Saddlemyer, L., Sivaramakrishnan, A., Wallace, J. K., Bauman, B., Erickson, D. A., Marois, C., Poyneer, L. A., & Soummer, R. 2008, *Adaptive Optics Systems*. Edited by Hubin, 7015, 31
- Marcy, G., Butler, R. P., Fischer, D., Vogt, S., Wright, J. T., Tinney, C. G., & Jones, H. R. A. 2005, *Progress of Theoretical Physics Supplement*, 158, 24
- Marley, M. 2007, *Proceedings of the conference In the Spirit of Bernard Lyot: The Direct Detection of Planets and Circumstellar Disks in the 21st Century*. June 04 - 08, 19
- Marley, M., Saumon, D., Guillot, T., & Freedman. . . , R. 1996, *Science*

- Marois, C., Doyon, R., Racine, R., Nadeau, D., Lafreniere, D., Vallee, P., Riopel, M., & Macintosh, B. 2005, *Journal of the Royal Astronomical Society of Canada*, 99, 130
- Marois, C., Lafrenière, D., Doyon, R., Macintosh, B., & Nadeau, D. 2006, *The Astrophysical Journal*, 641, 556
- Marois, C., Macintosh, B., Barman, T., Zuckerman, B., Song, I., Patience, J., Lafrenière, D., & Doyon, R. 2008, *Science*, 322, 1348
- Marois, C., Zuckerman, B., & Konopacky. . . , Q. 2010, *Nature*
- Martinache, F., Lloyd, J. P., Ireland, M. J., Yamada, R. S., & Tuthill, P. G. 2007, *The Astrophysical Journal*, 661, 496, 7 pages, 5 figures. Accepted for ApJ
- Martinache, F., Rojas-Ayala, B., Ireland, M. J., Lloyd, J. P., & Tuthill, P. G. 2009, *The Astrophysical Journal*, 695, 1183, 9 pages, 8 figures. Submitted to ApJ
- Mayor, M. 1995, *Nature*
- Metchev, S. A., Hillenbrand, L. A., & White, R. J. 2003, *The Astrophysical Journal*, 582, 1102
- Monnier, J. 2000, *Principles of Long Baseline Stellar Interferometry*
- . 2003, *Reports on Progress in Physics*
- Morgan, W. W., Keenan, P. C., & Kellman, E. 1943, *Chicago*, 6., ICCN: 43-2093 (BKS1); CALL NUMBER: QB881 .M6
- Nakajima, T. 1988, *JOSA A*
- . 1994, *Astrophysical Journal*, 425, 348
- Nakajima, T. & Haniff, C. A. 1993, *Astronomical Society of the Pacific*, 105, 509

- Nakajima, T., Kulkarni, S. R., Gorham, P. W., Ghez, A. M., Neugebauer, G., Oke, J. B., Prince, T. A., & Readhead, A. C. S. 1989, *Astronomical Journal* (ISSN 0004-6256), 97, 1510
- Nakajima, T., Oppenheimer, B. R., Kulkarni, S. R., Golimowski, D. A., Matthews, K., & Durrance, S. T. 1995, *Nature*, 378, 463
- Noll, R. J. 1976, *Optical Society of America*, 66, 207
- Oppenheimer, B. R., Kulkarni, S. R., Matthews, K., & Nakajima, T. 1995, *Science*, 270, 1478
- Oppenheimer, B. R., Kulkarni, S. R., Matthews, K., & van Kerkwijk, M. H. 1998, *Astrophysical Journal* v.502, 502, 932
- Osorio, M. R. Z., Lane, B. F., Pavlenko, Y., Martín, E. L., Britton, M., & Kulkarni, S. R. 2004, *The Astrophysical Journal*, 615, 958, (c) 2004: The American Astronomical Society
- Pinfield, D., Dobbie, P., Jameson, R., & Steele, I. 2003, *Monthly Notice of the Royal Astronomical Society*
- Poyneer, L. & Macintosh, B. 2004, *Journal of the Optical Society of America A*
- Pravdo, S. H., Shaklan, S. B., & Lloyd, J. 2005, arXiv, astro-ph
- Pravdo, S. H., Shaklan, S. B., Wiktorowicz, S. J., Kulkarni, S., Lloyd, J. P., Martinache, F., Tuthill, P. G., & Ireland, M. J. 2006, *The Astrophysical Journal*, 649, 389
- Racine, R., Walker, G., Nadeau, D., Doyon, R., & Marois, C. 1999, *Publications of the Astronomical Society of the Pacific*

- Raymond, S. N., Barnes, R., Veras, D., Armitage, P. J., Gorelick, N., & Greenberg, R. 2009, *The Astrophysical Journal Letters*, 696, L98
- Readhead, A., Nakajima, T., & Pearson, T. 1988, *Astronomical Journal* (ISSN 0004-6256)
- Rebolo, R., Martin, E. L., & Magazzu, A. 1992, *Astrophysical Journal*, 389, L83
- Reid, I. N., Gizis, J. E., Kirkpatrick, J. D., & Koerner, D. W. 2001, *The Astronomical Journal*, 121, 489, 38 pages, 11 figures; accepted for AJ
- Reid, I. N., Lewitus, E., Allen, P. R., Cruz, K. L., & Burgasser, A. J. 2006, *The Astronomical Journal*, 132, 891
- Reipurth, B., Jewitt, D., & Keil, K. 2007, *Protostars and Planets V*
- Roberts, J. E., Bouchez, A. H., Angione, J., Burruss, R. S., Cromer, J. L., Dekany, R. G., Guiwits, S. R., Henning, J. R., Hickey, J., Kibblewhite, E., McKenna, D. L., Moore, A. M., Petrie, H. L., Shelton, J. C., Thicksten, R. P., Trinh, T., Tripathi, R., Troy, M., Truong, T., & Velur, V. 2008, *Adaptive Optics Systems*. Edited by Hubin, 7015, 74
- Roddier, F. 1986, *Optics Communications*, 60, 145
- Schlieder, J. & Lepine, S. 2010, *The Astronomical Journal*
- Serabyn, E., Wallace, J. K., Troy, M., Mennesson, B., Haguenaer, P., Gappinger, R. O., & Bloemhof, E. E. 2006, *Advances in Adaptive Optics II*. Edited by Ellerbroek, 6272, 91
- Shaklan, S. B. & Roddier, F. 1987, *Applied Optics* (ISSN 0003-6935), 26, 2159
- Sivaramakrishnan, A., Koresko, C. D., Makidon, R. B., Berkefeld, T., & Kuchner, M. J. 2001, arXiv, astro-ph, to appear in *ApJ*, May 2001 (28 pages, 10 figs)

- Sivaramakrishnan, A., Lloyd, J. P., Hodge, P. E., & Macintosh, B. A. 2003, arXiv, astro-ph, accepted to ApJL
- Stassun, K. G., Mathieu, R. D., & Valenti, J. A. 2006, *Nature*, 440, 311
- Stevenson, D. 1986, *Astrophysics of Brown Dwarfs*
- Tatarskii, V. I. 1961
- Tatulli, E., Blind, N., Berger, J. P., Chelli, A., & Malbet, F. 2010, arXiv, astro-ph.IM
- Torres, C. A. O., Quast, G. R., da Silva, L., de La Reza, R., Melo, C. H. F., & Sterzik, M. 2006, *Astronomy and Astrophysics*, 460, 695
- Troy, M., Dekany, R., Brack, G., Shi, F., & Oppenheimer... , B. 2000, [trs-new.jpl.nasa.gov](http://trs-new.jpl.nasa.gov)
- Tsuji, T. 1995, *Laboratory and Astronomical High Resolution ...*
- Tuthill, P., Lloyd, J., Ireland, M., Martinache, F., Monnier, J., Woodruff, H., ten Brummelaar, T., Turner, N., & Townes, C. 2006, *Advances in Adaptive Optics II*. Edited by Ellerbroek, 6272, 103
- Tuthill, P. G., Monnier, J. D., Danchi, W. C., Wishnow, E. H., & Haniff, C. A. 2000, *The Publications of the Astronomical Society of the Pacific*, 112, 555, (c) 2000: The Astronomical Society of the Pacific
- Veras, D., Crepp, J. R., & Ford, E. B. 2009, *The Astrophysical Journal*, 696, 1600
- Weigelt, G. P. 1977, *Optics Communications*, 21, 55, a&AA ID. AAA020.031.281
- Wildi, F., Brusa, G., Lloyd-Hart, M., & Close... , L. 2003, *Proceedings of ...*
- Wizinowich, P. 2006, *Proceedings of SPIE*

Ziad, A., Schöck, M., Chanan, G. A., Troy, M., Dekany, R., Lane, B. F., Borgnino, J., & Martin, F. 2004, *Applied Optics*, 43, 2316

Zimmerman, N., Oppenheimer, B. R., Hinkley, S., Brenner, D., Parry, I. R., Sivaramakrishnan, A., Hillenbrand, L., Beichman, C., Crepp, J. R., Vasisht, G., Roberts, L. C., Burruss, R., King, D. L., Soummer, R., Dekany, R., Shao, M., Bouchez, A., Roberts, J. E., & Hunt, S. 2010, *The Astrophysical Journal*, 709, 733

Zimmerman, N., Sivaramakrishnan, A., Bernat, D., & et al. 2011, in preparation

Zuckerman, B. 2004, *Annu. Rev. Astron. Astrophys.*